2013

Searching for new gamma-ray sources using earth occultation imaging with the CGRO/Burst and Transient Source Experiment

Yuan Zhang
Louisiana State University and Agricultural and Mechanical College

SEARCHING FOR NEW GAMMA-RAY SOURCES USING EARTH OCCULTATION IMAGING WITH THE CGRO/BURST AND TRANSIENT SOURCE EXPERIMENT

A Dissertation

Submitted to the Graduate Faculty of the
Louisiana State University and
Agricultural and Mechanical College
in partial fulfillment of the
requirements for the degree of
Doctor of Philosophy

in

The Department of Physics & Astronomy

by
Yuan Zhang
B.A., Tsinghua University, 2006
December 2013

To Maoyuan Xie, Mom, and Dad.

Acknowledgements

First and foremost, I would like to thank my husband, Maoyuan Xie, for his tremendous support for my accomplishments in this research project. The sacrifices he has made in order for me to continue and finish this work are beyond anything I could have expected.

I would like to thank my parents, Xinhua and Yongjun, for their endless love and support during my life and especially during my time in graduate school. I would like to thank my godparents, Xiaomei and Ben Seal, and my best friends, Frances and John Hu, who provided constant encouragement and love.

I would like to thank my fellow graduate students (of which there are too many to name) for the valuable experiences we had, especially during the countless hours of homework sessions and studying. And thank you to the faculty in the physics department at LSU for being both knowledgeable and engaging. In partiular, "Thank you" to Gary Case for his mentorship. To my fellow lab mates, Brent Button, James Rodi, who helped me through research difficulties.

Also, I have to thank my friends for their countless support and friendship: to Dr. Glenn Sumners, who gave me confidence to speech in front of audience; to Dr. James Van Scotter, Dr. Joni Shreve, Dr. Young Chun, Dr. Bill Black, and Dr. Helmut Schneider, who gave me the opportunity to extend my knowledge to practice; to Dr. Pamela Pike, for giving me opportunity to continue my piano journey; and to my old roommates, Limin Xiao, Wanli Xu, Gaomin Wang, Wanshu Zhang, for the good times we had.

Finally, I extend thanks to my Ph.D. committee for providing VERY helpful comments and suggestions. In particular, I thank my advisor, Mike Cherry, for providing me with the

opportunity in his laboratory, steering my research focus, and for his patience during my never-ending research.

This work has been supported by the NASA/Louisiana Board of Regents Cooperative Agreement NNX07AT62A (LSU). This material is based upon work supported by High Performance Computing (HPC) @LSU computing resources as well as the Louisiana Optical Network Institute (LONI).

Table of Contents

List of Tables

List of Figures

Abstract

Earth occultation provides a means of monitoring gamma-ray sources over the entire sky. This technique has been demonstrated with the Burst And Transient Source Experiment (BATSE) on the Compton Gamma Ray Observatory (CGRO) active from 1991 to 2000, and is now being used with the Gamma-ray Burst Monitor (GBM) instrument on the Fermi mission. Although this approach provides a powerful wide field monitoring capability, the BATSE and GBM implementations of this technique have so far limited the analysis to a catalog of previously identified sources. In this dissertation, an indirect imaging method is described that permits searching for unknown sources by applying the Differential Filter Technique to archival BATSE data. Using this technique, occultation steps are transformed into gaussian-like features with amplitudes corresponding to the intensities measured from each pixel in the sky. With approximately 85% of the sky occulted every spacecraft orbit, the ~ 51 day precession period of the CGRO orbit makes it possible to perform an all-sky survey. By comparing both significance and the shape of the source of interest, we can finalize both known and unknown sources with spatial resolution to less than 0.5°. A reanalysis of the BATSE data has been performed, making it possible to complete the BATSE catalog of high energy sources, to address long-standing questions of systematic effects in the BATSE results, and to compare the new BATSE results to the current Fermi/GBM catalog in order to perform a study over 22 years of variations in the hard X-ray/low energy gamma-ray sky.

Chapter 1
Introduction

1.1 Astrophysical Motivation

The soft gamma-ray sky, covering three decades in energy from 30 keV to 30 MeV, is an important region in high-energy astrophysics. Many of the most intrinsically interesting objects in the universe emit much of their primary energy in this regime. These include gamma-ray bursts (GRB), the super-massive black holes that power the central engines of Active Galactic Nuclei (AGN), accreting binaries, very luminous yet heavily obscured x-ray sources such as Cygnus X-3, frequently observed outbursts of brilliant galactic γ-ray transients emitting on time scales ranging from a few minutes to months (e.g., GRO J0422+32, GRO J1719-24), micro-quasars including GRS 1915+105 and GRO J1655-40, neutron stars and supernova remnants like the Crab, and stellar-mass black holes such as Cygnus X-1.

In this energy regime when the number of sources is modest, an instrument with a large Field of View (FOV) may make it possible to observe many sources in a single observation, enabling an all-sky survey. Wide field imaging detectors can also have a large gain in sensitivity over narrow field pointed instruments if it is possible to measure the background at the same time as the source, thereby reducing the amount of time needed to observe. Finally, the ability to locate a source with an image potentially allows comparison with measurements made at different times with different instruments at different wavelengths. This depends on the resolution and is a major issue for the Burst And Transient Source Experiment (BATSE) on the CGRO mission and the Gamma-ray Burst Monitor (GBM) on Fermi.

Because gamma-rays are penetrating and have short wavelength, they are difficult to image, yet for the same reason they carry directly the primary evidence about heavily obscured sources that are otherwise unobservable. Since the birth of gamma-ray astronomy in the 1950's, substantial efforts to map the gamma-ray sky in the 30 keV - 30 MeV region have been made by several experiments, e.g. HEAO-1 A4 (Levine et al., 1984), COMPTEL (Schonfelder et al., 1995), CGRO/ BATSE(Harmon et al., 2002, Ling et al., 2000), INTEGRAL/ IBIS (Krivonos et al., 2010), and SWIFT (Baumgartner et al., 2013). A full survey of the gamma-ray sky is still relatively incomplete, especially in the region between 100 keV and a few MeV. This is due in part to a combination of at least four significant experimental obstacles:

- Source photon fluxes are typically quite low, generally decreasing with energy like E^{-2} or faster, requiring large areas, massive detectors, and long exposure times.

- Because of the highly penetrating nature of γ rays over 100 keV, the point response functions (PRFs) of collimated and coded aperture instruments tend to deteriorate rapidly at higher energies, making source confusion problems an increasingly serious problem above 100 keV.

- Non-γ-ray backgrounds are typically large, highly variable on timescales of an orbit (90 min in low earth orbit) or less, and complex combinations of many effects, frequently causing serious problems with systematic errors induced by imperfect background subtraction.

- Cosmic sources are frequently highly variable on a wide range of time scales, so that long, deep observations with sensitive small-field-of-view experiments risk missing source activity elsewhere in the sky.

In the hard X-ray and gamma ray energy band, existing all-sky maps have been produced by INTEGRAL(Fig. 1.1), Swift (Fig. 1.2), EGRET on CGRO (Fig. 1.3) and lately LAT on

Fermi (Fig. 1.4). INTEGRAL covers 17-60 keV with 7 years of data, Swift covers 14-195 keV with over 5 years of data, EGRET covers > 100MeV, and LAT sees from 100 MeV to 30 GeV with its best sensitivity above 10 GeV. A big gap is left from 200 keV to 100 MeV which can be filled by BATSE and GBM. GBM is an on-going experiment with real-time data, but BATSE has the longest data archive, containing 9 years of data, from 1991 to 2000. BATSE complements the instruments mentioned above by monitoring the energy range from 20 keV up to about 1 MeV. This covers the lower energy portion of the nonthermal regime, where the emission is produced by a variety of processes such as Compton scattering of soft photons by energetic particles, bremsstrahlung, and synchrotron radiation.

The purpose of this dissertation is to reanalyze the BATSE archival data to complete the BATSE catalog of high energy sources, to address long-standing questions of systematic effects in the BATSE results, to present lightcurves and spectra for the first time for the full catalog of BATSE sources, and to compare the new BATSE result to the current Fermi/GBM result in order to perform a study over 22 years of variations in the hard X-ray/low energy gamma-ray sky.

1.2 Burst and Transient Source Experiment (BATSE)

The Compton Gamma Ray Observatory (CGRO), one of NASA's four Great Observatories, was launched in April 1991 and operated in low Earth orbit until controlled re-entry in June 2000. BATSE on CGRO was primarily designed to study gamma-ray bursts, although the detectors also recorded data from pulsars, terrestrial gamma-ray flashes, soft gamma repeaters, black holes, and other exotic astrophysical objects over the energy range of 20 keV to 1.9 MeV.

BATSE consisted of eight large uncollimated detector modules arranged on the corners of the CGRO with normal vectors perpendicular to the faces of a regular octahedron. Any point on the sky could be viewed by four detectors at angles less than 90° to the source direction. This made BATSE capable of obtaining rough locations within a few degrees,

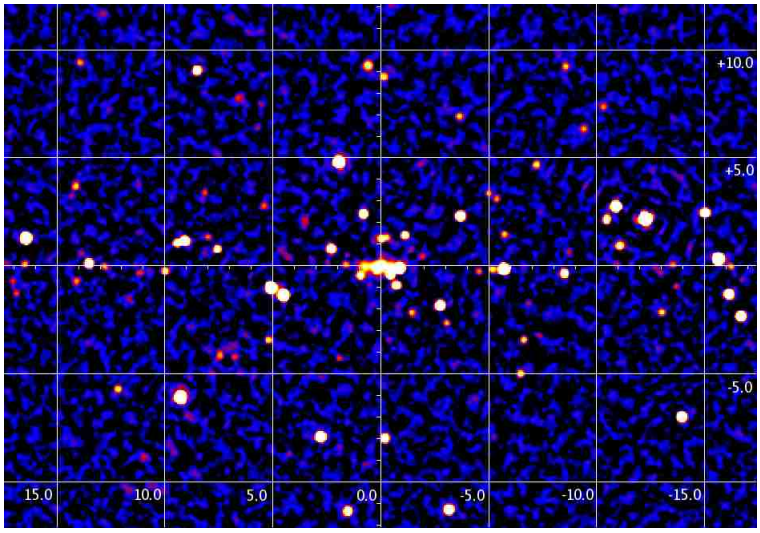

Figure 1.1: INTEGRAL Map of the Galactic Bulge region accumulated over seven years 2003-2012. This map is s mosaic image of the individual sky observations performed with IBIS/ISGRI in the 17-60 keV energy band (Krivonos et al., 2012).

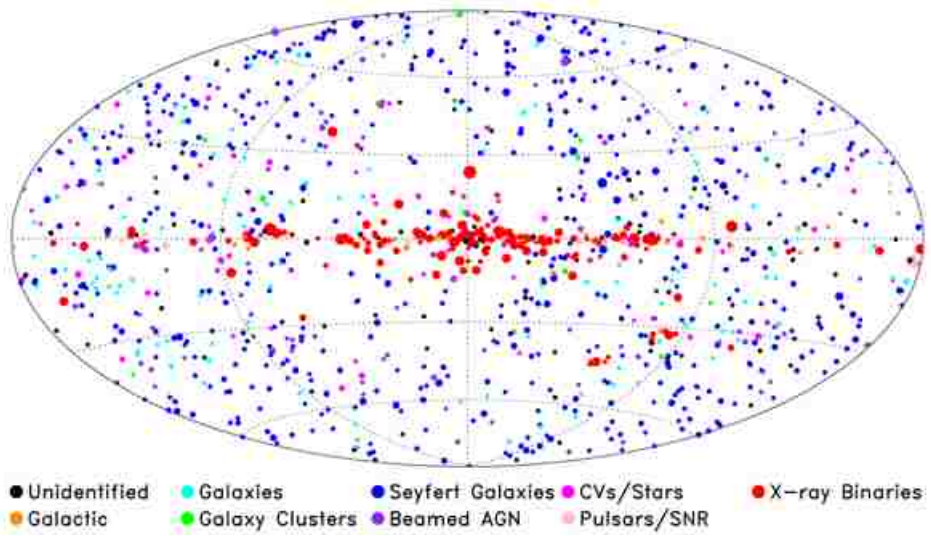

Figure 1.2: All sky map showing classfication of SWIFT BAT 70-month survey sources over the energy range of 14-195 keV. The figure uses an Aitoff projection in Galactic coordinates; the flux of the source is proportional to the size of the circle. The source type is encoded by the color of the circle (Baumgartner et al., 2013).

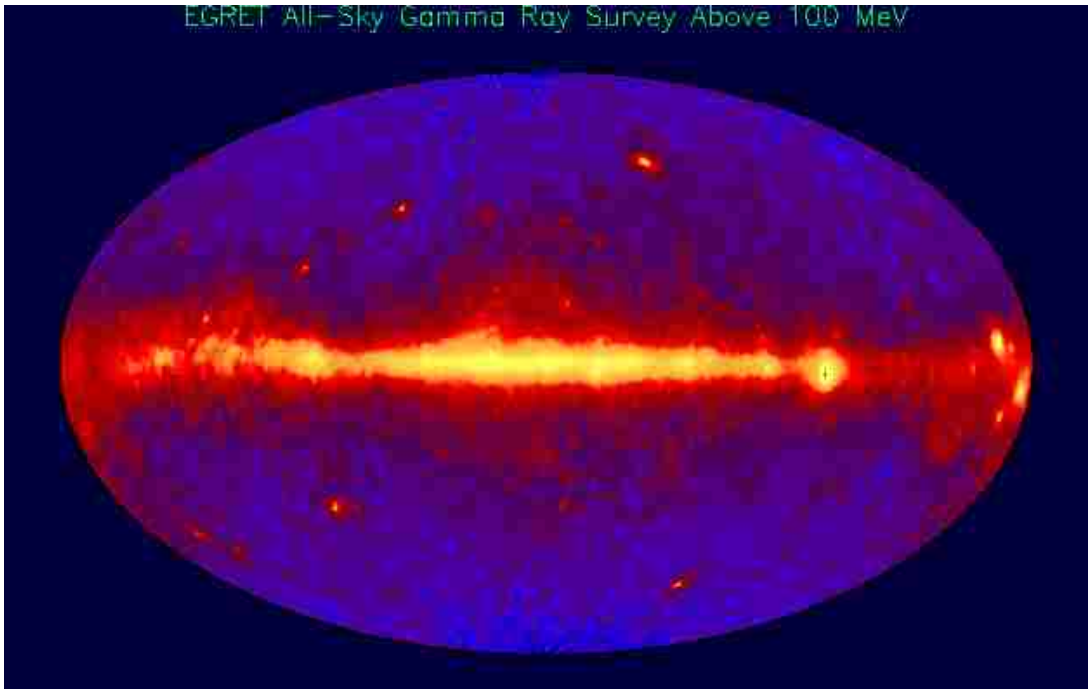

Figure 1.3: EGRET all sky map in gamma-rays above 100 MeV. Credit: EGRET Team.

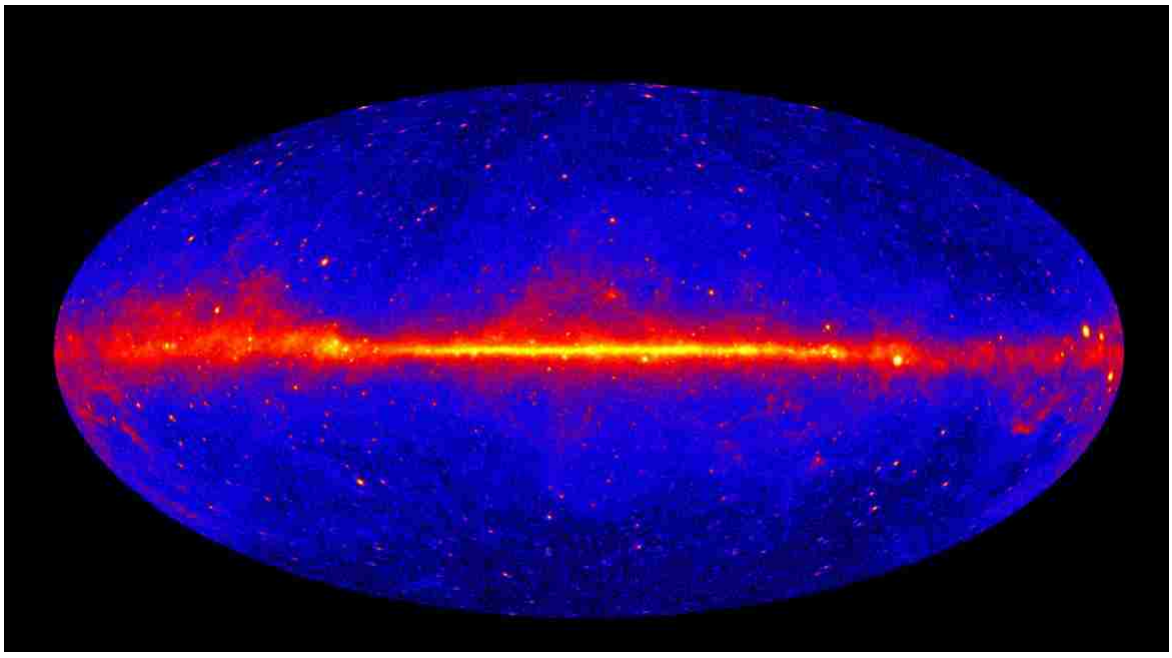

Figure 1.4: This view shows the entire sky at energies greater than 1 GeV based on five years of data from the LAT instrument on the Fermi Gamma-ray Space Telescope. Brighter colors indicate brighter gamma-ray sources. Credit: NASA/DOE/Fermi LAT Collaboration.

using the count rate calculated from numbers of photons and the known response matrix of each detector. Each detector module contained a Large-Area Detector (LAD) optimized for sensitivity and directional response, and a spectroscopy detector (SD) optimized for broad energy coverage and energy resolution. Since the SDs had a much smaller effective area for source monitoring ($\sim 600cm^2$), our study focuses on the LAD detectors, which are composed of sodium iodide (NaI(T1)) crystals 1.27 cm (0.5 inch) thick by 50.8 cm (20 inch) across ($2025cm^2$ total sensitive area for one detector). They were operated over the energy range of 20 keV - 1.9 MeV.

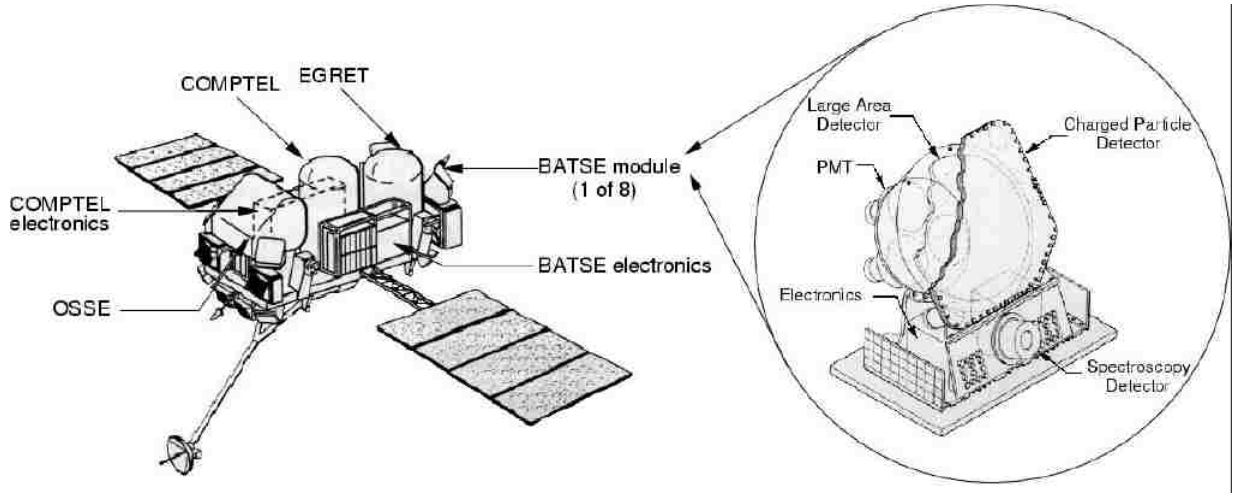

Figure 1.5: The Compton Gamma-Ray Observatory and one of the 8 BATSE detector modules (drawings courtesy of the National Space Science and Technology Centre, Huntsville, AL, USA).

BATSE was a highly successful experiment that provided the largest GRB database from a single experiment, consisting of observational data for 2704 GRBs (Paciesas et al., 1999). Earth occultation techniques were developed by both the Marshall Space Flight Center (MSFC) (Harmon et al., 2002) and Jet Propulsion Laboratory (JPL) (Ling et al., 2000) to permit a survey for steady sources and also allow fast monitoring by BATSE of bright transient or flaring sources by searching through the count rates for steplike occultation features. Examples of the use of this technique are the discovery of the gamma-ray sources GRS 1716- 249 (Ballet et al., 1993), GRO 0422+32 (Harmon et al., 1992b) and observations

of the X-ray nova 4U 1543-47 (Harmon et al., 1992a). The BATSE catalog of Ling et al., (2000) significantly extends the source information presented in the HEAO 1 A-4 catalog (Levine et al. 1984) by focusing on 34 of the stronger HEAO sources which have an average 35-200 keV flux over the 1200 day period of $\geq$ 20 mCrab. Thirty-three of 34 sources have shown positive flux, compared to 14 observed by HEAO 1 A-4. Harmon et al. (2004) expanded the catalog to 58 long-term monitored sources and 83 deep sample sources. These sources are classified into three classes: accreting black hole and neutron star binaries, active galaxies, and supernova remnants.

Both the Earth Occultation Technique (EOT) at MSFC (Harmon et al., 2002, 2004) and the Enhanced BATSE Occultation Package (EBOP) at JPL (Ling et al., 2000) used a predetermined catalog of sources to calculate occultation times. The EOT fit a 4-minute window of count rate data to a quadratic background plus an occultation step model for each source that occults during that period, while EBOP fit all the data for a day at once using a semi-physical background model. The EBOP background model was calculated from a complex multi-component model in order to account for such contributions as the local position in low Earth orbit and cosmic-ray interactions with the satellite (Ling et al., 2000). The expectation of the EBOP approach was that greater sensitivity could be achieved summing data over a full day than was possible with the EOT.

These two methods resulted in significant differences in flux measurements for some sources, especially above 100 keV (Harmon et al., 2004). Fig 1.6 shows examples of the potentially very interesting hard tails observed by EBOP for some sources but not confirmed by EOT. In addition, the high energy flux observed from some sources (e.g. Cyg X-1 and GRS 1915+105) is dependent on the orbital phase of the satellite. A possible cause of such variability could be high energy sources not included in the source catalog. Generating images in the 100-300 keV energy range presents an opportunity to test this hypothesis by searching for unaccounted-for high-energy sources. If no additional sources are detected, that suggests the discrepancies are likely not due to unaccounted-for sources. A more likely

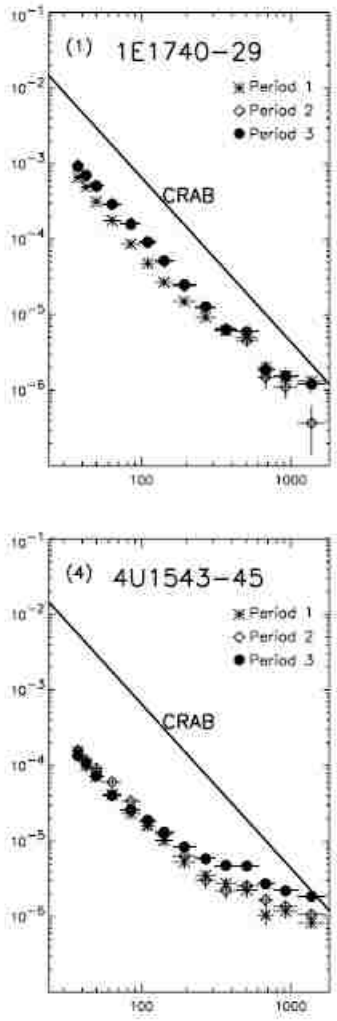

Figure 1.6: The EBOP Spectra for 1E 1740-29 and 4U 1543-45 using the first 3 years of BATSE data (Ling et al., 2000). Both sources show evidence of hard tails above 300 keV. Period 1,2,3 are the first three orbital precession periods, TJD 8393 - TJD 8942, TJD 8944 - TJD 9236, TJD 9237 - TJD 9628, respectively. A power law fit to the Crab spectrum is shown for comparison.

cause in that case is inaccuracies in the EBOP background model.

1.3 Gamma-Ray Burst Monitor (GBM)

After BATSE's success using the Earth Occultation Technique (EOT), the Gamma-Ray Burst Monitor (GBM) was developed as one of two instruments on board the Fermi satellite, which was launched in June 2008 to an orbit of 555 km with an orbital inclination of 25.6°

(Meegan et al., 2009). GBM is comprised of 12 Sodium Iodide (NaI) detectors with 12.7 cm diameter and 1.27 cm thickness and two Bismuth Germanate (BGO) detectors with 12.7 cm diameter and 12.7 cm thickness. The NaI detectors cover energies from 8 keV to 1 MeV, and the BGO detectors cover $\sim$ 200 keV to $\sim$ 40 MeV.

GBM has a large field of view that enables monitoring of numerous sources on a daily basis to look for long-term variability from sources. GBM also covers a broad energy range (8 keV to $\sim$ 40 MeV). GBM is currently the only wide field-of-view X-ray mission able to observe at energies above $\sim$ 200 keV. The Earth Occultation Technique (EOT) has been applied to GBM since launch in 2008 and has produced a number of noteworthy results during the first five years of the mission (Wilson-Hodge et al., 2012). One such result is the public availability of the daily lightcurves of the $\sim$ 200 sources in the GBM source catalog. These data are posted online for use by the scientific community (http://heastro.phys.lsu.edu/gbm).

A catalog of results above 100 keV has been published (Case et al., 2012) together with a catalog of results over the entire energy range from the first three years of occultation analysis (Wilson-Hodge et al., 2012). In the Wilson-Hodge et al. (2012) paper, fluxes and errors for 209 sources and source coordinates are reported in four broad energy bands (12-25, 25-50, 50-100, and 100-300 keV).

The BATSE and GBM capabilities are compared in Table 1.1. The two instruments together provide a 22-year record of the hard X-ray/low energy gamma-ray sky observed using the same Earth Occultation Technique with similar systematics and capabilities. A goal of this work is to apply new analysis techniques developed for GBM to the archival BATSE data, and to assemble a 22-year history of the sources observed by the two instruments.

1.4 Plan of the Dissertation

The goal of this dissertation is to apply an imaging technique to the BATSE Earth Occultation analysis to search for sources not included in the original BATSE catalogs, to attempt to eliminate unaccounted-for systematics especially at high energies, and to compare the

Table 1.1: Comparison of BATSE and GBM detector parameters.

	BATSE	GBM
Total Mass	850 kg	115 kg
Trigger Threshold	$\approx 0.2 ph/cm^2/s$	$0.61 ph/cm^2/s$
Telemetry Rate	3.55 kbps	15-25 kbps
	Large Area Detectors	Low-Energy Detectors
Material	NaI	NaI
Number	8	12
Area	2025 cm^2	126 cm^2
Thickness	1.27 cm	1.27 cm
Energy range	25 keV to 1.9 MeV	8 keV to 1 MeV

BATSE and GBM fluxes over a 22-year observation period in order to look for evidence of long-term variability in the hard X-ray sources detected by BATSE and GBM.

In Chap. 2 the Earth Occultation Technique (EOT) will be described along with a history of past occultation observations, including lunar occultations and use of EOT with the BATSE experiment. Chap. 3 explores imaging with Earth occultations and discusses previous work done in this area. Also, the imaging algorithm that has been developed for BATSE and GBM, Imaging with a Differential filter using the Earth Occultation Method (IDEOM), will be described. The results of analysis with IDEOM applied to 9 years of BATSE data in four energy ranges (23-98 keV, 98-230 keV, 230-595 keV, and 595-1798 keV) will be presented and discussed in Chap. 4. Chap. 5 introduces the Enhanced BATSE Occultation Package (EBOP) developed by JPL in 1997 and its implementation at LSU. Chap. 6 presents the lightcurve and spectral analysis results for the new Catalog 2013 sources, including 15 newly discovered BATSE sources. A discussion of the long-standing issue of systematic effects in the BATSE results is included here. It also covers the analysis of those sources detected by both GBM and BATSE. A 22-year combined lightcurve analysis shows significantly different behavior in 7 sources. Chap. 7 is the final conclusion.

Chapter 2
BATSE and Earth Occultation Technique

INTEGRAL (Krivonos et al., 2010) and SWIFT (Baumgartner et al., 2013) have demonstrated the capability of coded aperture detectors to do high resolution imaging. BATSE used the Earth Occultation Technique for observing sources with simple uncollimated, low spatial resolution detectors. At the CGRO orbital altitude of about 450 km, about 33% of the sky is occulted by the Earth at any given time. It was realised before the CGRO launch that the angular resolution for non-transient gamma-ray sources could be greatly improved over that obtainable for GRBs with knowledge of the position on the sky of the Earth limb (Fishman et al. 1982; Paciesas et al. 1985; Fishman et al. 1989). By measuring the change in count rate as a source moved behind or emerged past the Earth's limb, the flux could be determined for sources in a predetermined catalog. The method allowed BATSE to be very successful at observing a catalog of persistent sources, studying variable sources on timescales of hours to years, detecting unusual intensity or spectral changes, and stimulating observations in other wavelength bands.

The use of occultation by celestial bodies to measure the X-ray flux from astrophysical sources was not a new technique. The first use of occultation in X-rays was by Bowyer et al. (1964) using lunar occultation to observe the Crab Nebula. This experiment involved a rocket launch timed to observe the Crab while the central region of the nebula went into occultation. The goal of the mission was to determine whether the emission from the central region of the nebula was due to a point source or an extended source, with a point source expected to be a neutron star. A similar experiment was conducted by Palmieri et al. (1975)

with the intent to measure the X-ray size of the Crab nebula and its brightness variability. Also, the position of the low mass X-ray binary GX 9+1 was measured using lunar occultation with the *Copernicus* satellite (Davison & Morrison, 1977), and a motivation for the 90 hour orbit of the *EXOSAT* mission was to increase the number of observable lunar occultations (White & Peacock, 1988).

Because the Earth covers $\sim 33\%$ of the sky as seen by BATSE, however, Earth Occultation made it possible to monitor a much larger catalog of sources than could be observed with Lunar Occultations.

2.1 Earth Occultation Technique with BATSE

Earth Occultation makes it possible to monitor known sources with simple non-pixellated or low spatial resolution detectors by using the Earth as a temporal modulator of the gamma-ray flux. The technique can use data from both the BATSE SDs and LADs (see McNamara et al. (1998)); however, considering size and sensitivity, only data from the LADs has been used in this work.

The Earth, seen from a BATSE detector (Fig. 2.1), has a diameter of $\sim 140°$. As gamma-ray emitting objects set below the Earth's limb, downward steps appear in the detector count rate and vice-versa for rising steps (Fig. 2.2). The height above the background of the steps gives a direct measurement of the count rate of the occulted source.

Together with the detector orientation and the relative spacecraft position with respect to the Earth, it is possible to project the Earth's limb on the sky at the time of the source occultation. Then, an image of the gamma-ray emission from the sky can be constructed by building up the projections of the Earth's limb from many occultations. The intrinsic angular resolution depends on the duration of the rise (or set) time of an occultation step.

In one orbit around the Earth, two occultation step features, a rise and set pair, typically will be superimposed on the background counting rate as each point source is occulted. A measurement can be made of the intensity of a source in each energy channel for rise or set.

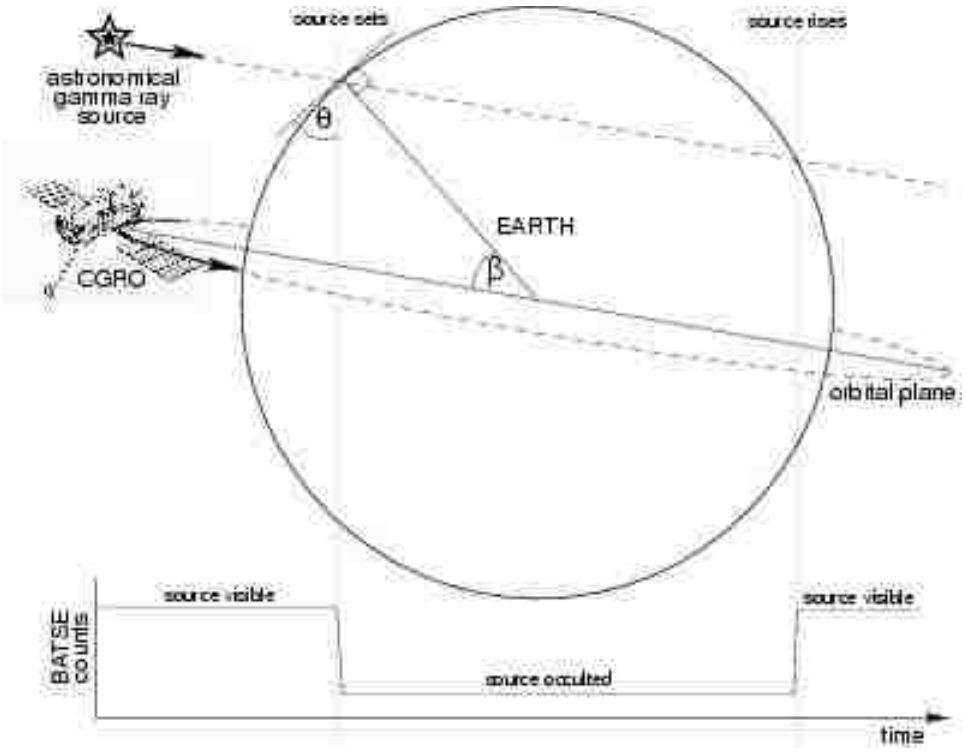

Figure 2.1: A schematic illustrating the geometry of the Earth Occultation technique for detecting astronomical gamma-ray sources with BATSE. The occultation angle, β, is defined as the angle between the orbital plane and the object measured at the spacecraft (Shaw et al., 2004).

In practice, two measurements per every orbit are not achieved. The most common reasons are passages through the lower Van Allen radiation belt at the South Atlantic Anomaly when the detector voltage is turned off, or periods when CGRO is out of line-of-sight contact with the NASA Tracking & Data Relay Satellites (TDRSS), or times when data have been flagged and are not available for analysis. High declination sources ($\sim \delta > 41°$) also experience an interruption of occultations near the orbital poles. Source confusion, where occultations of one source are indistinguishable from another, also limits the number of usable occultation steps. The impact of these effects combined causes Earth occultation coverage averaged over one precession cycle ($\sim 52d$) to range between $80\% - 90\%$ at best, and at worst about 50%.

2.1.1 Step Fitting

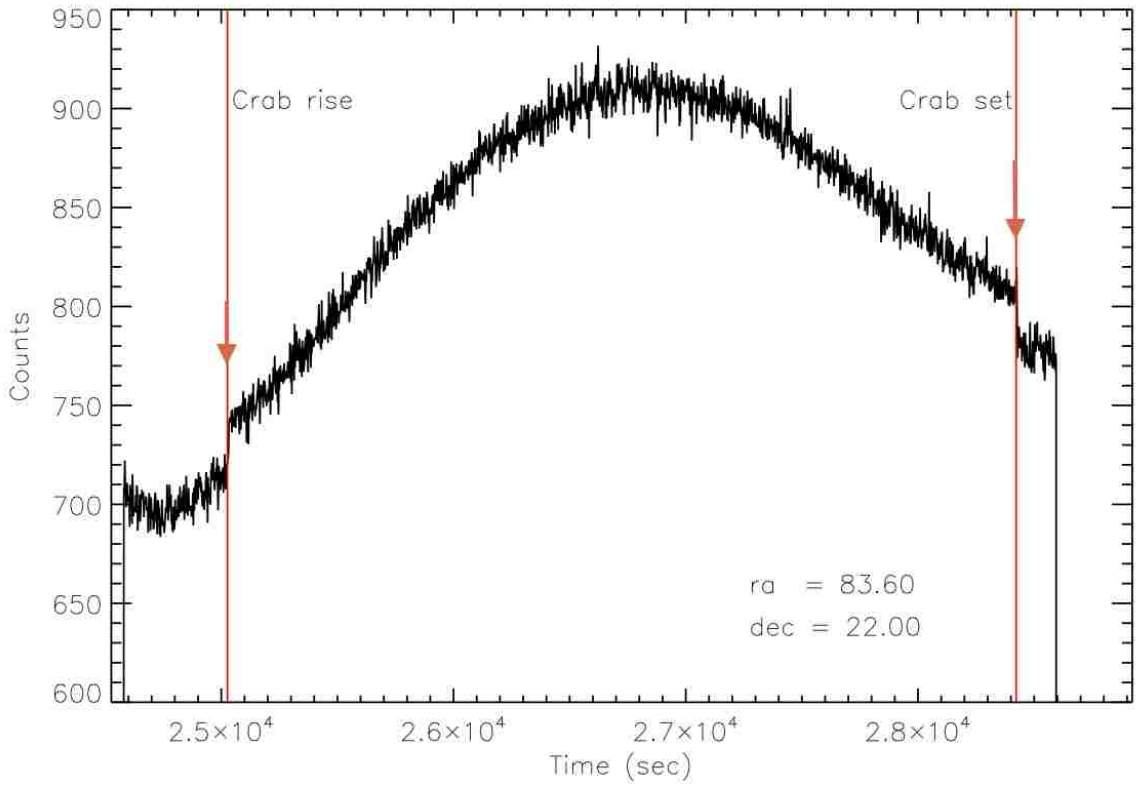

Figure 2.2: A typical set of rising and setting steps of the Crab on TJD 8393. The occultation times were 25026.39 sec and 28422.25 sec respectively.

In the Marshall EOT approach (Harmon et al., 2002), an occultation model is fit to a 4-minute window of count rate data with the window centered on the predetermined occultation time of the source of interest. The model is composed of a quadratic background model plus source models for each source that occults during that time period. Typically the background is smooth and slowly varying and thus is well fit to a quadratic polynomial. A source model consists of an assumed source spectrum combined with an atmospheric transmission model that is convolved with the time-dependent detector response. A scale factor is calculated for each detector that views the source of interest within 60° of the detector normal for each energy band by fitting the occultation window model to the data. The weighted average of the scale factors for the source of interest is calculated for each

energy band and then multiplied by the predicted flux to determine the measured flux. The analysis was performed for a predetermined catalog of 140 possible sources with known occultation times.

The Enhanced BATSE Occultation Package (EBOP) was developed by the Jet Propulsion Laboratory (JPL) group (Ling et al., 2000), and was applied to BATSE data to fit the occultation steps. Like EOT, the EBOP system also requires a catalog of known sources as input. It consists of two large parts, (a) the linear Earth occultation model analysis, which estimates backgrounds, count rates, and uncertainties for cosmic sources in each LAD and each energy channel, and (b) the spectral analysis section. This includes the XSPEC interface (Arnaud et al., 1996) which converts from instrument units (count rate) to physical units (photon fluxes) using the LAD response matrix, XSPEC itself, and MULPLOT, a package of displaying and manipulating the output. EBOP handles all the sources in the catalog at one time.

For known sources, a fitting procedure is used on a 240 second fitting window, centered at the expected occultation time bin. For each LAD and energy channel the model fit consists of a quadratic curve describing the background and a set of response vectors that model the effects of all sources contained within the fit window. EBOP sums up a day of data at a time before performing its fitting. The goal here was to improve the statistics over the individual occultation step approach of EOT. However, the sensitivity of the step searching technique is limited by the difficulty in accurately determining the background over several orbits, by non-statistical noise introduced by bright pulsating sources with periods of order a few minutes, such as Vela X-1, and by unknown sources. In particular, unknown sources in the background may introduce unknown systematic effects into the EBOP analysis.

2.1.2 Occultation Transition Duration

Since the variation of the column density of the Earth's atmosphere at different altitudes affects the absorption of gamma-rays, the transit duration from full transmission to 50%

attenuation for an occulted source, Δt, is defined as the energy-dependent duration of one occultation step. For a typical orbital speed of $8km/s$, Δt is ~ 9 seconds for normal incidence, and about $10 \sim 20$ seconds for more oblique angles (larger β, see Fig. 2.1):

$$\Delta t \approx (\frac{P_{orb}}{2\pi})(\frac{\Delta h}{r_{sc}\cos(\theta_{occ})})(\frac{\sin(\theta_{occ})}{\sqrt{\cos^2(\beta) - \cos^2(\theta_{occ})}}), \tag{2.1}$$

where P_{orb} is the orbital period of the satellite, Δh is the altitude difference between 90% transmission and 10% transmission, r_{sc} is the distance between the spacecraft and the center of the Earth, β is the occultation angle measured at the geocenter between the orbital plane and the source, and θ_{occ} is the angle between the source and the spacecraft at the time of the occultation (Harmon et al., 2002). The angle θ_{occ} is defined to be

$$\theta_{occ} = \sin^{-1}(\frac{r_E + h_{occ}}{r_{sc}}), \tag{2.2}$$

where r_E is the radius of the Earth and h_{occ} is the height above the atmosphere corresponding to 50% transmission. For BATSE, typically $r_{sc} = 7328.1$ km, $h_{occ} = 70$ km at 23-98 keV, and $r_E = 6878.1$ km, resulting in $\theta_{occ} = 71.3°$. Using this value of θ_{occ} with $P_{orb} = 90$ min, and $\Delta h = 25$ km, results in

$$\Delta t \approx \frac{8.75}{\sqrt{cos^2(\beta) - 0.101}} \text{ s} \sim \frac{8.75}{\cos\beta} \text{ s}, \tag{2.3}$$

corresponding to a typical angular resolution

$$\Delta\theta = \frac{\Delta t}{90min} \times 360° \sim 0.5°. \tag{2.4}$$

Atmospheric Transmission

The model of the atmospheric transmission is

$$T(t) = e^{-\mu(E)A(h(t))} \tag{2.5}$$

where $\mu(E)$ is the attenuation coefficient of the photons at energy E and $A(h)$ the airmass along the line of sight at an altitude $h(t)$. $A(h)$ is interpolated from a table of air masses for values of altitude h between 50 and 110 km, and is based on the US International Commercial Aviation Organization (ICAO) Standard Atmosphere (1976). The occultation time is defined when the transmission equals 50%.

As the source occultation happens further away from the orbital plane, Δt increases as $1/cos(\beta)$, where β is the occultation angle measured at the geocenter between the orbital plane and the source. For a source seen by a satellite with orbital period P, the occultation duration can be translated to an angle of $360^\circ \times \Delta t/P$. This is the optimum angular resolution for imaging a source that is obtainable with EOT. Hence, for BATSE, the optimum angular resolution is $\sim 0.58^\circ$.

The inclination of the CGRO orbit was 28° with a precession period of $49 - 53$ days. Given these, the whole sky could be occulted during the precession period, although regions of sky near the poles with $\mid \delta \mid > 41^\circ$ receive less coverage than the rest of the sky. In total, including effects for flagged data etc., 50% to 90% of the entire sky can be observed in any precession period (Fig. 2.3).

2.1.3 Sensitivity

As stated in Harmon et al. (2001), considering the sensitivity of Earth occultation without complicating factors such as nearby point sources and imperfections in the detector response function, for both EOT and EBOP, the sensitivity of the analysis with the BATSE LADs depends on several factors. The uncollimated detector geometry of the LADs and the fixed

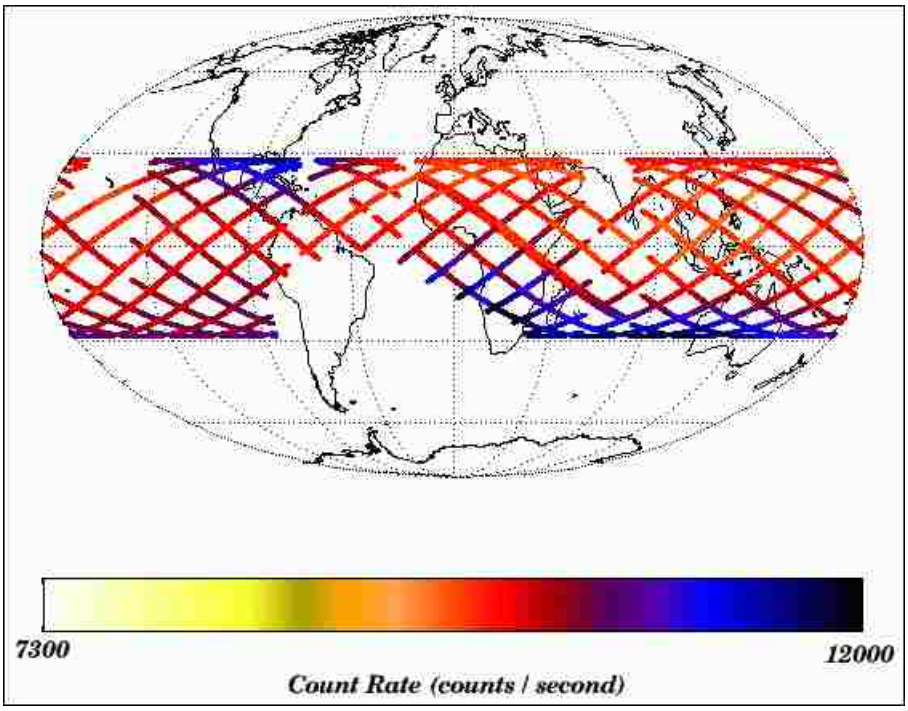

Figure 2.3: This image shows a typical one-day orbit of the Compton Gamma-Ray Observatory. The orbital inclination is 28 degrees, at an average altitude of approximately 470 km. The colors correspond to the count rates recorded by all eight BATSE Large Area Detectors (datatype DISCLA Channel 2). The temporal resolution of this datatype is 1.024 seconds. Darker colors correspond to higher count rates. Note how the count rate increases at high latitudes. The large gap in the orbit is the South Atlantic Anomaly (SAA). The high voltage power supply for the BATSE detectors is turned off when the spacecraft is in this region because of the high concentration of charged particles in the SAA. The SAA is due to the offset of the magnetic dipole field from the the center of the Earth, which causes charged particles to accumulate over the region (Harmon et al., 2002).

orientation of CGRO with respect to the sky (for a single pointing period) generates continuously varying backgrounds which range over a factor of two or more. The lower energy background (up to $\sim$ 100 keV) is dominated by the modulation of the diffuse sky flux by the Earth and at higher energies by the cosmic ray secondary radiation. Thus the low energy background exhibits a slow sinusoidal variation with the orbital period of the spacecraft. At high energy, the background is modulated more rapidly due to the changes in magnetic field strength and direction. Furthermore, a given source exposes a combination of several detectors at different angles. The effective area of the LAD (the product of the geometric area

and the efficiency) is also a strong function of energy just above the lower energy threshold due to the entrance window attenuation. It decreases more slowly at higher energies from Compton leakage. All these factors combine to produce complex energy and time-dependent variations in the background and instrument response.

Chapter 3
Imaging with Earth Occultation

3.1 Introduction

Both EOT and EBOP require an input catalog of source positions to predict occultation times and thus measure source fluxes. This requirement means that an imaging method is needed to locate sources not in the input catalog. Hard X-ray imaging presents challenges not faced at lower energies. Imaging at optical wavelengths uses the traditional methods of refractive lenses and mirrors producing a direct image on a focal plane. Higher energy photons are more difficult to focus. At soft X-ray energies ($\sim 0.1 - 10$ keV), photons can be focused using parabolic mirrors shaped so that photons enter at grazing angles which allows for total reflection down to the focal plane (Giacconi et al., 1972). Such an optical design was employed with the *Chandra* soft X-ray satellite. This basic design has also been used for the *NuSTAR* mission (5-80 keV), the first direct imaging satellite in the hard X-rays (Harrison et al., 2010).

A common design for imaging at hard X-ray and soft γ-ray energies (10 - 200 keV) employs an indirect imaging method using a coded aperture, e.g. *Swift*/BAT (Baumgartner et al., 2013) and *INTEGRAL*/SPI (Krivonos et al., 2010). This technique spatially modulates incident photons through a "coded mask" onto a detector plane below, resulting in a shadow pattern (Caroli et al., 1987). Using the known mask pattern, the shadow pattern can be deconvolved to form an image.

Several indirect imaging methods have been developed using Earth occultation. Occultation transform imaging (Zhang et al., 1993, 1994, 1995) and the Likelihood Imaging

Method for BATSE Occultation data (LIMBO, Shaw et al., 2004) were developed for use with BATSE, and Imaging with a Differential filter using the Earth Occultation Method (IDEOM) (Rodi 2013, Rodi et al., 2013) has been developed for GBM and adapted for BATSE (Zhang et al., 2012). Earth occultation imaging takes advantage of the wide field of view of BATSE and GBM to image large parts of the sky, which is not practical with *NuSTAR*'s $\sim 10'$ field of view. It also uses simple, uncollimated, non-imaging detectors (~ 10 detectors) unlike coded aperture imaging that requires a heavy mask of lead or tungsten and a read out channel for each detector pixel ($> 32,000$ channels for BAT (Barthelmy et al., 2005)).

Earth occultation imaging methods are tomographic methods that build images of the sky using projections of the Earth's limb on the sky. Because the detectors are uncollimated, the detector count-rate gives a measure of the brightness of the visible sky. Thus for a detector facing the Earth, the time derivative of the count rate is proportional to the line integral of the flux along the Earth's limb (Shaw et al., 2004) superimposed on changes in the background. For a point on the sky, the flux (line integral) is measured along different angles with respect to the Earth's limb for rise and set steps giving different projections on the sky. During the orbital precession period of the satellite, a source's elevation angle β (Fig. 2.1) changes, thus sampling all the available projection angles for that point on the sky. Following Rodi (2013) and Rodi et al. (2013), Figs. 3.1 - 3.5 show sampled projections from a single orbit for the Crab (declination of 22.01°) at $\sim$ 10 day intervals during the precession period from TJD 8407 to TJD 8447 (May 31, 1991 to July 10, 1991). The solid line marks the rise limb, and the dotted line marks the set limb. As the β angle changes, the rise/set limb projections cross the Crab's position at different angles. Fig. 3.6 overplots the sampled projections from the previous six figures to demonstrate how Earth occultation imaging samples a range of projections during an orbital precession period. The projections do not completely sample the entire region around the Crab, missing areas at roughly the same declination. The range of projection angles sampled is declination dependent with

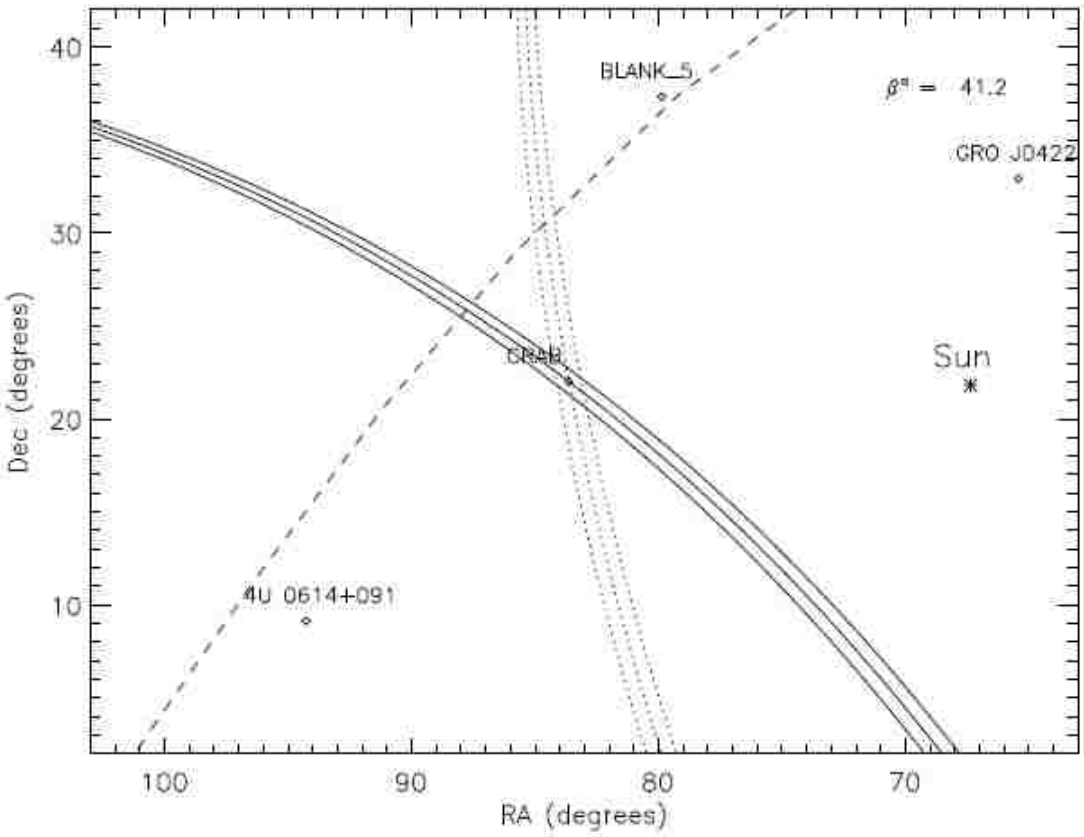

Figure 3.1: Limb Plot for the Crab on May 31, 1991 (TJD 8407) in the middle, and one day apart on each side.

a wider range of projection angles sampled as declination increases. This can be seen by comparing Fig. 3.6 for the Crab (declination of 22.5°) to Fig. 3.7 for 3C 273 (declination of 2.05°) and Fig. 3.8 for Cen A (declination of −43.02°).

3.2 Previous Work in Earth Occultation Imaging

3.2.1 Occultation Transform Imaging

The first technique to create images using Earth occultation was Occultation transform imaging (Zhang et al., 1995). This method images a region of the sky by performing an inverse Radon transform on the differentiated count-rate data that corresponds to projections for that area of the sky. Then the image is deconvolved using a maximum entropy method

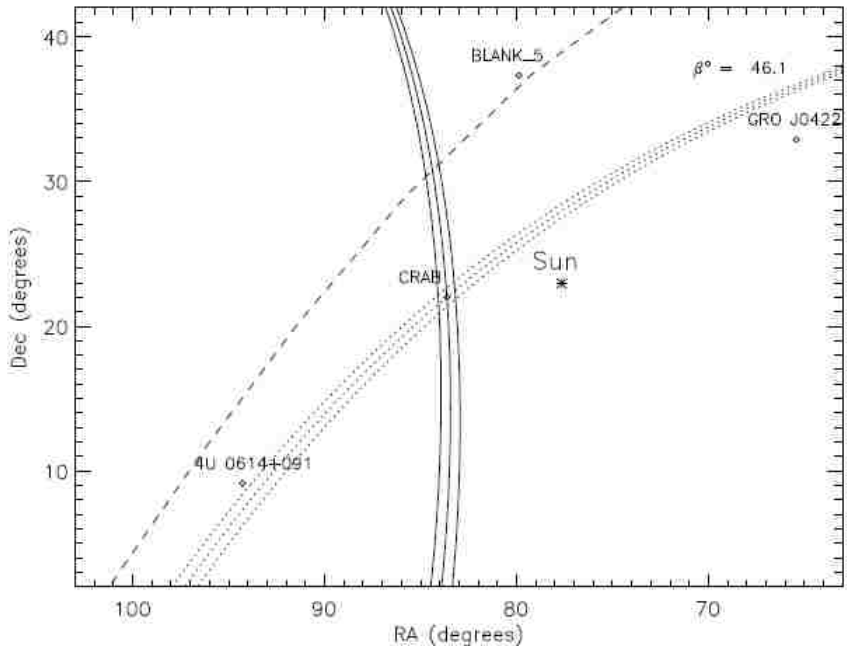

Figure 3.2: Limb Plot for the Crab on June 10, 1991 (TJD 8417) in the middle, and one day apart on each side.

(MEM) to locate sources in the image. Zhang et al. (1995) generated images for time periods covering days to weeks and energies 20-300 keV. Image sizes ranged from $5^\circ \times 5^\circ$ to $40^\circ \times 40^\circ$. Regular analysis consisted of imaging the galactic plane with 27 sections of $30^\circ \times 30^\circ$ images (Zhang et al., 1994). Occultation transform imaging was able to discover a number of transient sources (Zhang et al., 1995), but it had several limitations. Because the Earth's limb is an arc, the linear approximation used restricts the effective image size to $\sim 20^\circ \times 20^\circ$ (Shaw et al., 2004). For images larger than this, distortion effects can result in difficulty calculating the correct source position. Also, this technique does not account for bright sources outside the field of view biasing the background. Projections from sources such as the Crab, Sco X-1, and Cyg X-1 can extend for 10s of degrees. MEM is a non-linear iterative process, which can make comparing (Narayan et al., 1986) and combining images (Westmore et al., 2000) difficult.

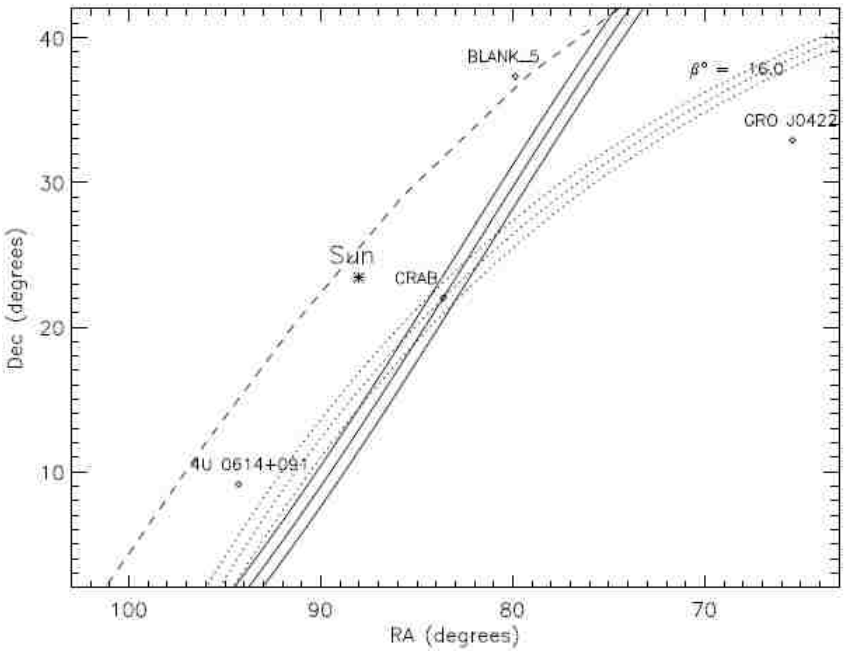

Figure 3.3: Limb Plot for the Crab on June 20, 1991 (TJD 8427) in the middle, and one day apart on each side. The rise limbs are the solid lines, and the set limbs are the dotted lines.

3.2.2 Likelihood Imaging Method (LIMBO)

LIMBO (Shaw et al., 2004) generated all-sky images using a likelihood statistic for a grid of predefined source positions on the sky. In this method, BATSE Mass Model (BAMM) was developed to account for background from cosmic ray interactions with the spacecraft, atmospheric albedo from Earth, and cosmic diffuse γ-rays. It was able to reduce the background flux by a factor of ~ 10. The data subtracted background were passed through a differential filter. A maximum likelihood statistic was calculated to determine the significance of a point on the grid of source positions based on the filtered data. All-sky images were generated using 489 days of BATSE data in a single energy range 25-160 keV. LIMBO showed improvements over occultation transform imaging with the ability to generate all-sky images, account for bright sources, and easily sum images, but LIMBO's resolution was limited by the 2° separation of its sky grid points. Also, spectral information about the sources was lost by imaging only a single energy range.

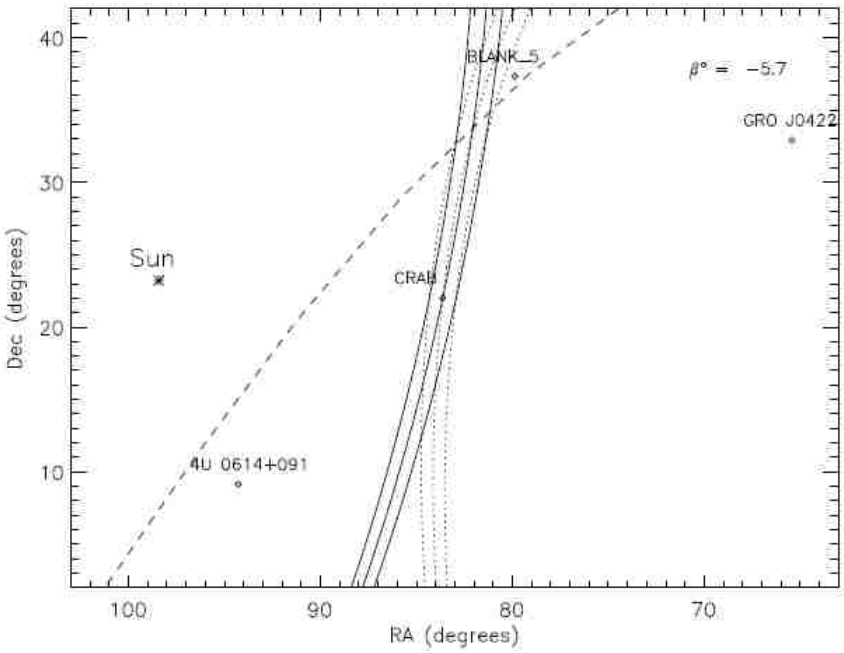

Figure 3.4: Limb Plot for the Crab on June 30, 1991 (TJD 8437) in the middle, and one day apart on each side. The rise limbs are the solid lines, and the set limbs are the dotted lines.

3.3 All-Sky Imaging with IDEOM

3.3.1 Differential Filter

To fully exploit the 4π field of view of the BATSE instrument, we have taken a different approach in reconstructing the image. Since occultations are relatively sharp features, and are superimposed on highly variable backgrounds, it is a challenge to search and fit the steps directly. The differential filter technique is an approach to transform those step features into gaussian-like peaks. This filter method is adapted from the technique of Shaw et al., (2004) and the approach developed for GBM by Rodi et al., (2013). The size of a differentiated occultation peak depends on the difference between the mean counts calculated before and after the occulted time bin.

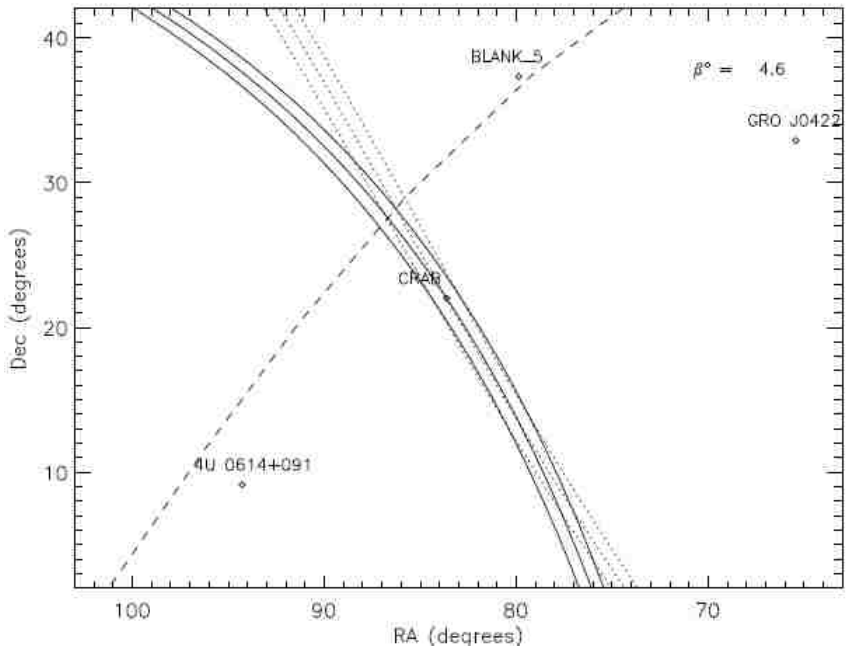

Figure 3.5: Limb Plot for the Crab on July 10, 1991 (TJD 8447) in the middle, and one day apart on each side. The rise limbs are the solid lines, and the set limbs are the dotted lines.

The data are passed through a simple differential filter, given by

$$o_i = \frac{\sum_{j=i+f_a}^{j=i+f_a+f_b} r_j - \sum_{j=i-f_a}^{j=i-f_a-f_b} r_j}{f_b} \tag{3.1}$$

where r_j is the number of counts in bin j, f_a is the inner boundary of the filter window, f_b is the outer boundary, and o_i is filtered result in bin i. Fig. 3.9 shows a square step at bin i transformed to a roughly triangular peak of width $2f_b$.

Since the occultation steps are not infinitesimal (they take about $8-20$ seconds), without f_a (or $f_a = 0$), the difference will be reduced. This causes a reduction in sensitivity which becomes more important as f_b decreases towards the step time of about $4 - 10$ bins. This can be avoided by adding an inner bound to the differential filter. By making a small gap in the centre of the filter, systematic errors in calculating the mean counts on either side of a step are reduced.

The choice of f_a and f_b therefore has implications for the sensitivity and angular resolution

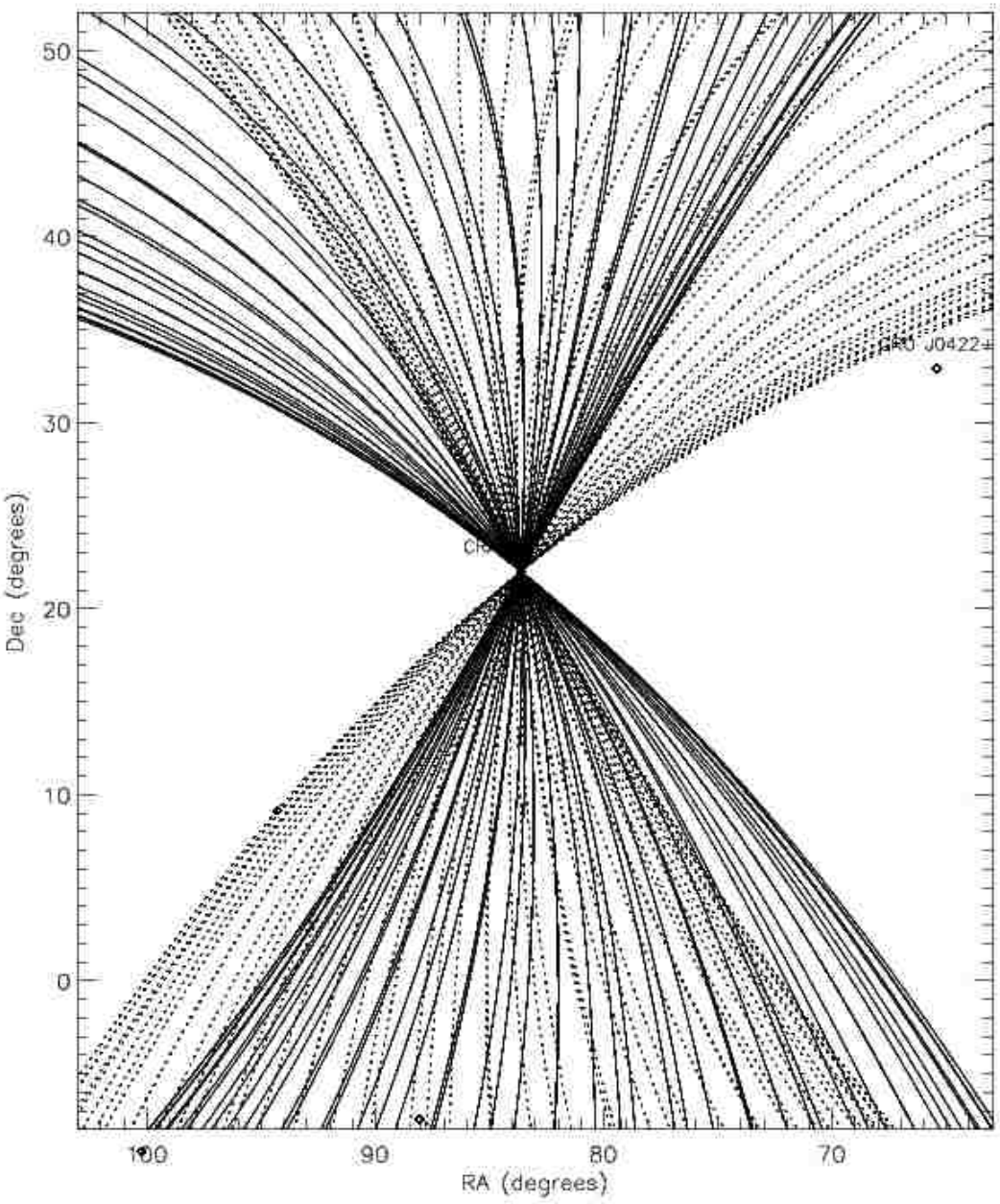

Figure 3.6: Limbs Overplotted for the Crab from Figs. 3.1 - 3.5

of the imaging technique. Larger f_a will give a better sensitivity, but lower angular resolution. However there is a limit to about half the duration of the step. If f_a is larger than this limit, the peak will be saturated. Likewise, larger f_b will give a more significant occultation peak but poorer resolution. Fig. 3.9 and Table 3.1 show the effect of applying several different

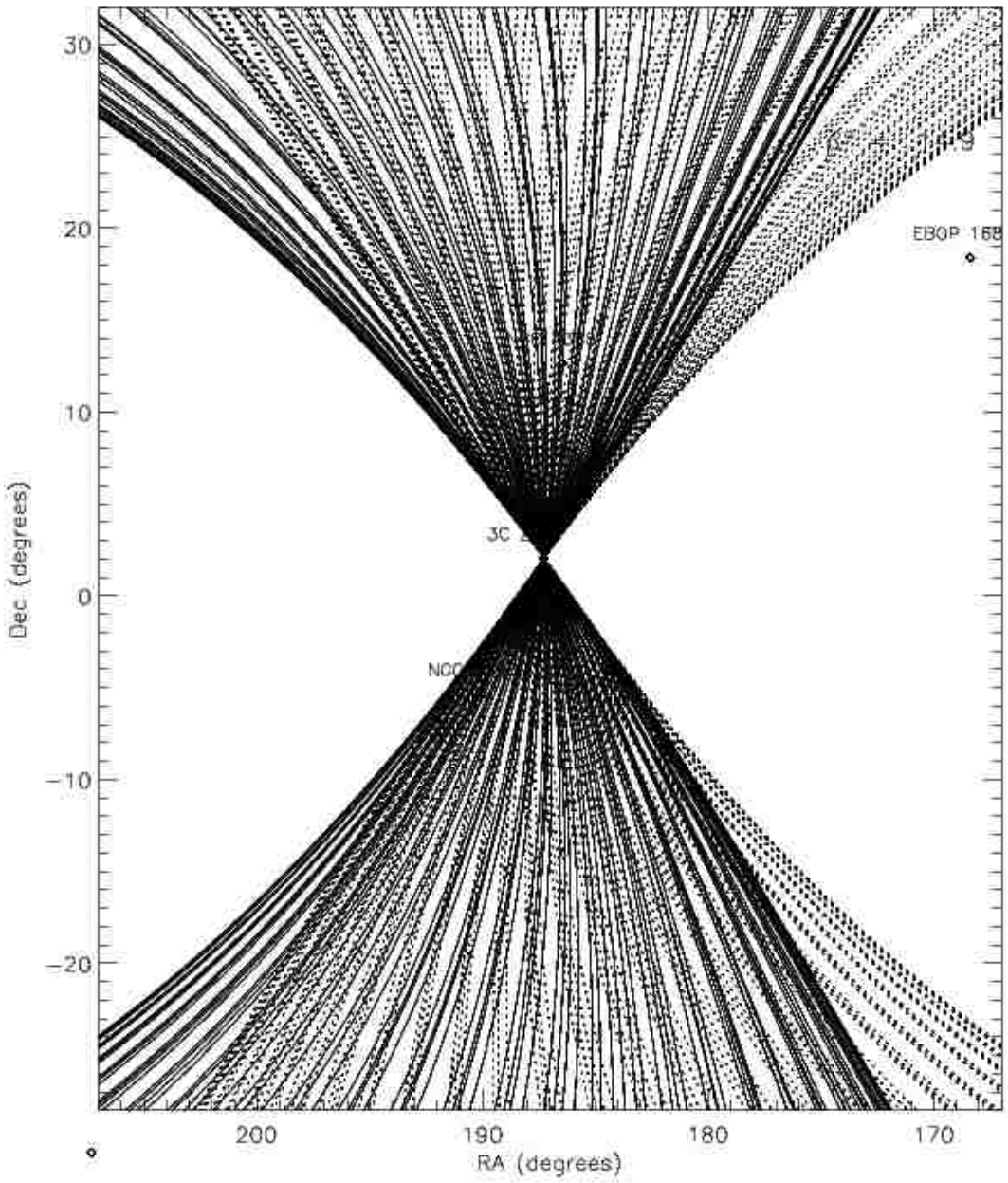

Figure 3.7: Limbs Overplotted for 3C 273 during precession period from (TJD 8407 - TJD 8507) May 31, 1991 to September 8, 1991

filters to a simple model of an occultation step. For a duration of 12 sec, $f_b = 8$ with a small inner gap ($f_a = 2$) offers a combination of good angular resolution (given by the HWHM of the curves) and good sensitivity.

A possible extension to the differential filtering technique may be to use different res-

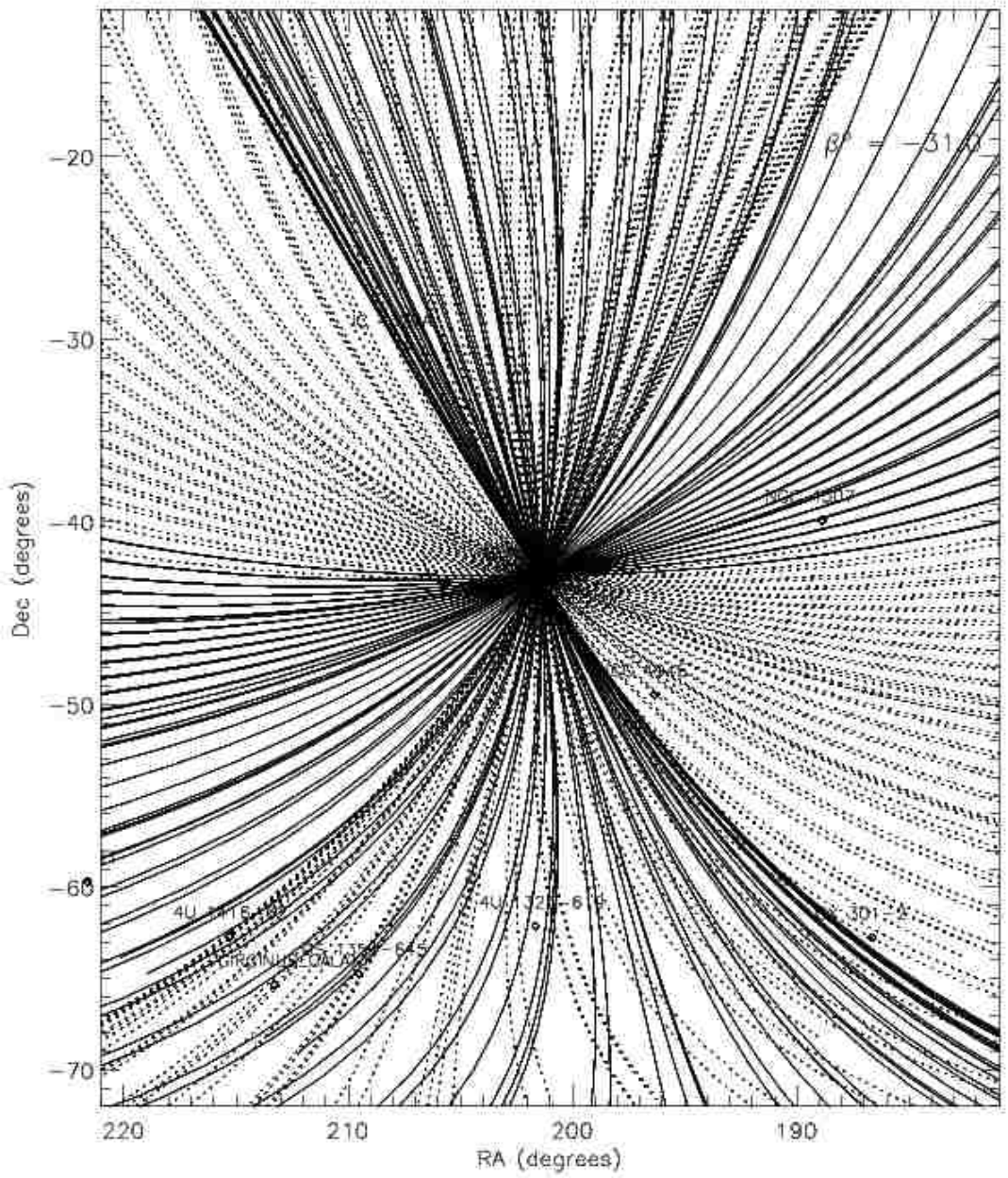

Figure 3.8: Limbs Overplotted for Cen A during precession period from (TJD 8407 - TJD 8507) May 31, 1991 to September 8, 1991

olution maps to build up images of extended emission. By choosing different values of f_a and f_b that optimize the coverage of spatial frequencies in the image, it may be possible to investigate, for example, diffuse gamma-ray emission from the Galactic Plane.

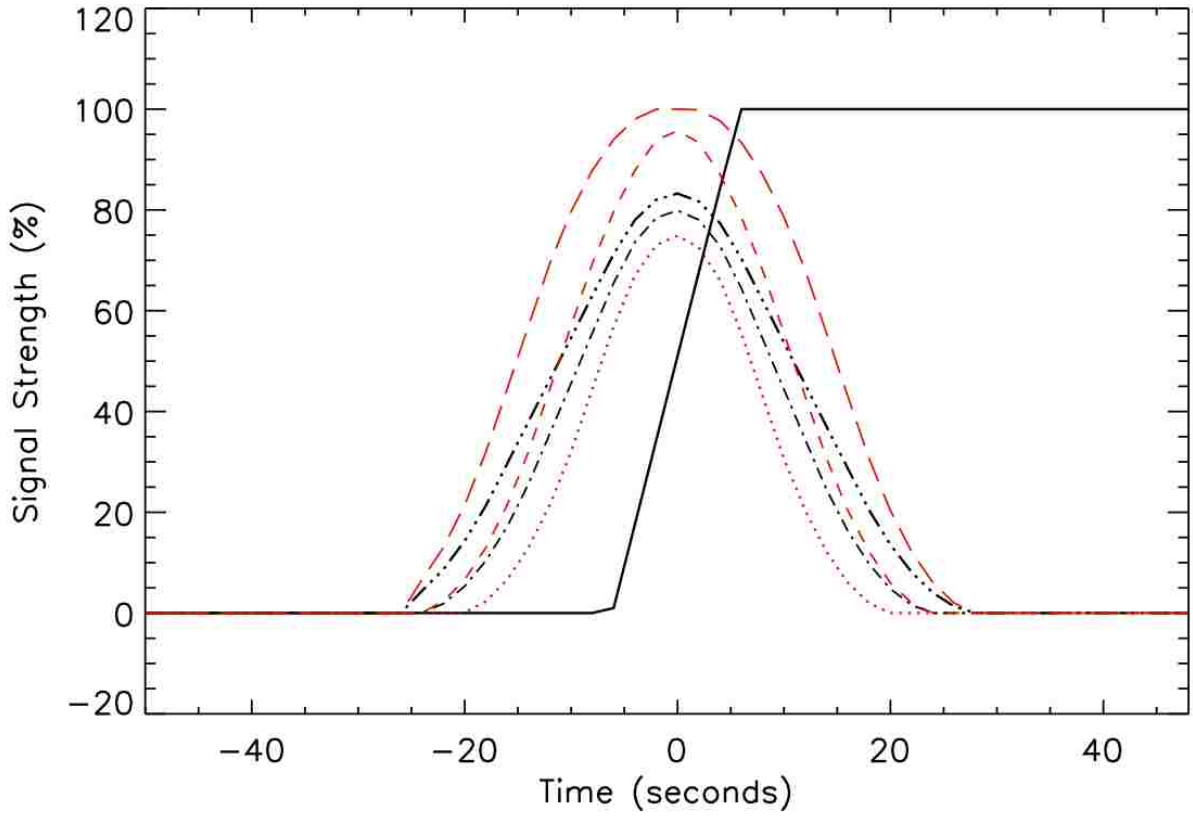

Figure 3.9: A simple model to show the effect of various differential filters on an occultation step of duration 12 seconds (solid line). Filters with $f_b = 8$ were applied with inner gaps, f_a= 0 (dotted in red), 2 (short dash in red) and 3 (long dash in red) as well as a filter with $f_b = 10$ and inner gap = 0 (dotted dash in black), filter with $f_b = 12$ and inner gap = 0 (dot-dot dash in black).

3.4 Imaging Methods Comparison

We implemented inverse Radon transform (IRT) imaging with our BATSE LAD 16 sec and 2 sec data (left-hand and middle columns in Fig. 3.10- 3.12). We can compare these two imaging results with our IDEOM result (right-hand column in Fig. 3.10- 3.12) on single sources (Crab, Vela X-1, and NGC4151). Based on a comparison of the FWHMs for both 2D Gaussian Fit and 1D Gaussian Fit, IDEOM results in better angular resolution.

Table 3.1: Approximate sensitivity and angular resolution of differential filters used in Fig. 3.9.

f_b (bins)	f_a (bins)	Sensitivity (%)	Angular resolution (°)
8	0	74	0.58
8	2	95	0.71
8	3	100	0.96
10	0	79	0.71
12	0	83	0.83

3.5 Differential Filter Imaging Procedure

3.5.1 Read in raw data

The BATSE LADs are well-suited to Earth occultation measurements because of their sensitivity, uniformity in energy range, and stabilized gain. Data from two or more LADs can be easily combined or fitted jointly, depending on the application. There are two different data types which are most convenient for occultation measurements: DISCLA (LAD discriminator data) and CONT (LAD continuous data) which cover the same energy range (20 keV - 1.8 MeV). The DISCLA data type provides four energy channels binned every 1.024 seconds, and the CONT datatype provides 16 channels every 2.048 seconds.

Occultation imaging with BATSE begins with reading in the CONT data (2.048 second intervals) for one day. Data from the 8 NaI detectors in 16 energy bands are combined into 4 broad energy bands ($23 - 98$ keV, $98 - 230$ keV, $230 - 595$ keV, and $595 - 1798$ keV) later. The corresponding spacecraft position file contains the position and orientation of the spacecraft at 2 second cadence for a single day.

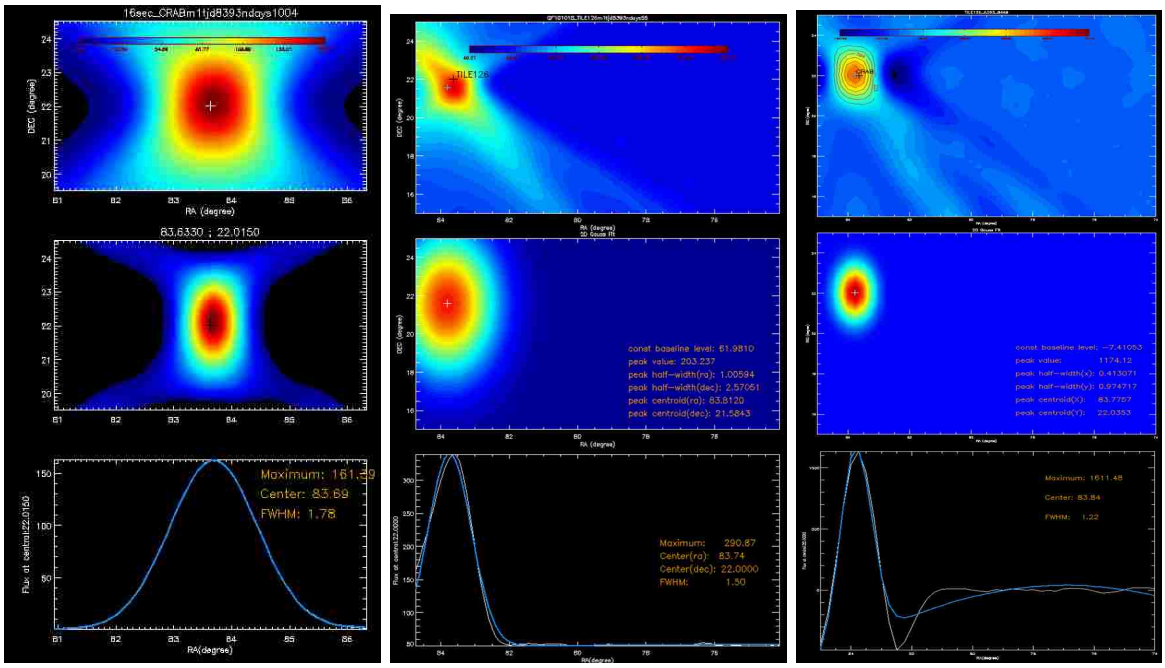

Figure 3.10: The upper panels are measured images for the Crab in units of standard deviations above background. The middle panels are 2D Gaussian Fits for the images. The lower panels are 1D Gaussian Fits for the x-axis of the images. Images from Inverse Radon Transform (IRT) with 16 sec data are on the left. Images by IRT with 2 sec data are in the center. Images from the differential filter method (IDEOM) with 2 sec data are on the right. Measured FWHM are 1.78°, 1.56°, and 1.22° respectively.

3.5.2 Data selection

The raw BATSE data contains occasional gaps of null data, for example, when the instrument is turned off during passage through the South Atlantic Anomaly (SAA) or where contact is lost between CGRO and its telemetry relay satellites. The untreated gaps produce uneven time intervals, which will mislead the differential results when calculating count rates. One way to reduce the effect is to insert missing time bins, and fill 0 for their data bins. The differential filter then jumps across the gaps when it finds them.

Data selection removes large fluctuations. The data must pass through three stages in the selection process.

The first stage is performed by using Quality Flag files which are provided along with

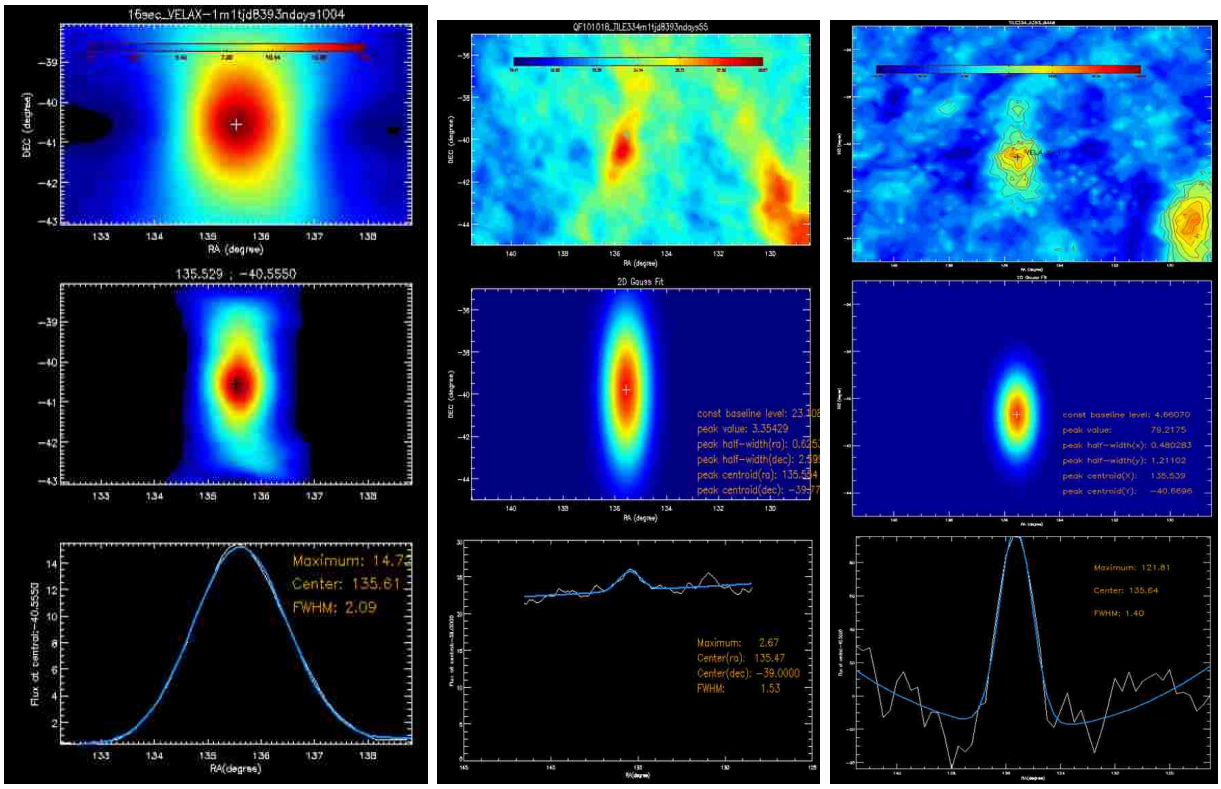

Figure 3.11: The upper panels are measured images for Vela X-1 in units of standard deviations above background. The middle panels are 2D Gaussian Fits for the images. The lower panels are 1D Gaussian Fits for the x-axis of the images. Images from Inverse Radon Transform (IRT) with 16 sec data are on the left. Images by IRT with 2 sec data are in the center. Images from the differential filter method (IDEOM) with 2 sec data are on the right. Measured FWHM are 2.09°, 1.53°, and 1.40° respectively.

the raw data. Any high-rate events triggering the GRB acquisition mode are flagged. These events may be caused by bursts, solar flares, bremsstrahlung from electron precipitation, terrestrial gamma-ray flashes (Fishman et al. 1994) or even flaring Galactic sources (Mallozzi et al. 1993). They produce a high data rate relative to the background in two or more detectors.

The second stage relates to SAA passages. The instrument may not be turned off early enough, or may be turned on before totally exiting the SAA area. They are step-like features extended in the timescale of seconds to minutes, very likely to be picked up when differential filtering. Hence, data bins within 20 seconds before and after SAA passage are excluded.

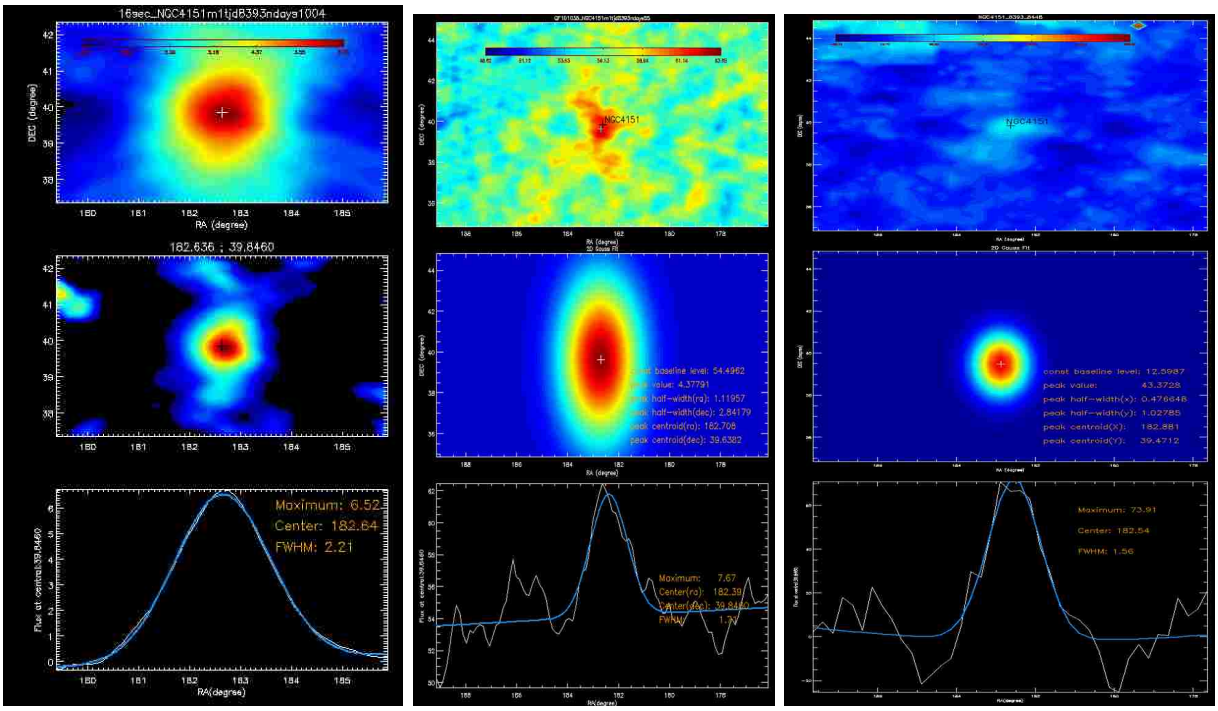

Figure 3.12: The upper panels are measured images for NGC4151 in units of standard deviations above background. The middle panels are 2D Gaussian Fits for the images. The lower panels are 1D Gaussian Fits for the x-axis of the images. Images from Inverse Radon Transform (IRT) with 16 sec data are on the left. Images by IRT with 2 sec data are in the center. Images from the differential filter method (IDEOM) with 2 sec data are on the right. Measured FWHM are 2.21°, 1.71°, and 1.56° respectively.

The last stage consists of additional flagging of very short ($< 1sec$) cosmic-ray events. They occur in only one detector at a time when a heavy cosmic ray, such as an iron nucleus, deposits a large amount of energy into the scintillation detector. This is observed as a sharp, positive-going spike in the background for one time bin. The affected data bins are flagged using a 5σ threshold in the raw counting rate in a single detector and single energy band.

3.5.3 Set virtual source catalog

As discussed above, the Earth occultation technique requires a known source catalog to predict the occultation time. A virtual source catalog is generated for IDEOM consisting of a grid with 0.25° spacing (corresponding to the angular resolution in Eq. 2.4) covering the

whole sky. In total, 660, 412 virtual sources are generated.

3.5.4 Predict occultation time

In one orbit around the Earth, two occultation step features, a rise and set pair, will be superimposed on the background count rate as each virtual point source is occulted. The prediction of occultation times is described by Harmon et al., (2002). In order to predict occultation times at given locations precisely, the use of an accurate spacecraft ephemeris and an accurate model of the shape of the Earth is required. The Earth's surface is approximately an oblate ellipsoid given by

$$x^2 + y^2 + (1-f)^{-2}z^2 = a^2 \tag{3.2}$$

where x, y, and z are geocentric Cartesian coordinates with the z-axis aligned with the north pole, $f = 1/298.257$ is the flattening factor of the Earth, and $a = 6378.136$ km is the Earth's equatorial radius. Near the Earth's surface, constant atmospheric density surfaces can be approximated by ellipsoids of the same oblateness. If the spacecraft is at position $R = (x_{sc}, y_{sc}, z_{sc})$, the source is in direction $\Omega = (\Omega_x, \Omega_y, \Omega_z)$, and the height above the surface of a point on the line of sight at a distance s from the spacecraft is $h(s)$, then we have

$$(a + h(s))^2 = (x_{sc} + s\Omega_x)^2 + (y_{sc} + s\Omega_y)^2 + (1-f)^{-2}(z_{sc} + s\Omega_z)^2 \tag{3.3}$$

The minimum height to the Earth and its distance along the line of sight are given by

$$h_{min} = [x_{sc}^2 + y_{sc}^2 + (1-f)^{-2}z_{sc}^2 - \frac{(x_{sc}\Omega_x + y_{sc}\Omega_y + (1-f)^{-2}z_{sc}\Omega_z)^2}{\Omega_x^2 + \Omega_y^2 + (1-f)^{-2}\Omega_z^2}]^{1/2} - a \tag{3.4}$$

$$s_{min} = -\frac{(x_{sc}\Omega_x + y_{sc}\Omega_y + (1-f)^{-2}z_{sc}\Omega_z)^2}{\Omega_x^2 + \Omega_y^2 + (1-f)^{-2}\Omega_z^2} \tag{3.5}$$

For 23-98 keV, if h_{min} passes 74 km, and $s_{min} > 0$ then an occultation step has occurred; for 98-230 keV, h_{min} needs to pass 69.67 km; for 230-595 keV, h_{min} has to pass 67.67 km; and for 595-1798 keV, 764.67 km is required. The numbers are derived from 50% atmospheric

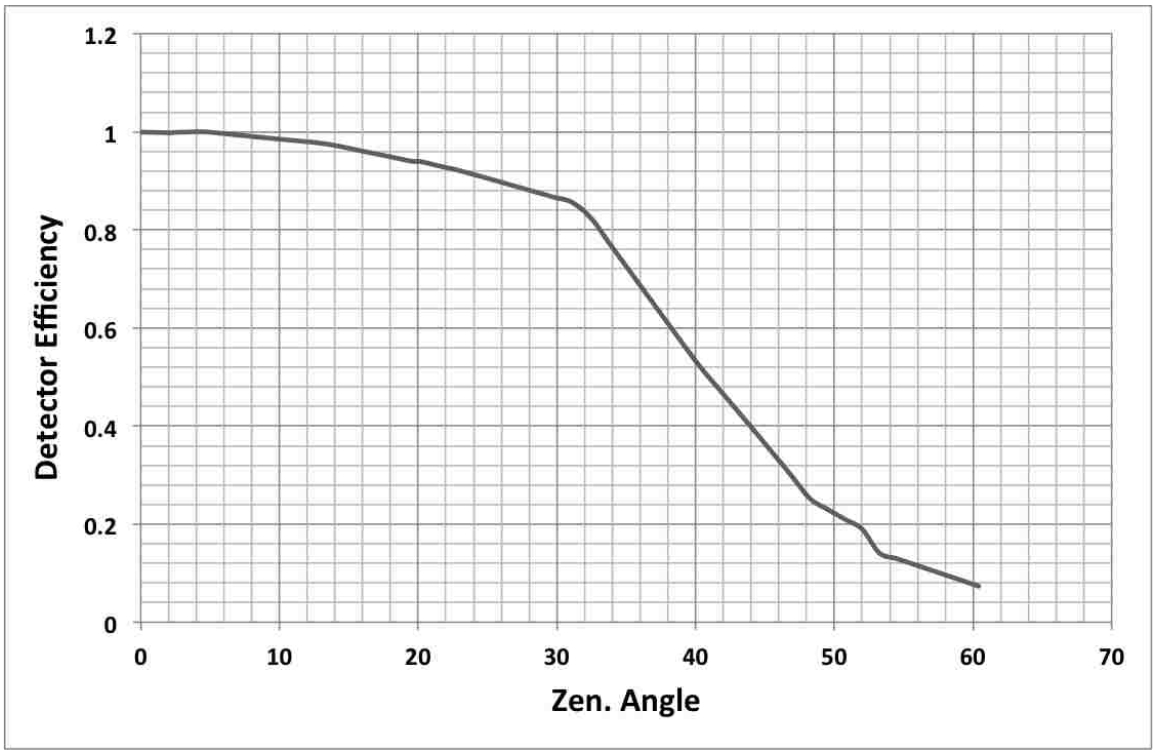

Figure 3.13: This figure shows the detector efficiency as a function of detector angle at 23-50 keV. The cut off is about 60°.

attenuation for each energy range.

For each occultation step, the angle between the sources and the detector normal is found by calculating the spacecraft orientation from the position history file, which contains the position and orientation of the spacecraft at 2 second cadence for a single day. For each virtual source, only detectors viewing the occultation at 60° or less are used. Figure 3.13 shows that the detector efficiency is a function of detector angle. First order detector response efficiency corrections are applied. This efficiency depends on the cosine of the angle between the normal to the detector and a vector pointing towards the source, and the energy channel.

3.5.5 Window selection (Source Confusion)

After determining the occultation time, a 4 minute window is defined with the occultation step at the center for each virtual source. Since the imaging method integrates an entire earth limb at one time, two or more sources on the same earth limb will introduce source interference, especially if one of them is a bright source such as the Crab or Cyg X-1. In order to eliminate this effect, we set up another catalog specially for the bright sources. When imaging other virtual sources around the bright ones (outside a $5^\circ \times 5^\circ$ box around the bright sources), we will ignore windows in which the bright sources are also crossing the limb.

3.5.6 Flip set steps

In order to analyze as many occultation steps from a position as possible in a single run, data from rise occultation steps are converted to set steps by rotating the occultation window about the occultation time at the center of the window.

3.5.7 Sum and average the windows

All the data for each window are lined up and stacked for an entire day, making sure each occultation step is at the center of the window. Then the windows are averaged to create an average occultation window. The averaged window is then passed through a differential filter with typical $f_a = 3$ and $f_b = 8$. Fig. 3.14 shows an example of an average ocultation window and the result of filtering for a virtual source near the Crab. In the figure the middle dotted line corresponds to the occultation time of the virtual source.

3.5.8 Fitting the filtered windows

The filtered window is then fit in two parts. The central part, $\pm(2f_a + f_b)$ bins from the middle, is fit to quadratic, qubic, and quartic functions, and the fit giving the lowest reduced χ^2 kept. The outer portions are fit to a spline function and joined by a straight line crossing

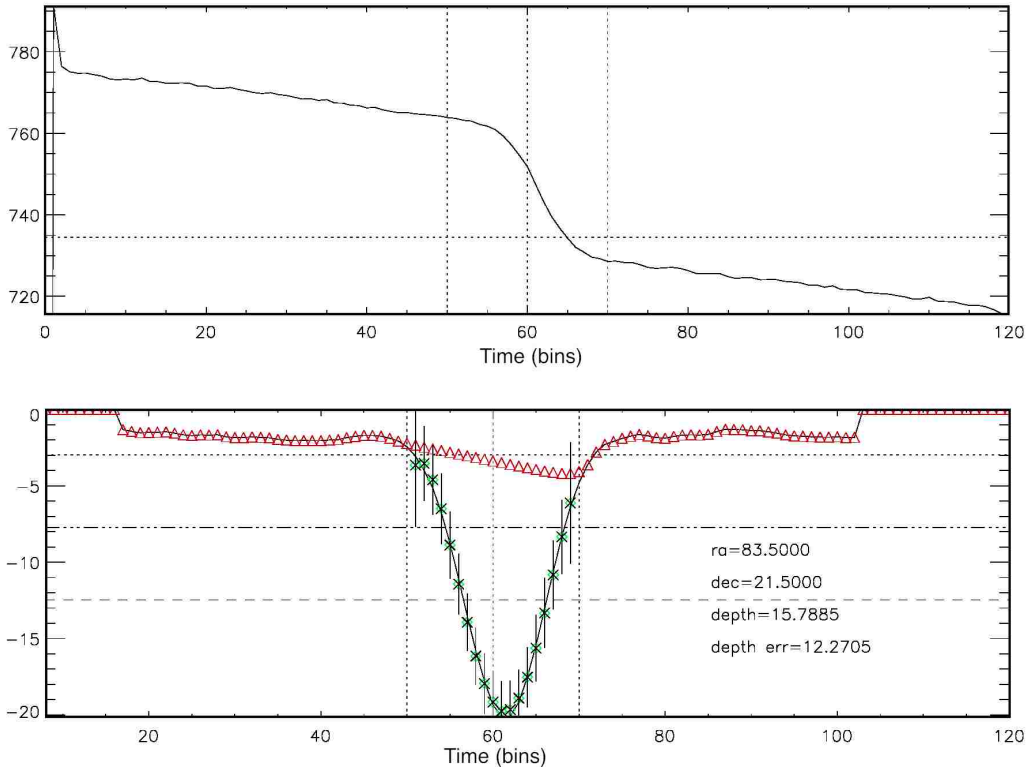

Figure 3.14: Top: Example of averaged occultation window. Bottom: The filtering results. The x-axes in both plots are 2 second time bins, and the y-axes are in counts.

the central region. The bottom of Fig. 3.14 shows the fit result with the red triangles from the spline fit and the green crosses from the polynomial fit. Note that, unlike the EBOP analysis that calculates a background to be subtracted, IDEOM determines the background directly from the data. The intensity of the virtual source is determined by taking the difference between the polynomial fit at the occultation time (the central bin) and the spline fit at the same bin.

3.5.9 Error propagation

To determine the significance of the calculated intensities, Poisson errors from the raw data are propagated throughout and combined with the fit errors. The statistical errors for the raw counts data are calculated by assuming, for the response corrected data,

$$\sigma^2 = \frac{N_i}{R^2} \tag{3.6}$$

where R is the response plotted in Fig. 3.13. The weighted error is calculated for each time bin of the averaged window. The errors are added in quadrature in the filtering. The polynomial fit is weighted by statistical errors and provides the fit error which is added with the statistical error. This final error is used with the intensity of the virtual source to determine its significance.

3.6 Implementation with HPC

The EOT analysis and initial IDEOM codes are written in Interactive Data Language (IDL). The average computing time to process a virtual source in IDL, which includes calculating the occultation times, stacking windows, and filtering and fitting the final window, is $\sim 1sec/(day * source)$ on a typical Linux machine. For all-sky maps, we have $\sim 660,000$ virtual sources, for nine years (3285 days), and in four energy bands, which means it will take $2,409,000$ hours, or $100,375$ days, or 275 years to finish all the maps using a single processor in IDL.

In order to reduce the time required to create an image, Message Passing Interface (MPI) is our best choice. However, MPI requires the code to be written in Fortran or C. Hence, our routines were translated to Fortran 90 and set up on LSU's High Performance Computing (HPC) machine Tezpur and the Louisiana Optical Network Initiative (LONI) Queen Bee.

LSU HPC quotes Tezpur as running at 15.322 TFlops with 360 nodes with 2 dual-core 2.66 GHz Intel Xeon 64 bit processors running Red Hat Enterprise Linux (RHEL) with 4 GB of RAM. LONI's Queen Bee runs at 50.7 TFlops with 680 nodes with 2 quad-core 2.33 GHz Intel Xeon 64 bit processors with RHEL and 8 GB of RAM. The virtual source catalog was separated into two roughly equal sections because of memory constraints. The first catalog covers declinations 0° to $+90^\circ$; the second -0.25° to -90°.

The average time to process a virtual source on a single processor now is $\sim 0.65 sec/(source * day)$. Because each virtual source is independent, analysis can be done in parallel on separate processors and the results combined afterwards. By using MPI, an all-sky map takes 8 hours to complete a precession period in one energy band on 50 nodes (200 processors in Tezpur or 400 processors on Queen Bee). It takes about one month to finish one all-sky map for the whole 9 years. In total, $2,418,095.75$ SUs were used to complete the calculation of all-sky maps for nine years in four energy bands. Imaging results will be presented in the following section.

Chapter 4
Differential Filter Imaging Result

4.1 Systematic Features on the All-Sky Maps

As discussed in detail by Rodi et al. (2013), two main systematic effects must be considered: 1) Source Confusion with bright sources 2) Cases in which rise and set steps for a nearby bright source contaminate the background fit.

Source confusion occurs when a bright source sits along the same Earth limb as a virtual source. Fig. 3.10 shows the characteristic X pattern centered on the bright source that can extend for tens of degrees. Any weaker source sitting along one of the bright source"arms" may be affected systematically by this background. To address this, bright sources that occult close in time (10 seconds)but are far away ($> 5°$) are eliminated from the analysis. As an example of effect 2 above, in(Fig. 4.1), the location of a virtual source is $RA = 82.5°$, $Dec = 21.5°$. The position of the Crab is $RA = 83.6332°$, $Dec = 22.0145°$. With the standard fit window of width $(2f_a + f_b)$, the filtered window of the virtual source contains both rise and set steps of the Crab, resulting in an apparently large negative amplitude. By shrinking the fit window width to $2f_a$, the negative amplitude is significantly reduced.

4.2 Source Identification and New Source Catalog

This source identification analysis consists of three parts: the significance, the shape, and cross-correlating with other major catalogs.

1) For the significance, the positions for potential sources in the images are determined

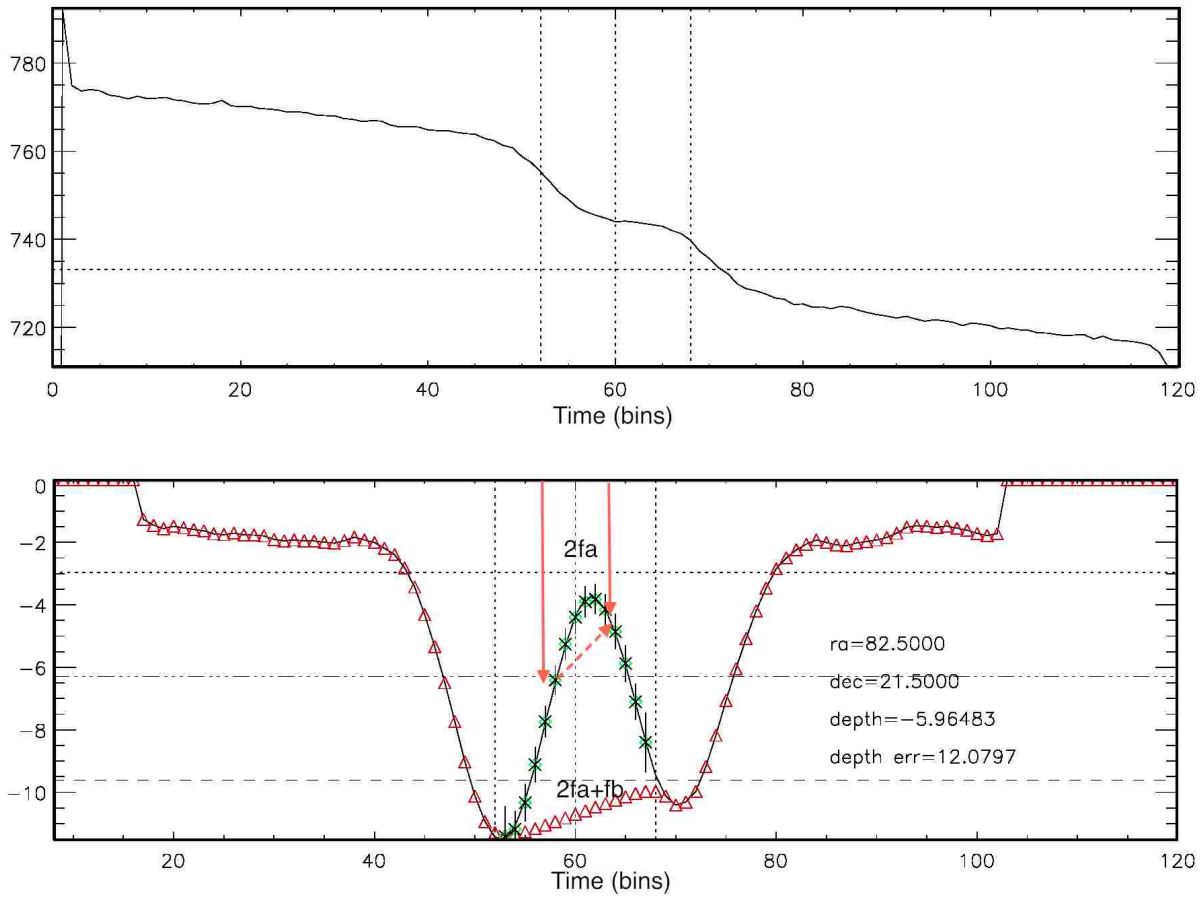

Figure 4.1: Example of averaged occultation window. The virtual source is only 1° in RA separated from the Crab. By shrinking the polynomial fitting window from $(2f_a + f_b)$ to $2f_a$, the negative depth will be greatly reduced.

by searching for points with intensities greater than 2σ above background. $5° \times 5°$ regions centered on each point were fit to a two-dimensional Gaussian. The maximum value of the fit in standard deviations above the background was taken as the source significance, and the centroid was taken to be the source position.

2) The shape of the potential sources is also considered. The $5° \times 5°$ regions centered on each point were cross-correlated with a simulated Point Spread Function (PSF) for its declination. PSFs were calculated by integrating all the possible step limbs with assumption of a standard 1000 mCrab intensity. Only the potential sources with cross-correlation > 0.3 are maintained.

3) Finally, the potential sources were cross-correlated with features in the *Swift*/BAT, *INTEGRAL*/SPI, and *Fermi*/GBM catalogs. New sources within 1° to the known sources were assigned with the known names.

Finally, all potential sources were plotted in $10^\circ \times 10^\circ$ and $20^\circ \times 20^\circ$ regions, and scanned by eye to remove sources on the extended bright arms or at the cross junction of two bright arms.

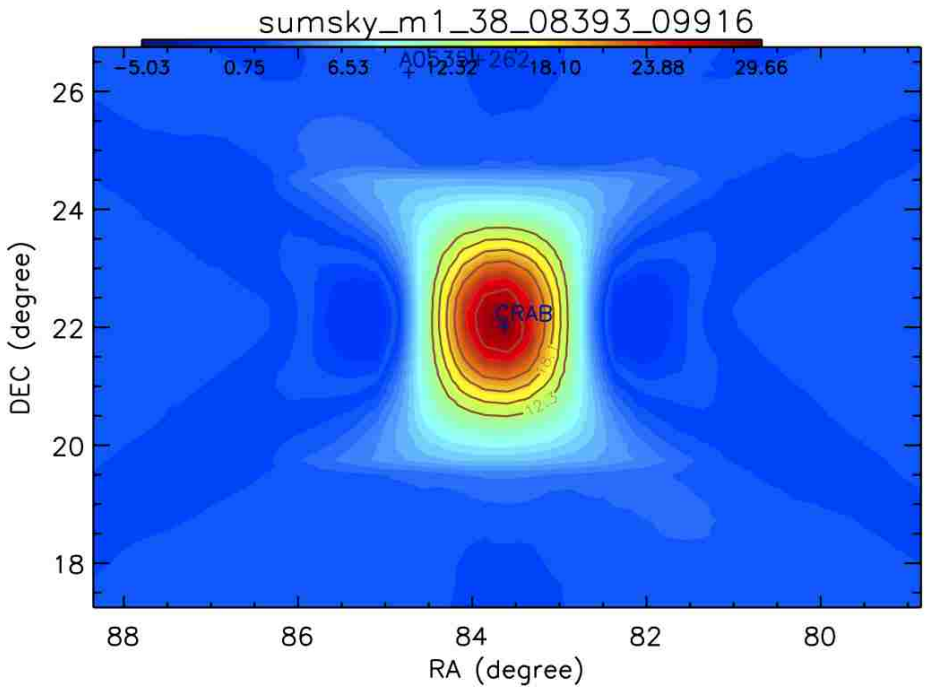

Figure 4.2: A $10^\circ \times 10^\circ$ image of Crab region, in the first energy band (23 - 98 keV), summing over 30 precession periods (TJD 08393 - TJD 09916). There is a $5^\circ \times 5^\circ$ box around the source; outside the box, the source confusion routine minimizes the extended bright arms.

Examples of bright sources (the Crab and Cyg X-1) are shown in Fig. 4.2 and 4.3. Fig. 4.2 shows a $10^\circ \times 10^\circ$ image centered on the Crab, summed over 30 precession cycles (~ 4.2 years data). The most significant pixel for the Crab is at $RA = 83.75^\circ, Dec = 22.05^\circ$, while the known location is $RA = 83.633^\circ, Dec = 22.015^\circ$. The difference is about 0.12°. The peak significance from the imaging analysis is 29.6σ. Fig. 4.3 shows a $10^\circ \times 10^\circ$ image of Cyg X-1, again based on stacking 30 precession cycles. The most significant pixel for Cyg X-1 is at

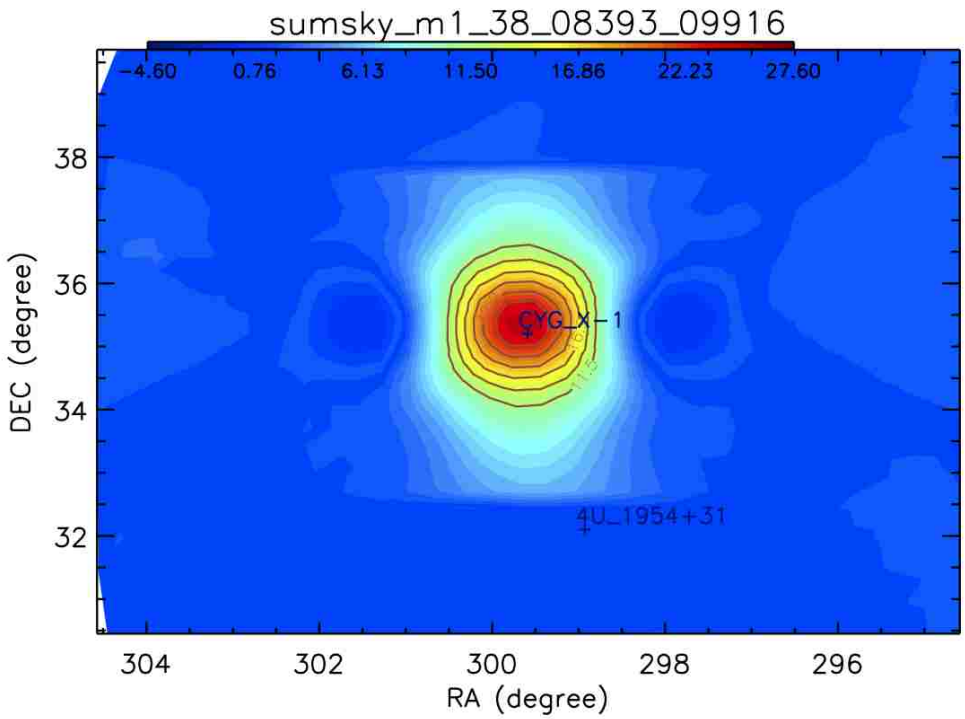

Figure 4.3: A $10° \times 10°$ image of Cyg X-1 region, in the first energy band (23 - 98 keV), summing over 30 precession periods (TJD 08393 - TJD 09916). The source confusion routine eliminateds the X pattern arms outside the box.

$RA = 299.75°, Dec = 35.25°$, while the known location is $RA = 299.59°, Dec = 35.20°$. The difference is about 0.17°. The peak pixel significance is 27.6σ, corresponding to a flux of 926 mCrab from EBOP (9 years average).

Fig. 4.4 is a $16° \times 50°$ image of the Galactic Center in galactic coordinates. Table 4.1 lists comparisons between the source positions and significances for the sources found in the 23-98 keV image.

One application of our imaging technique is monitoring the transient sources. Since we are processing images in each single precession period, it is a great opportunity to monitor and study the time evolution of the sources.

Figs. 4.5 and 4.6 are a demonstration of monitoring a transient source GRO J1719-24, in two following precession periods. In the first one, GRO J1719-24 was quiescent, and cannot be imaged at all, while in the next period, it was flaring so brightly that it overshadowed

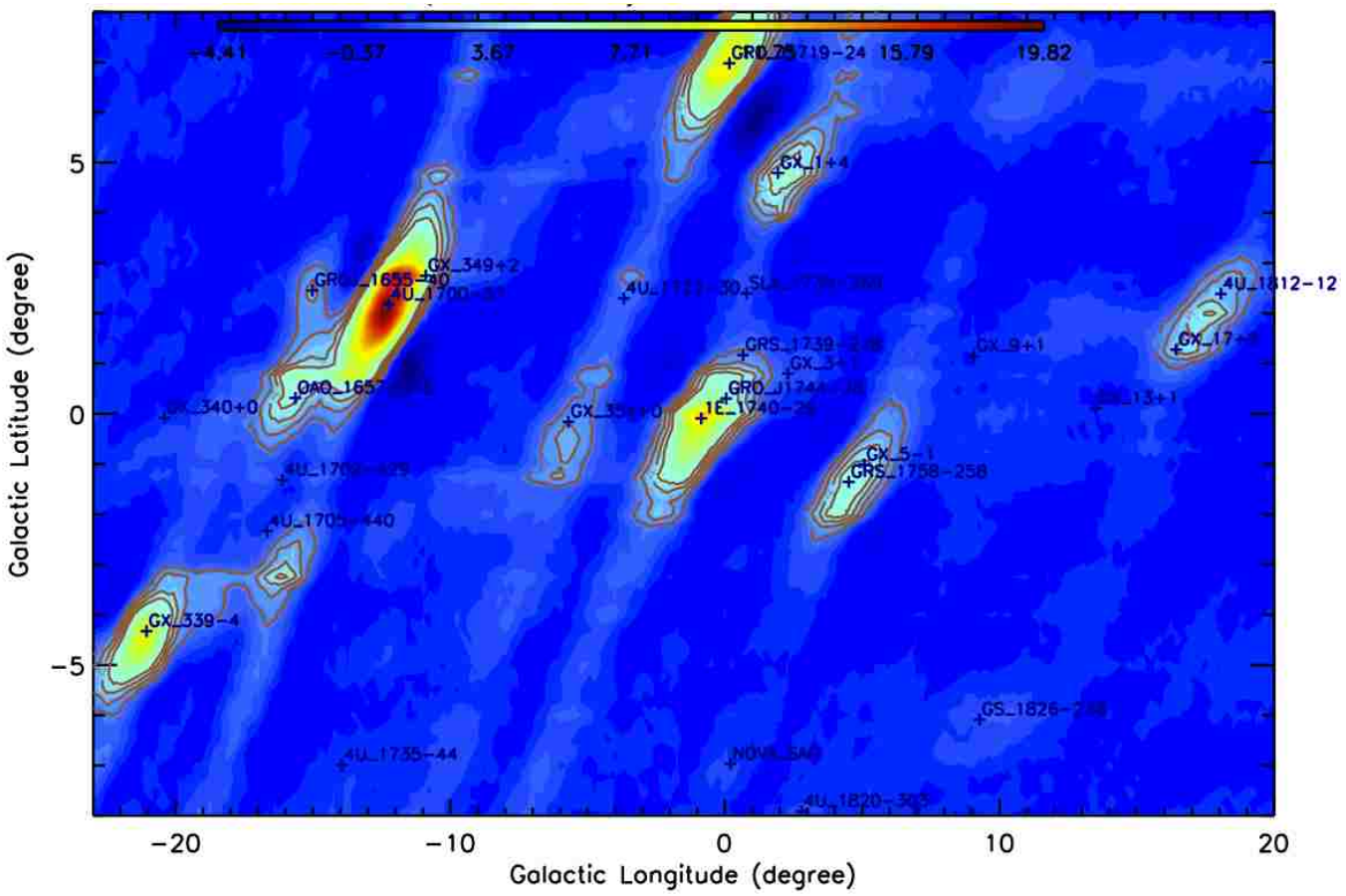

Figure 4.4: A 16° × 50° image in 23-98 keV of Galactic Center in galactic coordinates, summing over 30 precession periods (TJD 08393 - TJD 09916).

all the other Galactic Center sources, even the relatively bright one 4U 1700-37 (Ling et al., 2005).

4.3 All-Sky Map Results

IDEOM has been applied to the whole 9 years of BATSE data, covering from May 17, 1991 to May 26, 2000, which corresponds to 64 *CGRO* orbital precession periods. An all-sky image has been generated for each precession period for four broad energy bands, 23 - 98 keV, 98 - 230 keV, 230 - 595 keV, and 595 - 1798 keV. Table 4.2 shows the beginning and ending dates for each precession period in Truncated Julian Day (TJD). Single precession period images

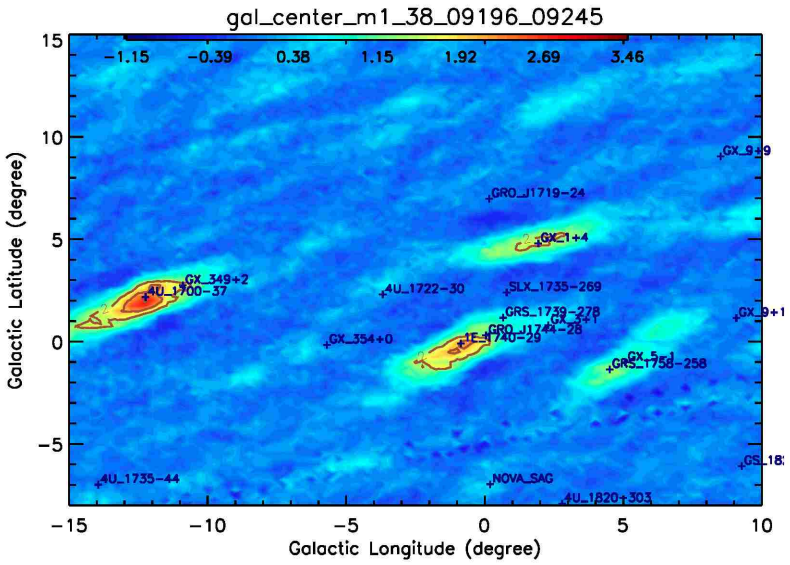

Figure 4.5: An image of Galactic Center in galactic coordinates around GRO J1719-24, in one precession period (TJD 09196 - TJD 09245), at 23 - 98 keV. The target source was quiescent.

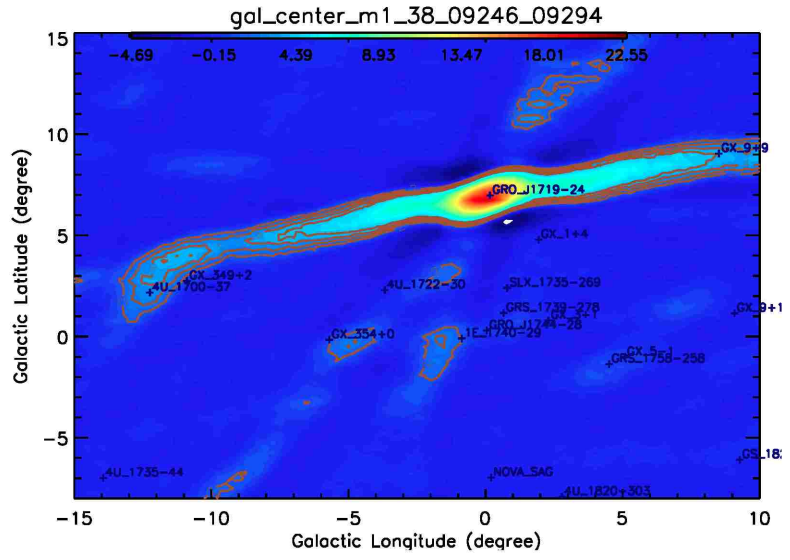

Figure 4.6: An image of Galactic Center in galactic coordinates around GRO J1719-24, over one precession period (TJD 09246 - TJD 09294), at 23 - 98 keV. It is the next precession period, following Fig. 4.5. The target source was flaring and was almost as bright as the Crab.

Table 4.1: The sources found in the Galactic Center image, Fig. 4.4. Differences between measured and known source positions are all within 0.51°. The fluxes are from EBOP analysis.

Source	Calc. RA, Dec	Known RA, Dec	$\Delta\theta$	Image Sig.	Flux (mCrab)
4U 1700-37	255.96, -38.15	255.99, -37.84	0.31°	19.82	147.4
1E 1740-29	265.96, -29.58	265.98, -29.72	0.14°	12.32	75.4
GRO J1719-24	260.04, -25.27	259.93, -25.01	0.28°	11.39	32.4
GX 339-4	255.97, -48.84	255.71, -48.79	0.26°	10.30	52.0
GX 1+4	263.24, -24.51	263.009, -24.71	0.30°	6.76	52.5
GRS 1758-258	270.33, -25.48	270.30, -25.74	0.26°	6.41	33.8
OAO 1657-415	254.86, -41.29	255.20, -41.67	0.51°	7.13	50.1
GX 17+2	274.19, -13.77	274.01, -14.04	0.32°	4.56	21.9
GX 354+0	263.31, -34.07	262.99, -33.83	0.40°	3.54	36.4

for an energy band were combined by summing the intensities for a virtual source weighted by the number of occultation steps for the point during a precession period. Fig. 4.7 - 4.10 show the combined significance maps for the whole nine years of the mission for 23 - 98 keV, 98 - 230 keV, 230 - 595 keV, and 595 - 1798 keV energy bands, respectively. Contours have been over plotted at $2.5\sigma, 5\sigma, 10\sigma,$ and 20σ. The source names plotted in black denote the original sources in the 2007 catalog; blue denotes the new sources; magenta marks 11 blank sources included to study systematic errors and sensitivity.

4.3.1 New BATSE Source Catalog

For the 23-98 keV energy band, 119 sources are identified, 29 of them new sources (marked with * in following tables) added into the BATSE catalog and 15 of them unidentified sources (Table. 4.3). For the 98-230 keV energy band, 42 sources are identified, and 5 of them new (Table. 4.4). For 230-595 keV, 13 sources are identified, only one of them (RBS 0315) new (Table. 4.5). For the highest energy band (595 - 1798 keV), only the Crab and Cyg X-1 are strong enough to pass the IDEOM source identification criteria.

Table 4.2: *BATSE* Orbital Precession Periods

Precession Period	Beginning Day (TJD)	Ending Day (TJD)	Precession Period	Beginning Day (TJD)	Ending Day (TJD)
1	8393	8448	33	10020	10071
2	8449	8489	34	10072	10122
3	8490	8542	35	10123	10174
4	8543	8592	36	10175	10226
5	8593	8644	37	10227	10277
6	8645	8695	38	10278	10329
7	8696	8746	39	10330	10380
8	8747	8796	40	10381	10432
9	8797	8847	41	10433	10483
10	8848	8897	42	10484	10535
11	8898	8947	43	10536	10588
12	8948	8997	44	10589	10641
13	8998	9047	45	10642	10694
14	9048	9097	46	10695	10748
15	9098	9146	47	10749	10802
16	9147	9195	48	10803	10855
17	9196	9245	49	10856	10909
18	9246	9294	50	10910	10962
19	9295	9346	51	10963	11016
20	9347	9397	52	11017	11069
21	9398	9449	53	11070	11123
22	9450	9501	54	11124	11176
23	9502	9553	55	11177	11230
24	9554	9605	56	11231	11283
25	9606	9657	57	11284	11337
26	9658	9709	58	11338	11390
27	9710	9760	59	11391	11443
28	9761	9812	60	11444	11496
29	9813	9864	61	11497	11550
30	9865	9916	62	11551	11603
31	9917	9968	63	11604	11656
32	9969	10019	64	11657	11690

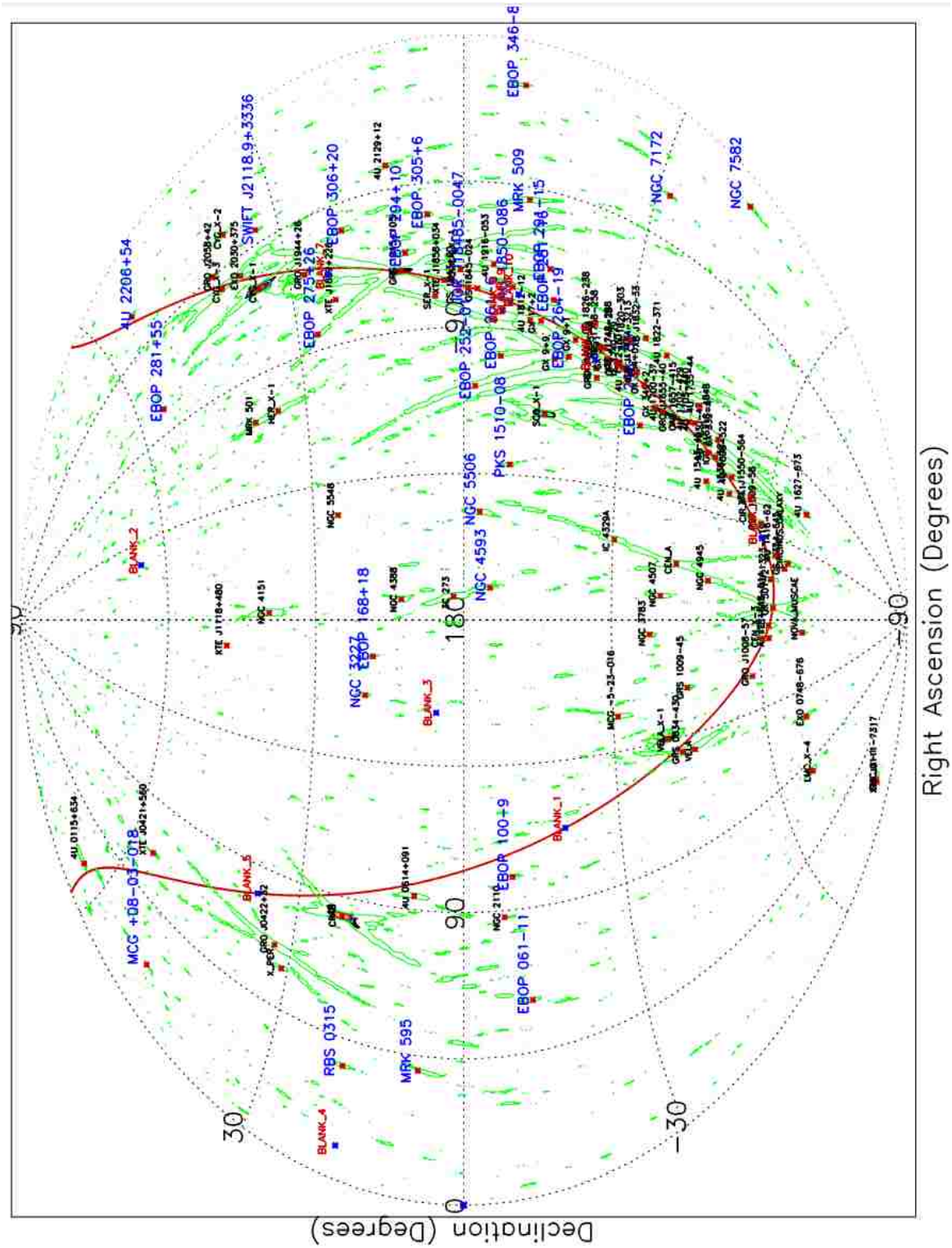

Figure 4.7: All-sky map summed over 64 precession periods (TJD 08393 - TJD 11690) over the energy range 23 - 98 keV. 3 sigma (statistical) features are contoured in green. The source names in black denote the original sources in the 2007 catalog; blue denotes the 29 new sources; red marks 11 blank sources included to study systematic errors and sensitivity.

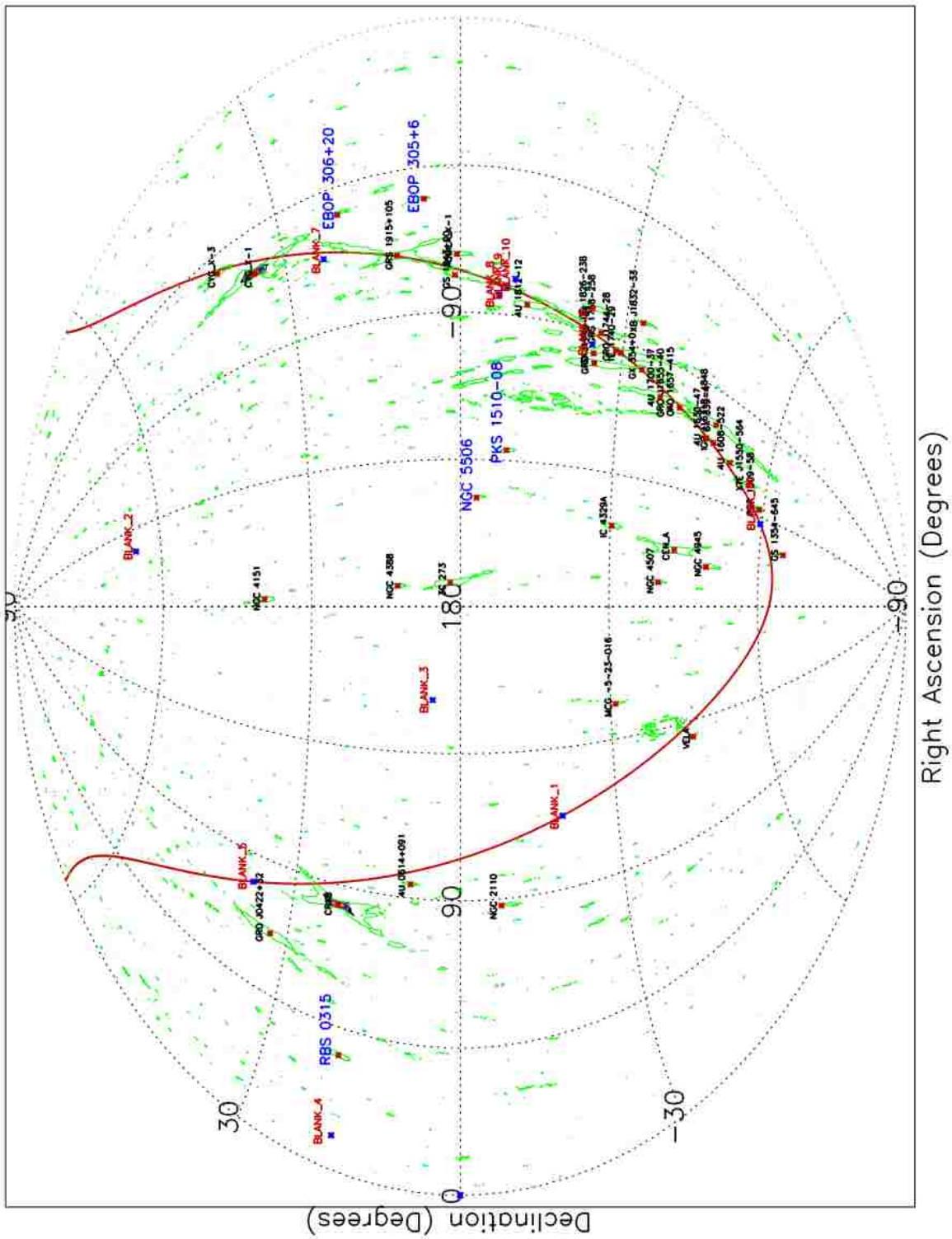

Figure 4.8: All-sky map summed over 64 precession periods (TJD 08393 - TJD 11690) over the energy range 98 - 230 keV. 3 sigma (statistical) features are contoured in green. The source names in black denote the original sources in the 2007 catalog; blue denotes the 5 new sources; red marks 11 blank sources included to study systematic errors and sensitivity.

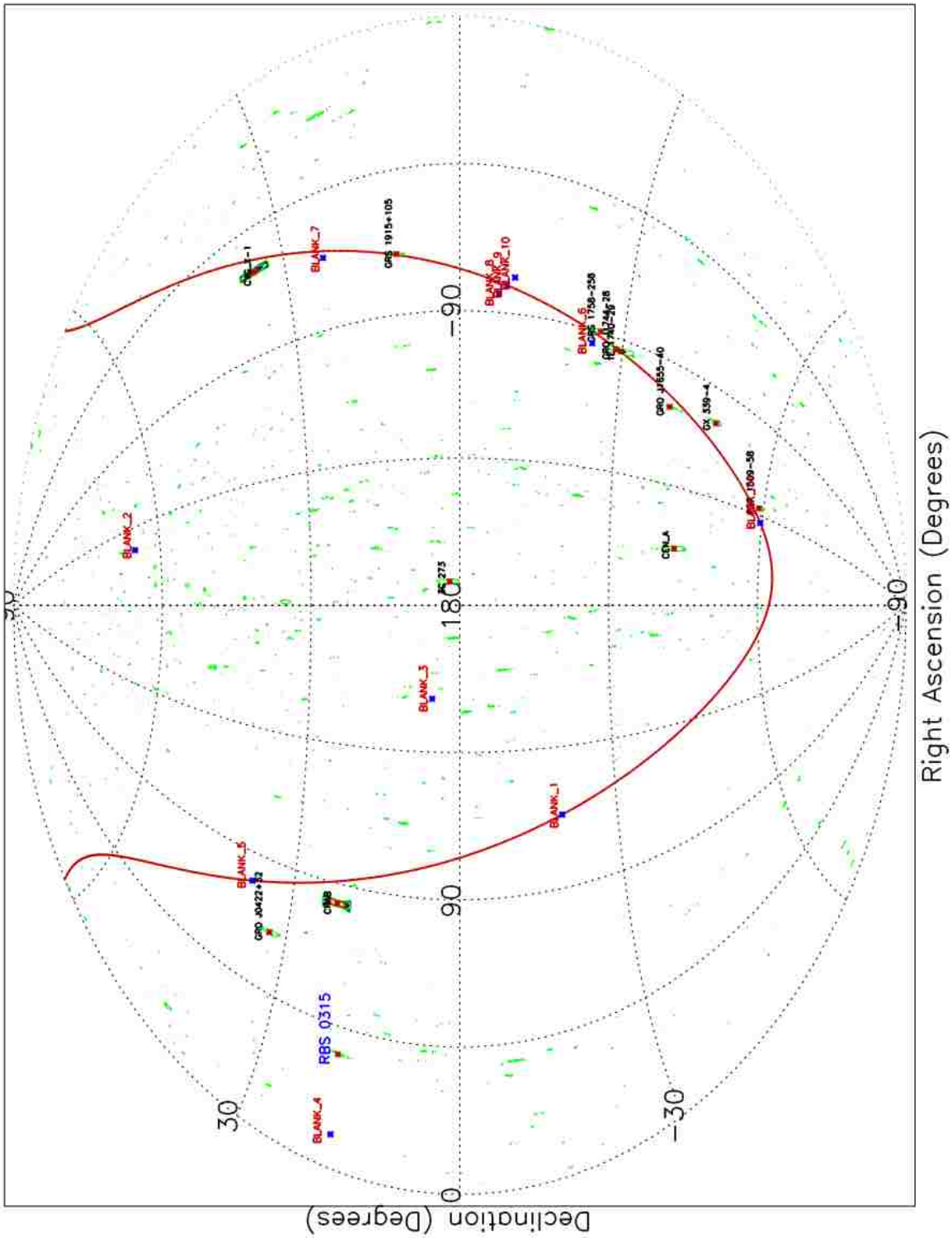

Figure 4.9: All-sky map summed over 64 precession periods (TJD 08393 - TJD 11690) over the energy range 230 - 595 keV. 3 sigma (statistical) features are contoured in green. The source names in black denote the original sources in the 2007 catalog; blue denotes the 1 new sources; red marks 11 blank sources included to study systematic errors and sensitivity..

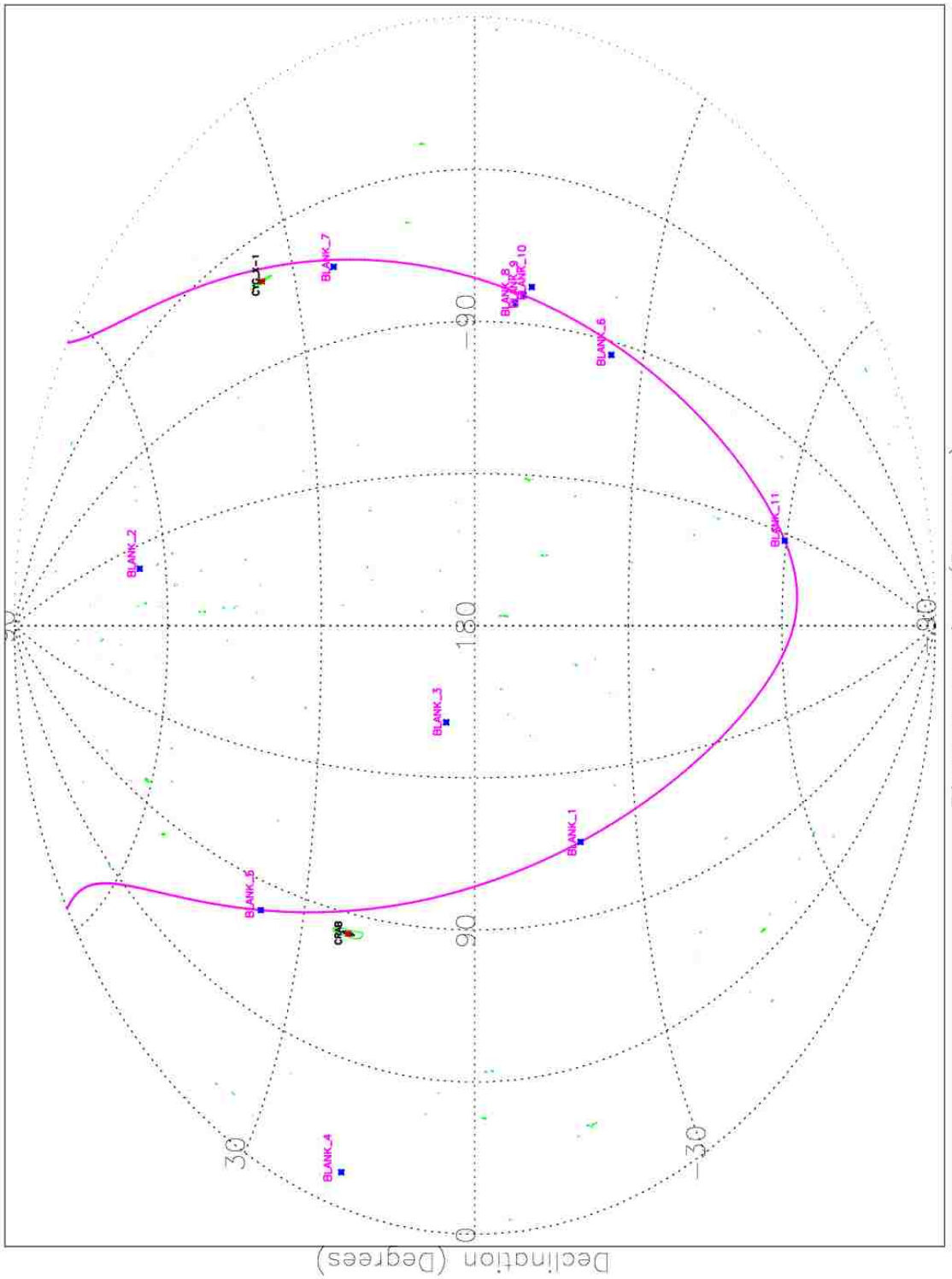

Figure 4.10: All-sky map summed over 64 precession periods (TJD 08393 - TJD 11690) over the energy range 595 - 1798 keV. 3 sigma (statistical) features are contoured in green. The source names in black denote the original sources in the 2007 catalog; magenta marks 11 blank sources included to study systematic errors and sensitivity.

Table 4.3: Source Catalog for 23 - 98 keV

Source Name	Known Position (Degrees)	Image Position (Degrees)	Pos. Err (Degrees)	Type of Source
XTE J0111-7317	(17.79 , -73.28)	(19.66 , -73.54)	1.89	HMXB,PSR
SMC X-1	(19.27 , -73.44)	(19.53 , -73.54)	0.28	HMXB,PSR
4U 0115+634	(19.63 , 63.74)	(19.81 , 64.41)	0.69	HMXB,PSR
*MCG +08-03-018	(20.67 , 50.07)	(21.59 , 53.93)	3.97	Galaxy
*RBS 0315	(36.26 , 18.81)	(36.53 , 18.2)	0.67	Quasar
*MRK 595	(40.46 , 7.19)	(40.49 , 6.09)	1.1	S1 Galaxy
X PER	(58.85 , 31.05)	(58.77 , 29.45)	1.6	HMXB,PSR
*EBOP 061-11	(61.19 , -11.7)	(61.11 , -7.47)	4.23	Unknown
XTE J0421+560	(64.93 , 56)	(64.71 , 57.24)	1.26	HMXB,BHC?
GRO J0422+32	(65.43 , 32.91)	(65.52 , 32.91)	0.09	LMXB,BHC
LMC X-4	(83.21 , -66.37)	(83.58 , -66.43)	0.37	HMXB,PSR
CRAB	(83.63 , 22.01)	(83.71 , 21.95)	0.1	SNR,PSR
NGC 2110	(88.05 , -7.46)	(87.91 , -9.01)	1.56	S2 Galaxy
4U 0614+091	(94.28 , 9.14)	(94.35 , 9.14)	0.07	LMXB,NS
*EBOP 100-9	(100.24 , -9.17)	(100.54 , -9.76)	0.66	Unknown
EXO 0748-676	(117.14 , -67.75)	(117.26 , -68.1)	0.37	LMXB,NS
VELA	(128.55 , -45.75)	(129.22 , -44.22)	1.67	SNR,PSR
GRS 0834-430	(129.16 , -43.26)	(129.3 , -44.13)	0.88	HMXB,PSR
VELA X-1	(135.53 , -40.55)	(135.44 , -40.55)	0.09	HMXB,PSR
MCG -5-23-016	(146.92 , -30.95)	(146.93 , -31.56)	0.61	S2 Galaxy
GRO J1008-57	(152.44 , -58.27)	(152.55 , -56.39)	1.88	HMXB,PSR
GRS 1009-45	(153.4 , -45.08)	(153.65 , -45.38)	0.39	LMXB,BHC
*NGC 3227	(155.87 , 19.86)	(156.09 , 20.04)	0.28	S1 Galaxy

Continued on next page

Table 4.3 continued

Source Name	Known Position (Degrees)	Image Position (Degrees)	Pos. Err (Degrees)	Type of Source
*EBOP 168+18	(168.4 , 18.4)	(168.21 , 18.4)	0.19	Unknown
XTE J1118+480	(169.55 , 48.04)	(169.21 , 50.82)	2.8	LMXB,BHC
A1118-616	(170.24 , -61.92)	(170.13 , -60.71)	1.21	HMXB,PSR
CEN X-3	(170.31 , -60.62)	(170.12 , -60.68)	0.2	HMXB,PSR
NOVA MUSCAE	(171.61 , -68.68)	(171.98 , -68.74)	0.37	LMXB,BHC
NGC 3783	(174.76 , -37.74)	(174.64 , -37.81)	0.14	S1 Galaxy
1E 1145-614	(176.87 , -61.95)	(176.94 , -61.87)	0.11	HMXB,NS
NGC 4151	(182.6 , 39.51)	(182.75 , 39.42)	0.17	S1 Galaxy
NGC 4388	(186.45 , 12.66)	(186.62 , 12.7)	0.17	S2 Galaxy
GX 301-2	(186.66 , -62.77)	(186.83 , -62.97)	0.26	HMXB,PSR
3C 273	(187.28 , 2.05)	(187.32 , 1.81)	0.24	Quasar
NGC 4507	(188.9 , -39.91)	(189.08 , -39.84)	0.19	S2 Galaxy
*NGC 4593	(189.91 , -5.35)	(189.6 , -3.59)	1.79	S1 Galaxy
NGC 4945	(196.36 , -49.47)	(196.77 , -51.71)	2.28	S2 Galaxy
CEN A	(201.47 , -42.97)	(201.42 , -43.08)	0.12	S2 Galaxy
4U 1323-619	(201.65 , -62.14)	(201.91 , -62.27)	0.29	LMXB,BHC
IC 4329A	(207.33 , -30.31)	(207.18 , -30.63)	0.35	S1 Galaxy
GS 1354-645	(209.54 , -64.73)	(209.45 , -64.73)	0.09	LMXB,BHC
CIRCINUS GALAXY	(213.29 , -65.34)	(213.36 , -65.77)	0.44	S2 Galaxy
*NGC 5506	(213.31 , -3.21)	(213.3 , -3.1)	0.11	S2 Galaxy
NGC 5548	(214.5 , 25.13)	(214.48 , 25.44)	0.31	S1 Galaxy
4U 1416-62	(215.3 , -62.7)	(215.21 , -62.7)	0.09	HMXB,PSR
*PKS 1510-08	(228.22 , -9.09)	(228.39 , -9.07)	0.17	Quasar
PSR 1509-58	(228.48 , -59.14)	(229.09 , -58.4)	0.96	SNR,PSR

Continued on next page

Table 4.3 continued

Source Name	Known Position (Degrees)	Image Position (Degrees)	Pos. Err (Degrees)	Type of Source
CIR X-1	(230.17 , -57.17)	(230.08 , -57.17)	0.09	LMXB,NS
4U 1538-522	(235.6 , -52.39)	(235.91 , -52.39)	0.31	HMXB,PSR
4U 1543-45	(236.79 , -47.67)	(236.6 , -47.67)	0.19	LMXB,BHC
XTE J1550-564	(237.77 , -56.48)	(237.58 , -56.48)	0.19	LMXB,BHC
4U 1608-522	(243.18 , -52.42)	(243.72 , -53.02)	0.81	LMXB,NS
SCO X-1	(244.98 , -15.64)	(245.08 , -15.75)	0.15	LMXB,NS
IGR J16318-4848	(247.97 , -48.81)	(248.18 , -48.81)	0.21	HMXB
4U 1627-673	(248.07 , -67.46)	(248.51 , -67.6)	0.46	LMXB,PSR
*EBOP 248-33	(248.39 , -33.92)	(248 , -33.92)	0.39	Unknown
4U 1630-47	(248.505 , -47.393)	(248.33 , -48.91)	1.53	LMXB,BHC
*EBOP 252-01	(252.02 , -2.19)	(251.98 , -1.21)	0.98	Unknown
MRK 501	(253.467 , 39.755)	(253.38 , 39.76)	0.09	Blazar
GRO J1655-40	(253.5 , -39.85)	(253.41 , -39.85)	0.09	LMXB,BHC
HER X-1	(254.46 , 35.34)	(254.51 , 35.53)	0.2	LMXB,PSR
OAO 1657-415	(255.2 , -41.67)	(255.11 , -41.67)	0.09	HMXB,PSR
GX 339-4	(255.71 , -48.79)	(255.95 , -48.98)	0.31	LMXB,BHC
4U 1700-37	(255.99 , -37.84)	(255.93 , -38.67)	0.83	HMXB,NS?
GX 349+2	(256.44 , -36.42)	(255.98 , -38.24)	1.88	LMXB,NS
4U 1702-429	(256.56 , -43.04)	(256.47 , -43.04)	0.09	LMXB,NS
4U 1705-440	(257.23 , -44.09)	(257.24 , -44.09)	0.01	LMXB,NS
GRO J1719-24	(259.93 , -25.01)	(259.84 , -25.01)	0.09	LMXB,BHC
*EBOP 261-6	(261.63 , -6.93)	(263.11 , -10.26)	3.64	Unknown
4U 1722-30	(261.89 , -30.8)	(262 , -30.8)	0.11	LMXB
GX 9+9	(262.93 , -16.96)	(262.94 , -16.96)	0.01	LMXB,NS

Continued on next page

Table 4.3 continued

Source Name	Known Position (Degrees)	Image Position (Degrees)	Pos. Err (Degrees)	Type of Source
GX 354+0	(263 , -33.84)	(263.41 , -33.84)	0.41	LMXB,NS
GX 1+4	(263.01 , -24.75)	(263.12 , -24.75)	0.11	HMXB,PSR
*EBOP 264-19	(264.47 , -19.53)	(266.61 , -17)	3.31	Unknown
4U 1735-44	(264.74 , -44.45)	(264.85 , -44.45)	0.11	LMXB,NS
1E 1740-29	(265.98 , -29.72)	(266.2 , -29.83)	0.25	LMXB?,BHC
GRO J1744-28	(266.138 , -28.739)	(266.19 , -29.8)	1.06	LMXB,PSR
IGR J17464-3213	(266.26 , -32.28)	(266.18 , -29.84)	2.44	LMXB,BHC
GX 3+1	(266.98 , -26.56)	(266.1 , -29.63)	3.19	LMXB,NS
XTE J1748-288	(267.021 , -28.474)	(266.12 , -29.78)	1.59	LMXB,BHC
GX 5-1	(270.28 , -25.08)	(270.49 , -26.08)	1.02	LMXB,NS
GRS 1758-258	(270.3 , -25.74)	(270.51 , -26.24)	0.54	LMXB,BHC
GX 9+1	(270.39 , -20.53)	(271 , -20.53)	0.61	LMXB,NS
4U 1812-12	(273.8 , -12.08)	(274.19 , -6.95)	5.14	LMXB,NS
GX 17+2	(274.007 , -14.037)	(274.62 , -14.34)	0.68	LMXB,NS?
*EBOP 275+26	(275.37 , 26.49)	(275.98 , 26.49)	0.61	Unknown
4U 1820-303	(275.92 , -30.36)	(276.13 , -30.36)	0.21	LMXB,NS
4U 1822-371	(276.45 , -37.11)	(276.51 , -37.97)	0.86	LMXB,NS
GS 1826-238	(277.368 , -23.797)	(277.55 , -23.91)	0.21	LMXB,NS
XB J1832-33	(278.93 , -32.99)	(279.14 , -32.99)	0.21	LMXB,NS
SER X-1	(279.99 , 5.04)	(279.6 , 5.04)	0.39	LMXB,NS
*EBOP 281+55	(281.38 , 55.51)	(281.67 , 55.51)	0.29	Unknown
*EBOP 281-16	(281.41 , -16.05)	(282.19 , -16.95)	1.19	Unknown
GS 1843+00	(281.386 , 0.954)	(281.09 , 0.16)	0.85	HMXB,PSR
GS 1845-024	(282.073 , -2.42)	(282.32 , 0.47)	2.9	HMXB,PSR

Continued on next page

Table 4.3 continued

Source Name	Known Position (Degrees)	Image Position (Degrees)	Pos. Err (Degrees)	Type of Source
*IGR J18485-0047	(282.17 , -0.79)	(282.11 , -0.06)	0.73	γ-ray Source
*4U 1850-086	(283.27 , -8.71)	(283.53 , -9.1)	0.47	LMXB,NS
XTE J1859+226	(284.67 , 22.66)	(288.52 , 16.76)	7.05	LMXB,BHC
XTE J1858+034	(284.68 , 3.43)	(284.29 , 3.43)	0.39	HMXB,NS
AQUILA X-1	(287.82 , 0.58)	(288.43 , 0.58)	0.61	LMXB,NS
GRS 1915+105	(288.82 , 10.97)	(288.77 , 10.85)	0.13	LMXB,BHC
4U 1916-053	(289.7 , -5.24)	(290.11 , -5.24)	0.41	LMXB,NS
*EBOP 291-15	(290.82 , -15.01)	(288.24 , -11.32)	4.5	Unknown
*EBOP 294+10	(294.25 , 10.01)	(293.86 , 10.01)	0.39	Unknown
GRO J1944+26	(296.41 , 27.37)	(297.02 , 27.37)	0.61	HMXB,PSR
CYG X-1	(299.59 , 35.2)	(299.69 , 35.12)	0.13	HMXB,BHC
*EBOP 305+6	(305.23 , 6)	(305.26 , 6.45)	0.45	Unknown
*EBOP 306+20	(306.03 , 20.29)	(306.14 , 20.29)	0.11	Unknown
EXO 2030+375	(308.06 , 37.64)	(308.17 , 37.64)	0.11	HMXB,NS
CYG X-3	(308.11 , 40.96)	(308.14 , 40.96)	0.03	HMXB,BH?
*MRK 509	(311.03 , -10.73)	(311 , -11.04)	0.31	S1 Galaxy
GRO J2058+42	(314.75 , 41.72)	(315.86 , 41.72)	1.11	HMXB,PSR
*SWIFT J2118.9+3336	(319.86 , 33.56)	(319.49 , 32.58)	1.05	S1 Galaxy
4U 2129+12	(322.49 , 12.17)	(322.26 , 11.67)	0.55	LMXB
CYG X-2	(326.17 , 38.32)	(326.1 , 38.52)	0.21	LMXB,NS
*NGC 7172	(330.51 , -31.87)	(330.58 , -32.02)	0.17	S2 Galaxy
*4U 2206+54	(331.96 , 54.51)	(332.18 , 54.49)	0.22	HMXB
*EBOP 346-8	(346.18 , -8.69)	(345.87 , -7.76)	0.98	Unknown
*NGC 7582	(349.6 , -42.37)	(349.86 , -42.97)	0.65	S2 Galaxy

Continued on next page

Table 4.3 continued

Source Name	Known Position (Degrees)	Image Position (Degrees)	Pos. Err (Degrees)	Type of Source
BLANK 1	(113.33 , -19.53)			Blank Source
BLANK 2	(212 , 65)			Blank Source
BLANK 3	(151.34 , 5.52)			Blank Source
BLANK 4	(10.682 , 17.822)			Blank Source
BLANK 5	(79.873 , 37.315)			Blank Source
BLANK 6	(265.7 , -24.379)			Blank Source
BLANK 7	(293.5 , 23.5)			Blank Source
BLANK 8	(275.85 , -7)			Blank Source
BLANK 9	(278.53 , -8.39)			Blank Source
BLANK 10	(281.23 , -9.76)			Blank Source
BLANK 11	(221.65 , -59.69)			Blank Source

Table 4.4: Source Catalog for 98 - 230 keV

Source Name	Known Position (Degrees)	Image Position (Degrees)	Pos. Err (Degrees)	Type of Source
*RBS 0315	(36.26 , 18.81)	(36.53 , 18.2)	0.67	Quasar
GRO J0422+32	(65.43 , 32.91)	(65.52 , 32.91)	0.09	LMXB,BHC
CRAB	(83.63 , 22.01)	(83.71 , 21.95)	0.1	SNR,PSR
NGC 2110	(88.05 , -7.46)	(87.91 , -9.01)	1.56	S2 Galaxy
4U 0614+091	(94.28 , 9.14)	(94.35 , 9.14)	0.07	LMXB,NS
VELA	(128.55 , -45.75)	(129.22 , -44.22)	1.67	SNR,PSR
MCG -5-23-016	(146.92 , -30.95)	(146.93 , -31.56)	0.61	S2 Galaxy
NGC 4151	(182.6 , 39.51)	(182.75 , 39.42)	0.17	S1 Galaxy
NGC 4388	(186.45 , 12.66)	(186.62 , 12.7)	0.17	S2 Galaxy
3C 273	(187.28 , 2.05)	(187.32 , 1.81)	0.24	Quasar
NGC 4507	(188.9 , -39.91)	(189.08 , -39.84)	0.19	S2 Galaxy
NGC 4945	(196.36 , -49.47)	(196.77 , -51.71)	2.28	S2 Galaxy
CEN A	(201.47 , -42.97)	(201.42 , -43.08)	0.12	S2 Galaxy
IC 4329A	(207.33 , -30.31)	(207.18 , -30.63)	0.35	S1 Galaxy
GS 1354-645	(209.54 , -64.73)	(209.45 , -64.73)	0.09	LMXB,BHC
*NGC 5506	(213.31 , -3.21)	(213.3 , -3.1)	0.11	S2 Galaxy
*PKS 1510-08	(228.22 , -9.09)	(228.39 , -9.07)	0.17	Quasar
PSR 1509-58	(228.48 , -59.14)	(229.09 , -58.4)	0.96	SNR,PSR
XTE J1550-564	(237.77 , -56.48)	(237.58 , -56.48)	0.19	LMXB,BHC
4U 1608-522	(243.18 , -52.42)	(243.72 , -53.02)	0.81	LMXB,NS
IGR J16318-4848	(247.97 , -48.81)	(248.18 , -48.81)	0.21	HMXB
4U 1630-47	(248.505 , -47.393)	(248.33 , -48.91)	1.53	LMXB,BHC
GRO J1655-40	(253.5 , -39.85)	(253.41 , -39.85)	0.09	LMXB,BHC

Continued on next page

Table 4.4 continued

Source Name	Known Position (Degrees)	Image Position (Degrees)	Pos. Err (Degrees)	Type of Source
OAO 1657-415	(255.2 , -41.67)	(255.11 , -41.67)	0.09	HMXB,PSR
GX 339-4	(255.71 , -48.79)	(255.95 , -48.98)	0.31	LMXB,BHC
4U 1700-37	(255.99 , -37.84)	(255.93 , -38.67)	0.83	HMXB,NS?
GRO J1719-24	(259.93 , -25.01)	(259.84 , -25.01)	0.09	LMXB,BHC
GX 354+0	(263 , -33.84)	(263.41 , -33.84)	0.41	LMXB,NS
GX 1+4	(263.01 , -24.75)	(263.12 , -24.75)	0.11	HMXB,PSR
1E 1740-29	(265.98 , -29.72)	(266.2 , -29.83)	0.25	LMXB?,BHC
GRO J1744-28	(266.138 , -28.739)	(266.19 , -29.8)	1.06	LMXB,PSR
GRS 1758-258	(270.3 , -25.74)	(270.51 , -26.24)	0.54	LMXB,BHC
4U 1812-12	(273.8 , -12.08)	(274.19 , -6.95)	5.14	LMXB,NS
GS 1826-238	(277.368 , -23.797)	(277.55 , -23.91)	0.21	LMXB,NS
XB J1832-33	(278.93 , -32.99)	(279.14 , -32.99)	0.21	LMXB,NS
GS 1843+00	(281.386 , 0.954)	(281.09 , 0.16)	0.85	HMXB,PSR
AQUILA X-1	(287.82 , 0.58)	(288.43 , 0.58)	0.61	LMXB,NS
GRS 1915+105	(288.82 , 10.97)	(288.77 , 10.85)	0.13	LMXB,BHC
CYG X-1	(299.59 , 35.2)	(299.69 , 35.12)	0.13	HMXB,BHC
*EBOP 305+6	(305.23 , 6)	(305.26 , 6.45)	0.45	Unknown
*EBOP 306+20	(306.03 , 20.29)	(306.14 , 20.29)	0.11	Unknown
CYG X-3	(308.11 , 40.96)	(308.14 , 40.96)	0.03	HMXB,BH?

Table 4.5: Source Catalog for 230 - 595 keV

Source Name	Known Position (Degrees)	Image Position (Degrees)	Pos. Err (Degrees)	Type of Source
*RBS 0315	(36.26 , 18.81)	(36.53 , 18.2)	0.67	Quasar
GRO J0422+32	(65.43 , 32.91)	(65.52 , 32.91)	0.09	LMXB,BHC
CRAB	(83.63 , 22.01)	(83.71 , 21.95)	0.10	SNR,PSR
3C 273	(187.28 , 2.05)	(187.32 , 1.81)	0.24	Quasar
CEN A	(201.47 , -42.97)	(201.42 , -43.08)	0.12	S2 Galaxy
PSR 1509-58	(228.48 , -59.14)	(229.09 , -58.4)	0.96	SNR,PSR
GRO J1655-40	(253.5 , -39.85)	(253.41 , -39.85)	0.09	LMXB,BHC
GX 339-4	(255.71 , -48.79)	(255.95 , -48.98)	0.31	LMXB,BHC
1E 1740-29	(265.98 , -29.72)	(266.2 , -29.83)	0.25	LMXB?,BHC
GRO J1744-28	(266.138 , -28.739)	(266.19 , -29.8)	1.06	LMXB,PSR
GRS 1758-258	(270.3 , -25.74)	(270.51 , -26.24)	0.54	LMXB,BHC
GRS 1915+105	(288.82 , 10.97)	(288.77 , 10.85)	0.13	LMXB,BHC
CYG X-1	(299.59 , 35.2)	(299.69 , 35.12)	0.13	HMXB,BHC

Chapter 5
Enhanced BATSE Occultation Package (EBOP) with Implementation

5.1 Introduction of EBOP

Independent of the Marshall Space Flight Center BATSE instrument team, the JPL group developed the Enhanced BATSE Occultation Package (EBOP), originally motivated by the analysis problems encountered in the HEAO 3 High-Resolution Spectroscopy experiment (Mahoney, Ling, & Jacobson 1981, Wheaton et al. 1995). The general approach was described by Mahoney et al. (1984), Wheaton et al. (1989), and Wheaton et al. (1995).

The JPL Earth-Occultation Analysis system consists of two major parts, (a) the linear Earth-occultation model analysis, which estimates count rates, backgrounds, and uncertainties for cosmic sources in each LAD and each energy channel, and (b) the spectral analysis section, including the interface to XSPEC which converts from instrument units [count rates] to physical units [photon fluxes] using the LAD response, XSPEC itself, and MULPLOT, a package for displaying and manipulating the output.

Fig. 5.1 shows a flow diagram of the EBOP system (Ling et al., 2000). First, the raw count data in the 16 COUNT energy channels from each of the eight LADs, all with 2.048 sec resolution, plus housekeeping and quality data files, was sent by MSFC (step 1). These data were then merged and reformatted (Step 2) to 16.384 sec resolution. MSFC also provided a program to compute the response matrix for each of the eight LADs as a function of energy and angle to the sight axis of the detector (The response matrix was updated in 2010). BATSE EOT data were organized by CGRO viewing period (VP, normally 14 days), during

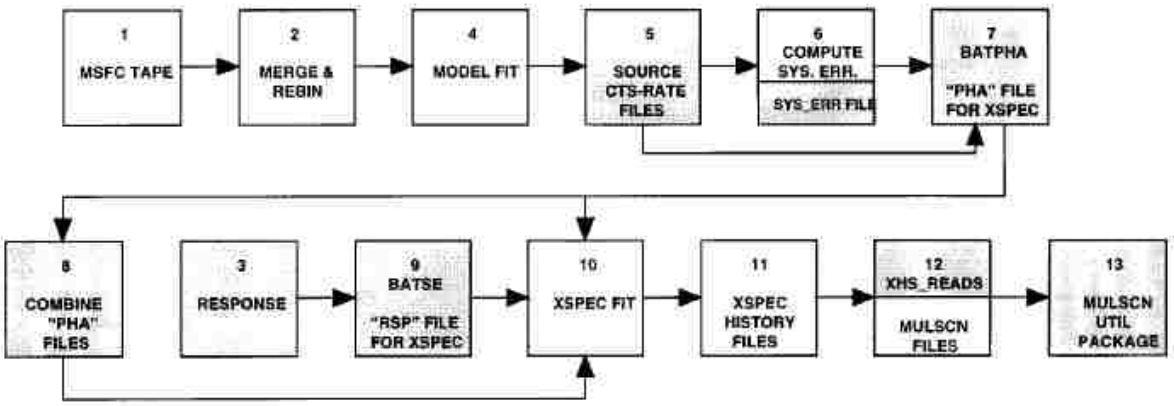

Figure 5.1: An end-to-end flow diagram of the EBOP system developed by the JPL team. The shaded boxes correspond to data files and programs delivered to the Compton Observatory Science Support Center and MSFC (Ling et al., 2000).

each of which the spacecraft's orientation in inertial space was held fixed. For each VP, the detector's response matrix to the cosmic source was first computed (step 3) and then converted to a format compatible with XSPEC (step 9). The heart of the EBOP system is step 4, which fits one day stretches of data to a physical model, linear in the (typically 45-75) unknowns, independently for each CONT energy channel and each LAD. Of these unknowns, 10-35 are count rates due to cosmic point sources, and the remainder (typically ~ 35) are due to background terms in the model. The results obtained are daily count rates and uncertainties for each cosmic source (and background term), for each energy, and for each detector. The remainder of the EBOP system includes procedures to estimate the systematic uncertainties associated with the source count rates (step 6); routines associated with the spectral analysis program XSPEC, which converts source count rates to photon fluxes (step 7, 8, 10, and 11); and utility programs to display and manipulate results, leading to flux histories and time-averaged spectra such as those shown in this chapter (step 12 and 13).

5.1.1 Linear Model Analysis

Earth occultation analysis may be approached in various ways. An important distinction is between methods (sometimes called "superposition ") which accumulate the data first and then subtract the background, and alternative methods which operate in essentially the reverse order. The former accumulate many orbits of data into a data array modulo the orbital period, so as to align the source rise/set edges, until sufficient data are superposed to give significant results. They then subtract the background, e.g., by a polynomial fit. The latter methods subtract the background first and then accumulate the net (i.e., background-subtracted) source count rate estimates (which may be individually of very low statistical significance) to build up significant results. The first class of methods seems natural and attractive and was historically used by early experimenters with the occultation method, but Wheaton et al. (1989, 1995) have given compelling reasons for preferring the second approach. The reason that the accumulate and subtract operations do not commute is essentially that, for small signals riding on top of a large and strongly variable background, the gaps and data cuts that are always present and necessary in real data will introduce into the accumulations a very large source of noise that typically swamps the signal, unless the processing order is as described.

The data analysis approach is based on multi-parameter linear least squares (LLSQ) fits to remove variable background effects from accumulations of data. A linear model for the observed counts n_i in time bins $i = 1, ..., I$ is developed with J terms, including both cosmic sources and uninteresting background effects. The analysis follows the general LLSQ scheme described, e.g., by Wheaton et al. (1995).

For the present results with a bin size of 16.384 s per bin, we have a maximum of 5274 bins per day (typically $I \sim 4300$, accounting for gaps), with $J \sim 45$ to 72 unknowns. Thus, we solve a LLSQ problem of around (4300×70) for each energy channel $k = 0, ..., 15$ and each LAD $n = 0, ..., 7$ for each day of BATSE data.

The background model is one of the most critical parts of the analysis system, since

it determines the accuracy of the background subtraction, which is the most important component of the systematic error. The model used is a semi-empirical one. The model currently in use has six general types of terms: (a) a constant rate, due to, e.g., long-term activation of the LADs and components of the spacecraft, (b) terms due to prompt effects of cosmic rays (CRs), (c) terms due to activation (Gruber, Jung, & Matteson 1989) of the LADs and spacecraft from passages through the trapped radiation belts (mainly in the South Atlantic Anomaly, SAA), with half-lives in the intermediate range (2 minutes$< \tau_{1/2} <$ 1 day), (d) terms due to the activation of the LADs and spacecraft by CRs, from the same activation species as those considered in (c), (e) a term due to the time-variable blockage of the diffuse cosmic γ-ray background by Earth, and (f) terms due to γ-rays from Earth's atmosphere, which are themselves prompt secondaries from CRs striking Earth causing electromagnetic showers in Earth's atmosphere (since the atmosphere is effectively not radioactive).

5.1.2 Post Procedures

After the Linear Model Fit, Steps 5 - 12 convolve systematic error, detector response matrix, outlier removal, and source confusion effects with our linear model results. Here, we take GX339-4 as an example to illustrate the steps in the process.

- Generate initial PHA files

  Restructure the raw data, and write into PHA FITS format.

- Generate initial RMF files

  Calculate response files per day per detector per energy band from response matrix provided by MSFC.

- Create initial lightcurves of all the catalog sources including blank sources

- Generate source confusion exclude list for all the sources:

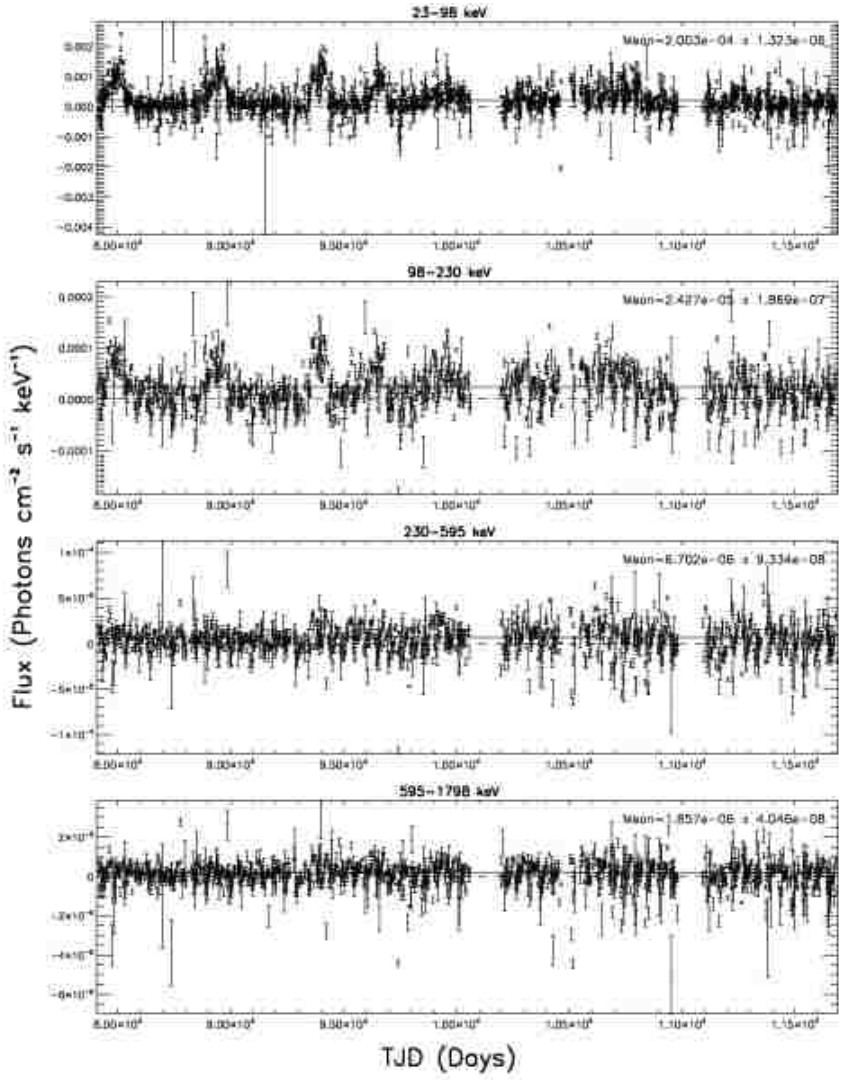

Figure 5.2: The initial lightcurve of GX339-4 for four energy bands.

If there is another bright source near our target source, the flux and error of the target source may be greatly influenced and be significantly greater than the normal level. In order to eliminate these source confusion effects, we exclude those days having source confusion problems. We folded the error onto the spacecraft phase period, and then excluded days with error level above twice of the median (cutoff), and if the cutoff is less than 8.0×10^{-5}, we set the cutoff to be 8.0×10^{-5}. Here, we take GX339-4 as an example (Fig. 5.3). It is clear that the source has source confusion problems during

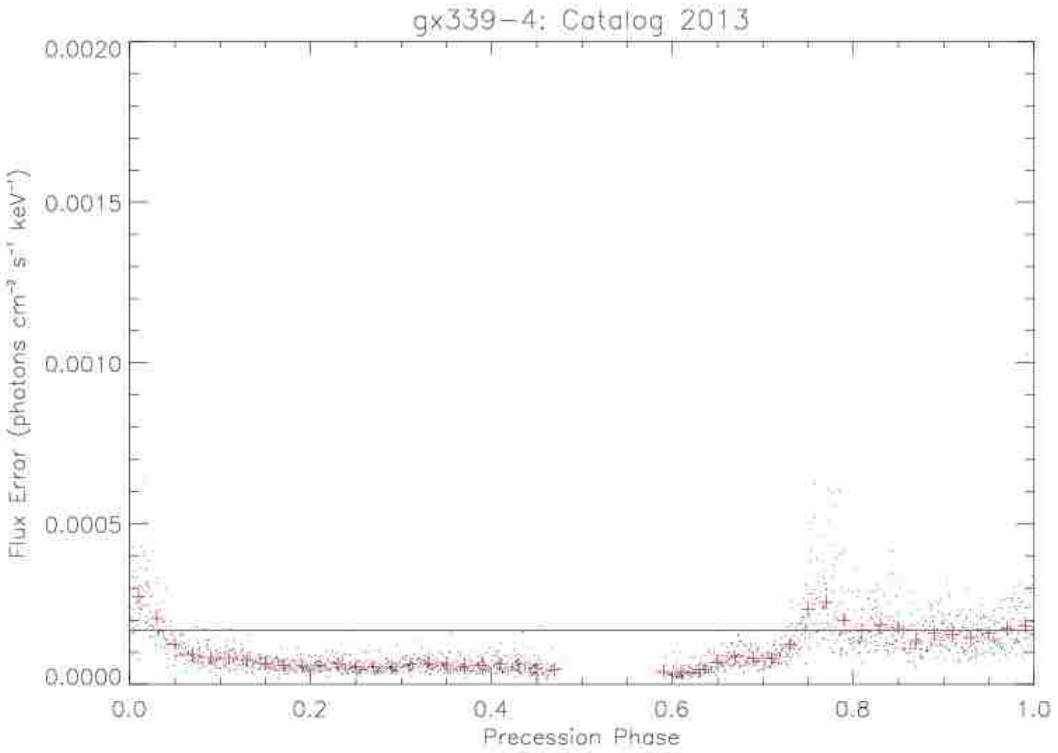

Figure 5.3: Phase bin error cut procedure for GX339-4. It is clear that the source has source confusion problems during phase 0.0-0.1 and phase 0.7-0.8. The red line is the cutoff.

phase 0.0-0.1 and phase 0.7-0.8. The red line is the cutoff. Fig. 5.4 is the limb plot for GX339-4 for TJD 8439-8444 in phase 0.0-0.1. Clearly, the source is confused by GRO J1655-40, OAO 1657-415, 4U 1702-429, and 4U 1705-440 during that period. In total, there are 215 days out of 3000 excluded by this criteria.

- Run systematic error for each viewing period:

  We use the eleven blank sources to measure the systematic error in our system. Fig. 5.5 shows an example for VP339 (TJD 9616-9628). The RMS flux for the eleven blank sources was calculated for each detector and each energy band and taken to be the systematic error.

- Generate PHA files with systematic error

  PHA files are regenerated, adding systematic errors onto statistical errors.

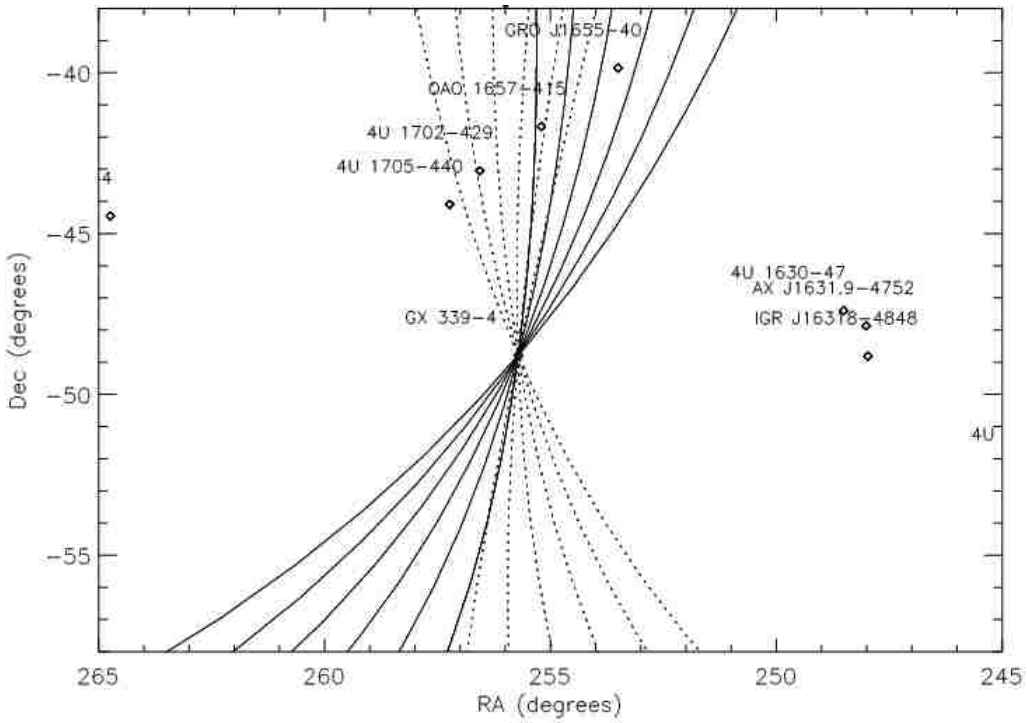

Figure 5.4: GX339-4 is confused by GRO J1655-40, OAO 1657-415, 4U 1702-429, and 4U 1705-440 during TJD 8439-8444, corresponding to its phase 0.0-0.1.

- Create second lightcurves of all the sources with source confusion removed and with systematic error considered

- Run Consistency Check

  Since the CGRO maintains a fixed orientation in inertial space during each VP, and the LADs are oriented differently, the count rate for a given source generally differs from LAD to LAD. Consequently, consistency of fluxes measured by the different LADs is an important check on the results. We assess the consistency among detectors of all the daily spectra as part of our routine data analysis procedure (Ling et al. 1996). We first compute for each of the 14 energy bands k, the weighted-average flux f_k, for each LAD n, where $n = 1, ..., N$, and N is the number of LADs (typically 2 to 4) exposed to the source for the VP, such that the cosine of the angle between source and the look-axis (i.e., normal to the LAD) vector of the detector is greater than 0.4. We take

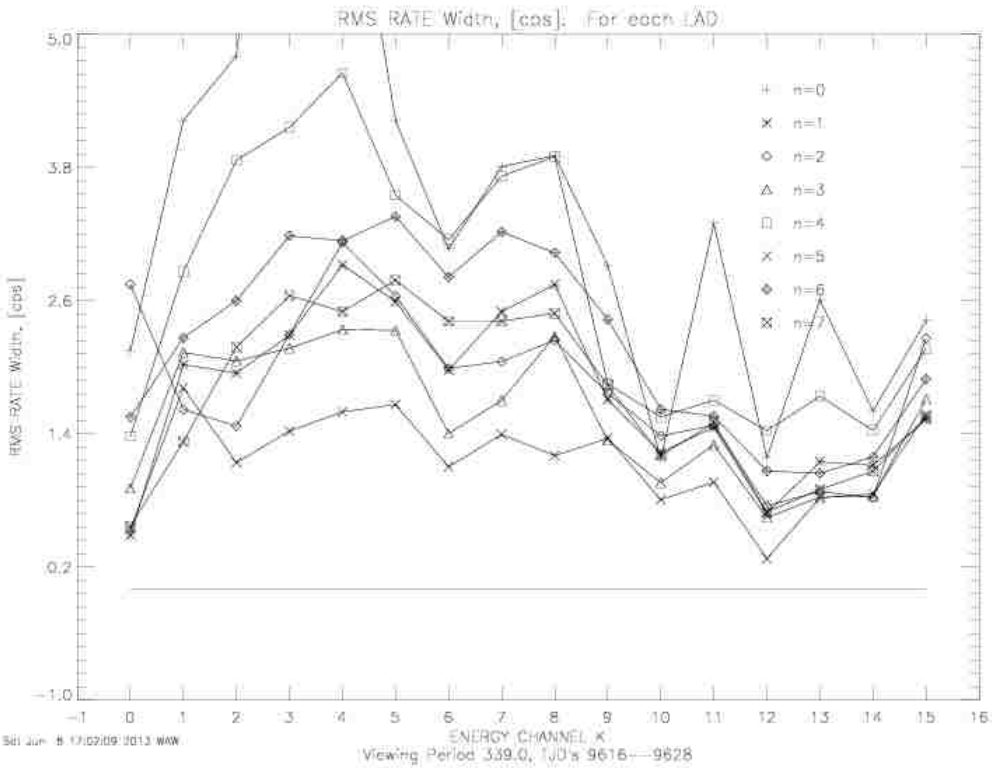

Figure 5.5: Systematic Error Plot for viewing period 339 (TJD 9616-9628) for each detector (0,...,7) and each energy band (1,...,14).

as inputs for each k the individual fitted photon fluxes f_{nk} from the XSPEC model fit. Then $\chi^2 = \Sigma_k \chi_k^2$, where $\chi_k^2 = \Sigma_n (f_{nk} - f_k)^2 \sigma_k^{-2}$, is a good measure of consistency, with degrees of freedom $\mu = 14(N-1)$. Large χ^2 is thus entirely due to inconsistency among detectors. We reject days with probability $P(\chi^2, \mu) < 5\%$.

- Merge exclude lists

  Three exclude lists are generated. One is the phase bin exclude list for confusing sources, the second is from the detector consistency check, the last is the days when only one detector sees the source. These three lists are then merged.

- Create final lightcurves for all the sources with merged exclude lists (Fig. 5.7)

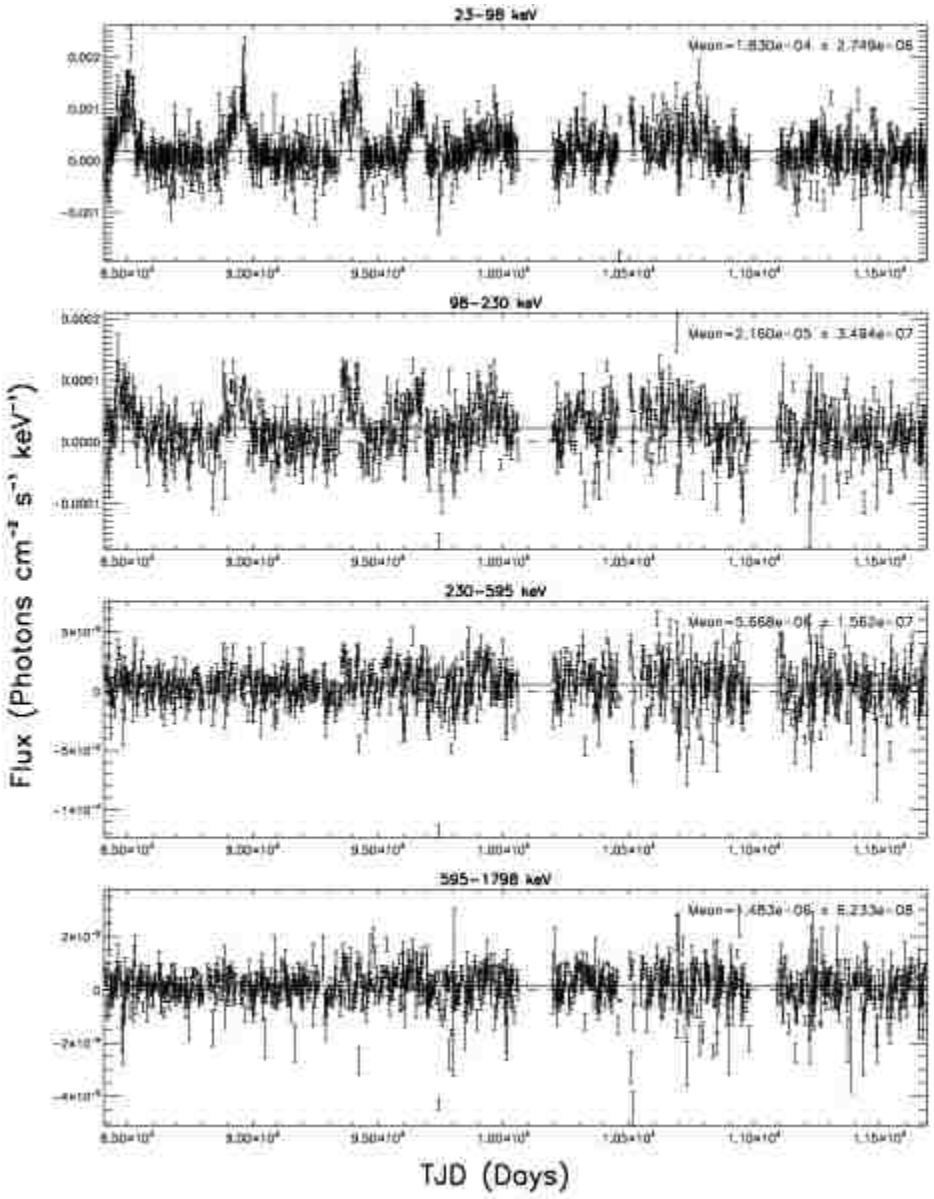

Figure 5.6: The second lightcurve of GX339-4 for four energy bands, excluding source confusion days and including the systematic error.

5.2 Implementation of EBOP

The EBOP routines were moved from the JPL JPLHEA machine to a single-core PC at LSU in 2007, and then moved to the four-core LSU BATSE machine in August 2012. The environment has been updated to version 7.1 of IDL and version 12.6 of XSPEC. The detector

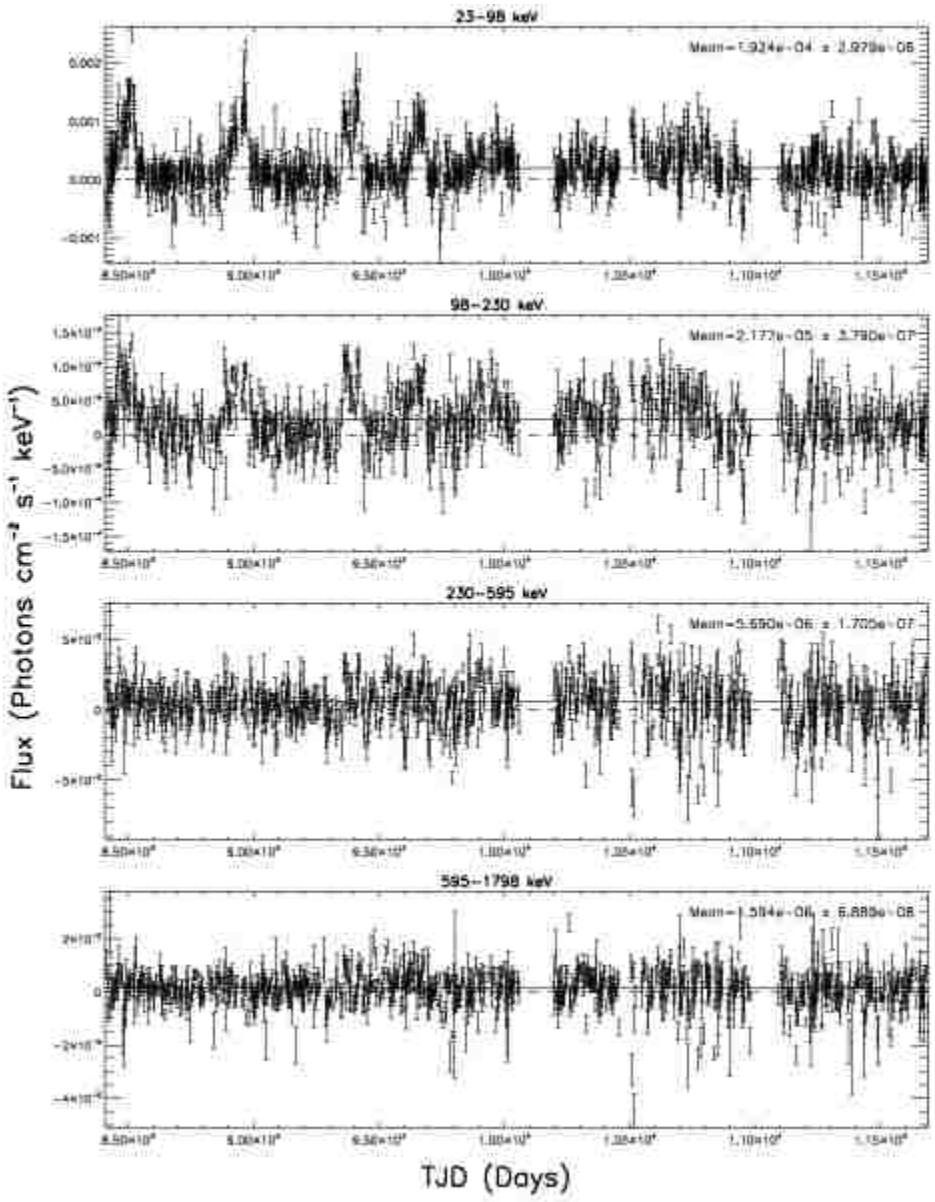

Figure 5.7: The final lightcurve of GX339-4 for four energy bands.

response files were updated by MSFC in 2010. The time required to finish the Linear Model Analysis for 140 sources in 2003 was approximately 1 year. Currently, on the four-core BATSE machine, the linear analysis requires $\sim$ 10 days. The full EBOP analysis now requires $\sim$ 1 month.

5.2.1 Calibration of EBOP

After the catalog was updated using the new IDEOM analysis, the new 2013 Catalog was processed through EBOP to generate revised lightcurves, fluxes, and spectra. With the newer versions of software and updated detector response matrix, we expect differences with the EBOP 2007 results. Two calibrations were used to determine the extent of the differences. The first one uses the same source catalog, EBOP 2007 Catalog, and compares between the 2007 JPL results and the new 2013 LSU results. The next calibration compares the new code with the 2007 and 2013 catalogs.

Calibration between EBOP2007 JPL and EBOP2007 LSU results

The EBOP2007 JPL result uses the EBOP2007 Source Catalogue, run back in 2007 on JPL's JPLHEA machine. The EBOP2007 LSU result uses the same EBOP2007 Source Catalogue, run in 2012 on LSU's BATSE machine with the updated software and response matrix.

The final averaged fluxes were compared for all the sources in the EBOP 2007 Catalogue. In Fig. 5.8, the EBOP 2007 LSU and EBOP 2007 JPL results in 23-98 keV are compared, showing agreement ($R^2 = 0.99$) to within $\sim 10\%$ for sources above ~ 30 mCrab.

A histogram analysis was performed on the 89 sources above 10 mCrab in both catalogs. In Fig. 5.9, the x-axis is calculated by $(EBOP2007LSU - R * EBOP2007JPL)$, where R is a normalization factor chosen such that the average EBOP2007 LSU and EBOP2007 JPL fluxes are equal. In this case, the normalization is 0.98. The dashed line is the expected gaussian, calculated with the expected error in $(EBOP2007LSU - R * EBOP2007JPL)$. From Fig. 5.9, the histogram standard deviation matches very well with the expected error for the difference. Based on a K-S test, the distance between the two distributions is 0.0009 corresponding to a probability of > 0.99 that these are identical distributions aside from the 0.98 normalization factor.

Calibration between EBOP2007 LSU and EBOP2013 LSU results

EBOP2013 LSU consists of the results using the new EBOP2013 source catalog (Chap 4) and updated software run in 2013 on the LSU BATSE machine compared to the results with the same analysis applied to the EBOP2007 Catalog.

96 sources appeared in both the EBOP2007 and EBOP2013 catalogs in the 23-98 keV energy band. Of these, 65 are above 10 mCrab in both catalogs. A similar histogram analysis was performed on these 65 sources. In Fig. 5.10, the x-axis is calculated by ($EBOP2013 - R*EBOP2007$), where R is a normalization factor chosen such that the average EBOP2007 and EBOP2013 fluxes are equal. In this case, the normalization is 0.97. The dashed line is the expected gaussian, calculated with the expected error in ($EBOP2013 - R*EBOP2007$). From Fig. 5.10, the histogram standard deviation matches very well with the expected error for the difference. Based on a K-S test, the distance between the two distributions is 0.0099 corresponding to a probability of > 0.99 that these are identical distributions aside from the 0.97 normalization factor. With the addition of new sources to the EBOP2013 catalog, EBOP 2013 and EBOP 2007 are in good agreement.

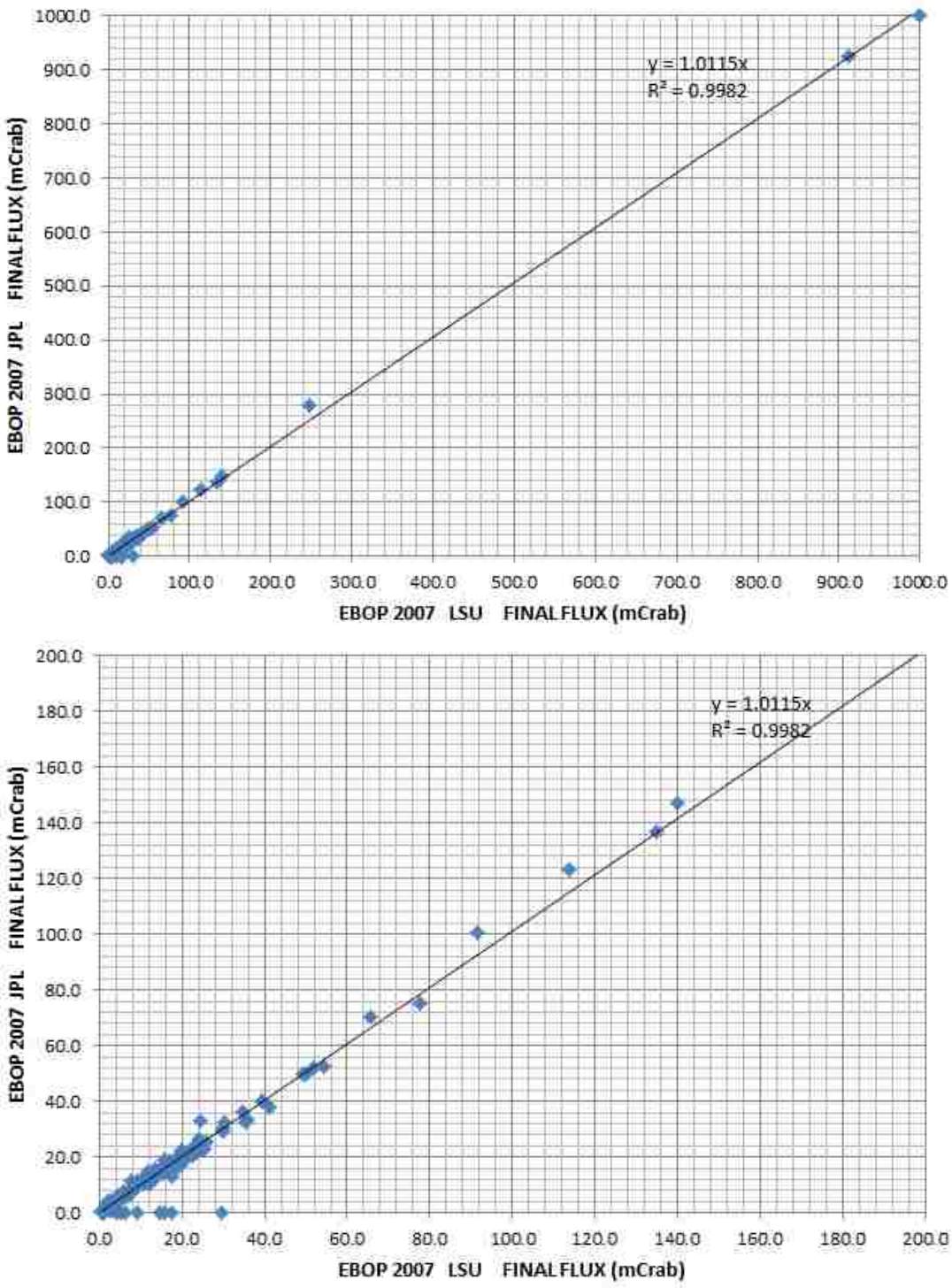

Figure 5.8: The final flux comparison between EBOP2007 JPL results and EBOP2007 LSU results. The upper panel is the whole catalog. The bottom panel only includes sources less than 200 mCrab in both catalogs.

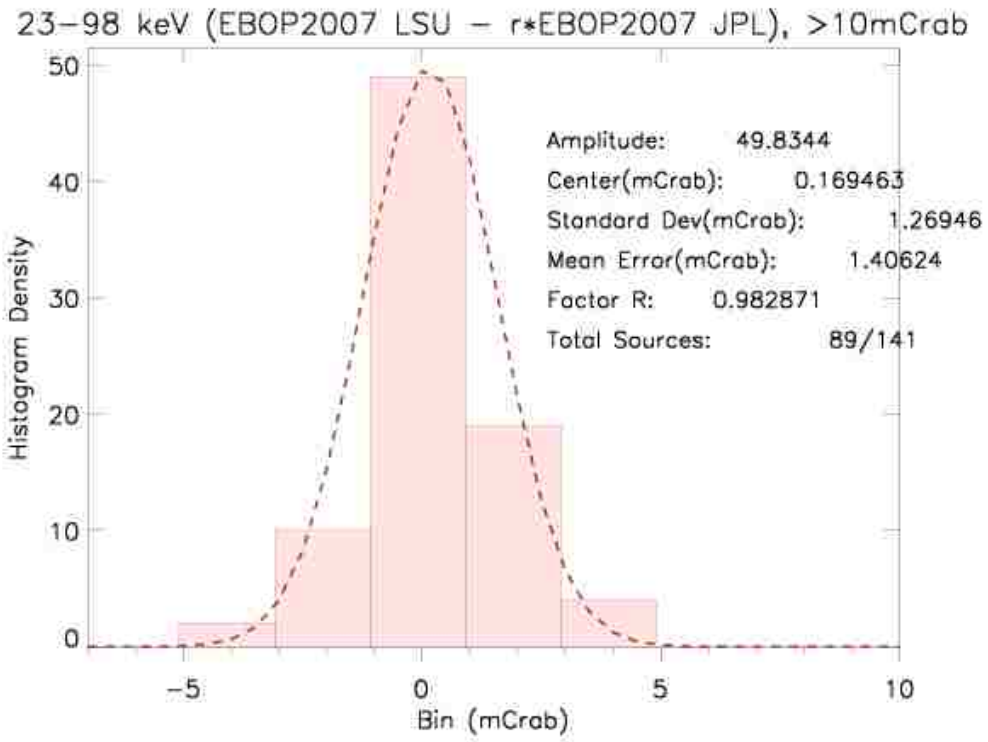

Figure 5.9: The histogram analysis on the normalized difference between EBOP2007 JPL and EBOP2007 LSU. The dashed line is the expected gaussian, calculated using the expected error in their difference.

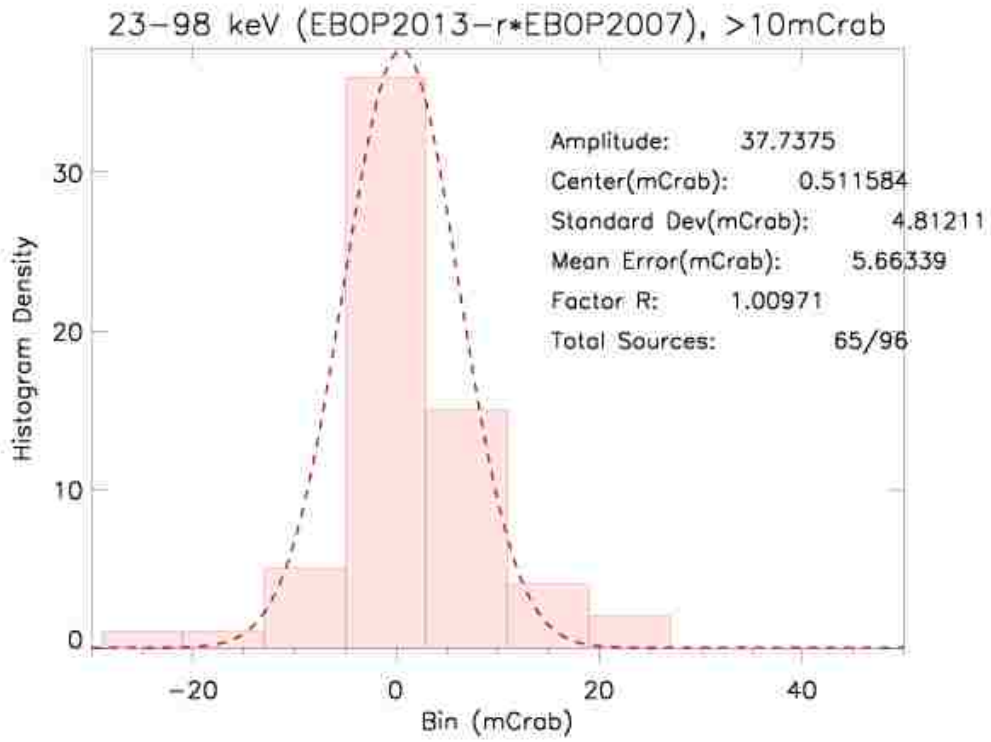

Figure 5.10: The histogram analysis on the normalized difference between EBOP2007 and EBOP2013. The dashed line is the expected gaussian, calculated using the expected error in their difference.

Chapter 6
EBOP 2013 Results

6.1 EBOP 2013 Lightcurves and Fluxes

Appendix A shows flux histories with 2 day resolution for the 23-98 keV energy band for each of the 120 sources covering the entire 9 years of the CGRO mission based on the updated EBOP2013 catalog. Error bars show our best estimate of the total uncertainty. This is the first publication of the 23-98 keV lightcurves measured by BATSE for most of these sources.

Table. 6.1 shows the average flux for four energy bands (23 - 98 keV, 98 - 230 keV, 230 - 595 keV and 595 - 1798 keV) respectively, in units of mCrab, where 1 Crab $= 3.17E-3 \pm 2.83E-6$, $3.17E-4 \pm 3.66E-7$, $3.50E-5 \pm 1.63E-7$, $4.39E-6 \pm 7.46E-8$, in unit of $photons\ cm^{-2}s^{-1}keV^{-1}$ for each of the four energy bands. For the higher energy bands (98-230 keV, 230-595 keV and 595-1798 keV), only sources identified with IDEOM (Table 4.4 and 4.5) have their average flux included in Table. 6.1.

Table 6.1: EBOP 2013 Catalog Average Flux

Source Name	23-98 keV Flux (mCrab)	98-230 keV Flux (mCrab)	230-595 keV Flux (mCrab)	595-1798 keV Flux (mCrab)
XTE J0111-7317	4.26 ± 0.83			
SMC X-1	5.56 ± 0.84			
4U 0115+634	3.55 ± 0.68			
MCG +08-03-018	9.35 ± 0.53			
RBS 0315	10.48 ± 0.44	22 ± 0.77	87.74 ± 2.5	
MRK 595	4.26 ± 0.47			
X PER	16.46 ± 0.47			
EBOP 061-11	14.79 ± 0.5			
XTE J0421+560	3.26 ± 0.53			
GRO J0422+32	31.59 ± 0.47	47.64 ± 0.81	40.07 ± 2.59	
LMC X-4	24.26 ± 0.53			
CRAB	1000 ± 0.89	1000 ± 1.35	1000 ± 4.67	1000 ± 16.98
NGC 2110	13.45 ± 0.47	13.46 ± 0.78		
4U 0614+091	15.14 ± 0.52	14.25 ± 0.84		
EBOP 100-9	8.58 ± 0.49			
EXO 0748-676	-1.26 ± 0.55			
VELA	7.67 ± 0.67	24.55 ± 1.05		
GRS 0834-430	20.87 ± 1.38			
VELA X-1	122.9 ± 0.68			
MCG -5-23-016	13.86 ± 0.56	7.11 ± 0.84		
GRO J1008-57	3.94 ± 0.61			
GRS 1009-45	22.76 ± 0.6			
NGC 3227	7.13 ± 0.51			

Continued on next page

Table – *Continued from previous page*

Source Name	23-98 keV Flux (mCrab)	98-230 keV Flux (mCrab)	230-595 keV Flux (mCrab)	595-1798 keV Flux (mCrab)
EBOP 168+18	10.29 ± 0.51			
XTE J1118+480	15.97 ± 0.54			
A1118-616	0.08 ± 0.84			
CEN X-3	30.12 ± 0.85			
NOVA MUSCAE	0.36 ± 0.66			
NGC 3783	18.81 ± 0.61			
1E 1145-614	17.91 ± 1.84			
NGC 4151	38.59 ± 0.52	36.79 ± 0.85		
NGC 4388	14.47 ± 0.56	17.14 ± 0.91		
GX 301-2	65.24 ± 0.76			
3C 273	18.18 ± 0.62	33.09 ± 0.98	55.65 ± 3.25	
NGC 4507	18.29 ± 0.65	28.45 ± 0.93		
NGC 4593	2.31 ± 0.63			
NGC 4945	23.17 ± 0.74	44.2 ± 1.04		
CEN A	47.83 ± 0.73	76.63 ± 1.05	120.61 ± 3.68	
4U 1323-619	23.57 ± 0.73			
IC 4329A	20.45 ± 0.71	27.49 ± 1.01		
GS 1354-645	17.41 ± 0.76	23.8 ± 1.08		
CIRCINUS GALAXY	9.78 ± 1			
NGC 5506	11.12 ± 0.66	10.94 ± 1		
NGC 5548	14.04 ± 0.55			
4U 1416-62	10.06 ± 0.78			
PKS 1510-08	9.66 ± 0.69	11.54 ± 1.05		
PSR 1509-58	17.45 ± 0.82	31.71 ± 1.21	77.99 ± 4.18	

Continued on next page

Table – *Continued from previous page*

Source Name	23-98 keV Flux (mCrab)	98-230 keV Flux (mCrab)	230-595 keV Flux (mCrab)	595-1798 keV Flux (mCrab)
CIR X-1	21.17 ± 0.82			
4U 1538-522	24.47 ± 0.81			
4U 1543-45	14.33 ± 0.8			
XTE J1550-564	18.23 ± 0.79	35.69 ± 1.17		
4U 1608-522	39.4 ± 0.8	54.4 ± 1.16		
SCO X-1	229.9 ± 1.08			
IGR J16318-4848	34.45 ± 1.16	51.81 ± 1.86		
4U 1627-673	5.74 ± 0.7			
EBOP 248-33	5.51 ± 0.81			
4U 1630-47	31.26 ± 1.23	32.64 ± 1.96		
EBOP 252-01	4.35 ± 0.86			
MRK 501	11.65 ± 0.64			
GRO J1655-40	51 ± 0.97	40 ± 1.43	21.29 ± 5.11	
HER X-1	27.1 ± 0.68			
OAO 1657-415	47.11 ± 1.12	10.6 ± 1.67		
GX 339-4	60.58 ± 0.94	80.25 ± 1.4	162.6 ± 4.87	
4U 1700-37	131.57 ± 1.24	37.3 ± 1.74		
GX 349+2	25.44 ± 1.05			
4U 1702-429	19.99 ± 1.22			
4U 1705-440	28.13 ± 1.13			
GRO J1719-24	32.56 ± 1.03	13.84 ± 1.55		
EBOP 261-6	-0.26 ± 0.92			
4U 1722-30	34.72 ± 1.16			
GX 9+9	7.59 ± 1.2			

Continued on next page

Table – *Continued from previous page*

Source Name	23-98 keV Flux (mCrab)	98-230 keV Flux (mCrab)	230-595 keV Flux (mCrab)	595-1798 keV Flux (mCrab)
GX 354+0	39.76 ± 1.11	35.91 ± 1.66		
GX 1+4	49.67 ± 1.24	7.87 ± 1.84		
EBOP 264-19	6.38 ± 1.29			
4U 1735-44	18.3 ± 0.82			
1E 1740-29	74.61 ± 1.79	112.59 ± 2.81	186.98 ± 10.65	
GRO J1744-28	39.26 ± 1.79	7.96 ± 2.83	-9.33 ± 10.53	
IGR J17464-3213	16.2 ± 1.18			
GX 3+1	13.24 ± 1.59			
XTE J1748-288	21.19 ± 1.61			
GX 5-1	6.13 ± 2.33			
GRS 1758-258	54.58 ± 2.26	79.81 ± 3.58	160.83 ± 13.4	
GX 9+1	27.44 ± 1.11			
4U 1812-12	30.8 ± 1.26	20.77 ± 1.95		
GX 17+2	23.57 ± 1.3			
EBOP 275+26	13.89 ± 0.69			
4U 1820-303	14.69 ± 0.94			
4U 1822-371	13.8 ± 0.89			
GS 1826-238	35.4 ± 0.99	32.84 ± 1.5		
XB J1832-33	15.23 ± 0.86	22.25 ± 1.32		
SER X-1	11.69 ± 1.02			
EBOP 281+55	9.52 ± 0.63			
EBOP 281-16	7.54 ± 1.03			
GS 1843+00	9.87 ± 1.43	9.02 ± 2.31		
GS 1845-024	3.32 ± 1.38			

Continued on next page

Table – *Continued from previous page*

Source Name	23-98 keV Flux (mCrab)	98-230 keV Flux (mCrab)	230-595 keV Flux (mCrab)	595-1798 keV Flux (mCrab)
IGR J18485-0047	20.06 ± 1.79			
4U 1850-086	20.56 ± 0.96			
XTE J1859+226	11.38 ± 0.74			
XTE J1858+034	15.37 ± 0.93			
AQUILA X-1	30.16 ± 0.94	23.93 ± 1.48		
GRS 1915+105	137.71 ± 0.98	65.59 ± 1.5	72.1 ± 5.28	
4U 1916-053	10.22 ± 0.9			
EBOP 291-15	16.81 ± 0.8			
EBOP 294+10	9.08 ± 0.75			
GRO J1944+26	10.09 ± 0.73			
CYG X-1	913.41 ± 0.96	1056.79 ± 1.47	692.69 ± 5.04	337.9 ± 18.33
EBOP 305+6	18.89 ± 0.68	28.28 ± 1.11		
EBOP 306+20	11.68 ± 0.67	21.42 ± 1.11		
EXO 2030+375	11.14 ± 0.68			
CYG X-3	92.81 ± 0.79	31.37 ± 1.23		
MRK 509	13.16 ± 0.64			
GRO J2058+42	9.52 ± 0.61			
SWIFT J2118.9+3336	5.3 ± 0.7			
4U 2129+12	16.08 ± 0.61			
CYG X-2	15.32 ± 0.56			
NGC 7172	16.57 ± 0.51			
4U 2206+54	14.01 ± 0.62			
EBOP 346-8	7.56 ± 0.5			

Continued on next page

Table – *Continued from previous page*

Source Name	23-98 keV Flux (mCrab)	98-230 keV Flux (mCrab)	230-595 keV Flux (mCrab)	595-1798 keV Flux (mCrab)
NGC 7582	9.19 ± 0.47			

6.2 EBOP 2013 Spectra

Spectra integrated over the 9-yr mission are shown in Appendix B and C. Units are keV for the energies and $photons\ cm^{-2}s^{-1}keV^{-1}$ for flux and errors. Error bars give our best estimate of the total uncertainties. Most panels also show a representative power-law fit to the Crab Nebula spectrum measured by BATSE, overlaid as a reference. Spectrum for each source was fitted by single powerlaw, broken powerlaw, comptonization model after Sunyaev and Titarchuk 1980 (CompST), and CompST + powerlaw. The best fitted model is selected and presented.

Because the energy sensitivity decreases above 300 keV and unresolved Galactic diffuse emission becomes significant, we separate the sources into two groups based on their coordinates. If the distance from the source to the Galactic Plane is within 5°, we classify that source as ON Galactic Plane source. Otherwise, it is OFF Galactic Plane Source. OFF Galactic Plane source spectra are given up to 2 MeV in Appendix B. For ON Galactic Plane sources, spectra up to 300 keV are shown in Appendix C. This is the first publication of BATSE spectra for most of these sources, especially up to 2 MeV.

Previous analysis based on EBOP have shown a number of sources with hard spectra above 300 keV (Fig. 1.6 and Ling et al. 2000). These "hard tails" have not been confirmed by the MSFC analysis. Ling et al. (2000) proposed that because EBOP is based on a catalog of known sources, it is vulnerable to contributions due to sources omitted from the catalog. An enlarged source catalog might therefore resolve the hard tail issue. However, in this

dissertation, a differential filtering imaging analysis has been used to locate additional sources and complete the source catalog. Unknown sources are not now expected to contribute significantly to the results.

Another possibility is that there are systematic errors due to backgrounds that are not included in EBOP's linear background model. As an example, Fig. 1.6 shows the spectrum of 4U 1543-45. Fig. 6.1 shows the spectrum as a function of precession phase. The variation with precession phase cannot be due to the source, and indicates a background or systematic problem in the data at high energies. This can be explored by studying the spectra of blank sources. Blank sources have been placed at locations with significance less than 1σ in the 23-98 keV imaging map (Fig. 4.7). The spectrum of blank source 11 in Fig. 6.2 is clearly non-zero and appears to show a hard tail at high energies. In addition, the average intensity of blank sources 1-5 off the Galactic Plane in Fig. 6.3 is distinctly lower than that of sources 6-11 near the Plane.

The blank source spectrum also varies over the spacecraft precession period (Figs. 6.4 and 6.5). The ON Plane vs. OFF Plane difference suggests that the effect is due to the presence of unmodelled diffuse emission from the Galactic Plane.

We therefore took an average of ON Plane blank sources (blanks 6-11) in each of ten phase bins, 0.1 apart. For the ON Galactic Plane sources, the average blank 6-11 source spectrum was subtracted phase by phase from each source spectrum. Appendix D shows the results for the ON Plane sources after subtraction phase by phase of the average blank source spectrum extended up to 2 MeV, where it can be seen that the hard tails persist above 300 keV.

The dependence of the hard tail emission and blank source spectra on precession phase above 300 keV strongly suggests that the measurements above 300 keV are still affected by systematic errors or remaining background contamination. The ON Plane spectra in Appendix C therefore extend only up to 300 keV.

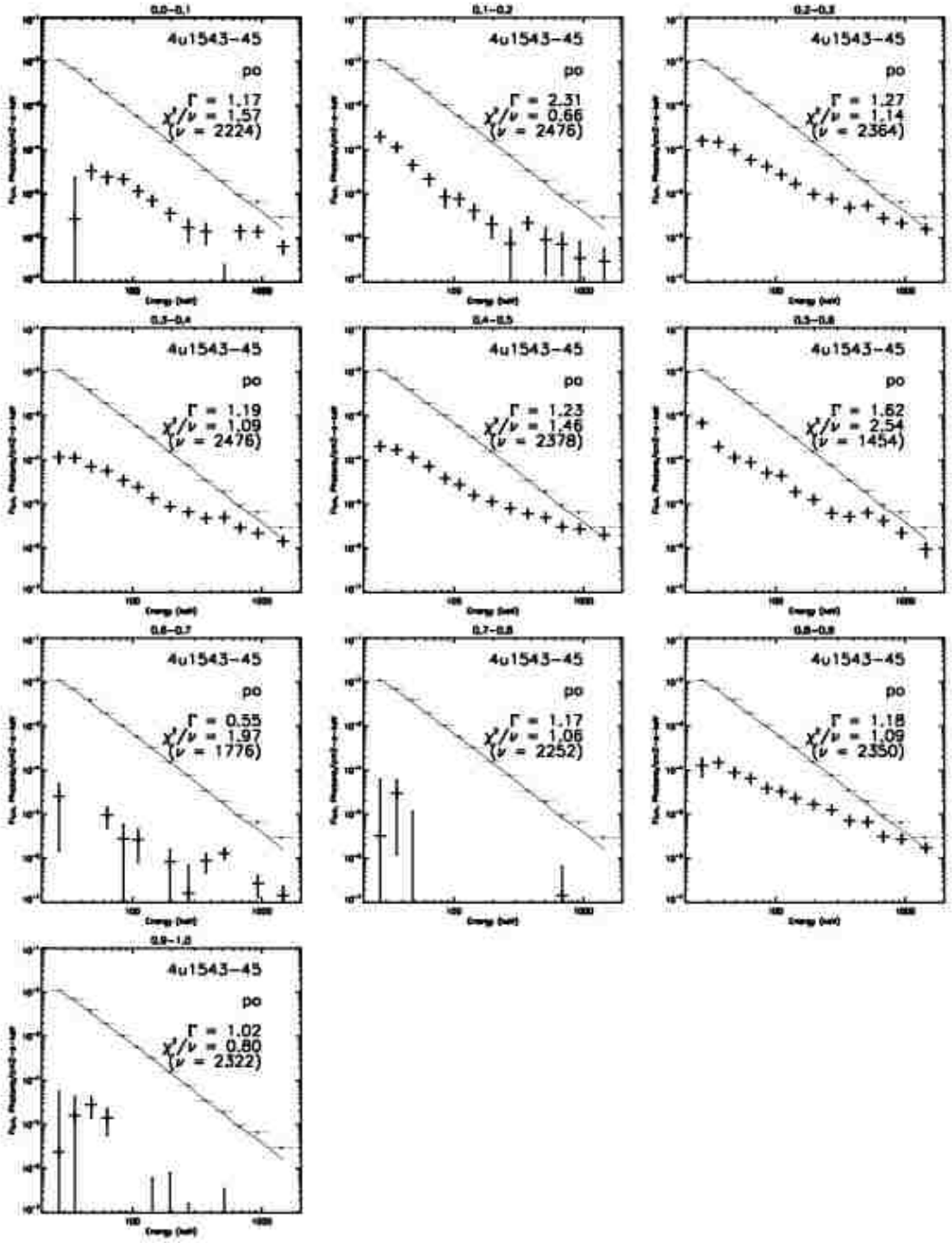

Figure 6.1: Spectra for 4U 1543-45 per each phase bin.

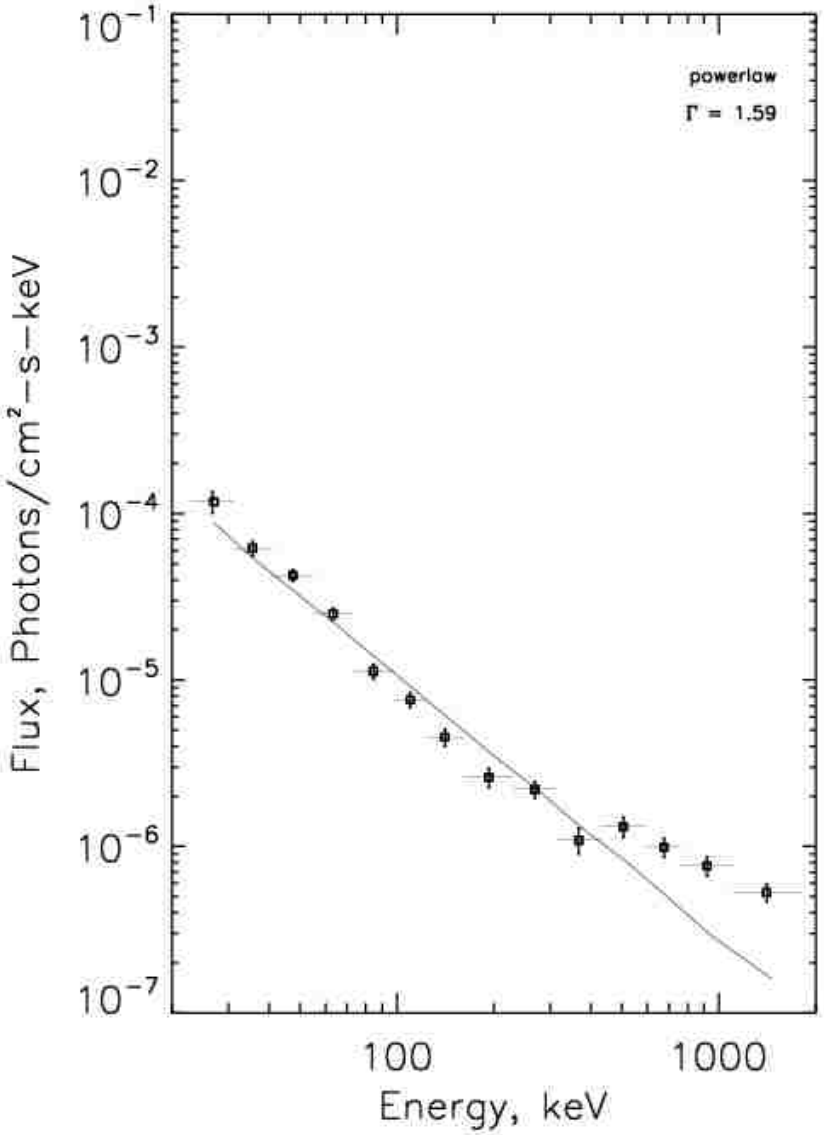

Figure 6.2: 9-yr Spectra for Blank Source 11.

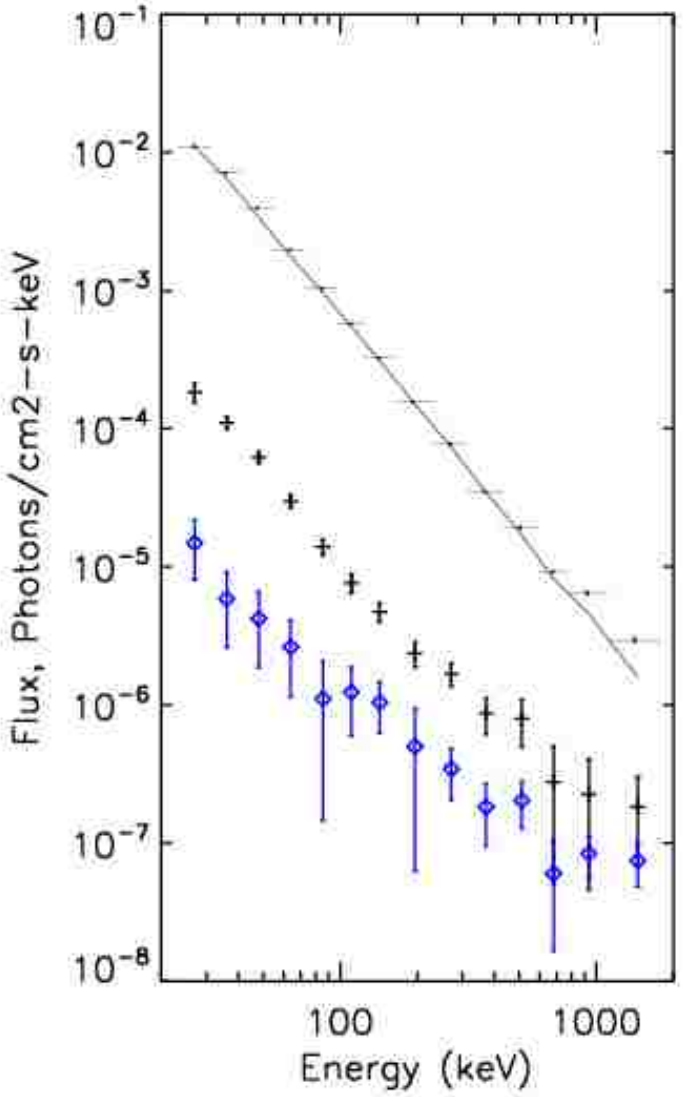

Figure 6.3: Spectra for averaged blank sources. OFF Galactic sources (Blank source 1-5) are the blue diamonds, and ON Galactic sources (Blank source 6-11) are the black plus. Crab spectra is plotted as reference in light black line.

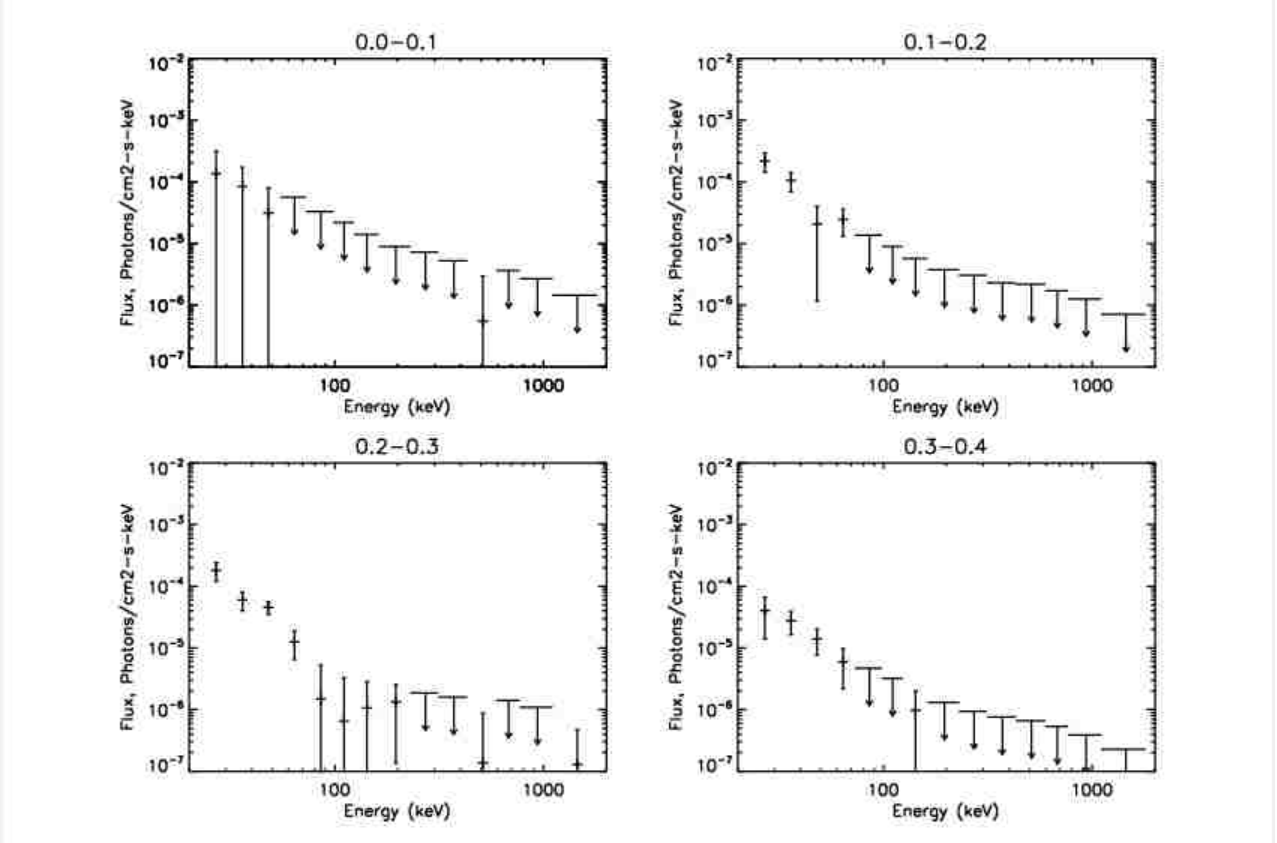

Figure 6.4: Spectra for averaged blank sources per phase bin.

6.3 Comparison of EBOP Results with GBM

BATSE and GBM have both applied the earth occultation approach with presumably similar systematic errors. The comparison of the results potentially gives a unique picture of source variability over 22 years. 67 sources appear in both the EBOP2013 and GBM catalogs in the 25-50 keV energy band. Of these, 40 are above 10 mCrab in both catalogs. A histogram is shown in Fig. 6.6 for the flux difference $EBOP2013 - R * GBM$ for these 40 sources. For On Galactic Plane sources, the average blank source background was subtracted from the EBOP2013 average flux. For OFF Galactic Plane sources, no blank source background was subtracted.

As in Section 5.2.1, R is a normalization factor chosen such that the average GBM and

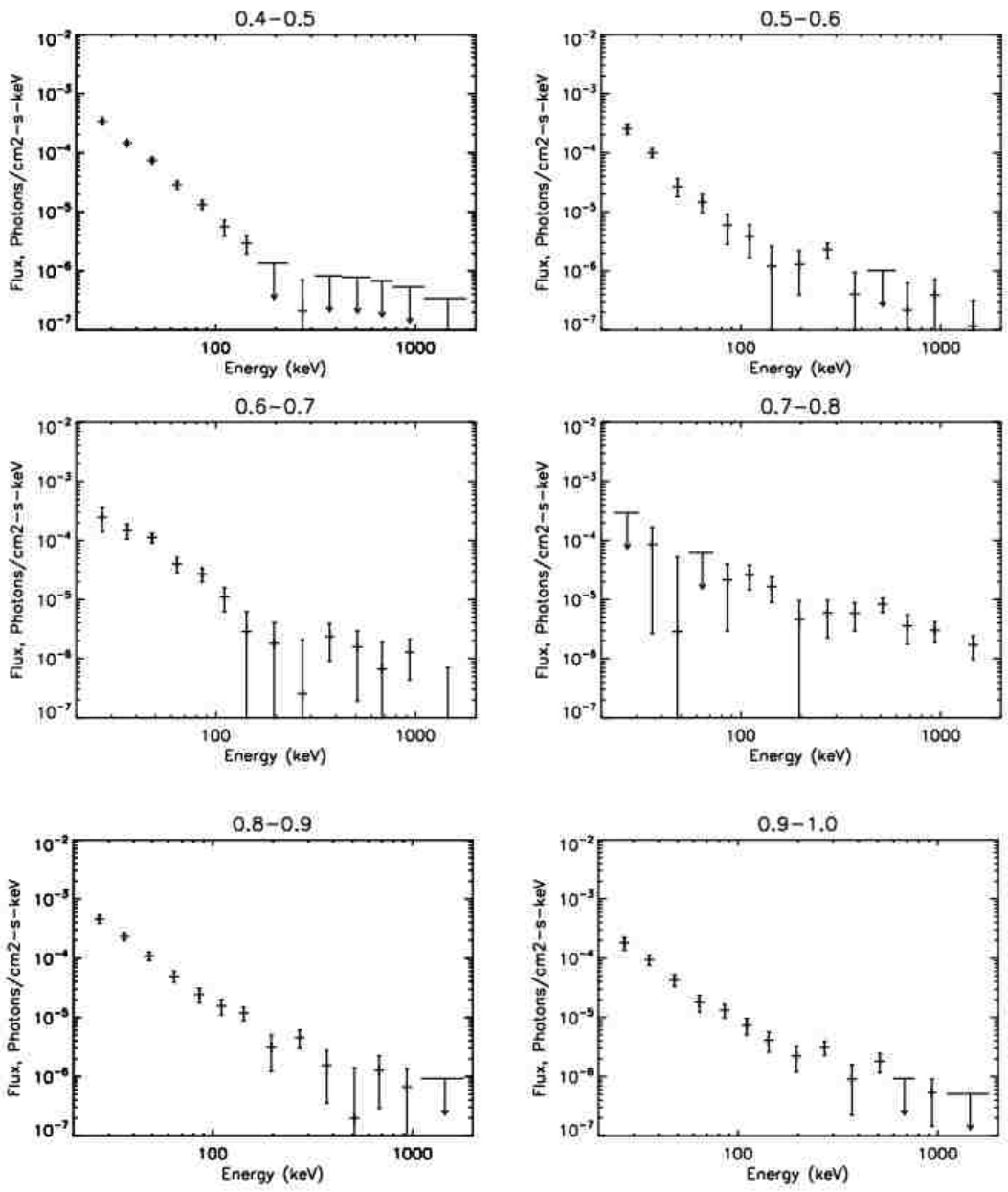

Figure 6.5: Spectra for Averaged Blank Sources per phase bin - Continued.

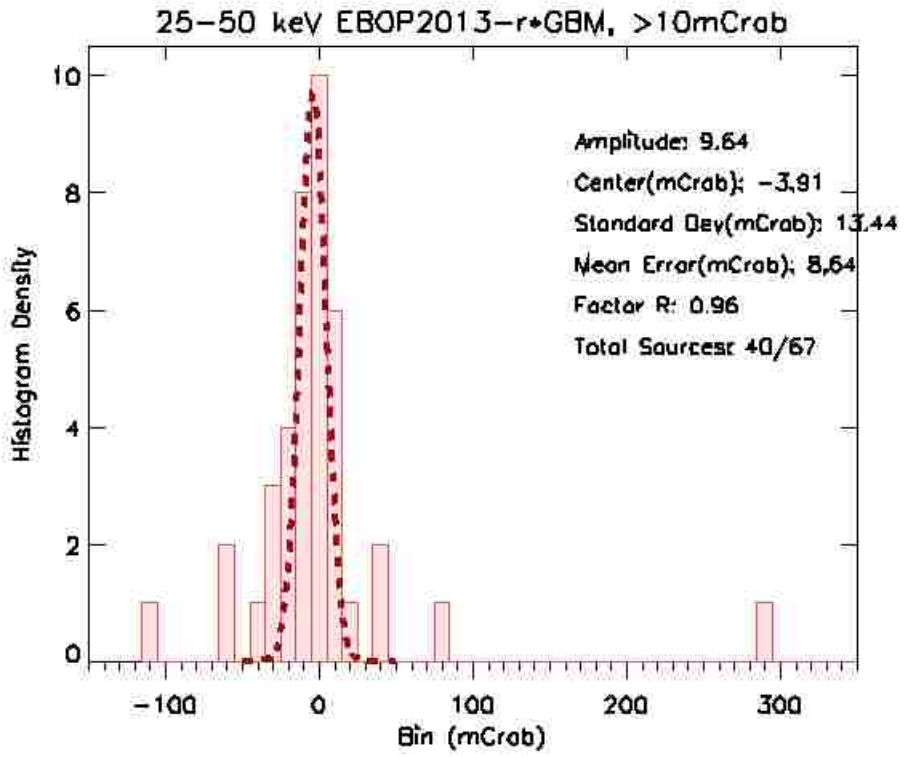

Figure 6.6: The histogram analysis on the normalized difference between EBOP2013 and GBM. The dash line is expected gaussian, calculated by expected error of their difference.

EBOP2013 fluxes are equal. In this case, the normalization is 0.96. The dashed line is the expected gaussian, calculated with expected error in $(EBOP2013 - R * GBM)$. From Fig. 6.6, the standard deviation of the histogram is 13.44 mCrab compared to 8.64 mCrab for the expected distribution. For 33 sources, the difference between normalized EBOP2013 and GBM stays within 3 sigma ($(EBOP2013 - R * GBM) < 3\sigma$). However, for 7 sources, the difference are larger, $(EBOP2013 - R * GBM) < -32.83 mCrab$, and $(EBOP2013 - R * GBM) > 25.01 mCrab$ corresponding to 3σ in the expected distribution. These sources, all known to be variable, are 4U 1700-37, Cyg X-1, GRO J1655-40, GRS 1915+105, GX 339-4, SCO X-1, VELA X-1. They are discussed separately below.

4U 1700-37

4U 1700-37 / HD 153919 is a high-mass X-ray binary (HMXB) discovered by the Uhuru satellite (Jones et al. 1973). Located at a distance of 1.9 kpc (Ankay et al. 2001), 4U 1700-37 is powered by the dense stellar wind of the O6.5 Iaf+ supergiant HD 153919. It is the hottest and most luminous optical companion known in HMXBs. The X-ray spectrum of 4U 1700-37 can be modelled as a power law with a high-energy cutoff (Haberl et al. 1989; Reynolds et al. 1999), modified by an absorption column which depends on the orbital phase of the system.

As shown in the combined BATSE-GBM lightcurve (Fig. 6.7), 4U 1700-37 had an average 25-50 keV flux of 147.17 ± 1.52 mCrab measured over the period 1991-2000 with BATSE and EBOP, and an 30% increase to 203.57 ± 3.15 mCrab measured since 2008 with GBM. From 2008 to 2013 at energies up to $100keV$, 4U 1700-37 apparently exhibited smaller variability than in the 90's. The higher energy bands are more consistent across the 22 years. The hardness ratio $50-100keV flux/25-50keV flux$ decreased from 0.71 ± 0.01 as measured by BATSE to 0.52 ± 0.03 as measured by GBM while the hardness ratio $100-30keV flux/25-50keV flux$ slightly decreased, from 0.25 ± 0.01 in BATSE to 0.20 ± 0.04in GBM.

Cyg X-1

Cygnus X-1 is one of the brightest X-ray sources in the sky. It was discovered as an X-ray source 30 years ago (Bowyer et al. 1965). It is a micro-quasar, as confirmed by the detection of relativistic jets (Stirling et al. 2001), and displays variability on time scales from minutes to months. During the BATSE observation, Cyg X-1 spent most of its time in the so-called hard state, characterized spectrally by a hard power law with an exponential cutoff at ~ 100 keV. Occasionally, Cyg X-1 transitions into a thermal dominant, or soft, state. This state is characterized by a strong thermal component arising from a geometrically thin but optically thick accretion disk. Cyg X-1 does not remain in the soft state for long (typically < 100 days) before returning to the hard state. However, recently, Cyg X-1 made a transition to

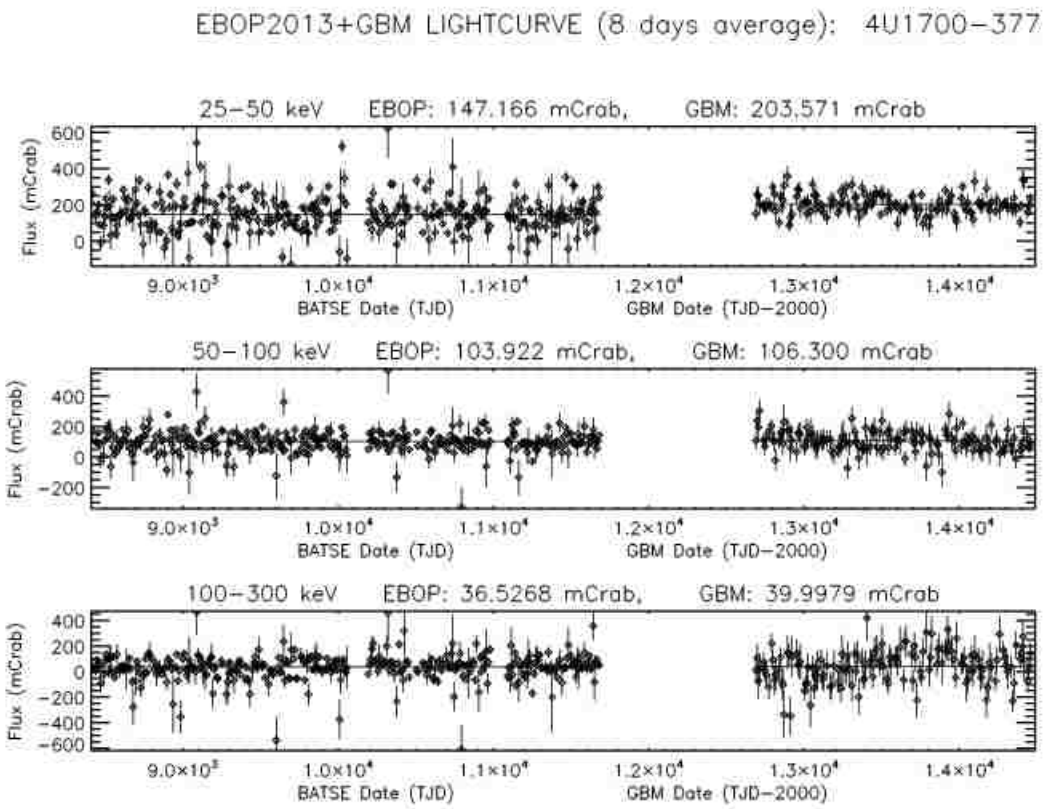

Figure 6.7: EBOP + GBM Lightcurve for 4U 1700-37.

the canonical soft state in July 2010 (Case et al. 2011). After the initial decline, Cyg X-1 rebrightened as part of a broad "flare" lasting about 45 days, and then remained in the soft state. Hence, its averaged 25-50 keV flux decreased from 866.04 ± 1.16 mCrab as measured by EBOP to 587.43 ± 1.78 mCrab as measured by GBM. The higher energy bands show the same behavior as the $25 - 50$ keV energy band. However, the hardness ratios are about the same. 1.18 ± 0.01 and 1.14 ± 0.01 in $50 - 100keV/25 - 50keV$ for BATSE and GBM respectively. 1.18 ± 0.01 and 1.02 ± 0.01 at $100 - 30keV/25 - 50keV$ for BATSE and GBM respectively.

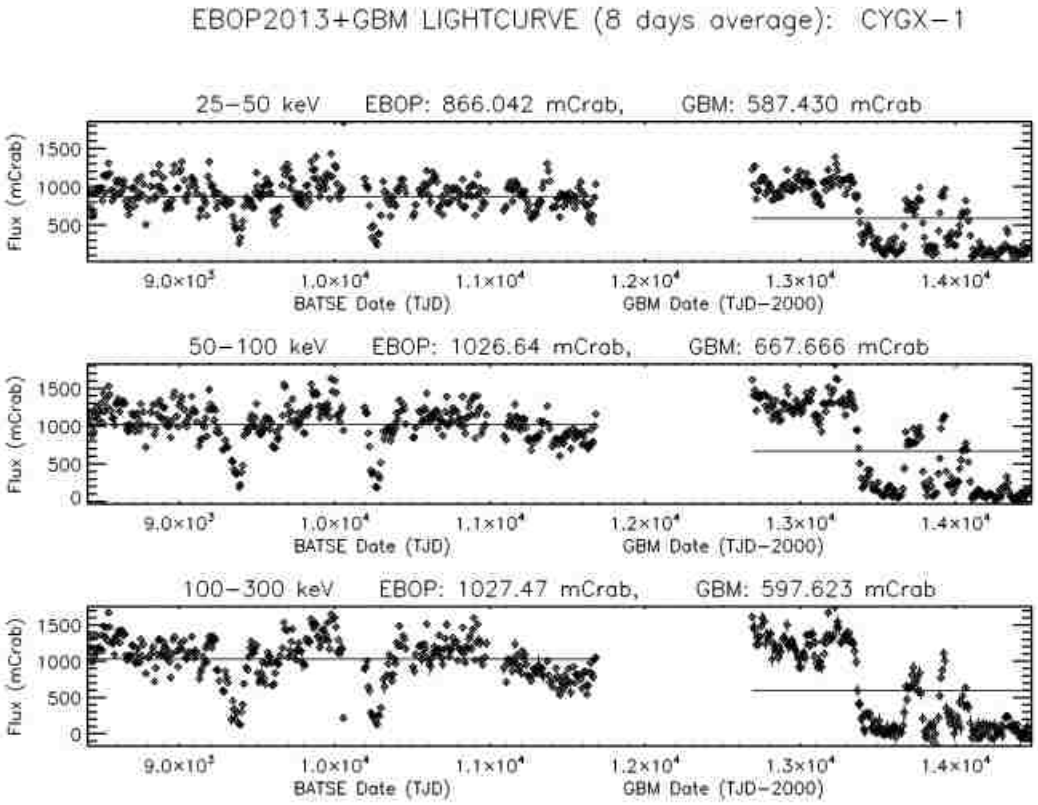

Figure 6.8: EBOP + GBM Lightcurve for CYG X-1.

GRO J1655-40

GRO J1655-40, a black-hole candidate low mass X-ray binary, was discovered by BATSE on the Compton Gamma Ray Observatory (CGRO) during an outburst that started on July 27, 1994 (Zhang et al. 1994). Radio observations revealed superluminal jets that allowed a distance determination of 3.2 ± 0.2 kpc (Hjellming & Rupen 1995). Periodic dips have been observed in the optical and X-ray lightcurves during outburst (Bailyn et al. 1995, Kuulkers et al. 1998). GRO J1655-40 underwent two other major outbursts, one in April 1996 (Remillard et al. 1996) and another in February 2005 (Markwardt & Swank 2005). Miller et al. (2008) reported simultaneous Chandra/HETGS and RXTE observations of its 2005 outburst. Chandra revealed a line-rich X-ray absorption spectrum consistent with a disk wind. Prior modelling of the spectrum suggested that the wind may be magnetically

driven, potentially providing insights into the nature of disk accretion onto black holes.

In the combined BATSE-GBM lightcurve in Fig. 6.9, GRO J1655-40 had an average 25-50 keV flux about 54.56 ± 1.18 mCrab in the 1990s, but was not detected (average flux of -8.70 ± 2.66 mCrab in GBM) since 2008. Two outbursts were observed by BATSE, but none between 2008 and now. The results are similar at higher energies.

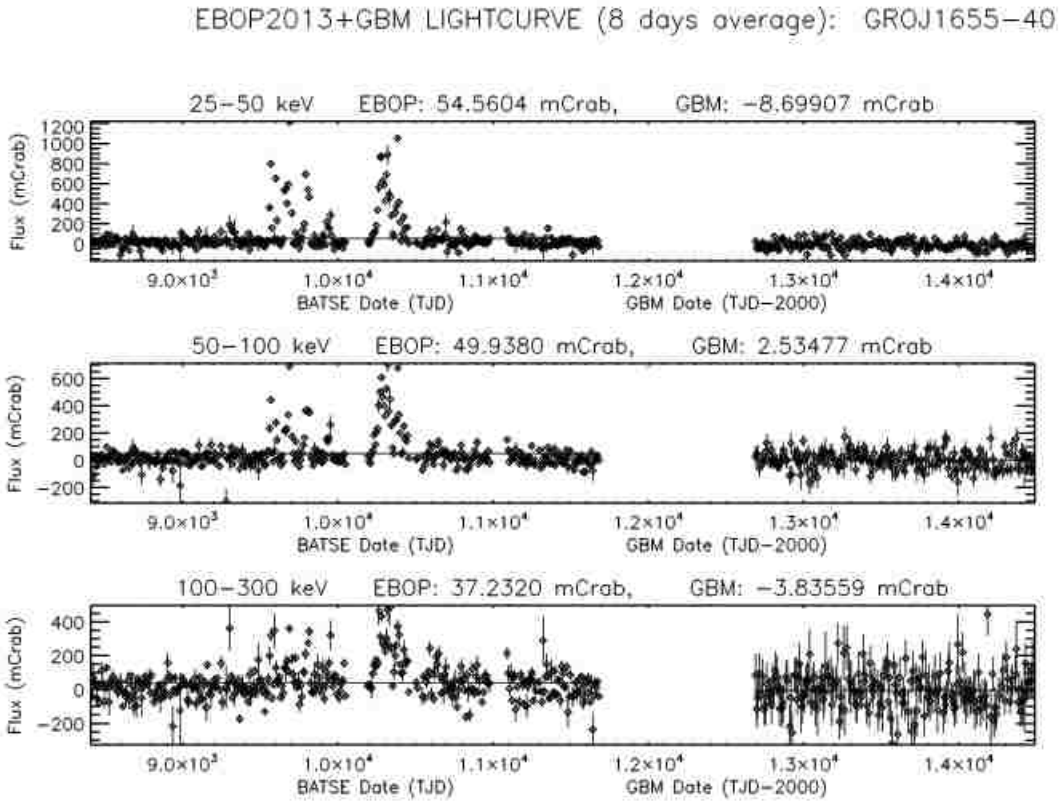

Figure 6.9: EBOP + GBM Lightcurve for GRO J1655-40.

GRS 1915+105

On 1992 August 15 the WATCH detectors on Granat discovered a new X-ray transient (Castro-Tirado et al. 1992) which was designated GRS 1915+105. Follow-up monitoring with WATCH and BATSE (Harmon et al. 1992) revealed an unusual lightcurve consisting of a 3 month rise, an 8 month high-intensity plateau phase, and a 2 month decline. Since

then, both BATSE and RXTE observed the source to be highly variable on all timescales from milliseconds to months (Belloni et al. 2000; Morgan et al. 1997). Belloni et al. (2000) categorized the variability into twelve distinct classes and identified three distinct X-ray states: two softer states and a harder state. The source was detected up to 700 keV by OSSE (Zdziarski et al. 2001). For a comprehensive review of GRS 1915+105 see Fender & Belloni (2004). As far as long-term variability, GRS 1915+105 has increased in average 25-50 keV flux from 152.20 ± 1.18 mCrab in the 1990s to 269.02 ± 1.63 mCrab since 2008. The behavior is similiar at $50 - 100keV$. The $50 - 100keV/25 - 52$ hardness ratio changes from 0.74 ± 0.01 with BATSE to 0.52 ± 0.01 in GBM for $50 - 100keV/25 - 50keV$, and 0.42 ± 0.01 with BATSE to 0.23 ± 0.02 with GBM for $100 - 30keV/25 - 50keV$.

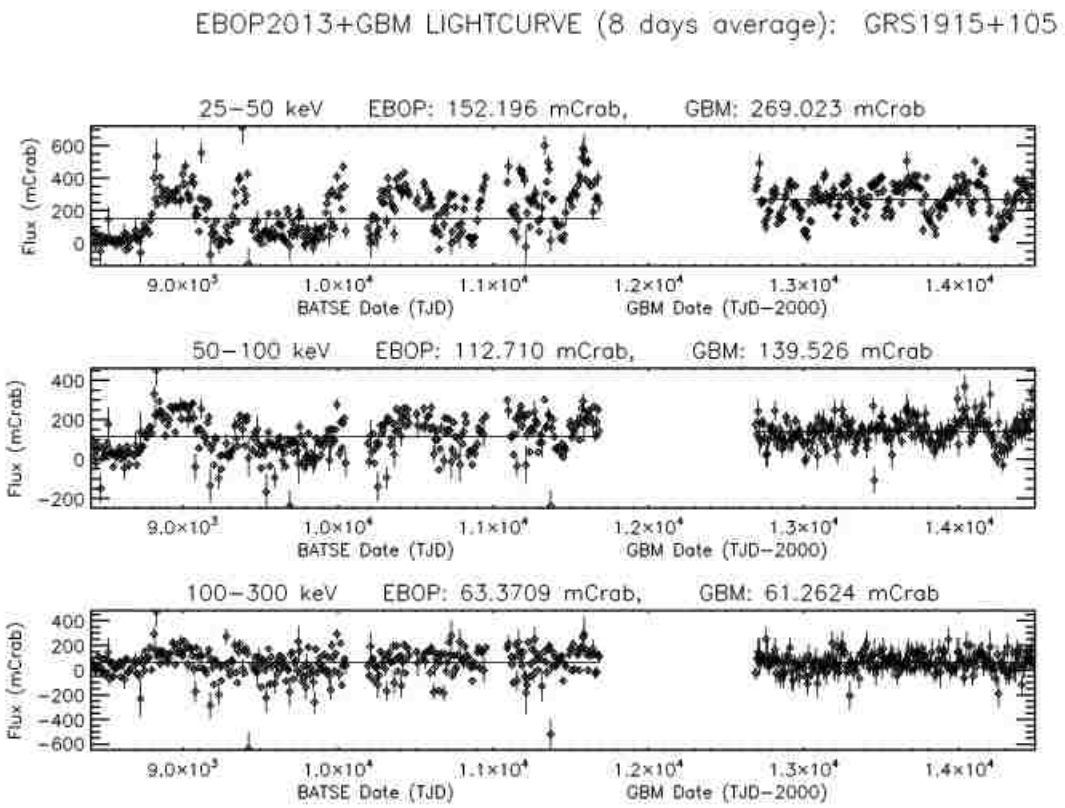

Figure 6.10: EBOP + GBM Lightcurve for GRS 1915+105.

GX 339-4

GX 339-4, a low mass X-ray binary hosting a black hole with mass $> 6M_{\circ}$ (Hynes et al. 2003) and well known for its transient, multiwavelength variability on a broad range of timescales (Motch et al. 1982, Dunn et al. 2008, Gandhi et al. 2009, Casella et al. 2010). Its donor star is a late-type companion in a long ($\sim 1.7 days$) orbit, much fainter than the primary when active (Shahbaz et al. 2001, Munoz-Darias et al. 2008). GX 339-4 shows evidence of relativistic jets and has proven to be a key objhect for jet studies across the electromagnetic spectrum (Fender et al. 2001, Corbel et al. 2003, Markoff et al. 2003, Gandhi et al. 2008).

During the 22 years of history, eight outbursts (4 strong ones) were observed by BATSE (Rubin et al., 1997), while two has been detected by GBM (Case et al., 2011). The first eight occurred in a declining sequence with two types of outbursts. A rough linear correlation exists between the fluence emitted during an outburst and the time elapsed between the end of the previous outburst and the beginning of the current one. More outbursts in BATSE generate higher average flux. In 25-50 keV, it is 56.62 ± 1.14 mCrab with BATSE and 10.57 ± 2.67 mCrab with GBM. GBM gives higher hardness ratio in $50 - 100 keV/25 - 50 keV$, 1.32 ± 0.03 and 2.25 ± 0.68 with BATSE and GBM respectively.

SCO X-1

Sco X-1 (Giacconi et al. 1962) is the brightest persistent X-ray source in the sky and has been the target of detailed analysis for the last 51 years in all energy bands, from radio to X-rays. It is a Z source (Hasinger & van der Klis 1989), a luminous low-mass X-ray binary containing a low magnetic field neutron star accreting matter from a Roche-lobe-filling companion star. An orbital period of 18.9 hr was reported by Gottlieb, Wright, & Liller (1975) based on brightness estimates measured on 1068 plates during the interval 18901974. Bradshaw, Fomalont, & Geldzahler (1999) measured the trigonometric parallax of Sco X-1 using Very Long Baseline Array (VBLA) radio observations and deduced a distance of 2.8 ± 0.3 kpc. As far as long-term variability, Sco X-1 exhibited more flaring and variability during the BATSE

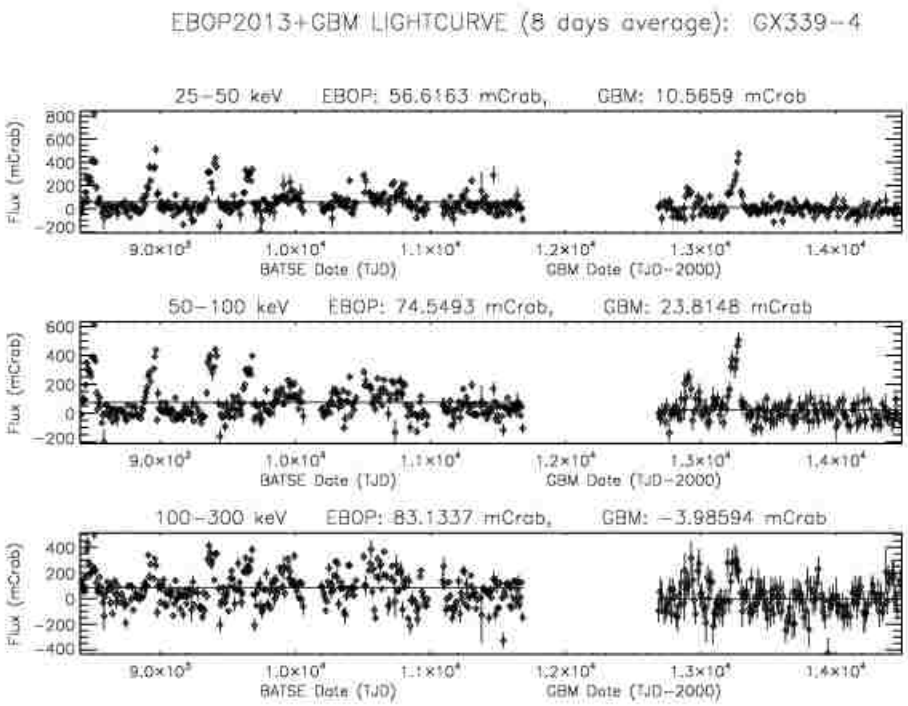

Figure 6.11: EBOP + GBM Lightcurve for GX 339-4.

era than in the recent 5 years. The average 25-50 keV flux decreased from 289.50 ± 1.31 mCrab in 1991-2000 to 220.83 ± 1.59 mCrab since 2008. In contrast to the $25 - 50keV$ results, the average fluxes are consistent at 50-100 keV. The large fluctuations measured by BATSE at 100-300 keV gave a negative average flux, compared to the GBM average flux of 10.4 ± 4.61 mCrab.

VELA X-1

Vela X-1 is the archetype HMXB, consisting of a neutron star and a massive companion star, and as such it has been the most well-studied object in this class since its discovery. It is an eclipsing HMXB system containing a pulsar with a pulse period of 283 s (McClintock et al. 1976) and an orbital period of 8.964 days (Forman et al. 1973). The optical companion star, HD 77581, is a B0.5 Ib supergiant (Brucato & Kristian 1972; Hiltner et al. 1972), which drives a stellar wind with a mass-loss rate in the range $1 - 7 \times 10^{-6} M_{sun} yr^{-1}$ (Hutchings

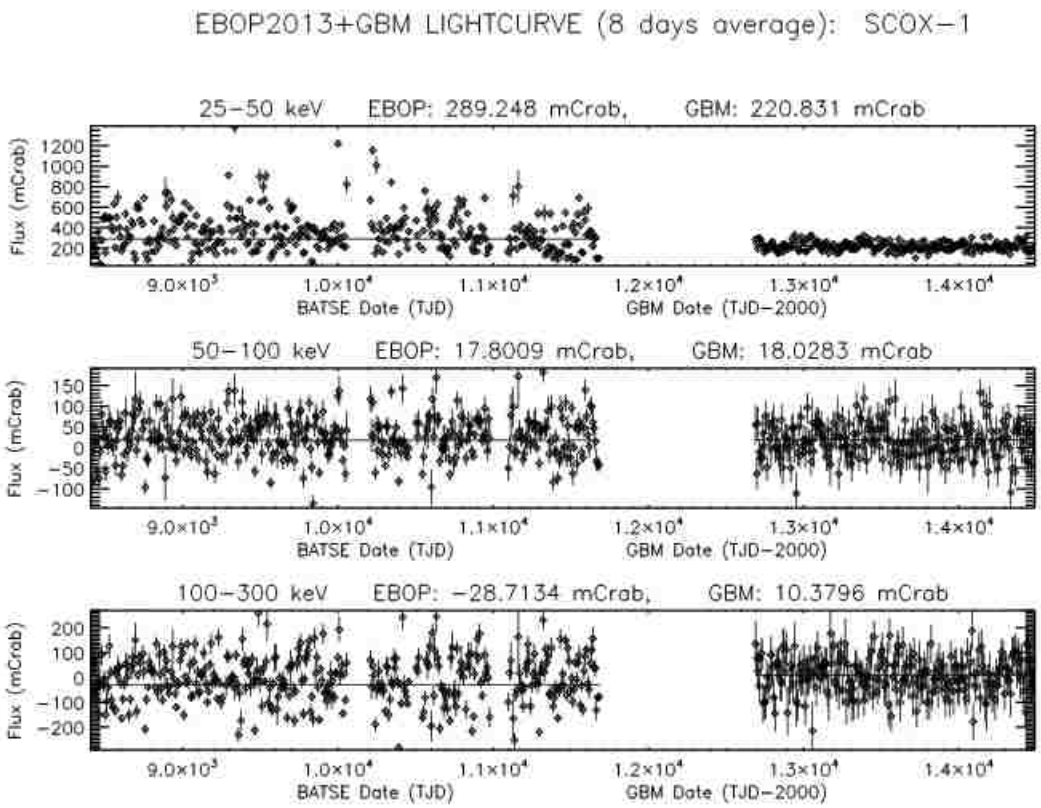

Figure 6.12: EBOP + GBM Lightcurve for SCO X-1.

1976; Dupree et al. 1980; Kallman & White 1982; Sadakane et al. 1985; Sato et al. 1986). The terminal velocity of the stellar wind was determined to be 1100 km s^{-1} from the P Cygni profile of UV resonance lines (Prinja et al. 1990). Its average intrinsic X-ray luminosity is about $10^{36} ergs^{-1}$, which is consistent with accretion of the stellar wind by the gravitational field of a neutron star.

As far as long term variability, Vela X-1 has exhibited smaller variability since 2008 than was observed by BATSE. The average 25-50 keV flux increased from 152.54 ± 0.82 mCrab as measured by BATSE to 212.38 ± 1.52 mCrab as measured by GBM. The hardness ratio of $50 - 100keV/25 - 50keV$ flux decreased from 0.24 ± 0.01 in 1990s to 0.12 ± 0.01 since 2008. The negative average flux at 100-300 keV energy range as measured by BATSE precludes a meaningful hardness ratio at the higher energies.

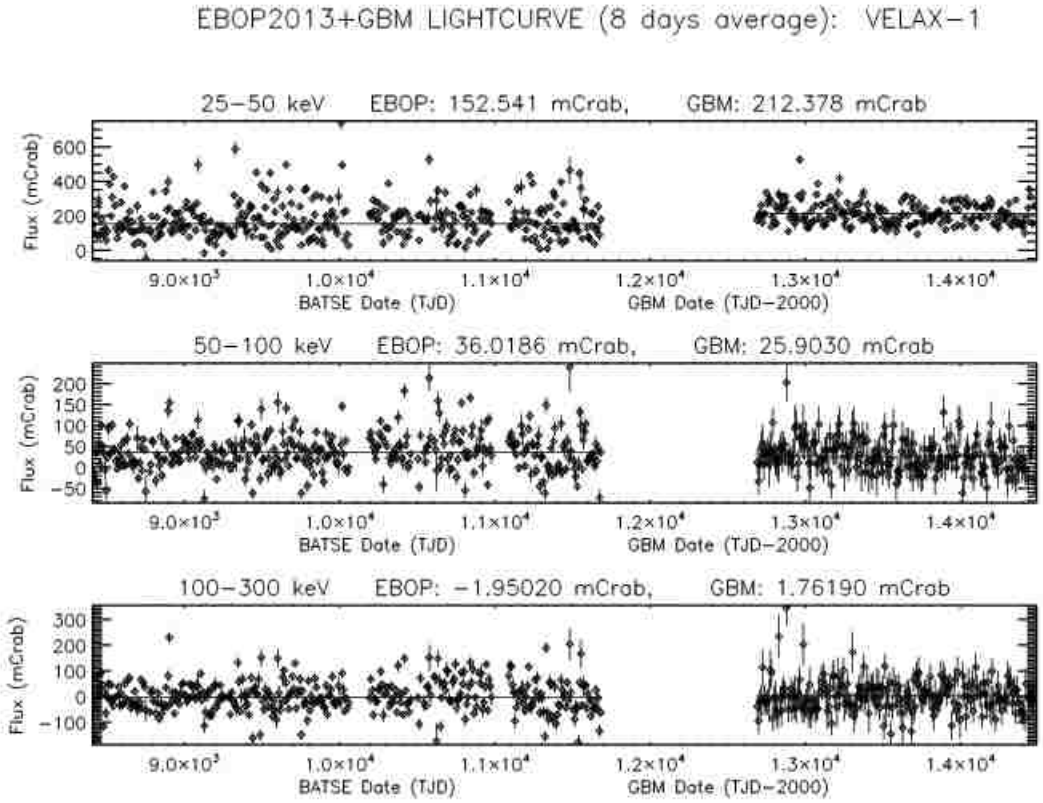

Figure 6.13: EBOP + GBM Lightcurve for VELA X-1.

Chapter 7
Conclusions

Due to the difficulties of focusing hard X-ray and soft Gamma-ray sources, an alternative Earth Occultation Technique was developed for BATSE on CGRO for observing sources with simple uncollimated, low spatial resolution detectors. Earth Occultation provides a means of monitoring gamma-ray sources over the entire sky, and is now being used with GBM on the Fermi mission. Although this approach provides a powerful wide field monitoring capability, the BATSE and GBM implementations of this technique have so far limited the analysis to a catalog of previously identified sources.

In addition to monitoring a catalog of predetermined sources, the imaging method Imaging with a Differential filter using the Earth Occultation Method (IDEOM) (Rodi et al. 2013) was developed to generate all-sky images to search for sources not in the BATSE catalog. IDEOM has been applied to the 9 years of BATSE data to produce all-sky broad band images in the 23-98 keV, 98-230 keV, 230-595 keV, and 595-1795 keV energy ranges. Using source identification routines, 119 sources are identified in the 23-98 keV energy band. 28 are new sources added into the BATSE catalog, and 15 are unidentified sources. Most of the calculated source positions were within $\sim 0.5^{\circ}$ of the known source position, which is near the minimum angular resolution as constrained by the Earth's atmosphere.

For the 98-230 keV energy band, 43 sources are identified with 5 of them new. At 230-595 keV, 13 sources are identified, with only one of them (RBS 0315) new. For the highest energy band (595-1798 keV), only the Crab and Cyg X-1 are strong enough to pass the selection criteria.

The EBOP analysis was performed for the new BATSE source catalog. Lightcurves and spectra were generated for each of the sources (Appendices A, B, C and D). Comparisons between the EBOP2007 JPL and EBOP2007 LSU results, and between the EBOP2007 LSU and EBOP2013 LSU results were made to ensure the consistency of the new results with the newer versions of software (IDL and XSPEC) and updated detector response matrix. In order to understand the long-standing questions of systematic effects and the presence of hard tails in the BATSE results, multiple approaches have been applied. The hard tails still exist above approximately $300keV$. The conclusion is that the hard tails may be a contribution from the Galactic Diffuse Emission.

Finally, the new BATSE results are compared to the current Fermi/GBM catalog in order to perform a study of source variations over 22 years in the hard X-ray/law energy gamma-ray sky. Among the common 67 sources in the 25-50 keV energy band, 40 are above 10 mCrab in both catalogs and have intensities measured by BATSE and GBM to be the same within 3σ. Seven sources have average flux differences larger than 3σ. The combined lightcurves have been shown for each source.

Bibliography

Aschwanden, M. J., Schwartz, R. A., & Dennis, B. R. 1998, ApJ, 502, 468.

Arnaud, K.A. 1996, Astronomical Data Analysis Software and Systems V, eds. Jacoby G. and Barnes J., p17, ASP Conf. Series volume 101.

Bailyn, C. D., Orosz, J. A., Girard, T. M., et al. 1995, NATURE, 374, 701.

Ballet, J. et al. 1993, IAU Circ, 5874.

Barret, D., Grindlay, J. E., Bloser, P. F., et al. 1996, A&AS, 120, 121

Barret, D., Grindlay, J. E., Bloser, P. F., Monnelly, G. P., Harmon, B. A., Robinson, C. R., & Zhang, S. N. 1997, Proceedings of the Fourth Compton Symposium, 410, 1498.

Barthelmy, S. D. et al. 2005, Space Science Reviews, 120, 143

Bartlett, L. M. 1994, Ph.D. Thesis,

Baumgartner, W. H., Tueller, J., Markwardt, C. B., et al. 2013, ApJS, 207, 19.

Belloni, T., Mndez, M., King, A. R., van der Klis, M., & van Paradijs, J. 1997, ApJ, 488, L109.

Belloni, T., Klein-Wolt, M., Mndez, M., van der Klis, M., & van Paradijs, J. 2000, A&A, 355, 271.

Bildsten, L., Chakrabarty, D., Chiu, J., et al. 1997, ApJS, 113, 367

Bodaghee, A., Tomsick, J. A., Pottschmidt, K., et al. 2013, ApJ, 775, 98.

Bowyer, S., Byram, E. T., Chubb, T. A., & Friedman, H. 1964, Science, 146, 912.

Bracewell, R. N. 1956, Australian Journal of Physics, 9, 198

Bradshaw, C. F., Fomalont, E. B., & Geldzahler, B. J. 1999, ApJL, 512, L121.

Bradt, H. V., Rothschild, R. E., & Swank, J. H. 1993, A&AS, 97, 355

Brandt, S. 1994, Ph.D. Thesis,

Briggs, M. S. 1996, American Institute of Physics Conference Series, 384, 133

Brucato, R. J., & Kristian, J. 1972, ApJL, 173, L105.

Caroli et al. 1987, Space Science Reviews, 45, 3-4, pp349-403.

Case, G. L., Cherry, M. L., Ling, J. C., Lo, M., Shimizu, T., & Wheaton, W. A. 2009, 2009 Fermi Symposium, eConf C091122.

Case, G. L., et al. 2011, ApJ, 729, 105.

Casella, P., Maccarone, T. J., O'Brien, K., et al. 2010, MNRAS, 404, L21

Castro-Tirado, A. J., Brandt, S., & Lund, N. 1992, IAUC, 5590.

Conner, J. P., Evans, W. D., & Belian, R. D. 1969, ApJL, 157, L157

Corbel, S., Nowak, M. A., Fender, R. P., Tzioumis, A. K., & Markoff, S. 2003, A&A, 400, 1007

Davison, P. J. N., & Morrison, L. V. 1977, MNRAS, 178, 53P.

Dunn, R. J. H., Fender, R. P., Körding, E. G., Cabanac, C., & Belloni, T. 2008, MNRAS, 387, 545

Dupree, A. K., Gursky, H., Black, J. H., et al. 1980, ApJ, 238, 969.

Fender, R. P. 2001, MNRAS, 322, 31

Fender, R., & Belloni, T. 2004, ARA&A, 42, 317.

Finger, M. H., Wilson, R. B., & Harmon, B. A. 1996, ApJ, 459, 288

Fishman, G. J., & Austin, R. W. 1976, Nuclear Instruments and Methods, 140, 193

Fishman, G. J., Meegan, C. A., Parnell, T. A., & Wilson, R. B. 1982, in AIP Conf. Proc. 77, Gamma-Ray Transients and Related Astrophysical Phenomena, ed. R. E. Lingenfelter, H. S. Hudson, & D. M. Worral (New York: AIP), 443

Fishman, G. J., et al. 1989, in Proc. Gamma Ray Observatory Science Workshop, ed. W.Johnson (Greenbelt: GSFC), 2.

Fishman, G. J., et al. 1994, Science 27 May 1994: 264 (5163), 1313-1316.

Forman, W., Jones, C., Tananbaum, H., et al. 1973, ApJL, 182, L103.

Gandhi, P., Makishima, K., Durant, M., et al. 2008, MNRAS, 390, L29

Gandhi, P. 2009, ApJL, 697, L167

Gehrels, N., & Shrader, C. R. 1997, X-Ray Imaging and Spectroscopy of Cosmic Hot Plasmas, 593

Giacconi, R., Murray, S., Gursky, H., et al. 1972, ApJ, 178, 281

Gottlieb, E. W., Wright, E. L., & Liller, W. 1975, ApJL, 195, L33.

Hamuy, M. 1993, IAU Circ, 5687, 3

Harmon, B. A., Wilson, R. B., Finger, M. H., et al. 1992a, IAU Circ., 5510, 2.

Harmon, B. A., Wilson, R. B., Fishman, G. J., et al. 1992b, IAU Circ., 5584, 2.

Harmon, B. A., et al. 2002, ApJS, 138, 149.

Harmon, B. A., et al. 2004, ApJS, 154, 585.

Harrison, F. A., Boggs, S., Christensen, F., et al. 2010, Space Telescopes and Instrumentation 2010: Proceedings of the SPIE, Volume 7732, article id. 77320S, 8 pp.

Hasinger, G., & van der Klis, M. 1989, A&A, 225, 79.

Hiltner, W. A., Werner, J., & Osmer, P. 1972, ApJL, 175, L19.

Hjellming, R. M., & Rupen, M. P. 1995, Nature, 375, 464.

Holt, S. S. 1976, ApSS, 42, 123

Hutchings, J. B. 1976, ApJ, 203, 438.

Hynes, R. I., Steeghs, D., Casares, J., Charles, P. A., & O'Brien, K. 2003, ApJL, 583, L95

Jenke, P. et al. 2012, Fermi Symposium Proceedings - eConf C121028

Kallman, T. R., & White, N. E. 1982, ApJL, 261, L35.

Krivonos, R., Tsygankov, S., Revnivtsev, M., et al. 2010, A&A, 523, A61.

Krivonos, R., Tsygankov, S., Lutovinov, A., et al. 2012, A&A, 545, A27

Kuulkers, E., Wijnands, R., Belloni, T., et al. 1998, ApJ, 494, 753.

Levine, A. M., Lang, F. L., Lewin, W. H. G., et al. 1984, ApJS, 54, 581.

Ling, J. C., et al. 2000, ApJS, 127, 79.

Ling, J. C., & Wheaton, W. A. 2005, ApJ, 622, 492.

Ling, J. C., Case, G. L., Lo, M., Shimizu, T., Reddick, R., Wheaton, W. A.,& Cherry, M. 2009, American Astronomical Society Meeting Abstracts, 214, #407.12.

Louisiana State University High Performance Computing 2012, http://www.hpc.lsu.edu/resources/hpc/system.php?system=Tezpur

Louisiana Optical Network Institute 2012, http://www.loni.org/systems/system.php?system=QueenBee

Mallozzi, R. S., et al. 1993, in AIP Conf. Proc. 280, Compton Gamma Ray Observatory, ed. M. Friedlander, N. Gehrels, & D. J. Macomb (New York: AIP), 1122.

Markoff, S., Nowak, M., Corbel, S., Fender, R., & Falcke, H. 2003, A&A, 397, 645

Markwardt, C. B., & Swank, J. H. 2005, The Astronomer's Telegram, 414, 1.

McClintock, J. E., Rappaport, S., Joss, P. C., et al. 1976, ApJL, 206, L99.

McNamara et al. 1998 ApJS 116, 287.

Meegan, C., et al. 2007, in AIP CP 921: The First GLAST Symposium, ed. S. Ritz, P. Michelson & C. Meegan, p. 13.

Meegan, C., et al. 2009, ApJ, 702, 791

Miller, J. M., Raymond, J., Reynolds, C. S., et al. 2008, ApJ, 680, 1359.

Morgan, E. H., Remillard, R. A., & Greiner, J. 1997, ApJ, 482, 993.

Motch, C., Ilovaisky, S. A., & Chevalier, C. 1982, A&A, 109, L1

Muñoz-Darias, T., Casares, J., & Martínez-Pais, I. G. 2008, MNRAS, 385, 2205

Narayan, R., & Nityananda, R. 1986, ARA&A, 24, 127.

National Institute of Standards and Technology 1998,http://www.nist.gov/pml/data/xcom/index.cfm

National Institute of Standards and Technology 1998, http://physics.nist.gov/PhysRefData/XrayMassCoef/ComTab/air.html

Paciesas, W. S., Meegan, C. A., Pendleton, G. N., et al. 1999, ApJS, 122, 465.

Palmieri, T. M., Seward, F. D., Toor, A., & van Flandern, T. C. 1975, ApJ, 202, 494.

Prinja, R. K., Barlow, M. J., & Howarth, I. D. 1990, ApJ, 361, 607.

Remillard, R. A. & McClintock, J. E. 2006, ARA&A, 44, 49.

Rodi, J., PhD Dissertation, Louisiana State University, 2013

Rodi, J., et al. 2013 submitted

Rodriguez, J., Tomsick, J. A., Foschini, L., et al. 2003, A&A, 407, L41

Rubin, B. C., Harmon, B. A., Paciesas, W. S., et al. 1997, Proceedings of the Fourth Compton Symposium, 410, 927

Sadakane, K., Hirata, R., Jugaku, J., et al. 1985, ApJ, 288, 284.

Sato, N., Hayakawa, S., Nagase, F., et al. 1986, ApJS, 38, 731.

Schonfelder, V., Bennett, K., Bloemen, H., et al. 1995, Seventeeth Texas Symposium on Relativistic Astrophysics and Cosmology, 759, 226.

Shahbaz, T., Fender, R., & Charles, P. A. 2001, A&A, 376, L17

Shaw, S. E., Westmore, M. J., Bird, A. J., Dean, A. J., Ferguson, C., Gurriaran, R., Lockley, J. J., & Willis, D. R. 2003, A&A, 398, 391.

Shaw, S. E., et al. 2004, A&A, 418, 1187.

Stirling, A., et al. 2001, MNRAS, 327, 1273.

Sugizaki, M., Mitsuda, K., Kaneda, H., et al. 2001, ApJS, 134, 77

Tomsick J.A., Lingelfelter R., Walter R., et al. , 2003, IAUC, 8076

Tueller, J., et al. 2010, ApJS, 186, 378.

U.S. Standard Atmosphere, 1976, U.S. Committee on Extension to the Standard Atmosphere. 1976, U.S. Standard Atmosphere, NOAA-S/T 76-1562 (Washington, DC: U.S. Govt Printing)

Westmore,M. J., Gurriaran, R., Dean, A. J., et al. 2000, in Proceedings of the fifth Compton Symposium, Vol. 510 (AIP Conference Proceedings Series,Woodbury, NY), 387.

White, N. E., & Peacock, A. 1988, MEMSAI, 59, 7.

Wilson, C. A., Harmon, B. A., McCollough, M. L., Fishman, G. J., Zhang, S. N., & Paciesas, W. S. 2000, Astronomical Data Analysis Software and Systems IX, 216, 587.

Wilson-Hodge, C. A., Cherry, M. L., Case, G. L., & et al. 2011, ApJ, 727, L40.

Wilson-Hodge, C. A., Case, G. L., Cherry, M. L., & et al. 2012, ApJS, 201, 33.

Zdziarski, A. A., Grove, J. E., Poutanen, J., Rao, A. R., & Vadawale, S. V. 2001, ApJ, 554, L45.

Zhang, S. N., Fishman, G. J., Harmon, B. A., & Paciesas, W. S. 1993, Nature, 366, 245.

Zhang, S. N., Wilson, C. A., Harmon, B. A., et al. 1994, IAU Circ., 6046, 1.

Zhang, S. N., Harmon, B. A., Fishman, G. J.,& Paciesas, W. S. 1995, Experimental Astronomy, 6, 57.

Zhang, Y., Hynes, R. I., & Robinson, E. L. 2012, MNRAS, 419, 2943

Zhang, Y., Cherry, M. L., Case, G. L., Ling, J., Wheaton, W., 2012, Fermi Symposium Proceedings - eConf C121028

Zimmermann, H. U., Lewin, W., Magnier, E., et al. 1993, IAU Circ, 5748, 1

Appendices

Appendix A
EBOP 2013 Lightcurves for 23-98 keV

23-98 keV flux histories with 2 day resolution covering the entire 9 years of the CGRO mission for each of the 119 sources in the updated EBOP2013 catalog.

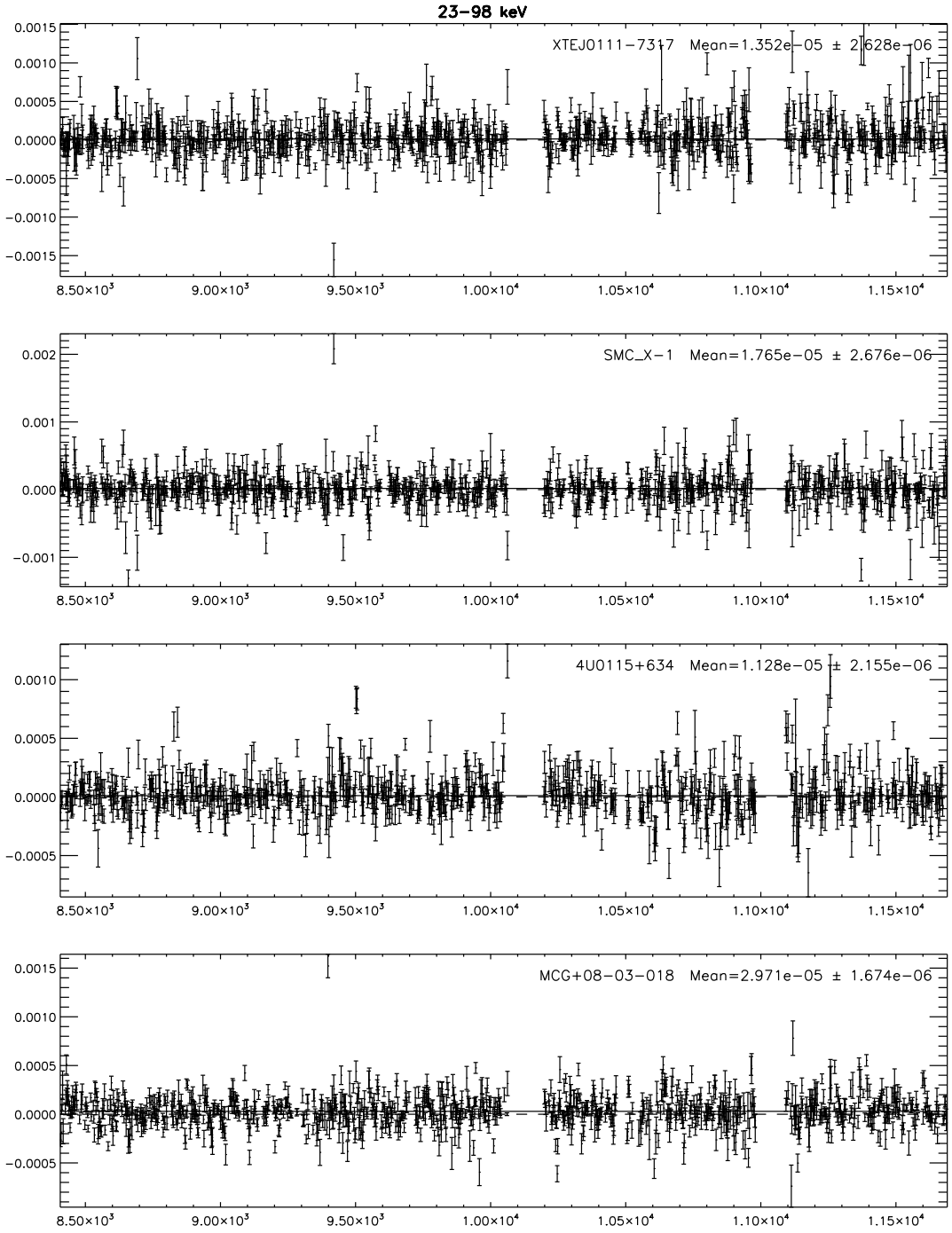

Figure A.1: 23-98 keV lightcurves for EBOP 2013 Catalog with 2 day resolution from TJD 8393-11690.

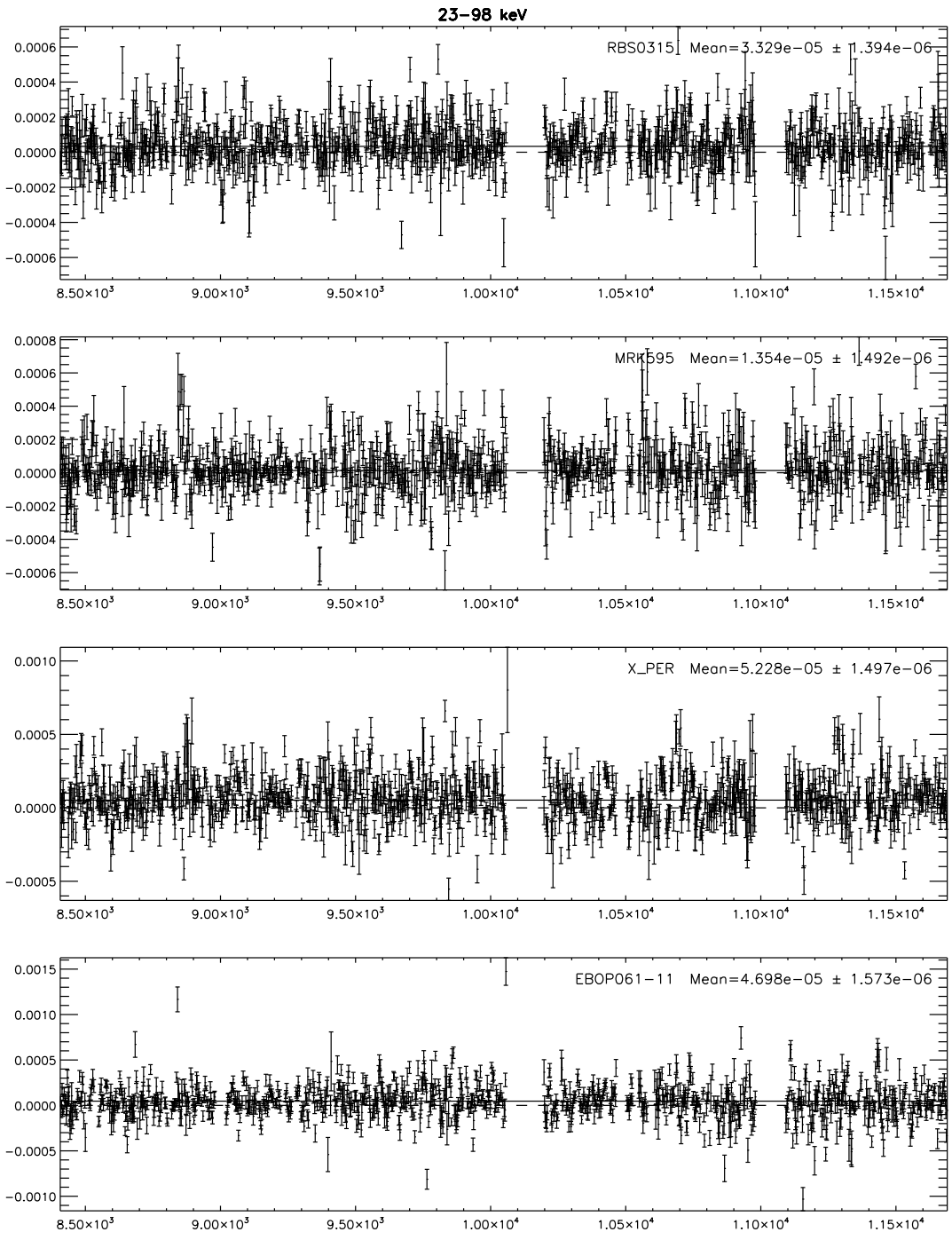

Figure A.1: continued.

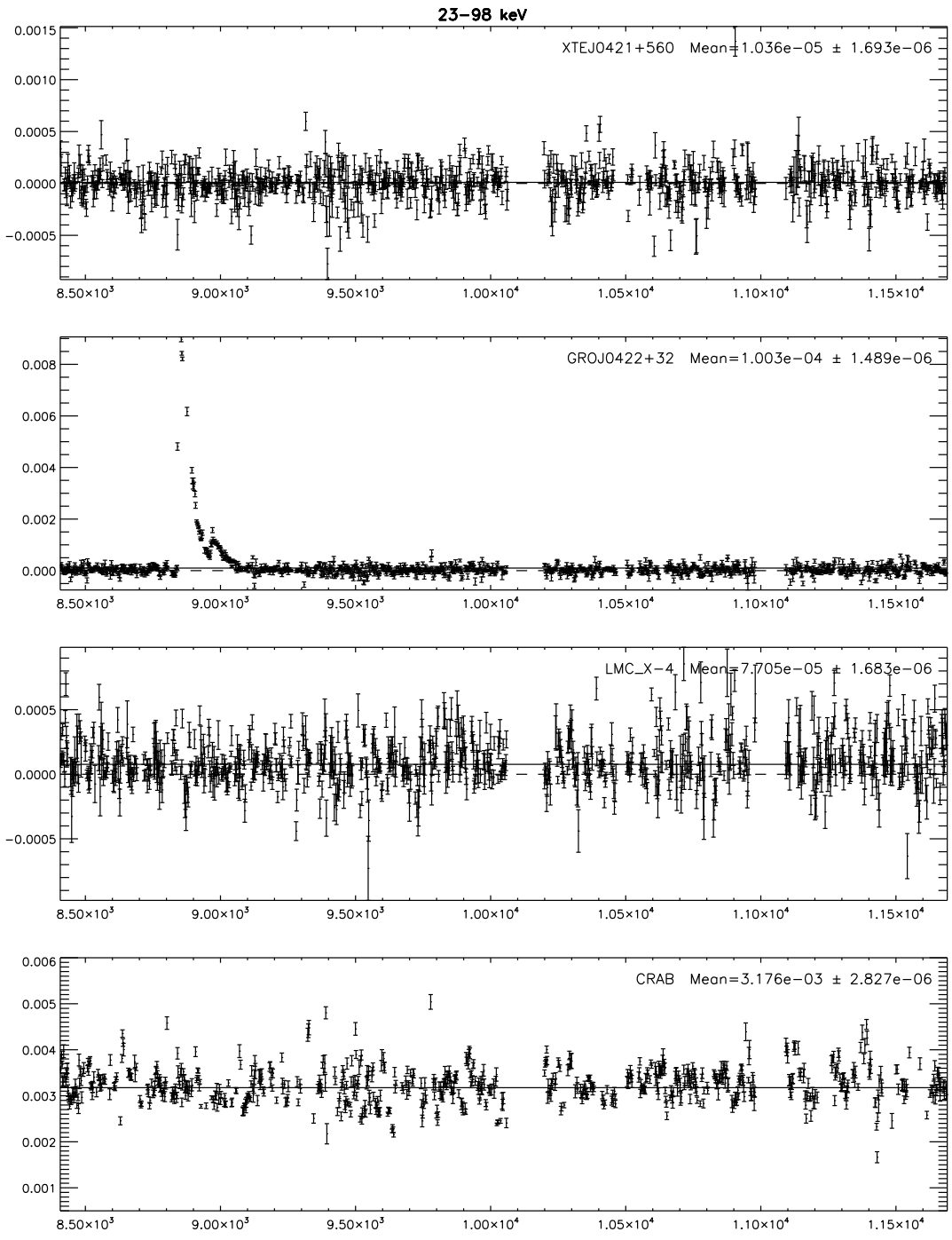

Figure A.1: continued.

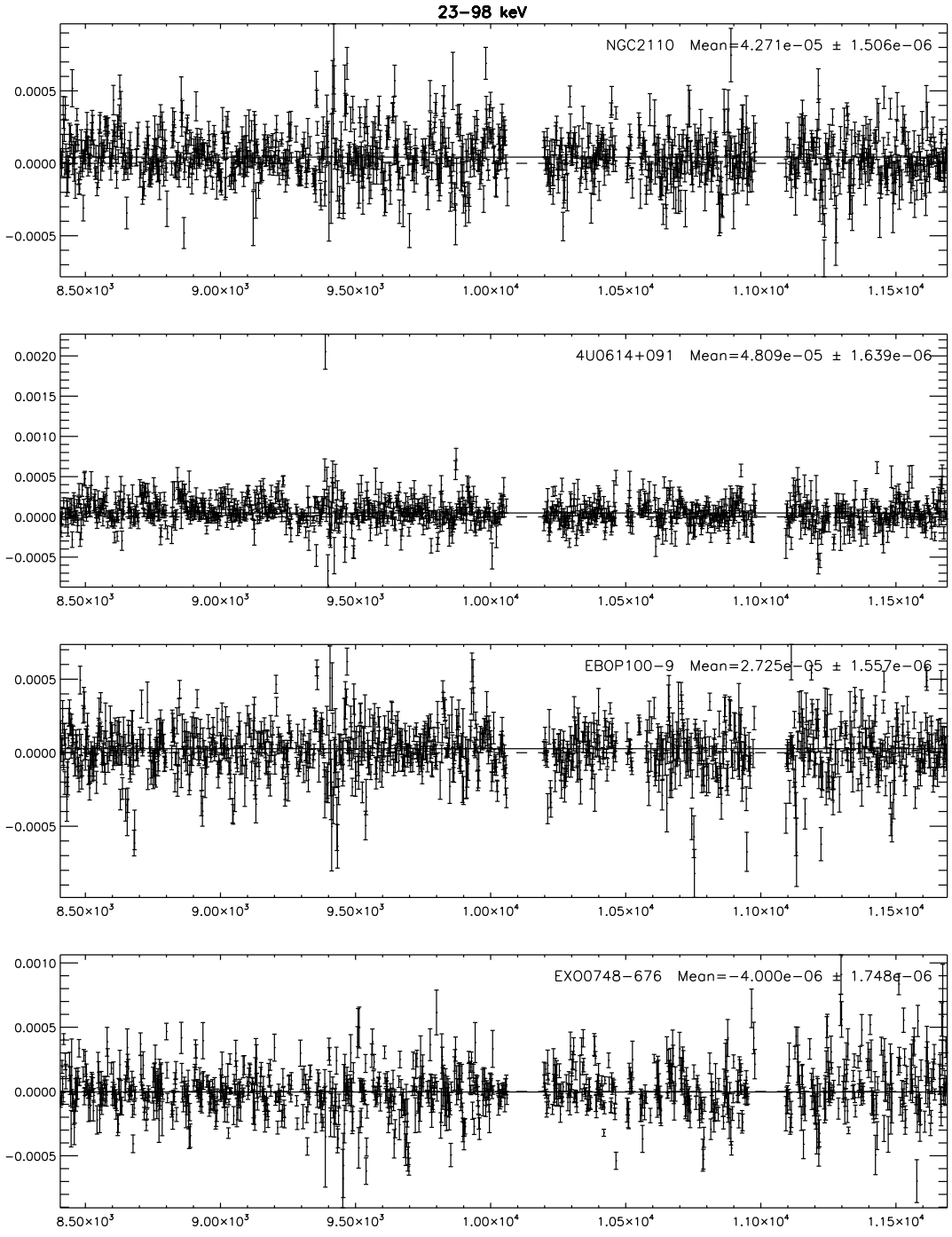

Figure A.1: continued.

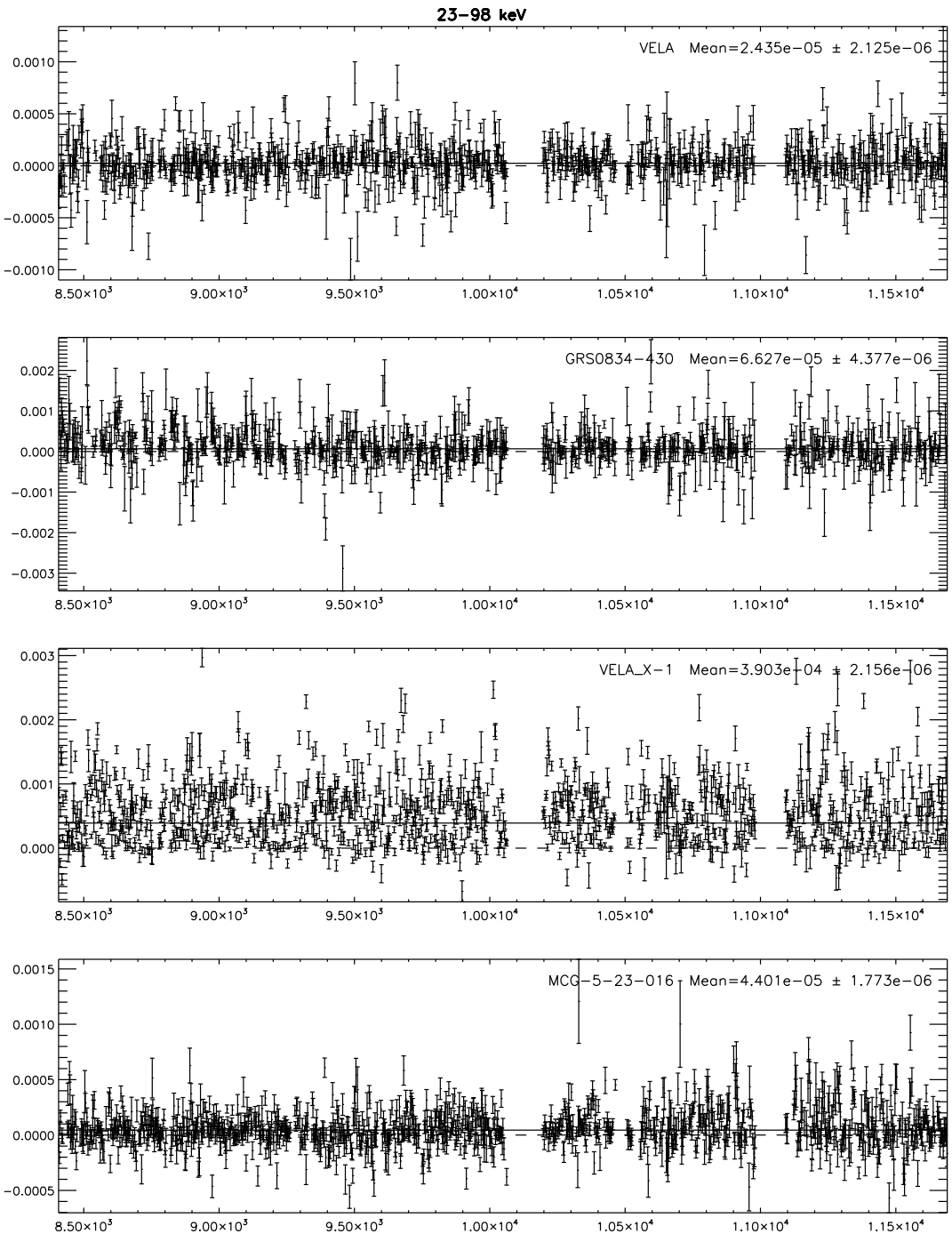

Figure A.1: continued.

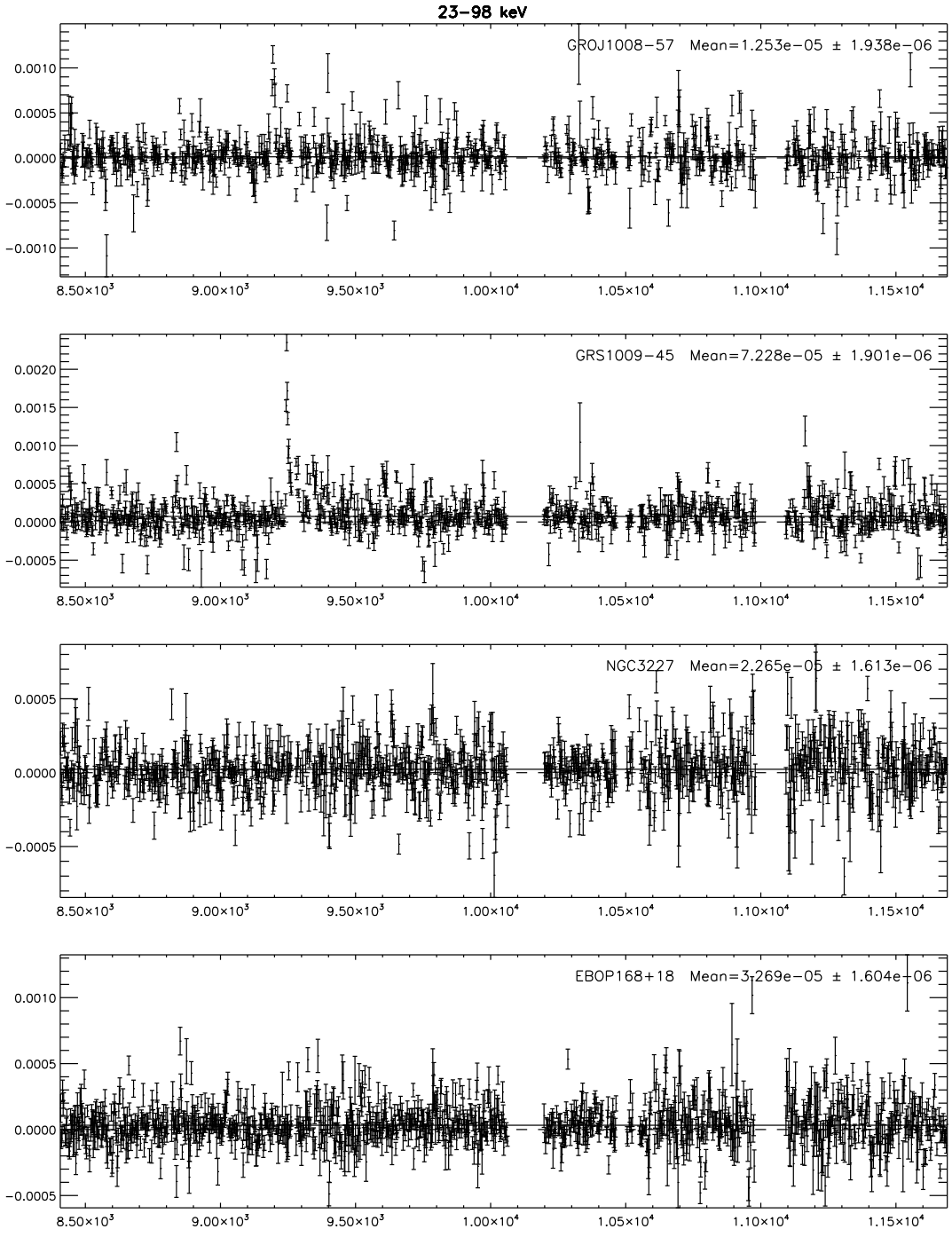

Figure A.1: continued.

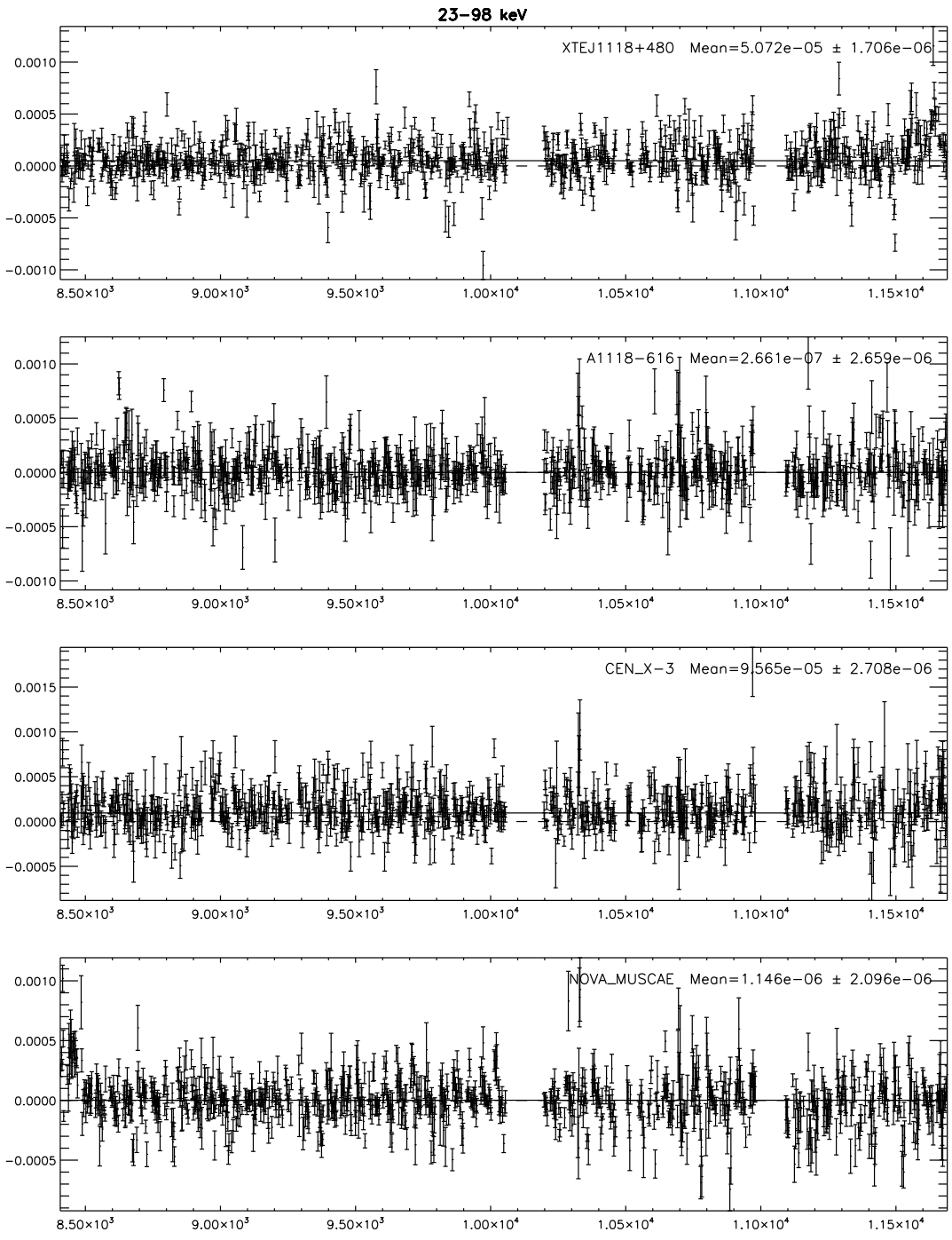

Figure A.1: continued.

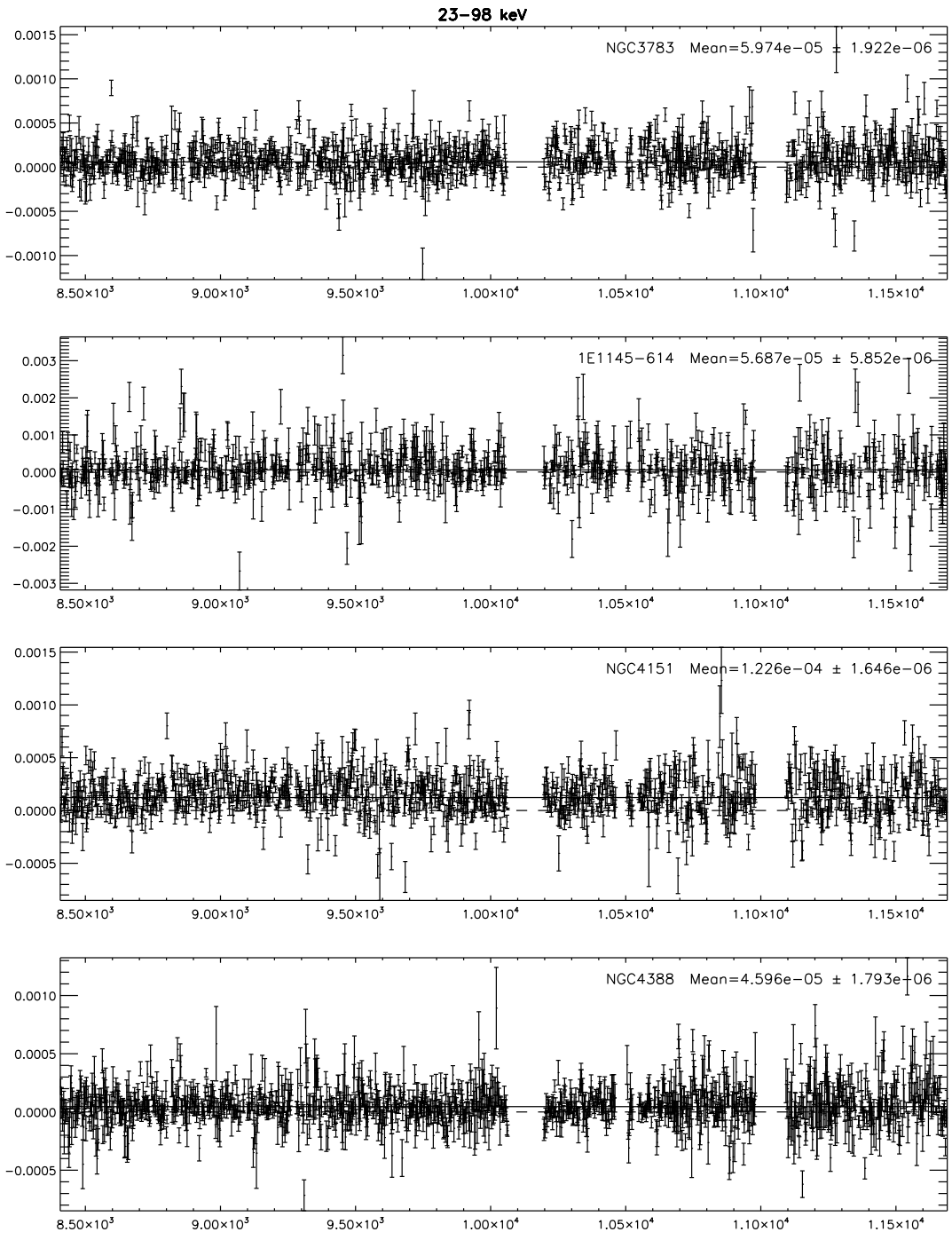

Figure A.1: continued.

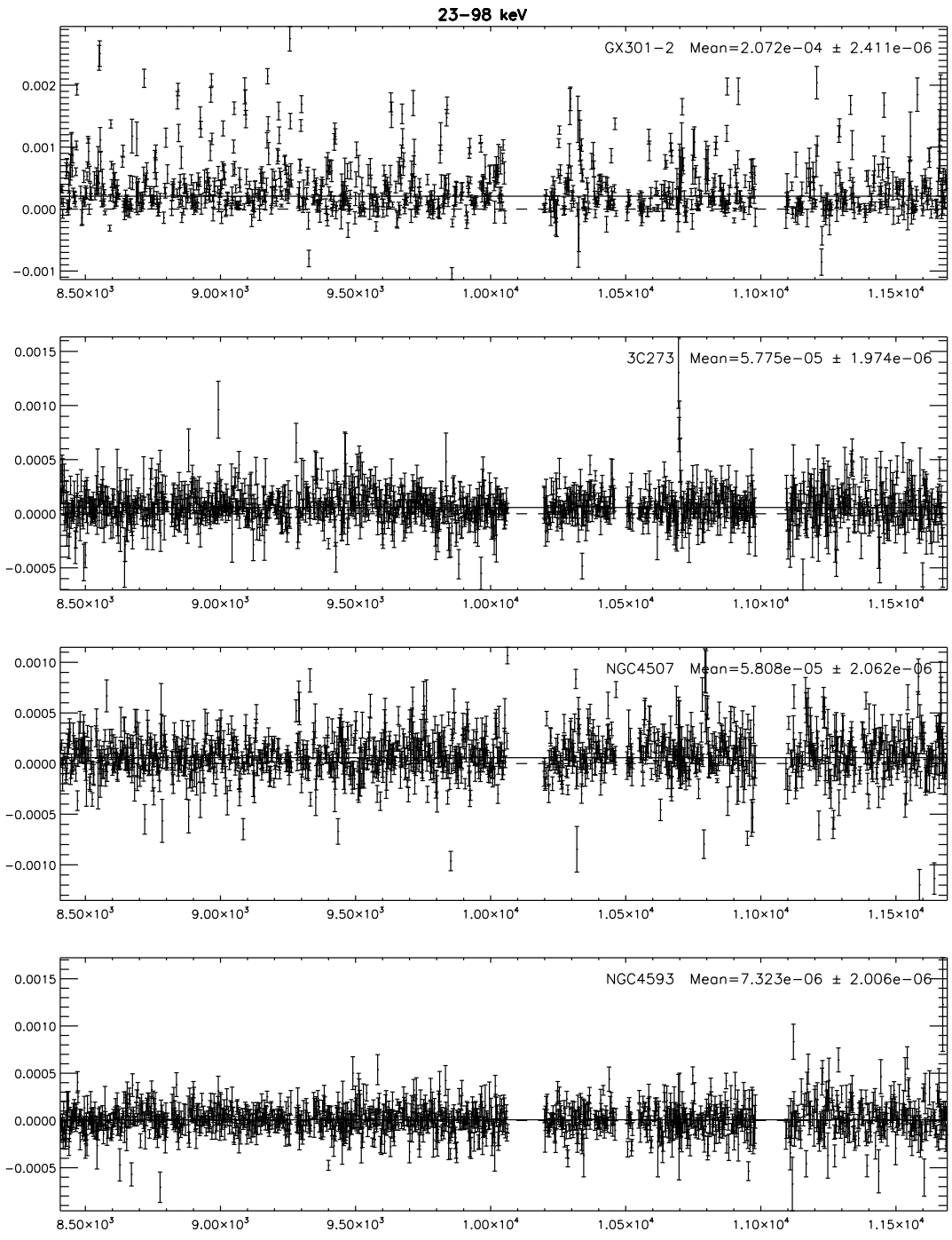

Figure A.1: continued.

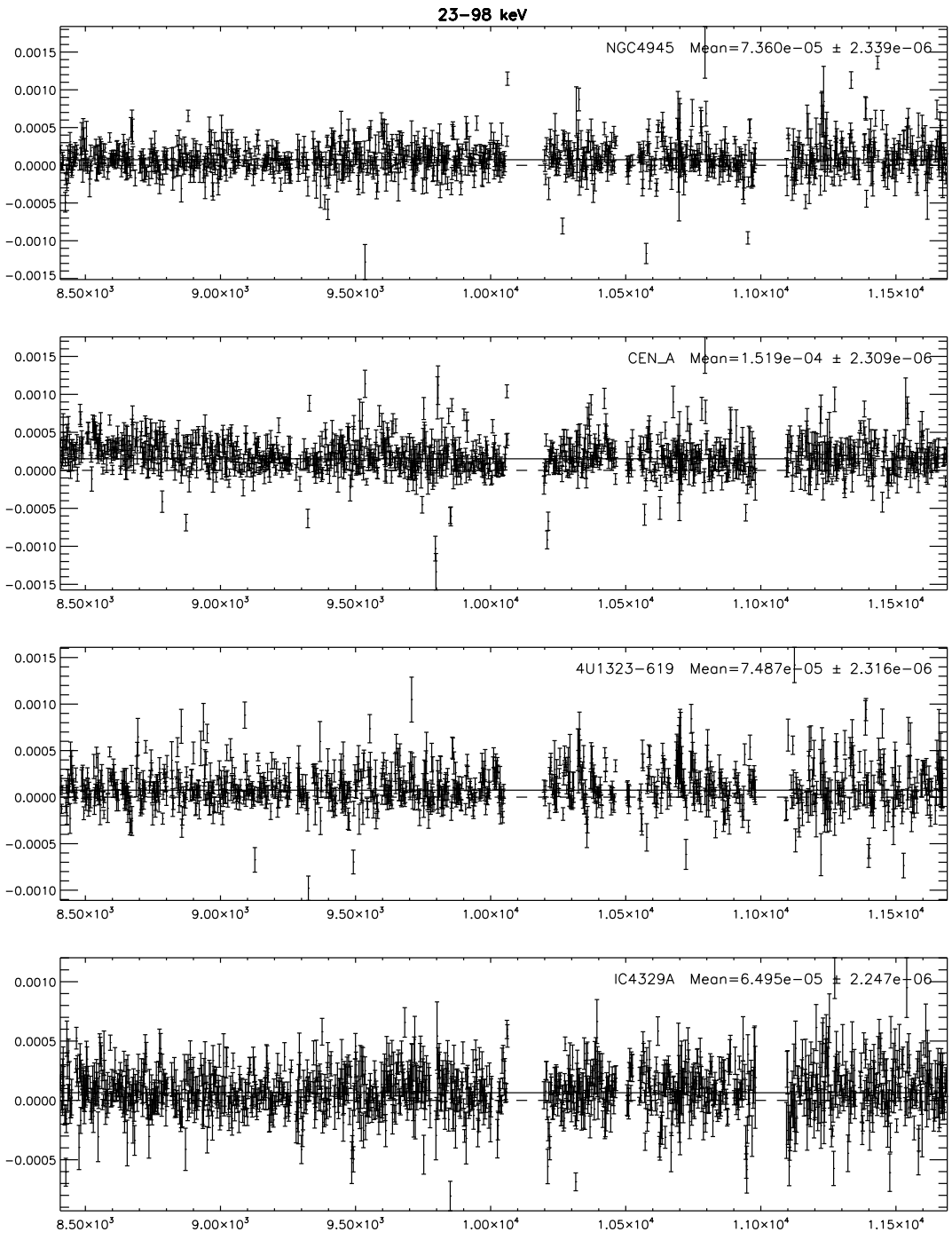

Figure A.1: continued.

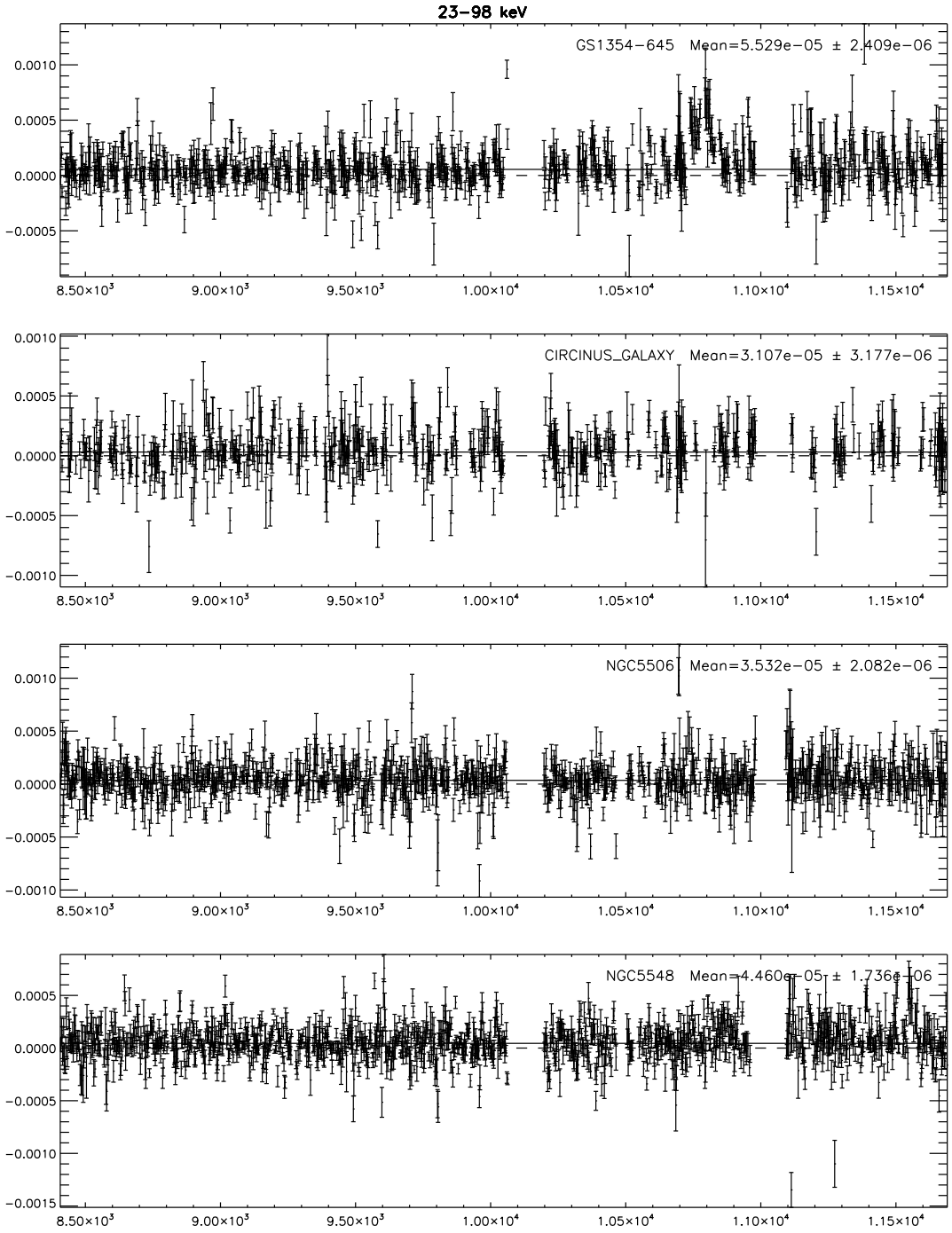

Figure A.1: continued.

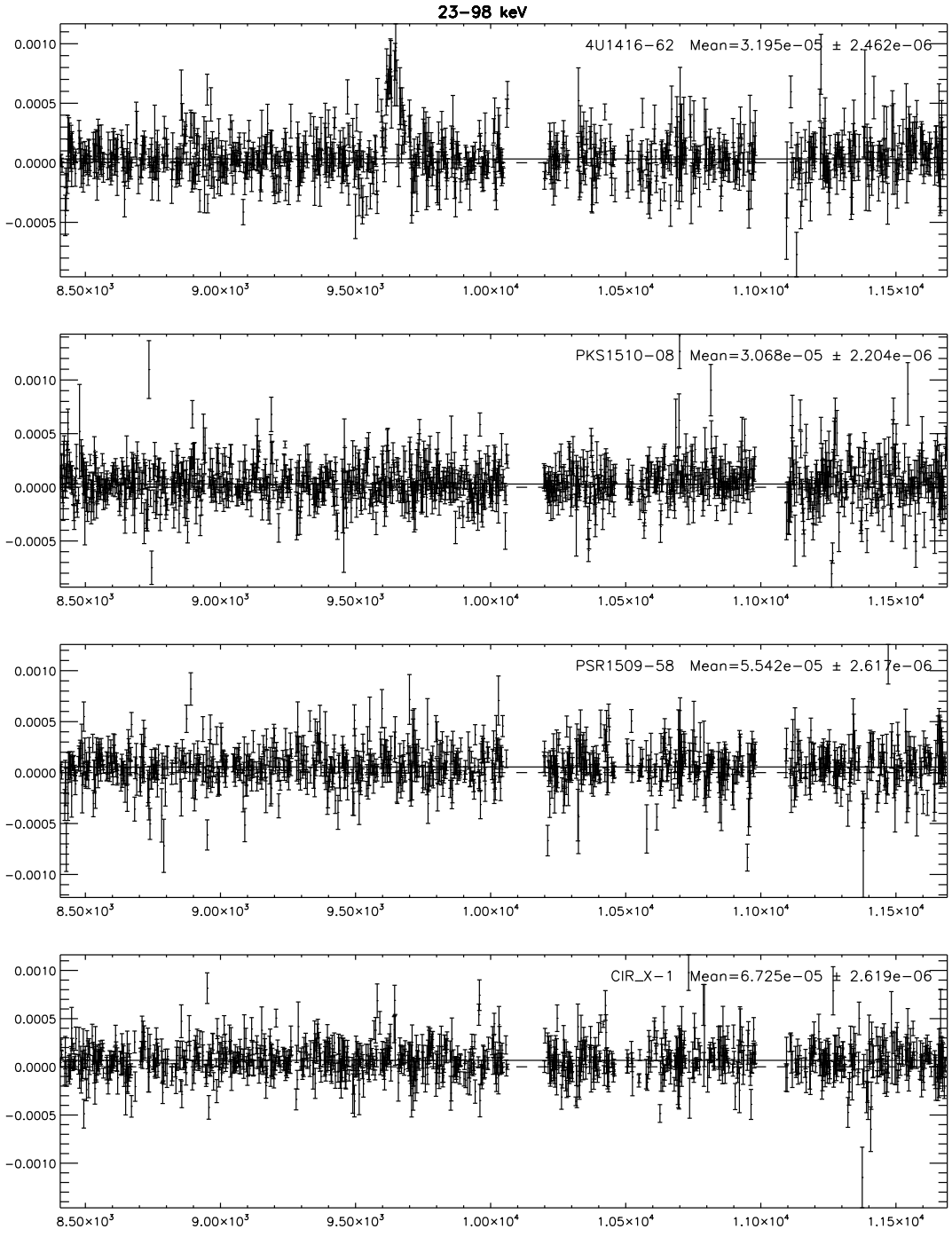

Figure A.1: continued.

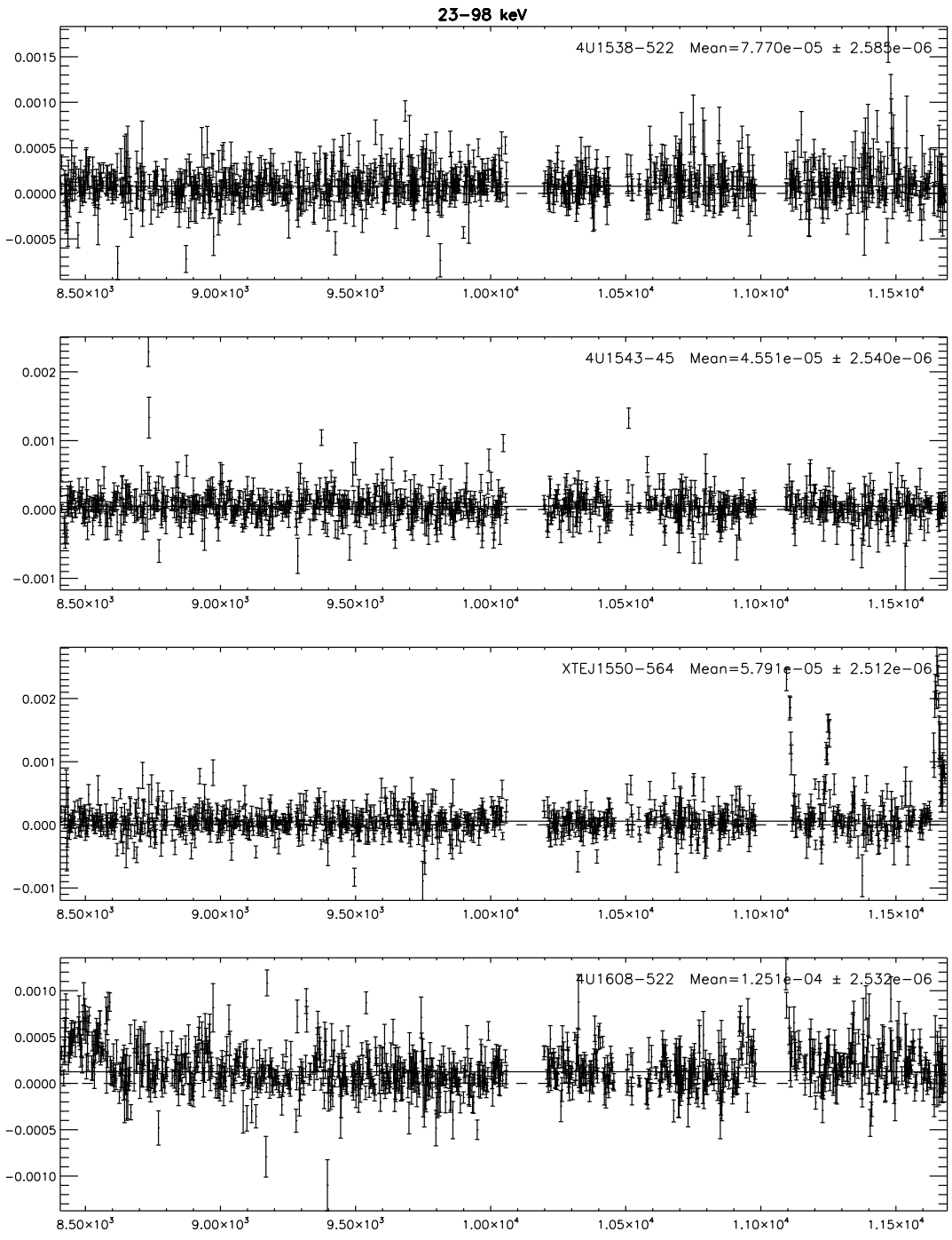

Figure A.1: continued.

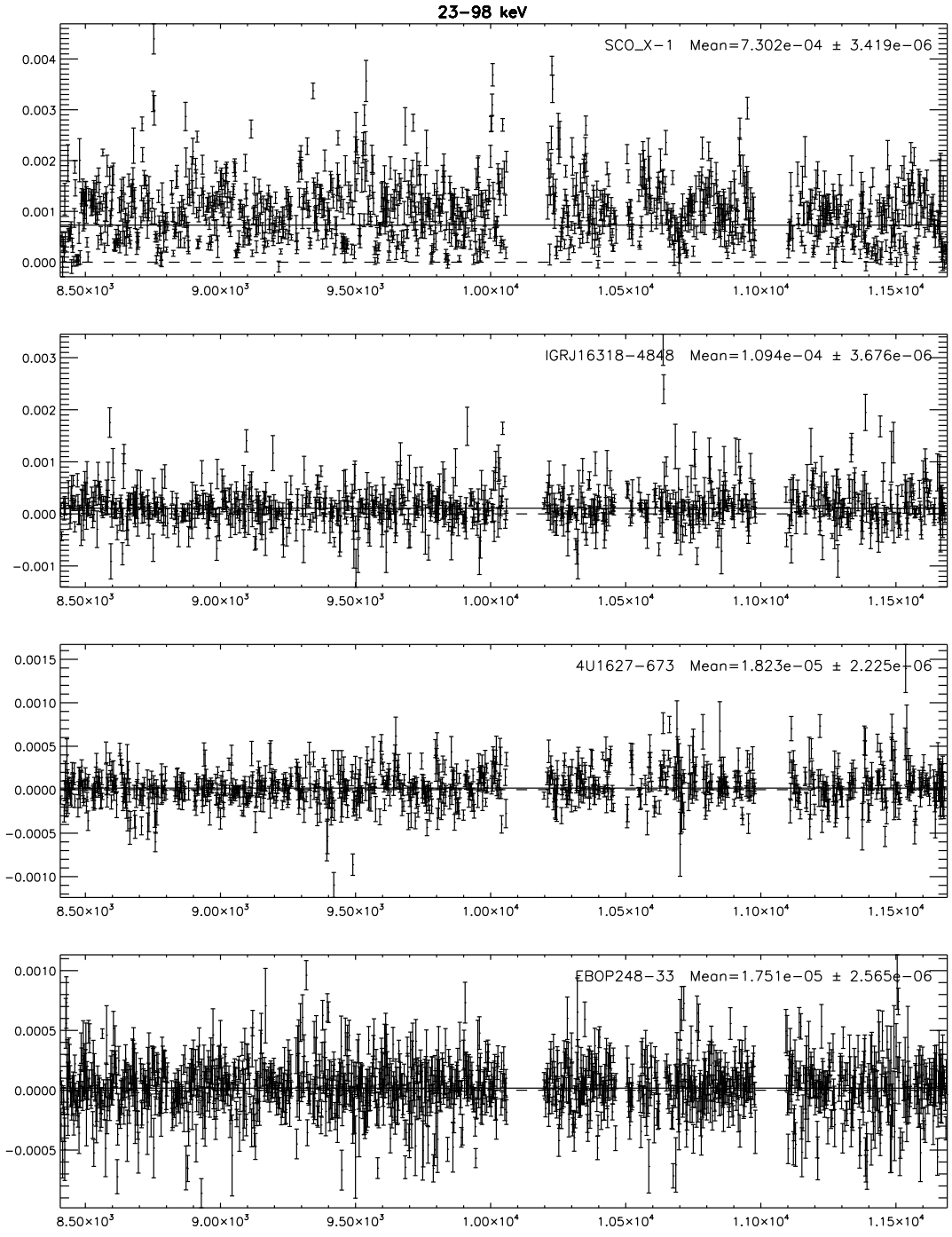

Figure A.1: continued.

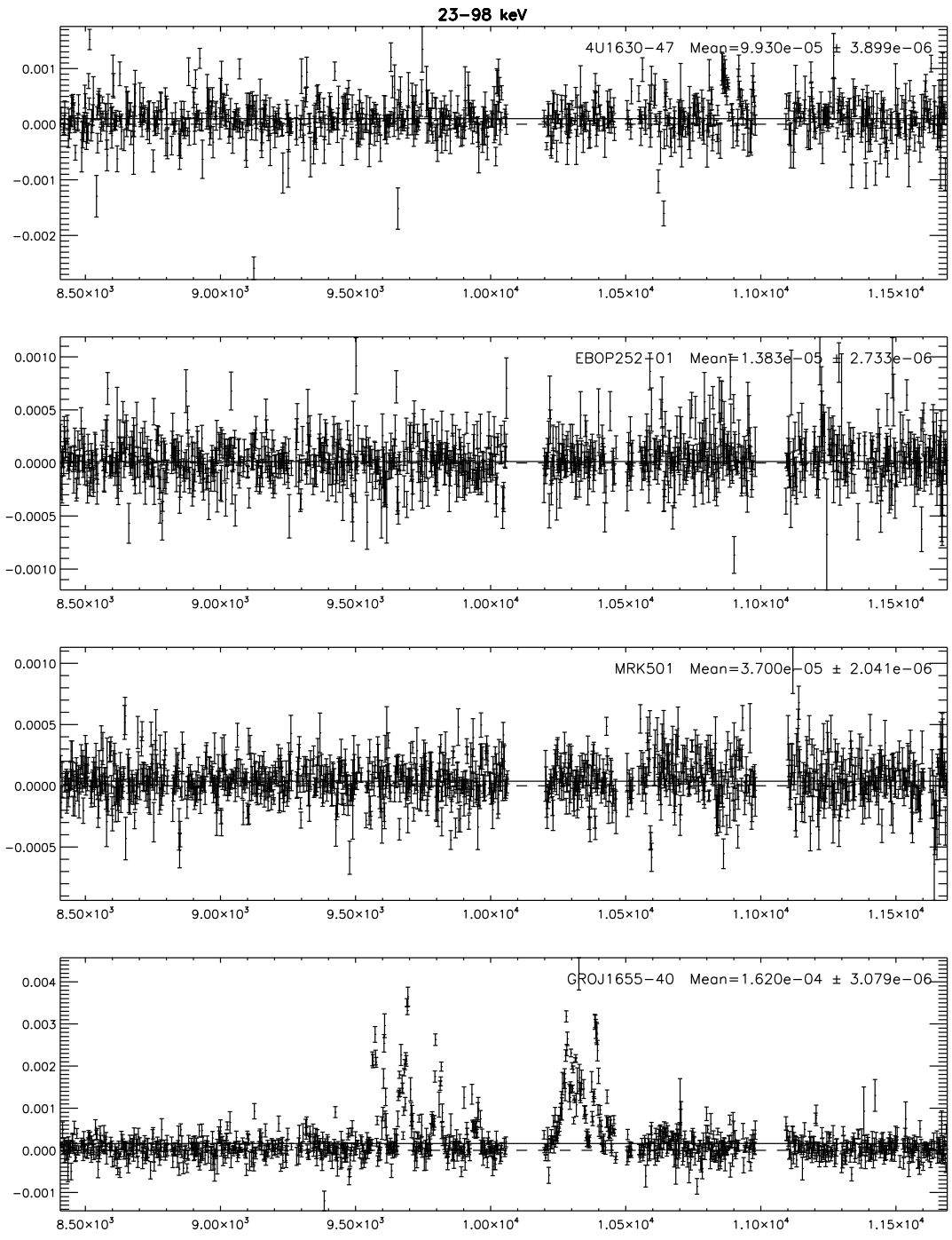

Figure A.1: continued.

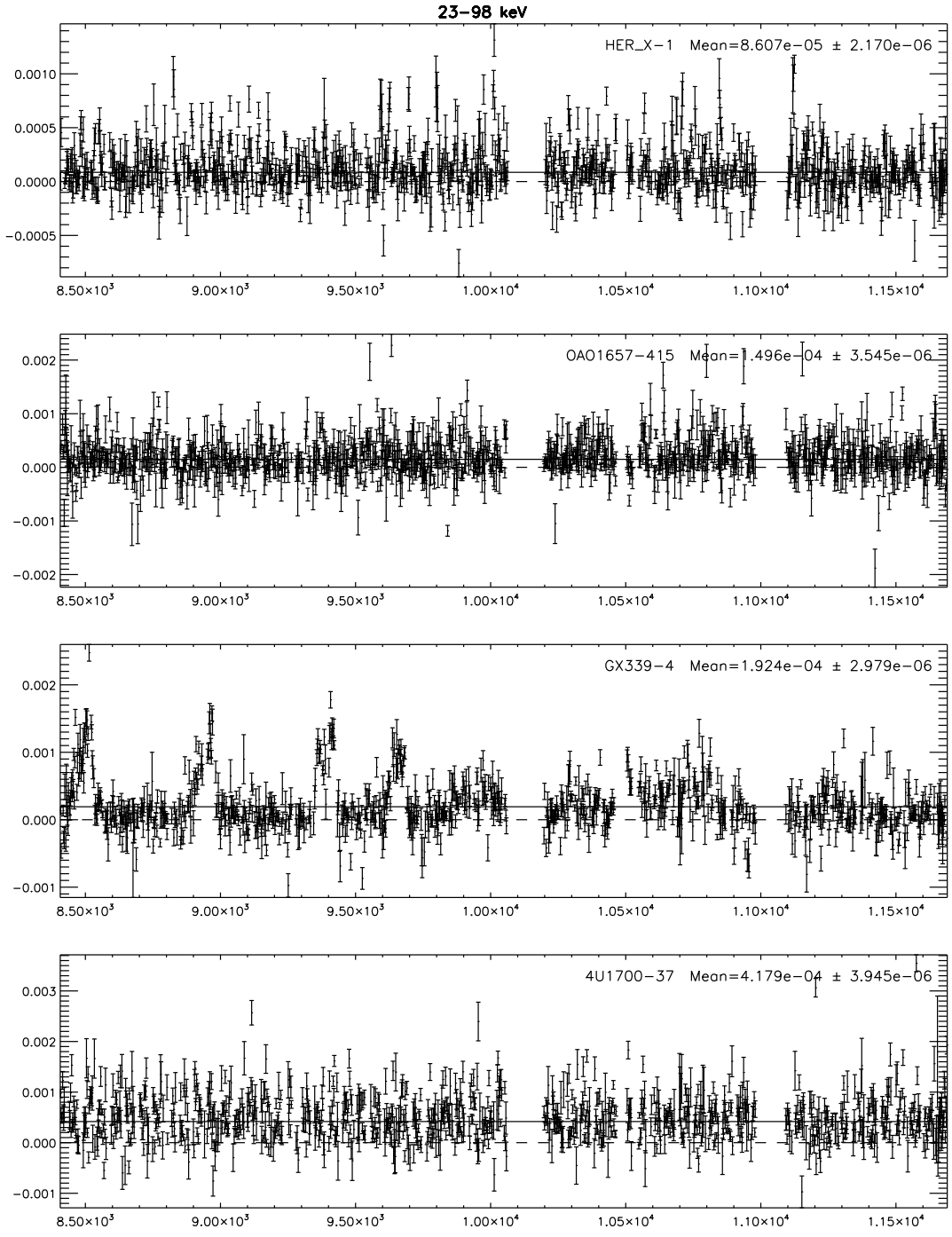

Figure A.1: continued.

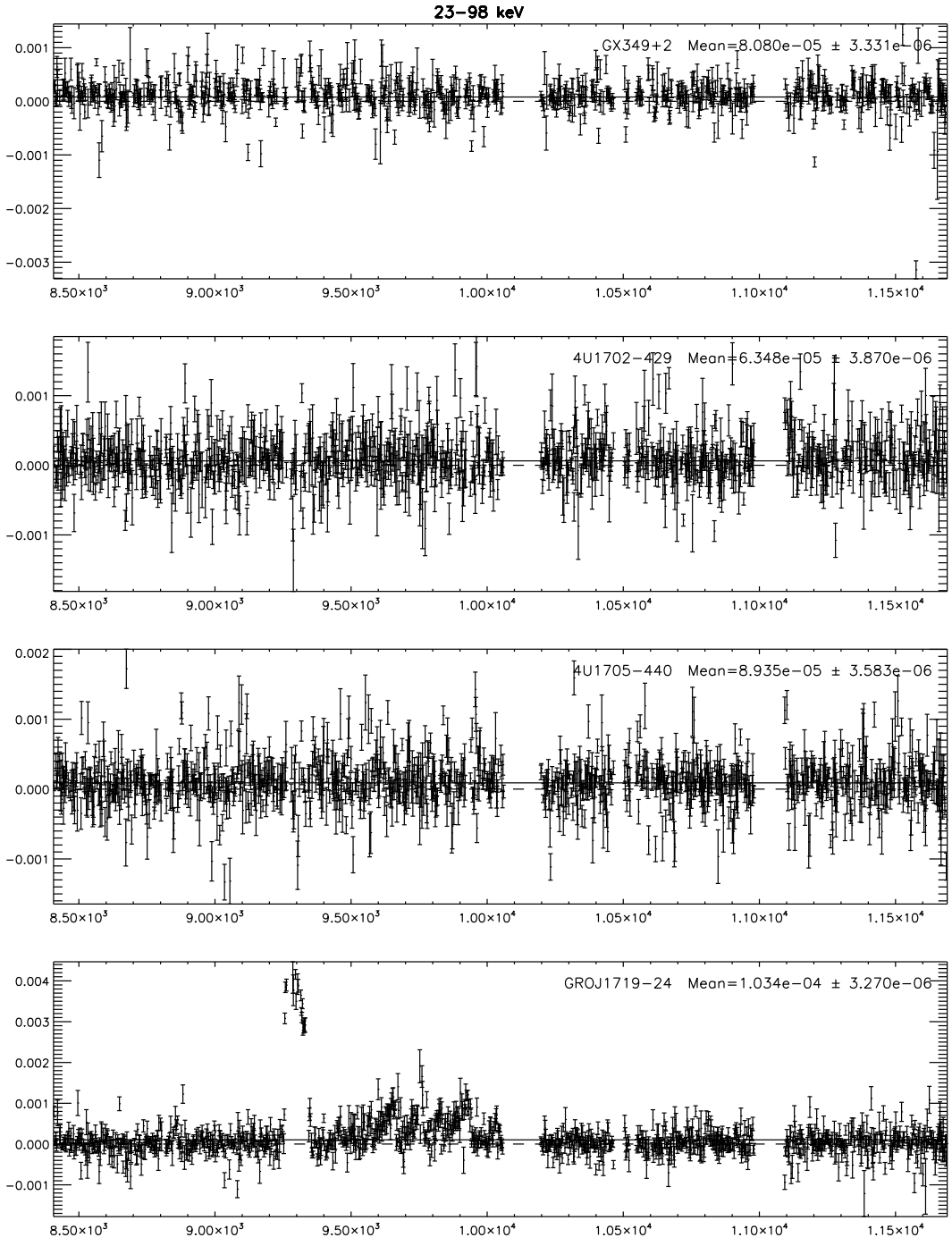

Figure A.1: continued.

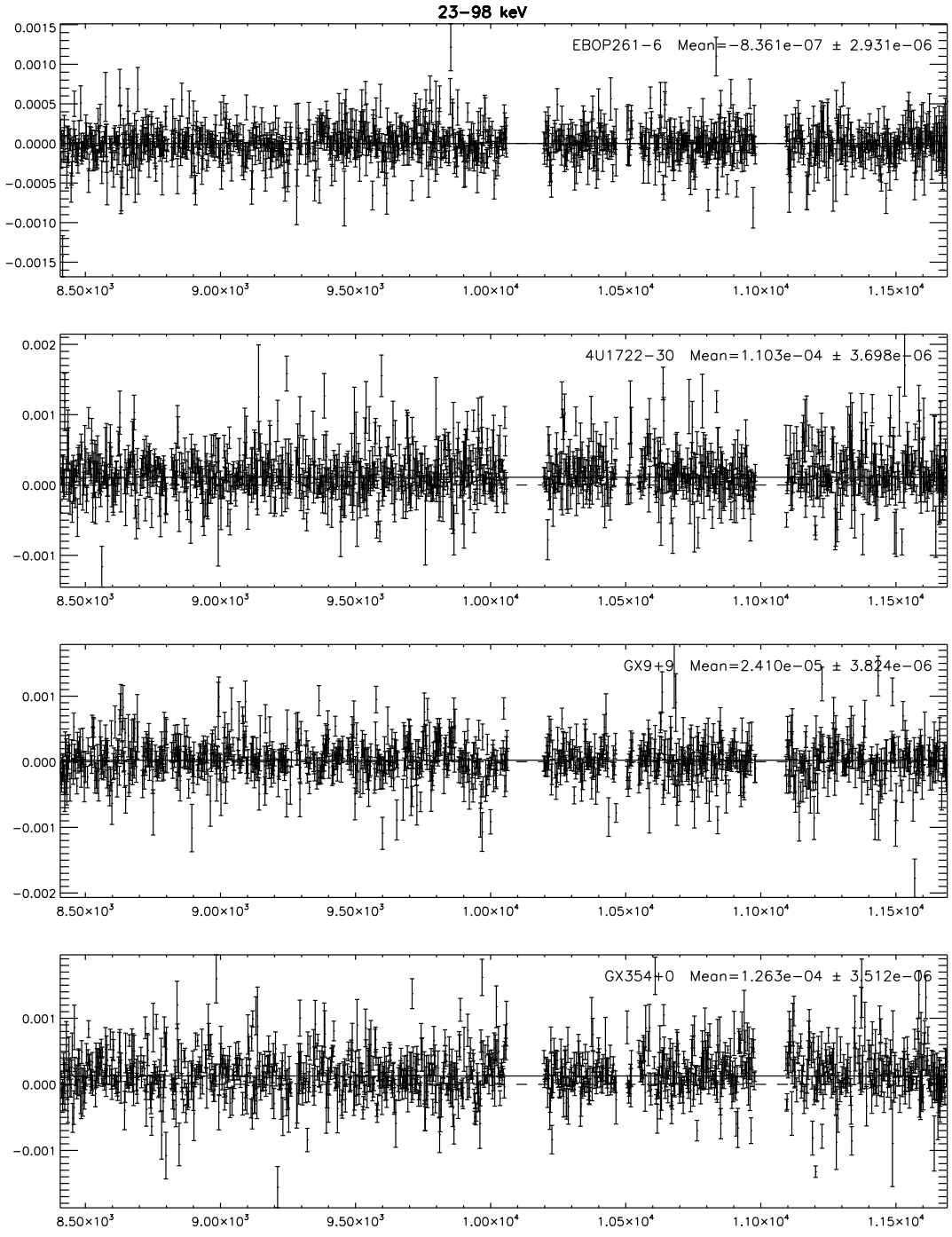

Figure A.1: continued.

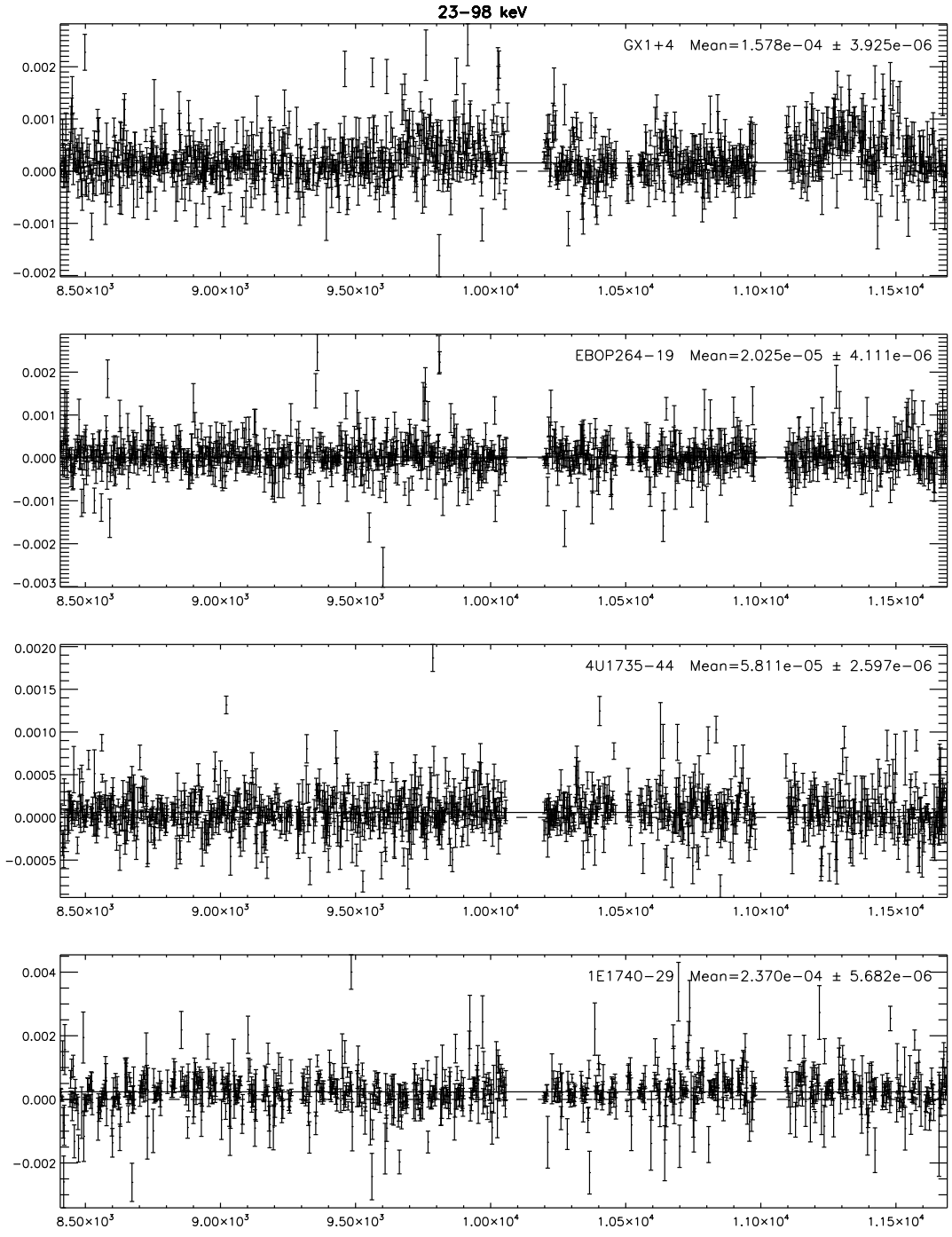

Figure A.1: continued.

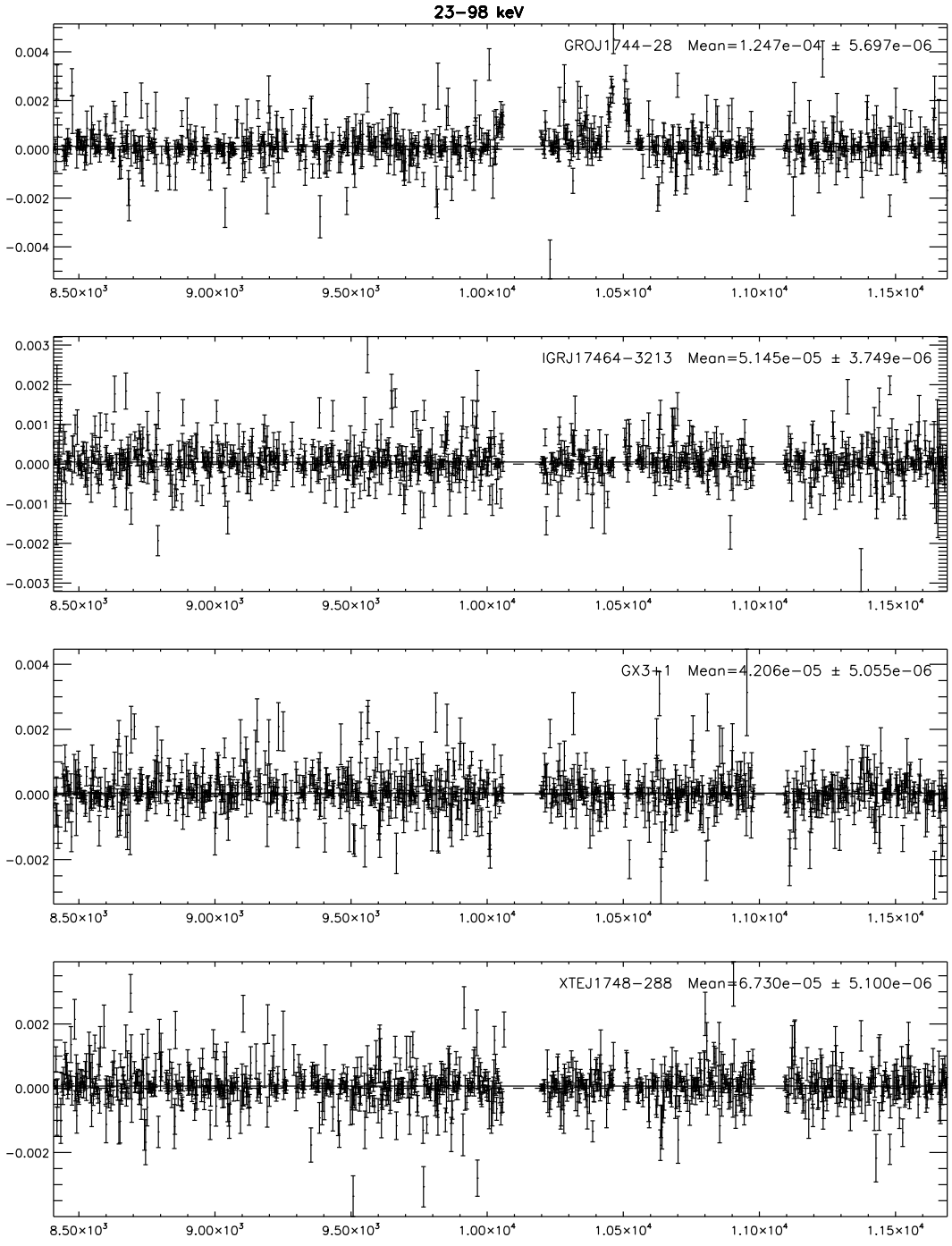

Figure A.1: continued.

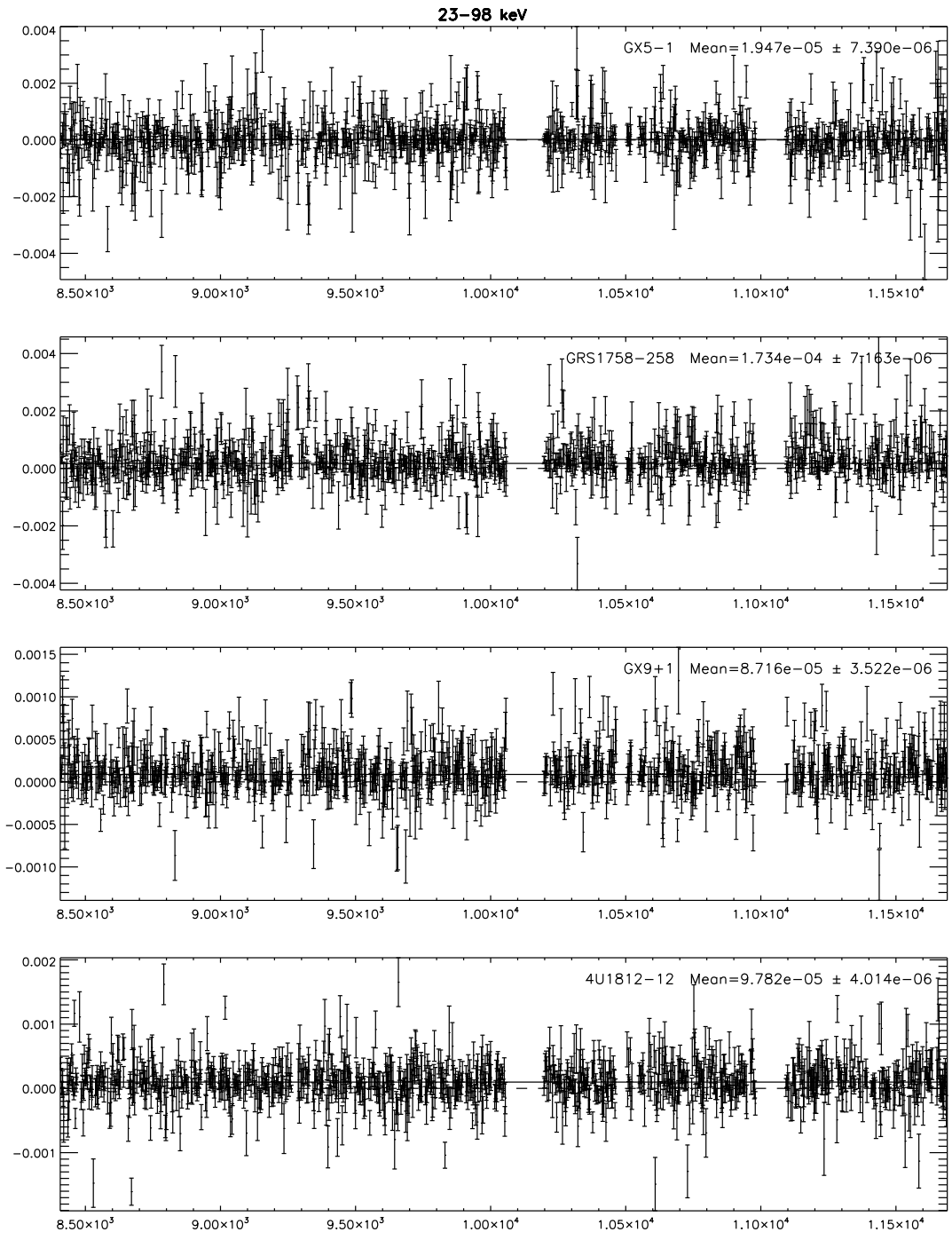

Figure A.1: continued.

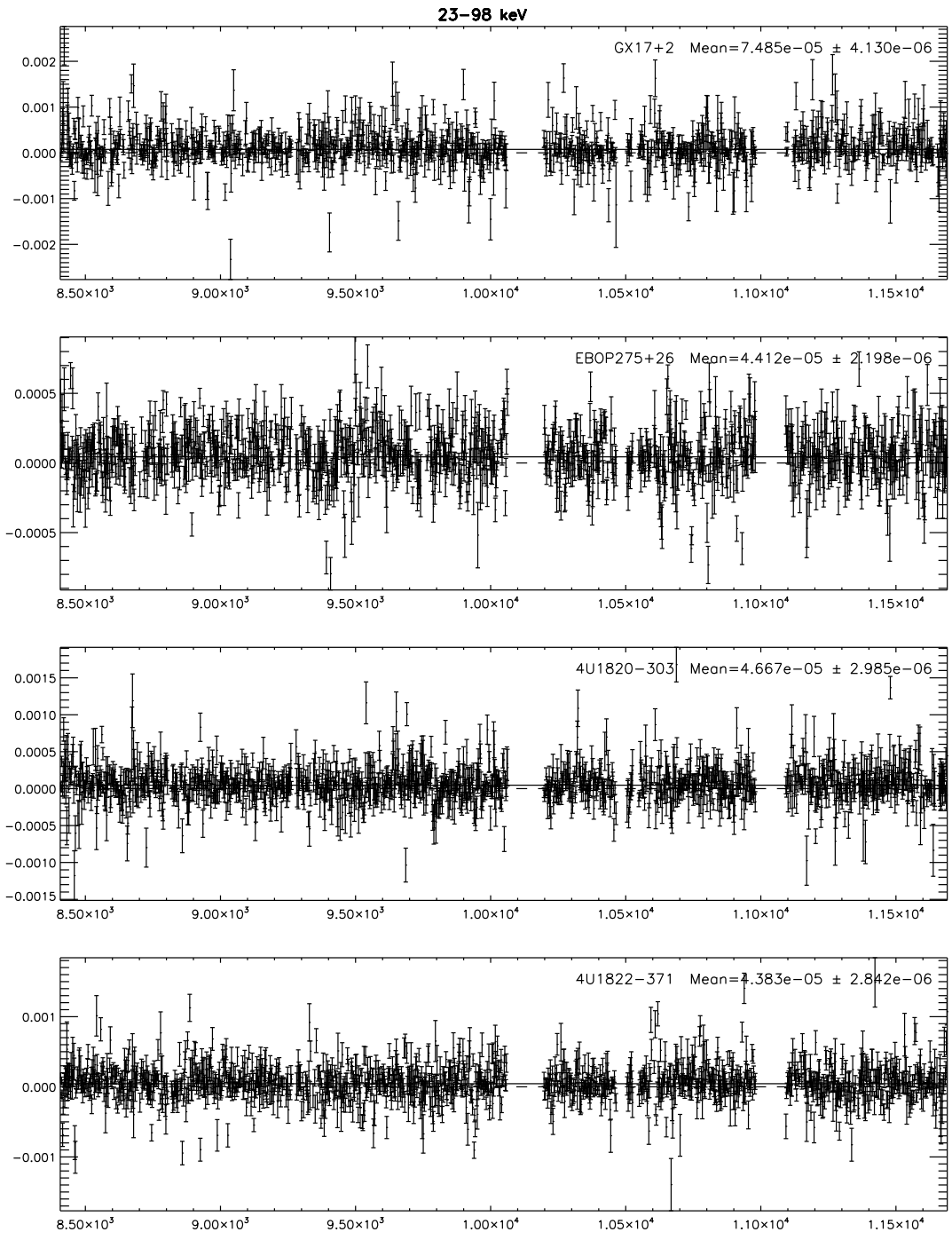

Figure A.1: continued.

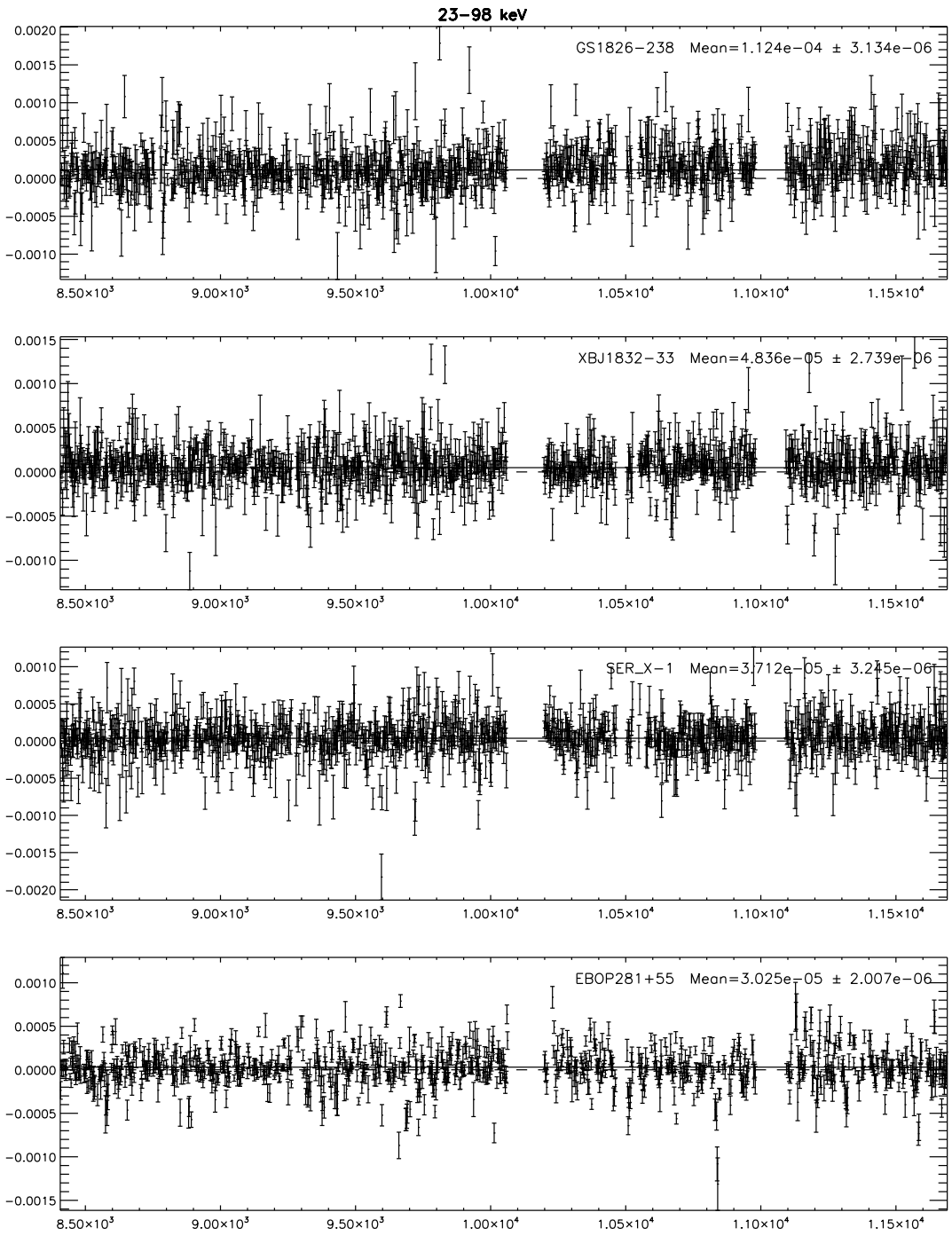

Figure A.1: continued.

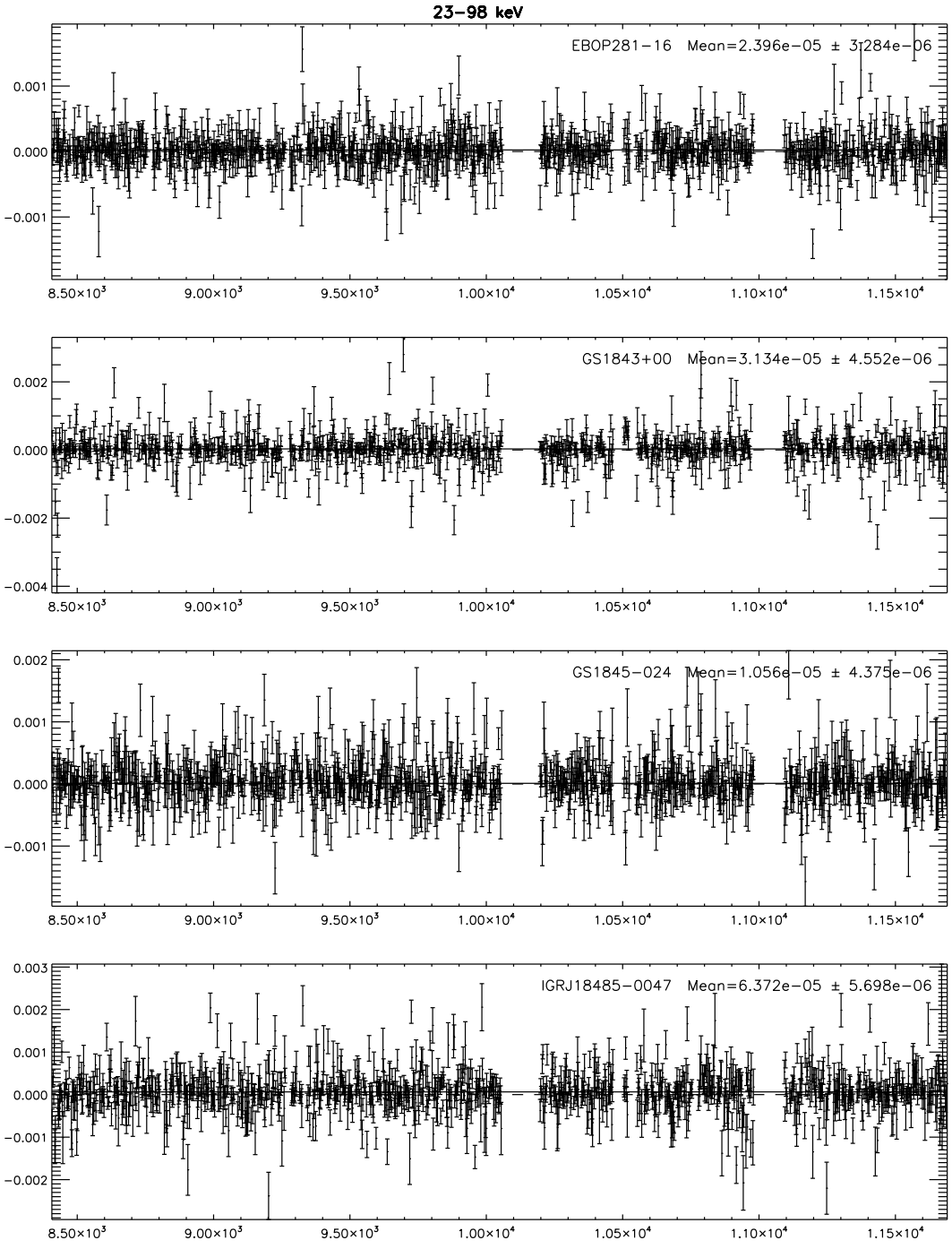

Figure A.1: continued.

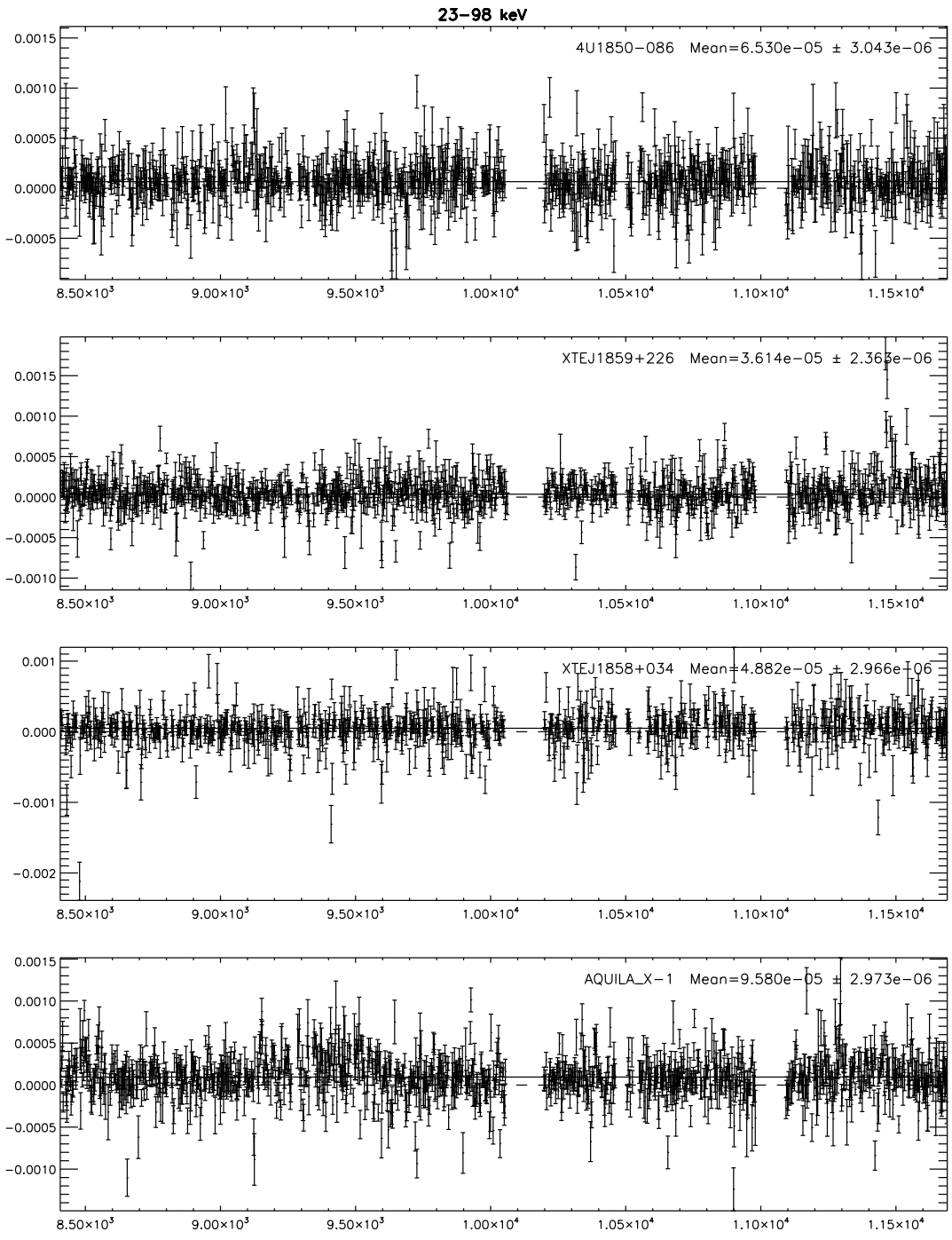

Figure A.1: continued.

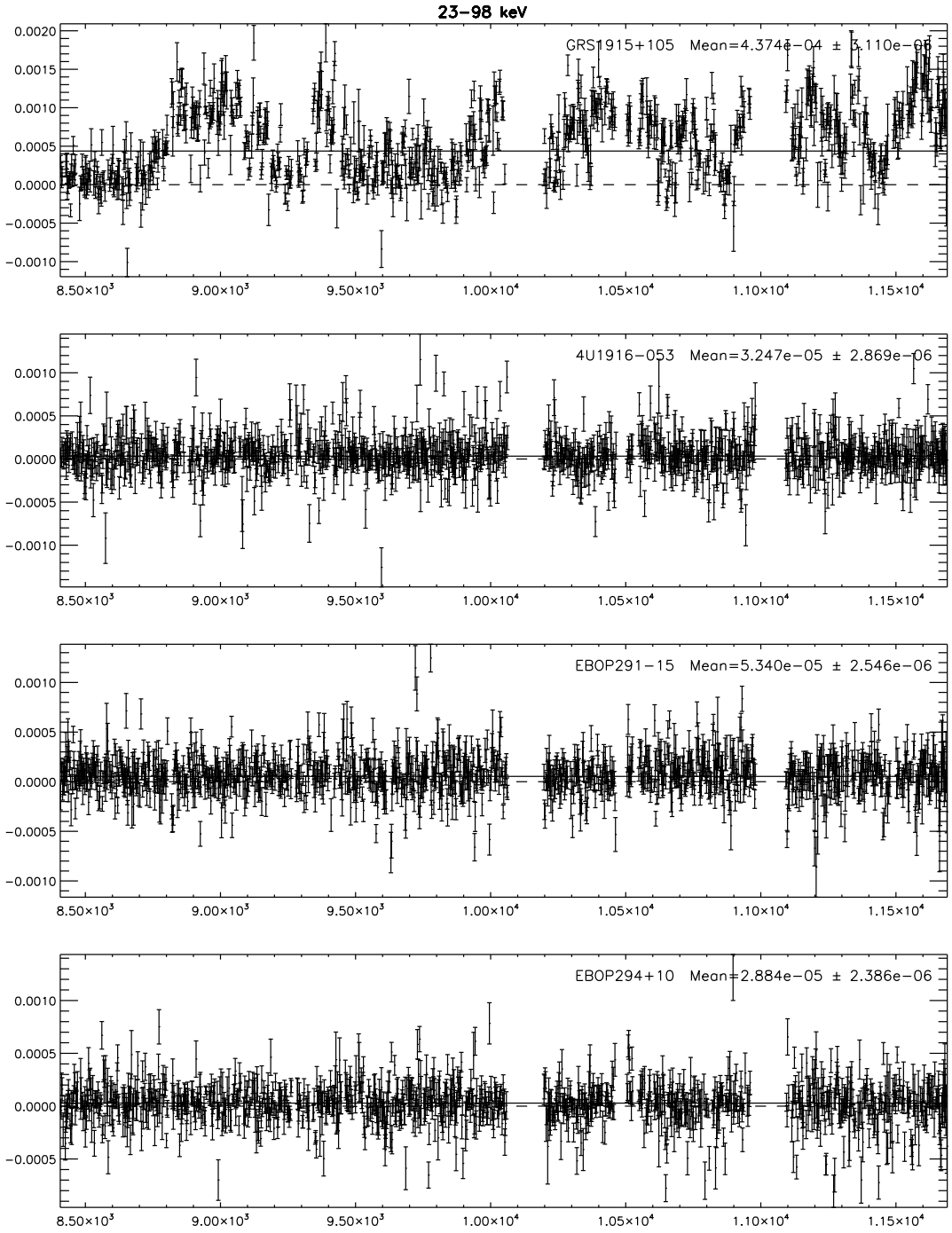

Figure A.1: continued.

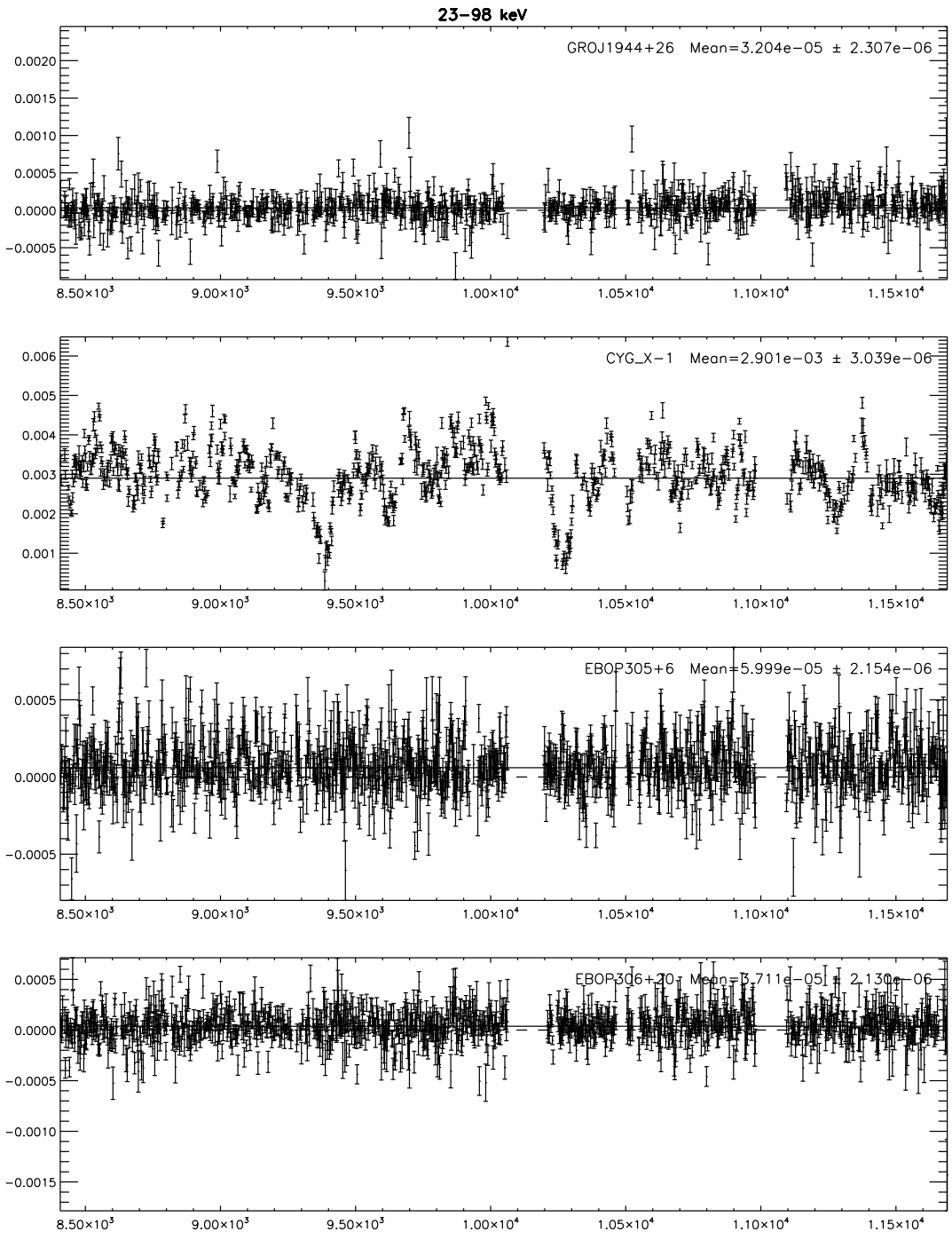

Figure A.1: continued.

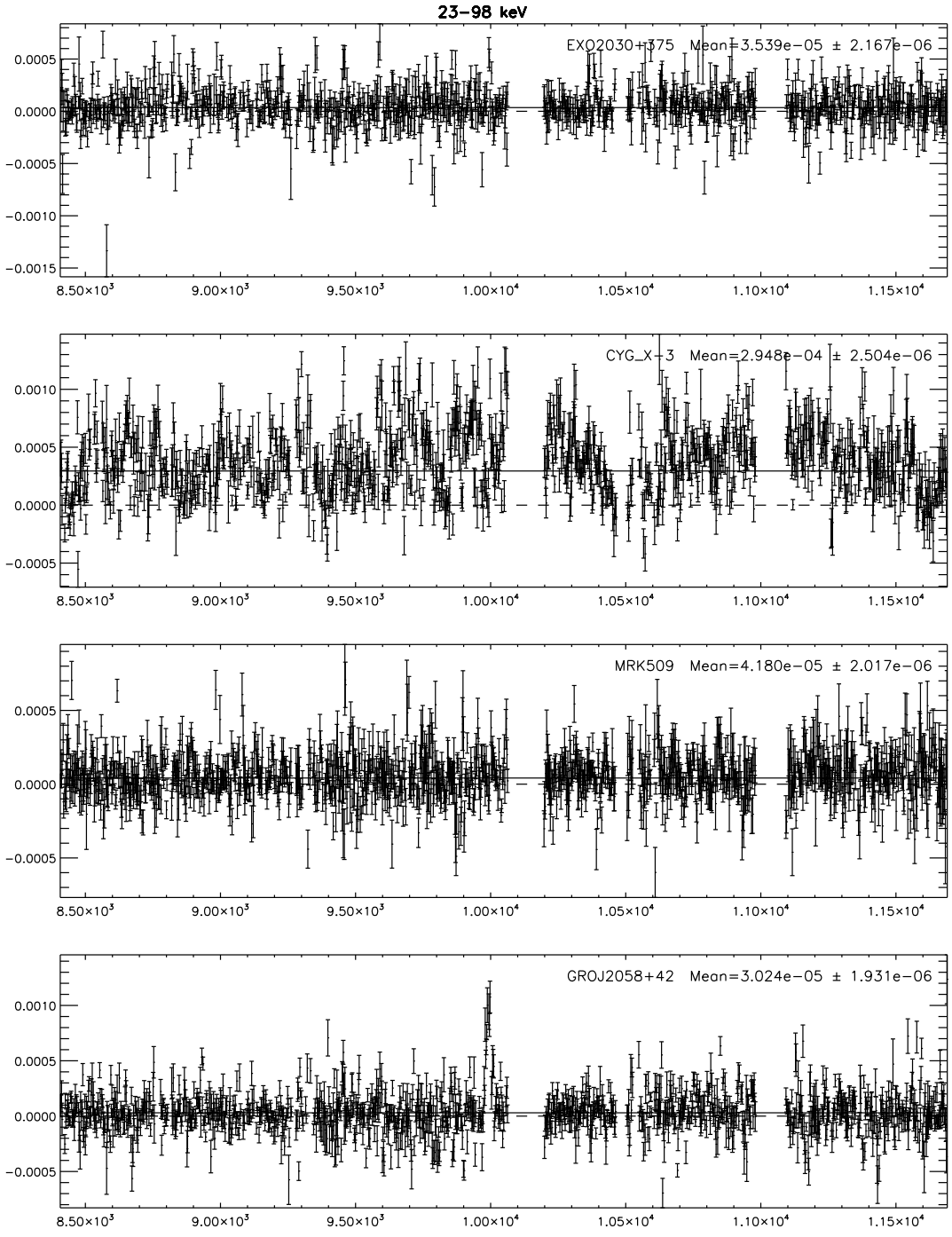

Figure A.1: continued.

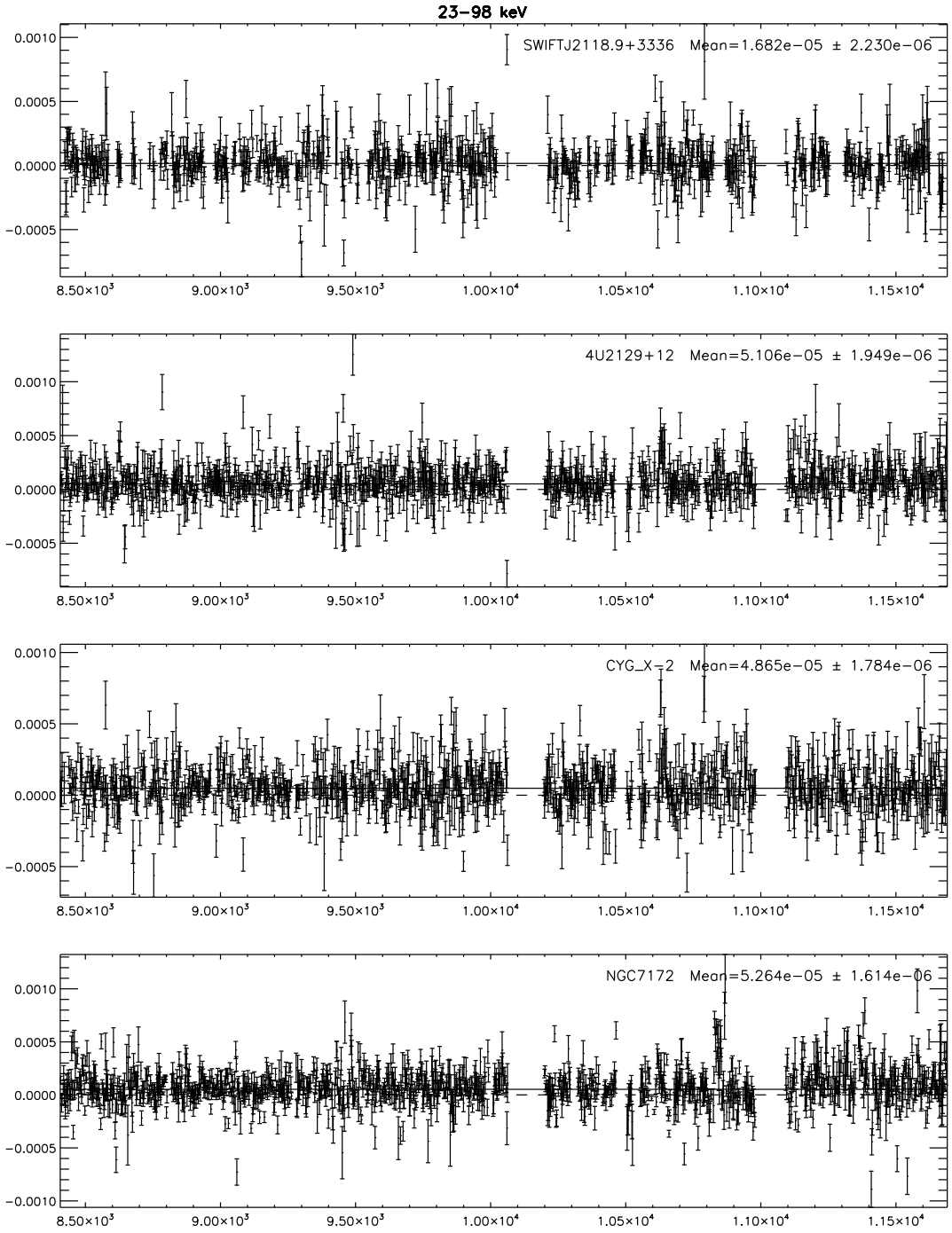

Figure A.1: continued.

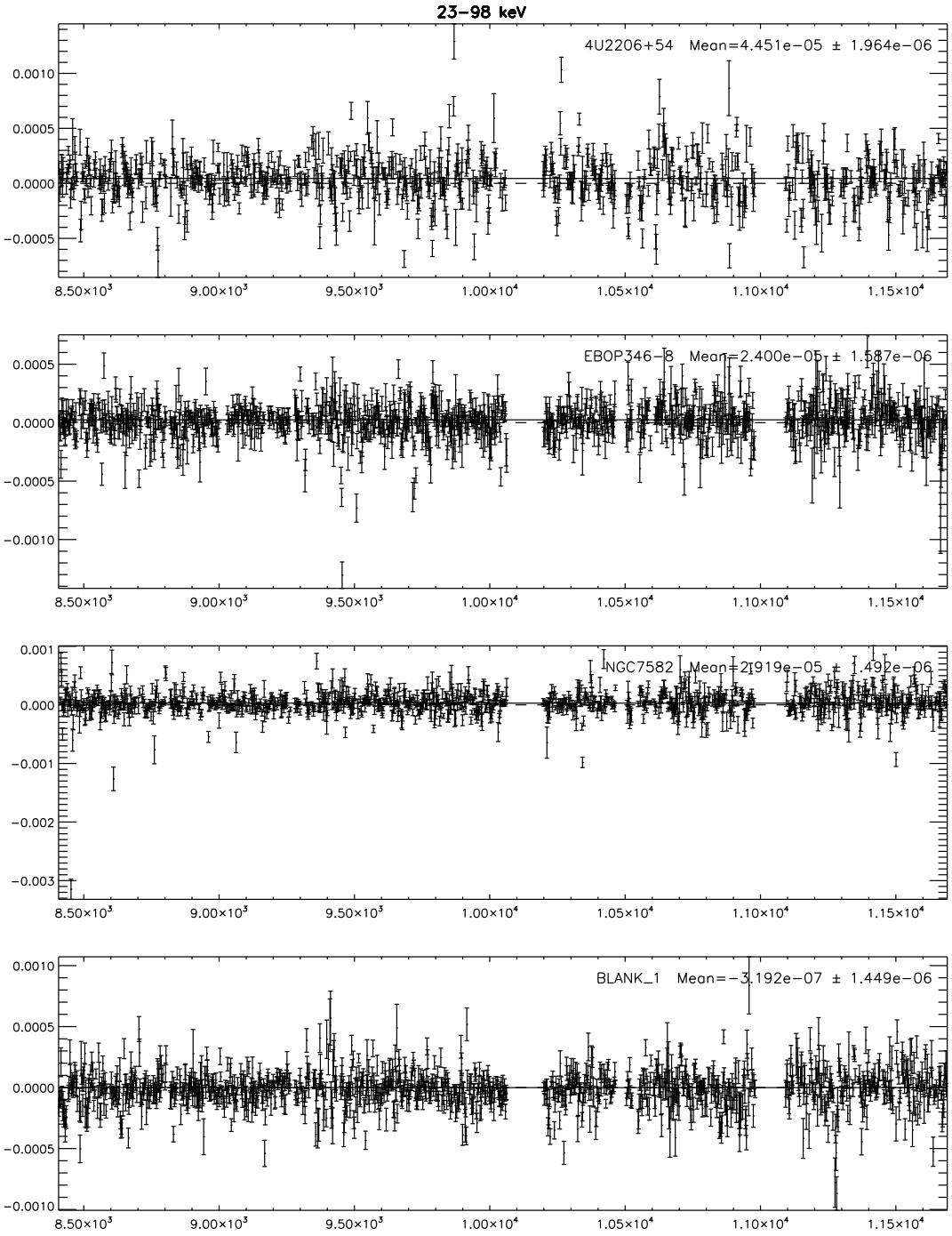

Figure A.1: continued.

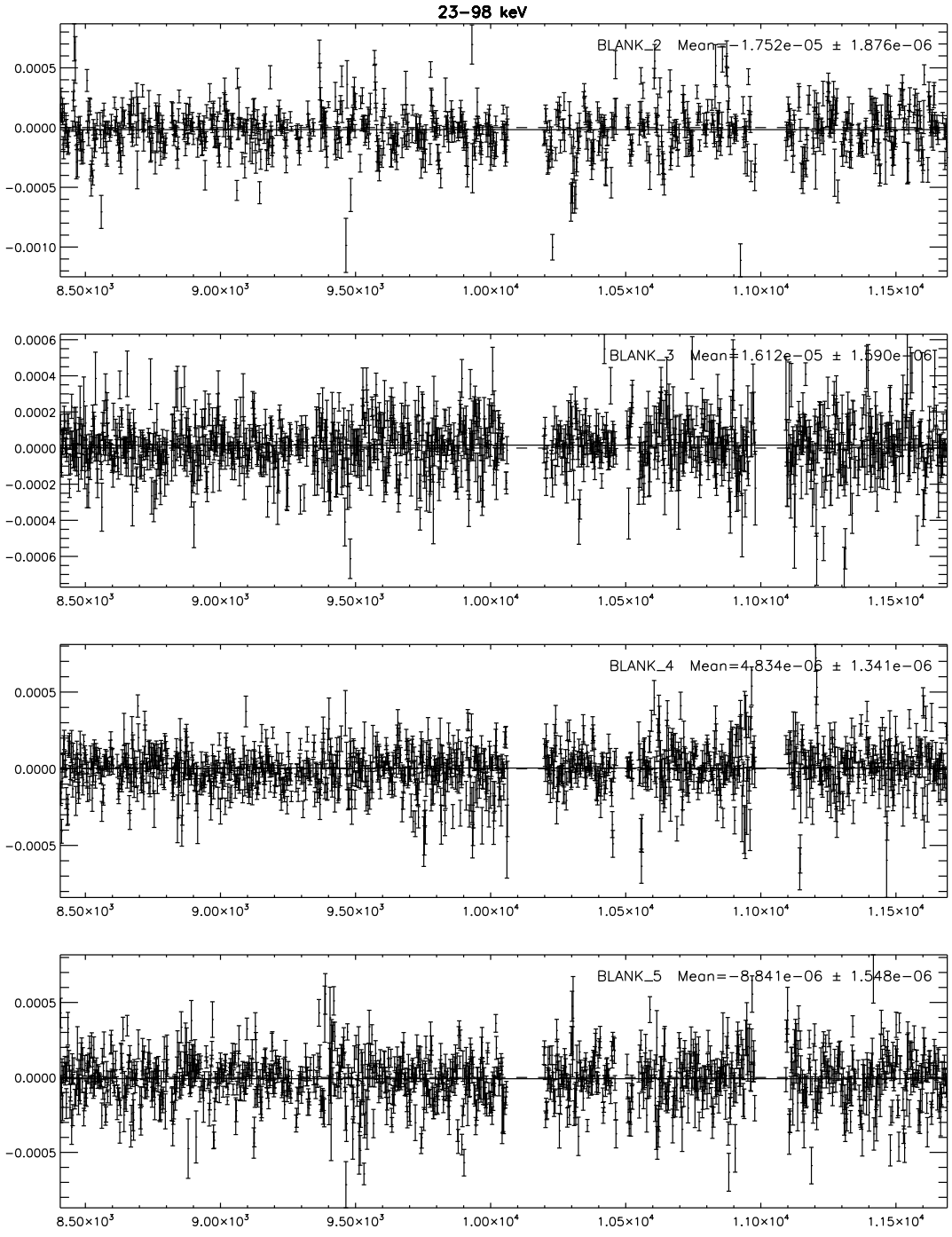

Figure A.1: continued.

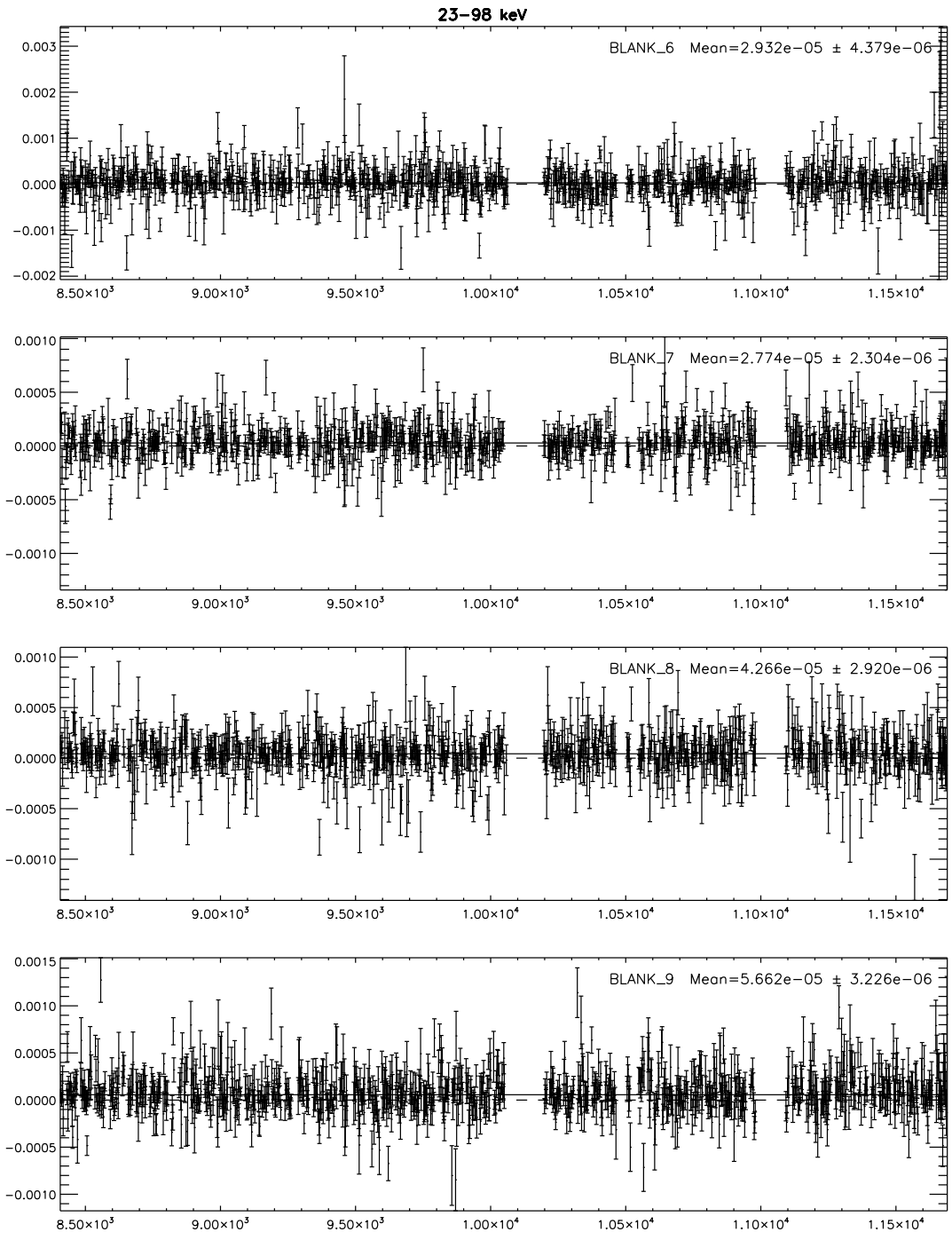

Figure A.1: continued.

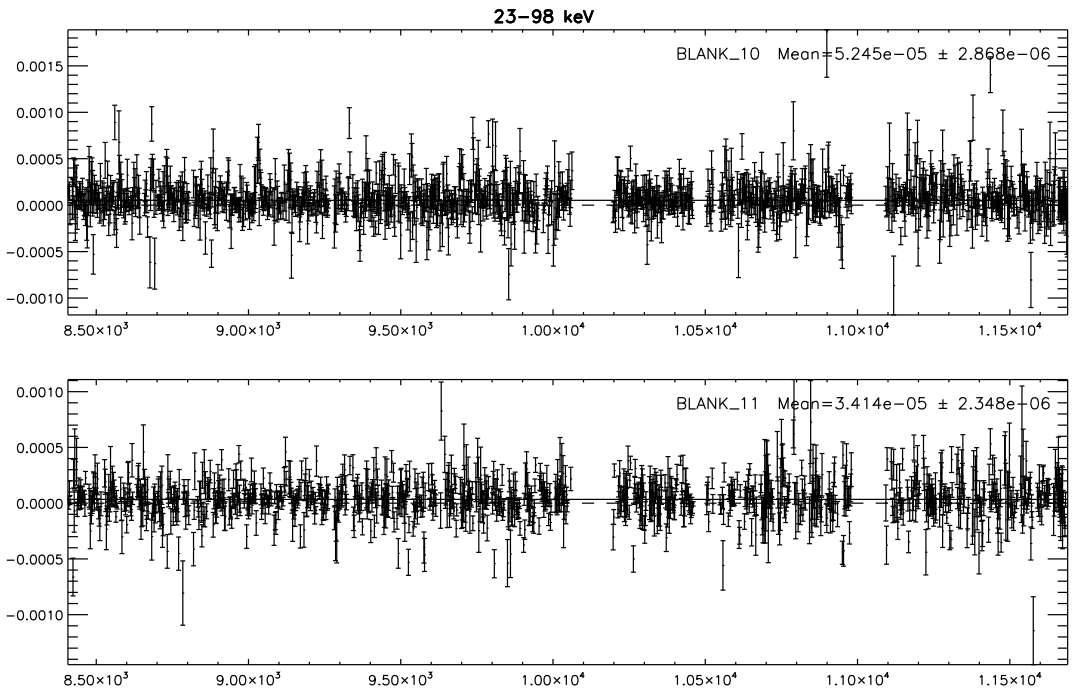

Figure A.1: continued.

Appendix B
EBOP 2013 Spectra for OFF Galactic Plane Sources

Spectra for the OFF Galactic Plane sources. Spectra are shown up to 2 MeV integrated over the full 9 years of the CGRO mission. The Crab spectrum is shown for comparison. Parameters are shown for the best fit to either a power law, broken power law, or Compton spectrum.

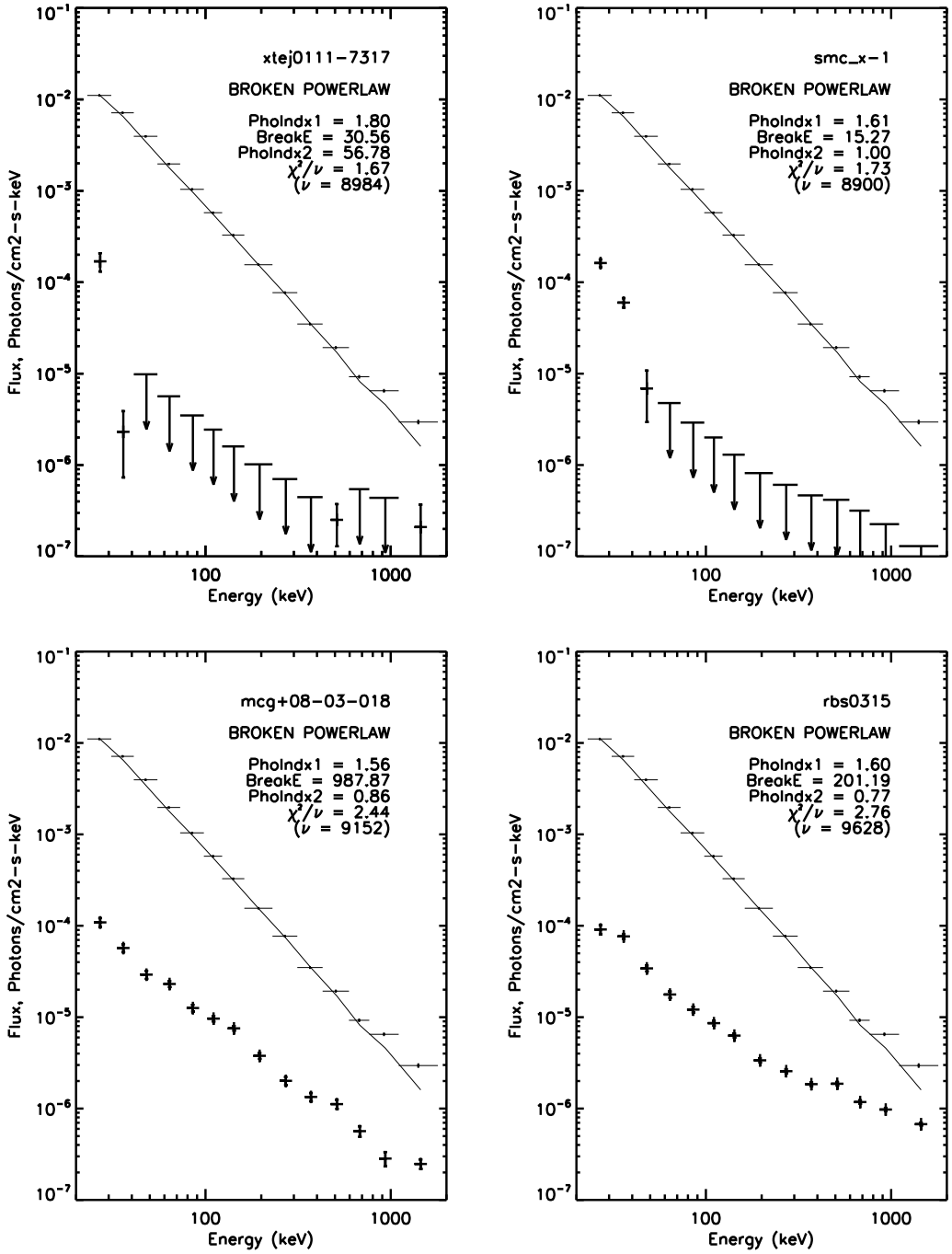

Figure B.1: EBOP 2013 spectra for OFF Galactic Plane sources.

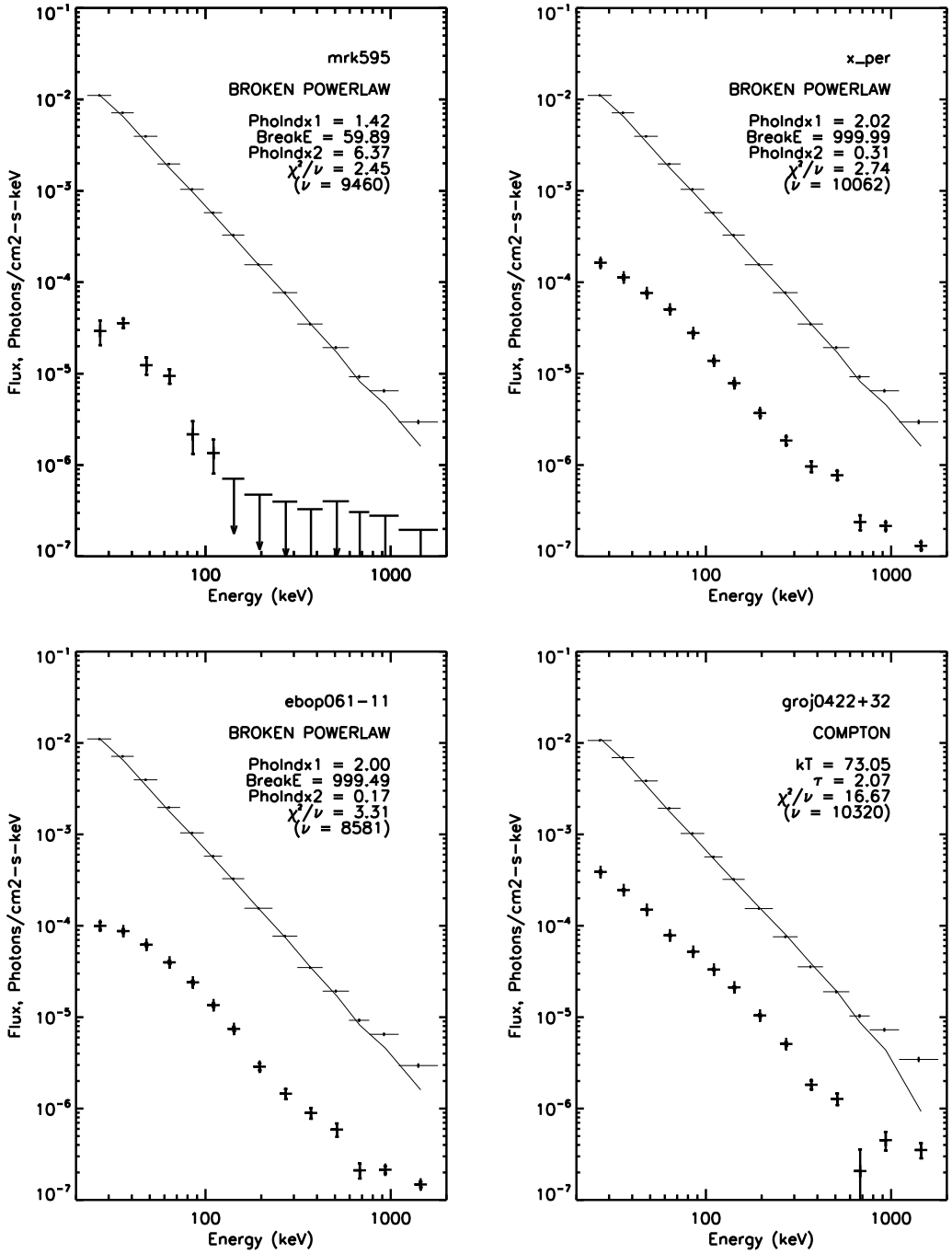

Figure B.1: continued.

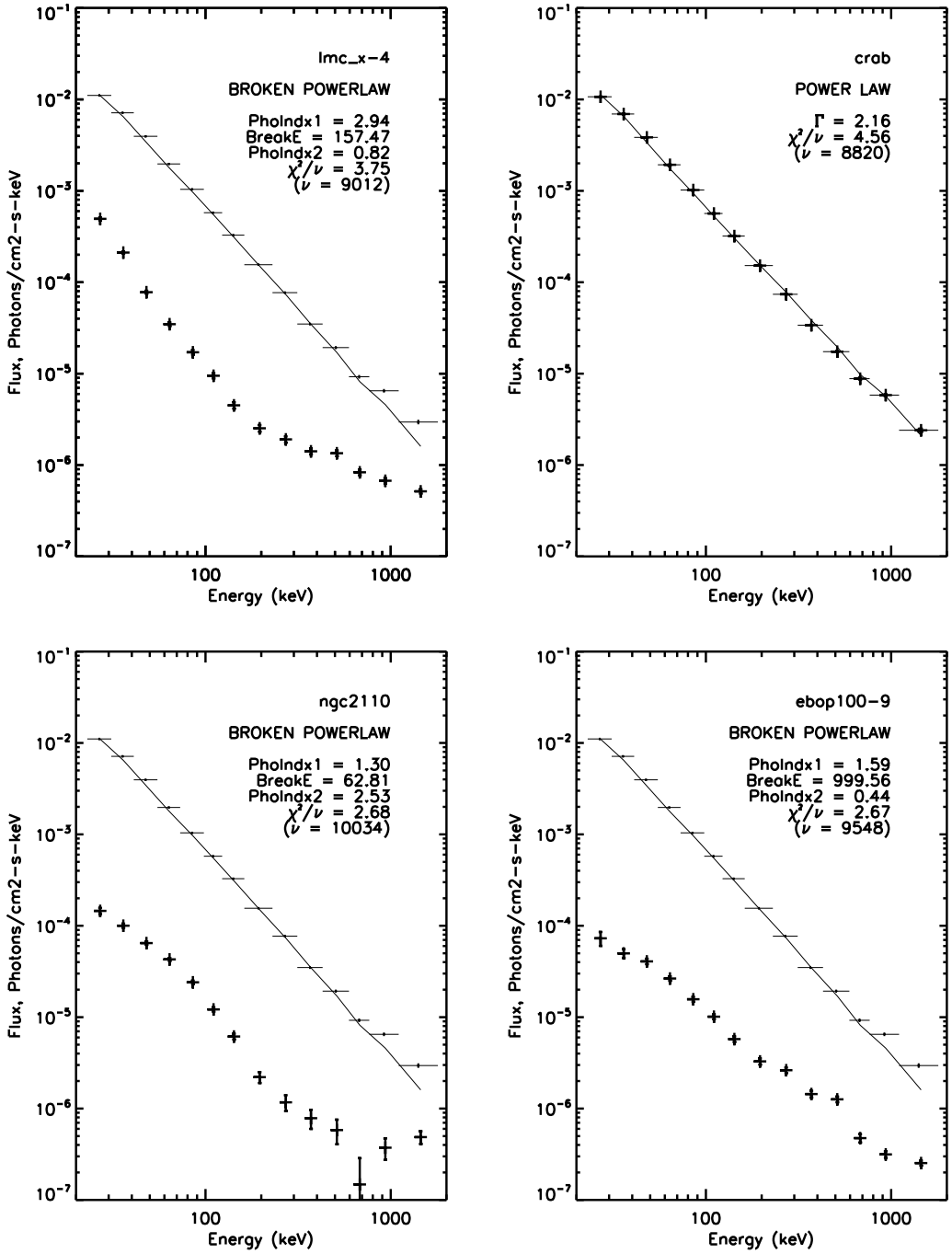

Figure B.1: continued.

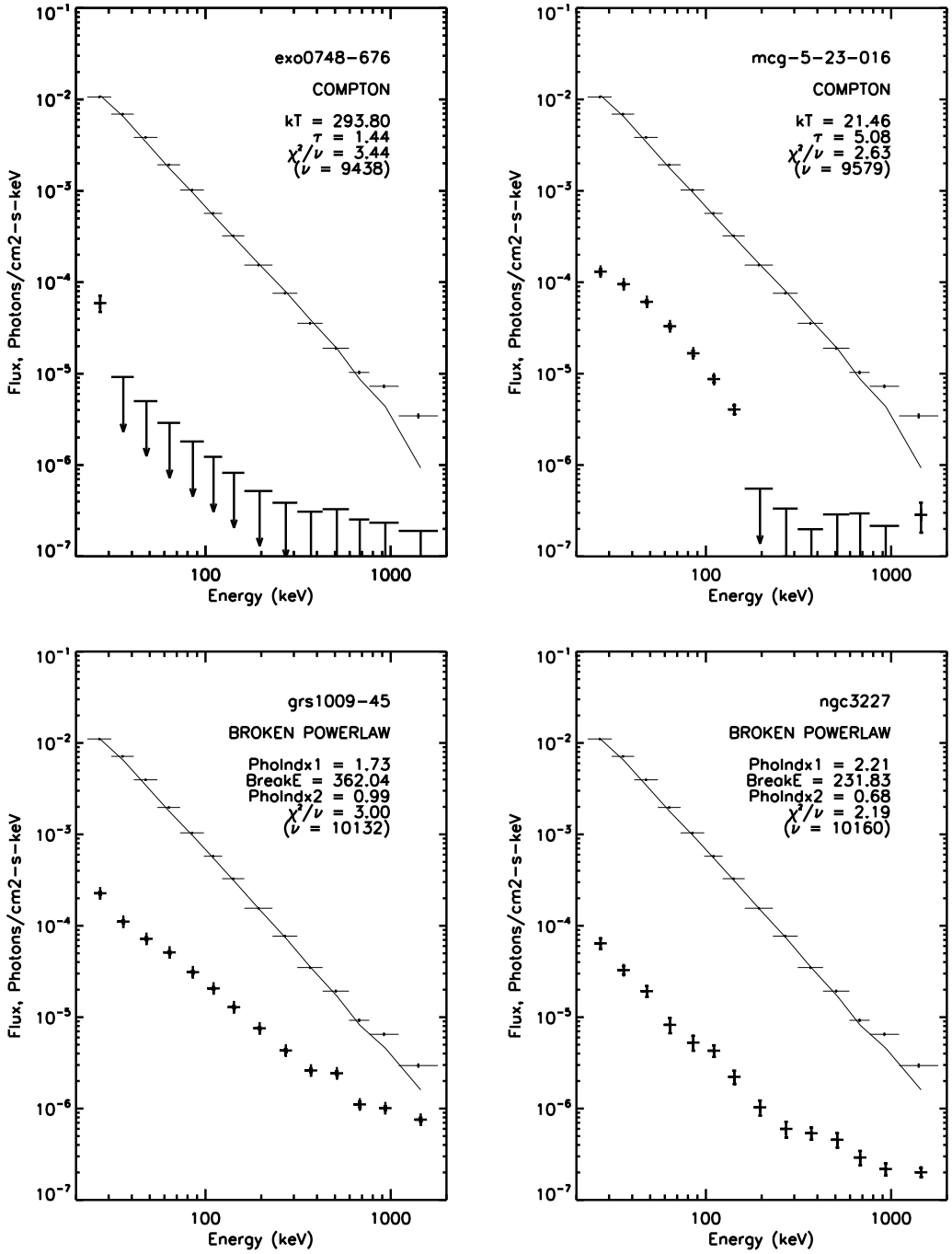

Figure B.1: continued.

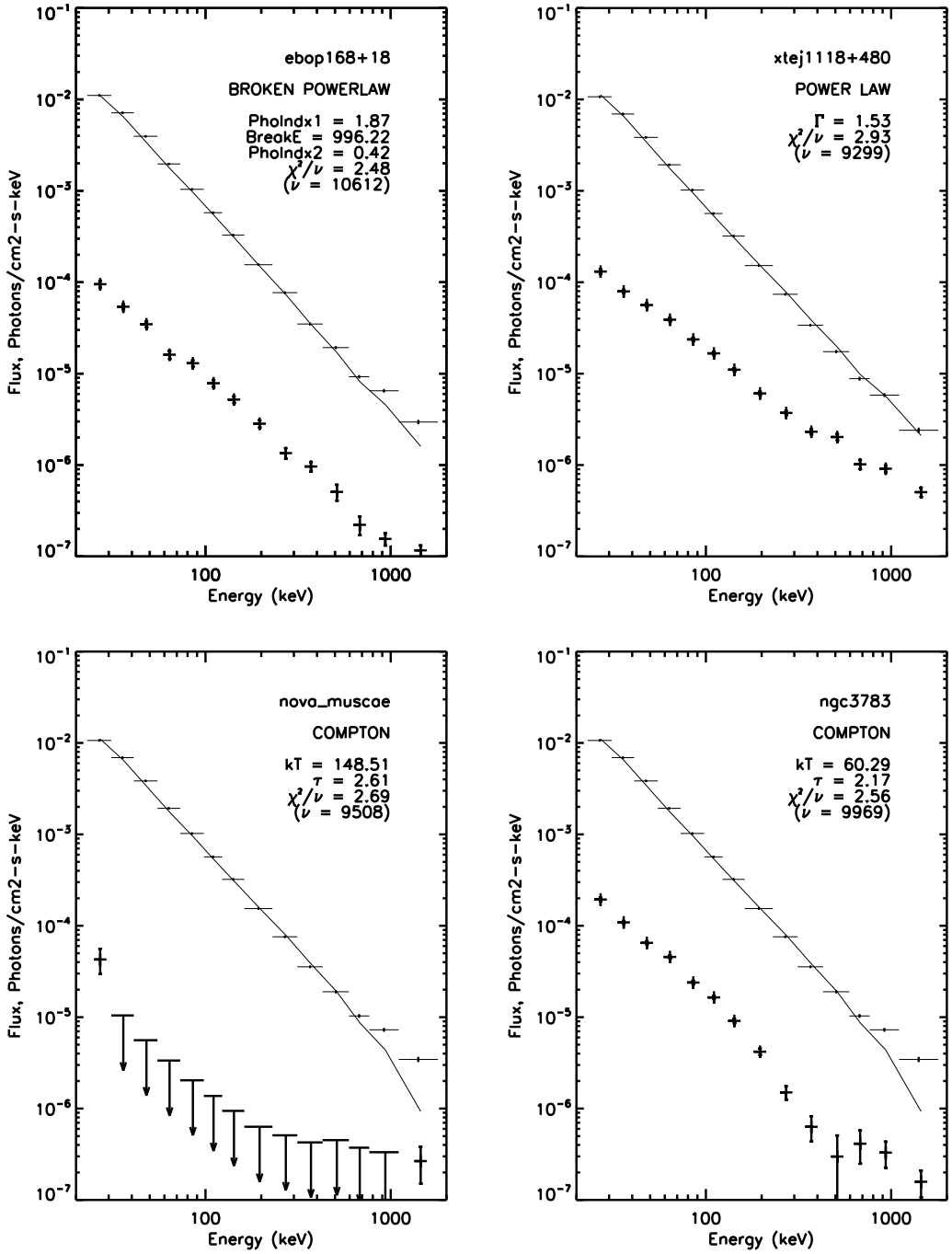

Figure B.1: continued.

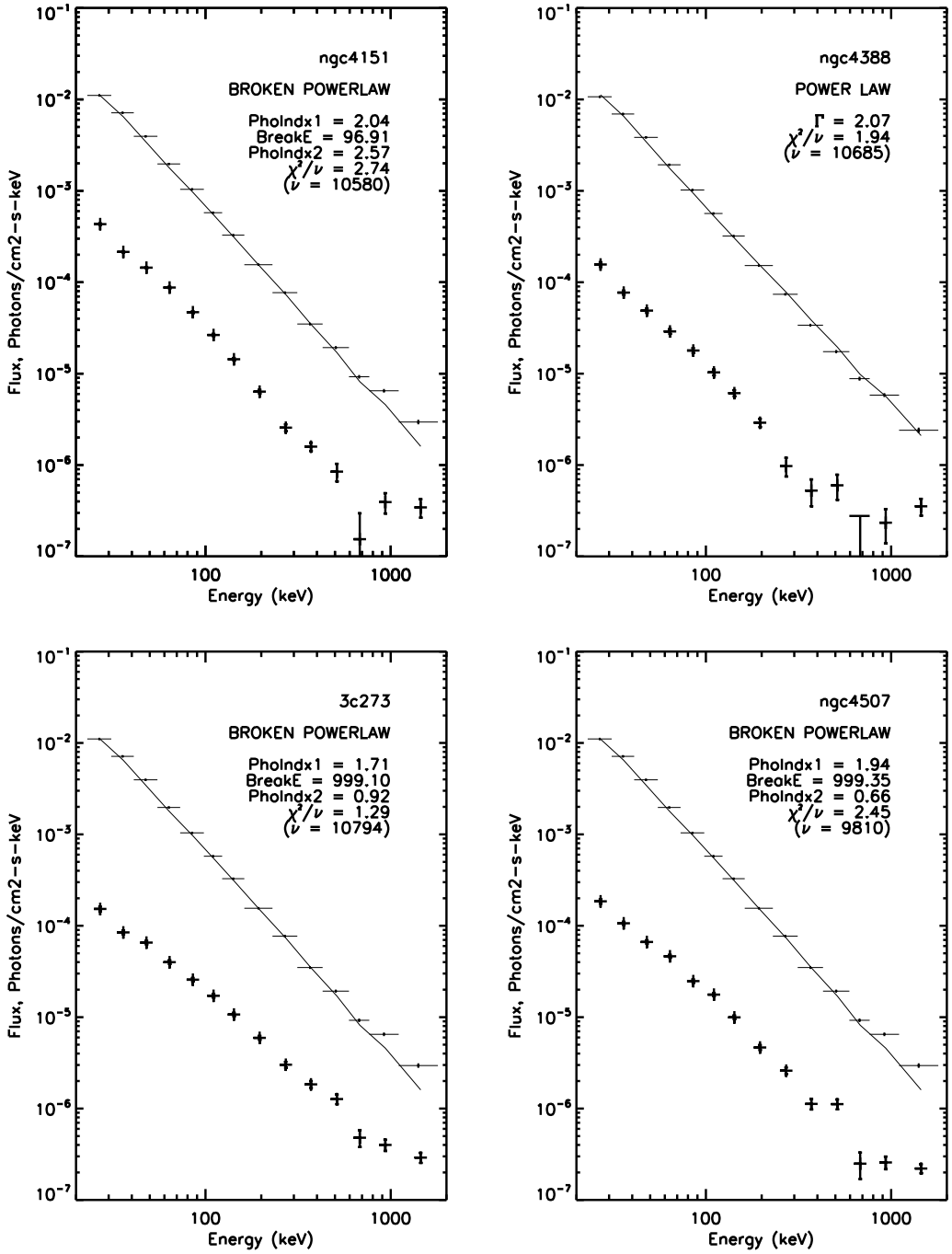

Figure B.1: continued.

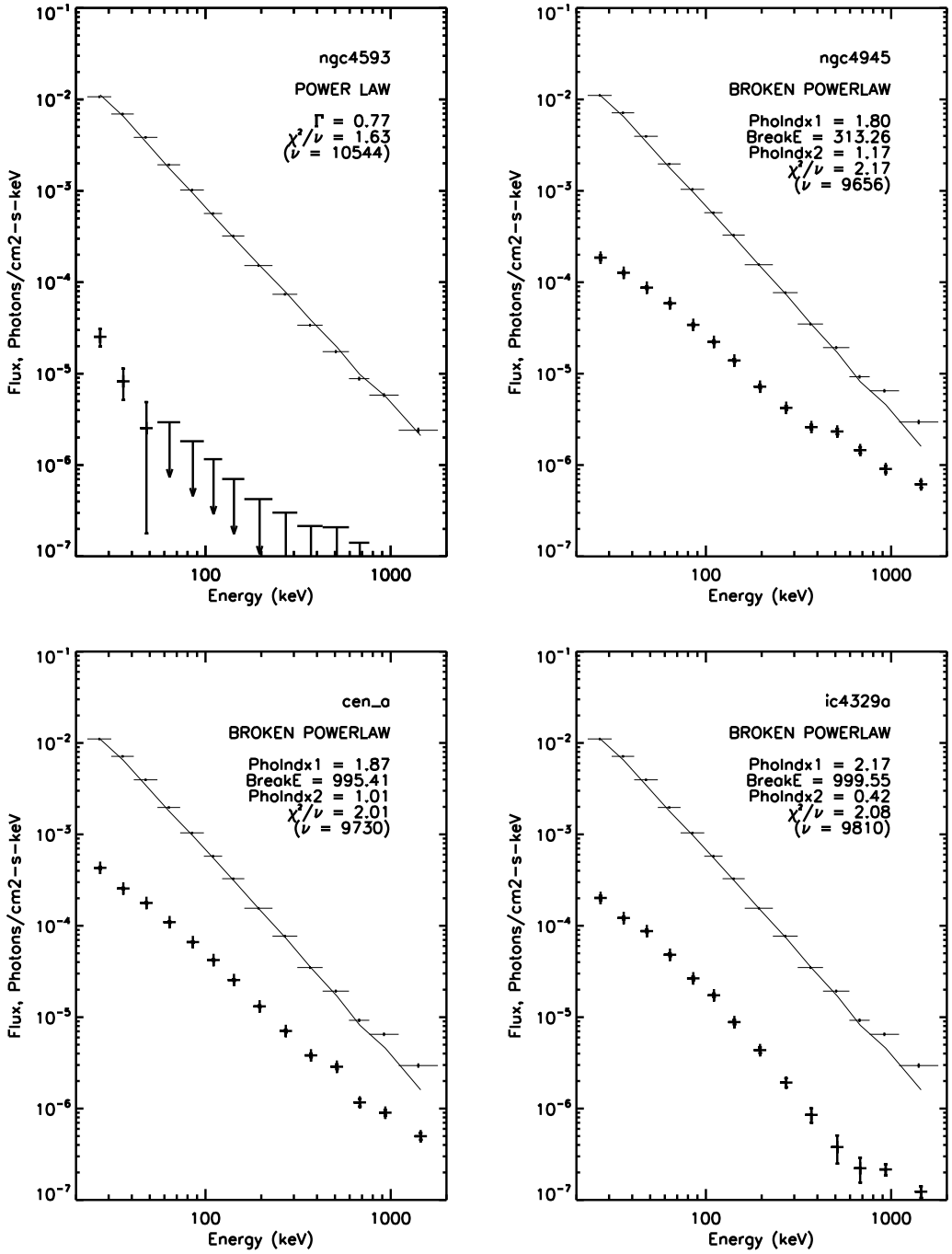

Figure B.1: continued.

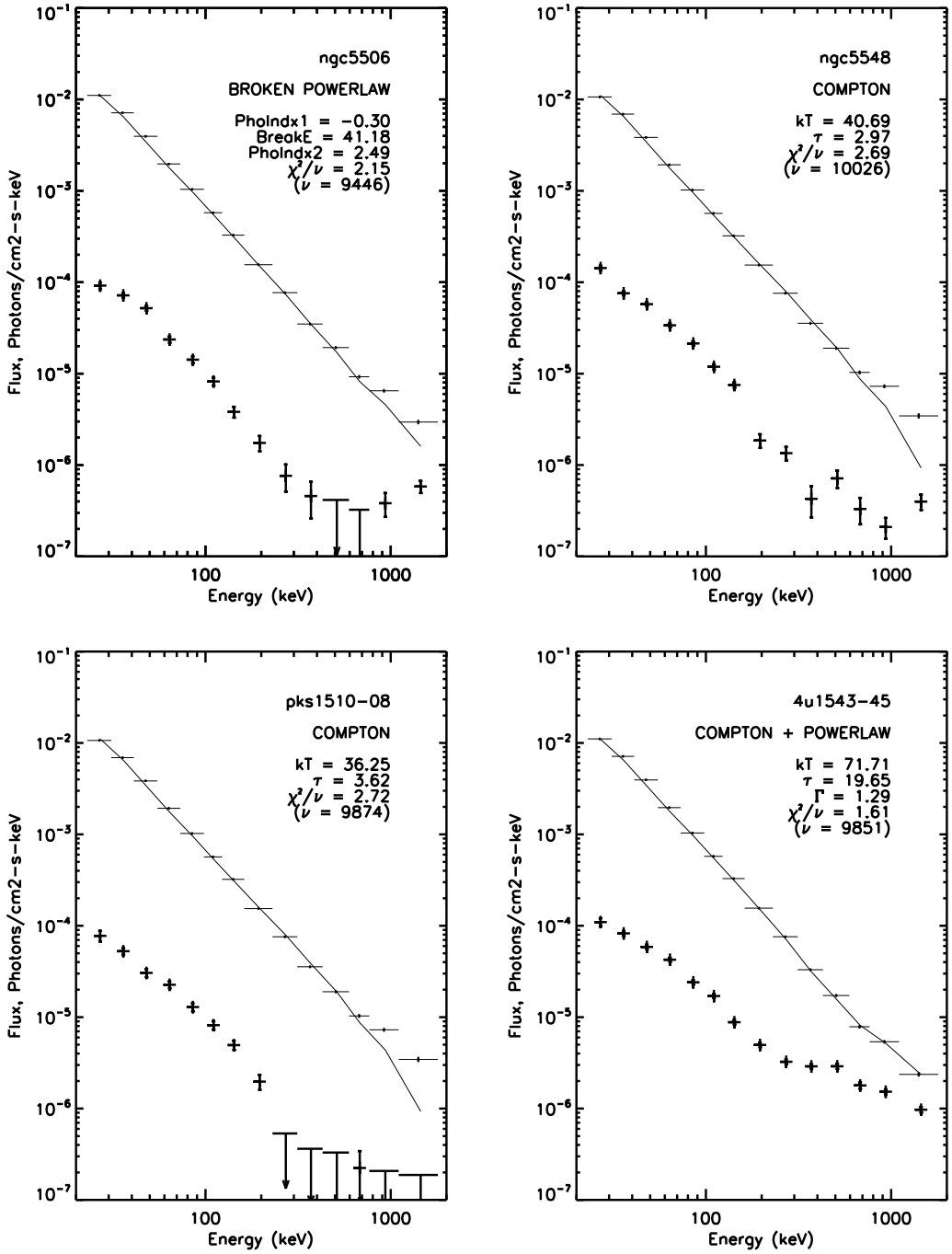

Figure B.1: continued.

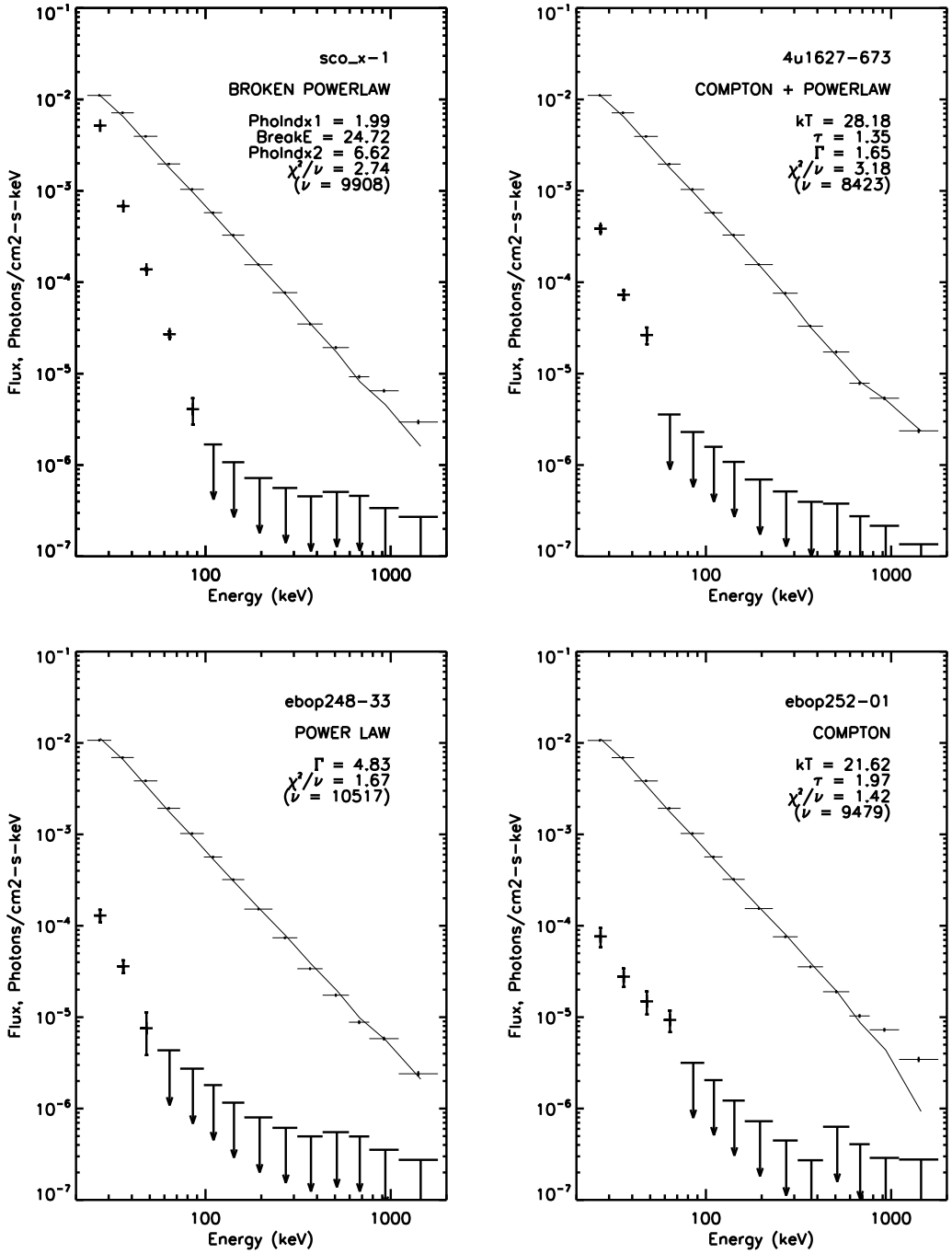

Figure B.1: continued.

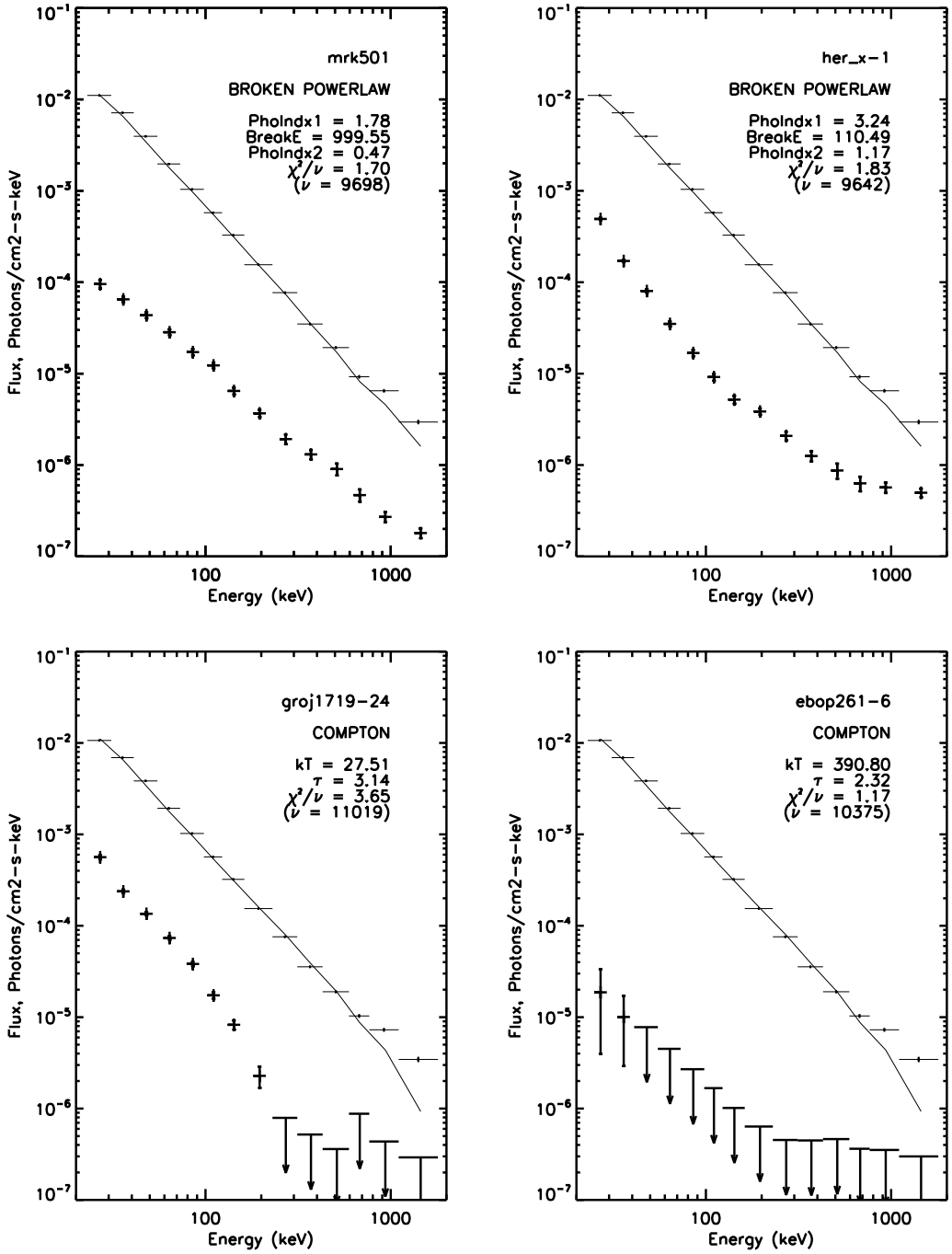

Figure B.1: continued.

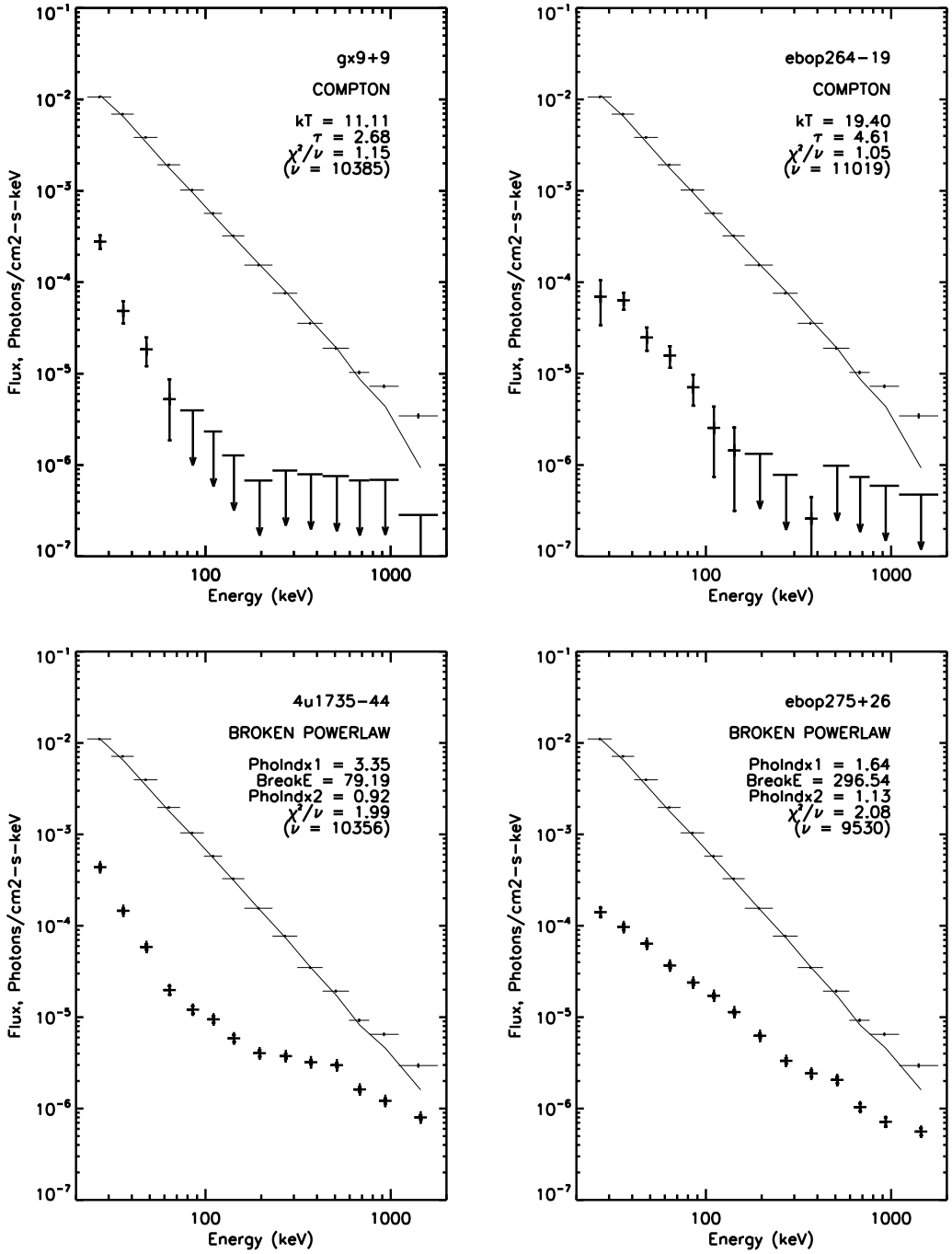

Figure B.1: continued.

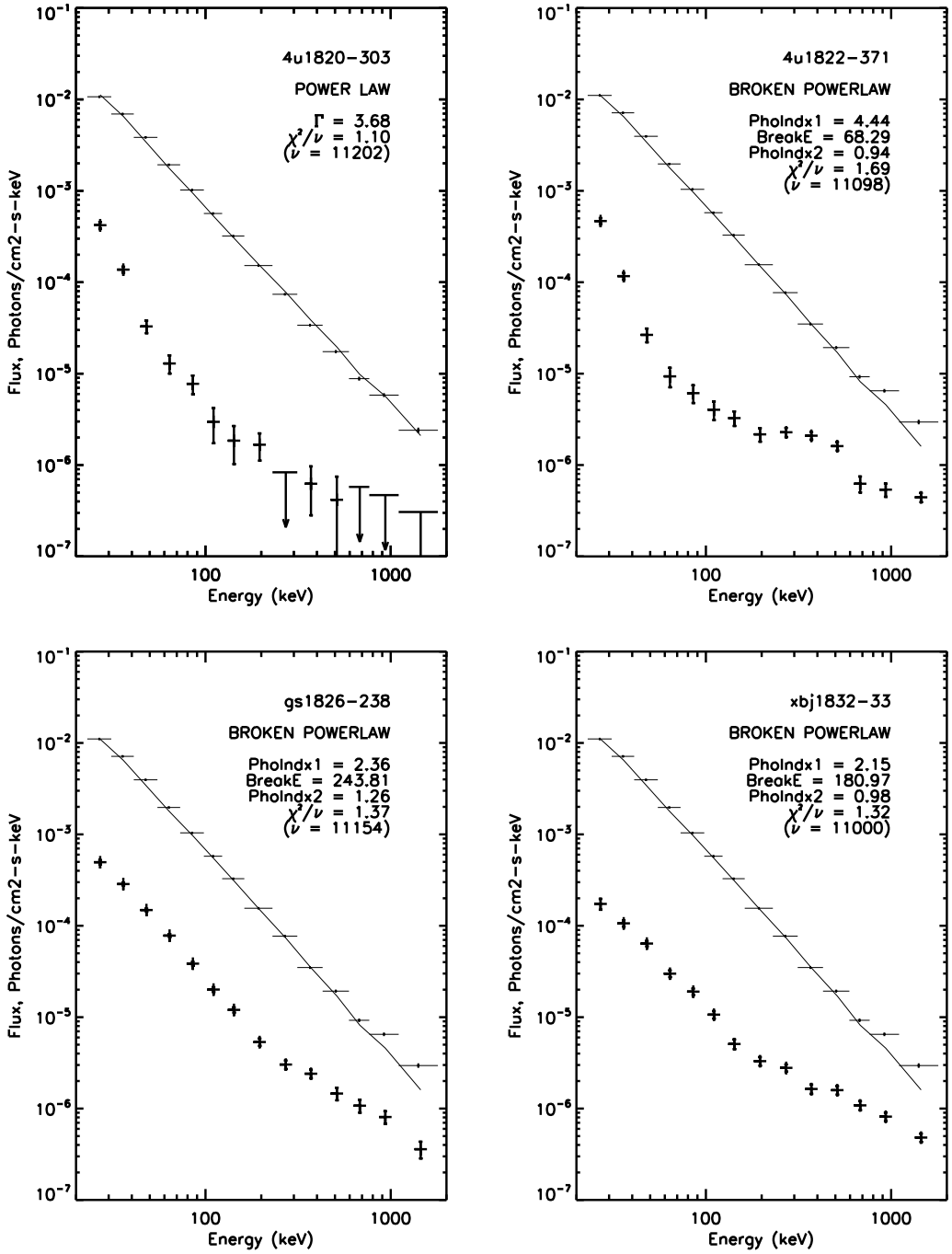

Figure B.1: continued.

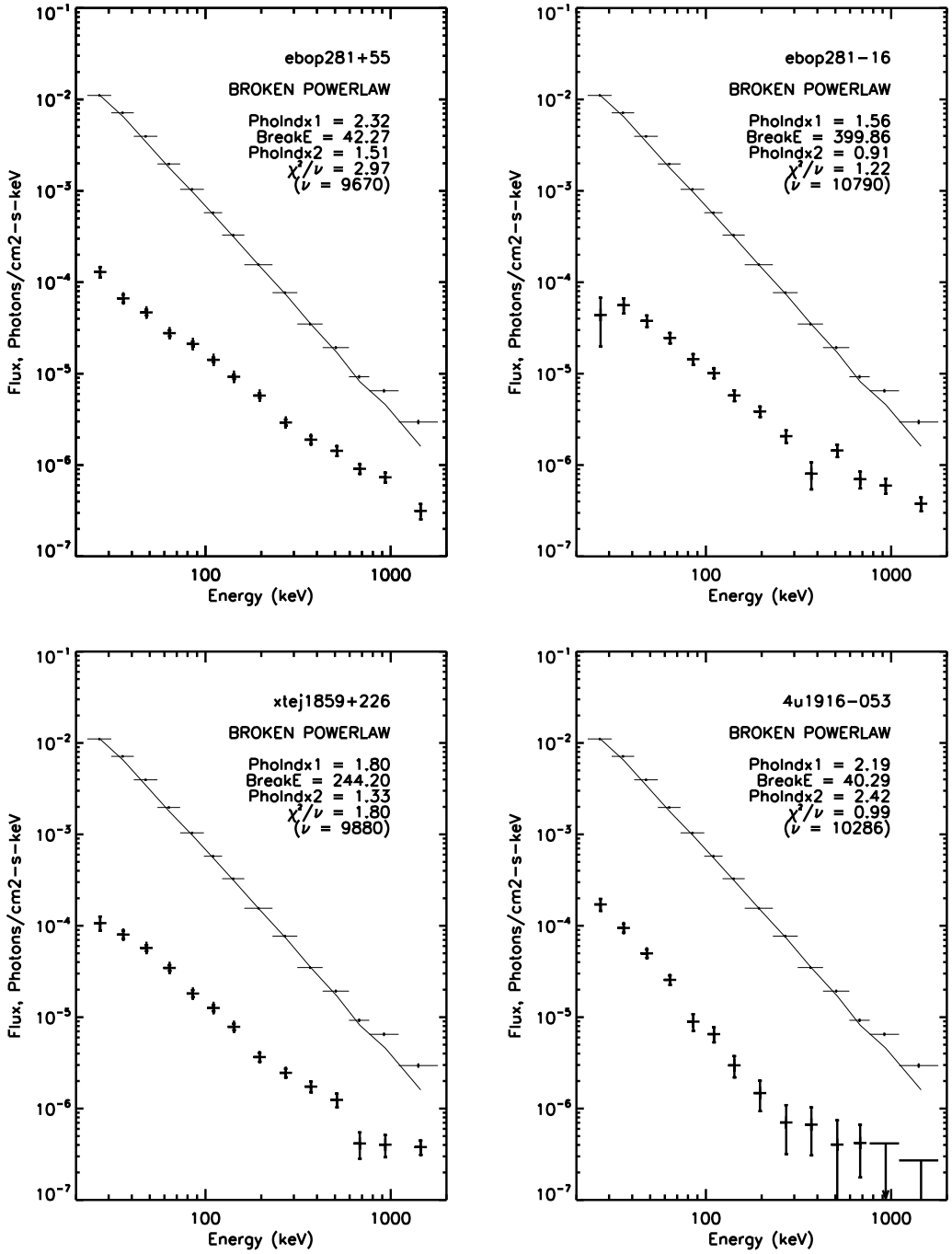

Figure B.1: continued.

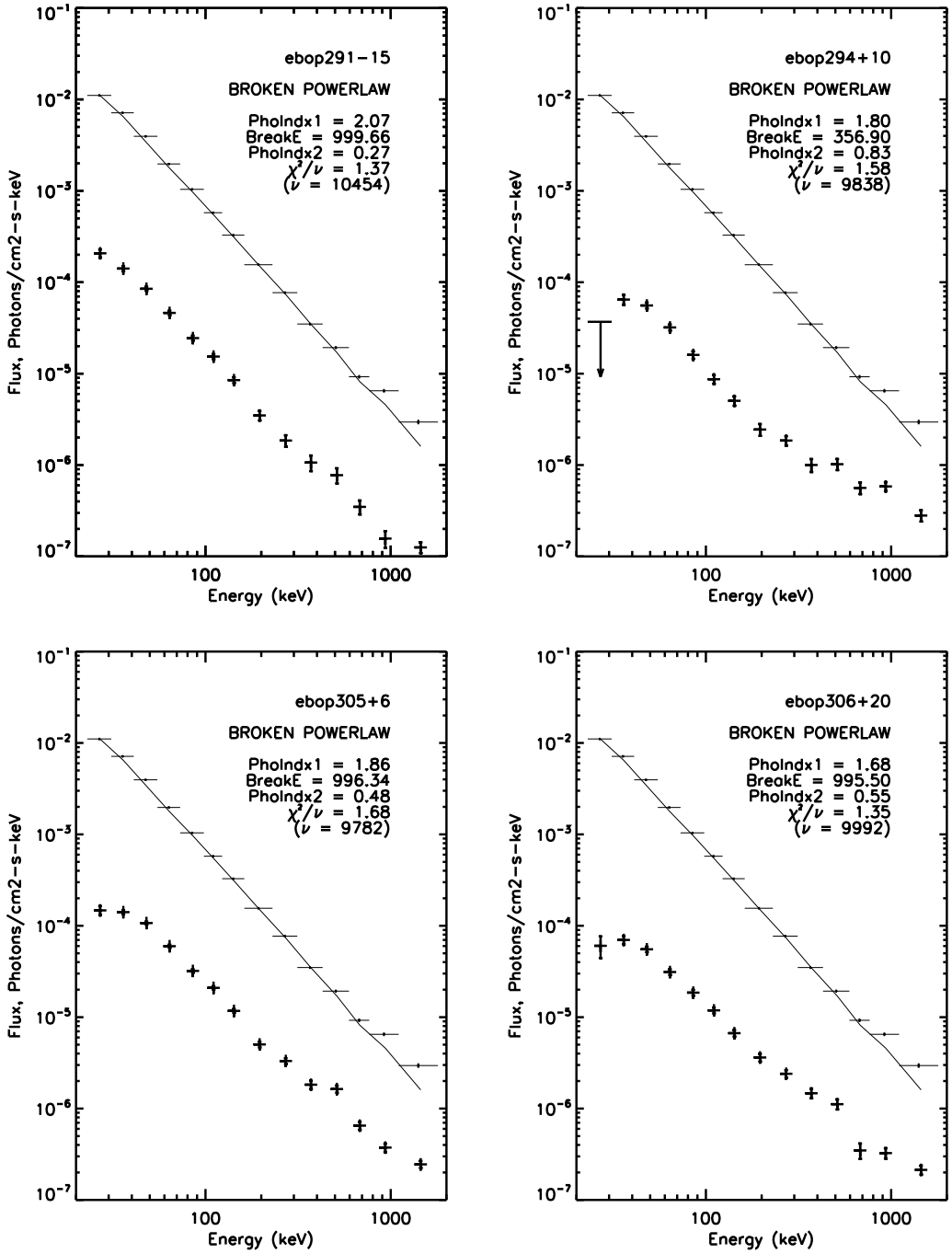

Figure B.1: continued.

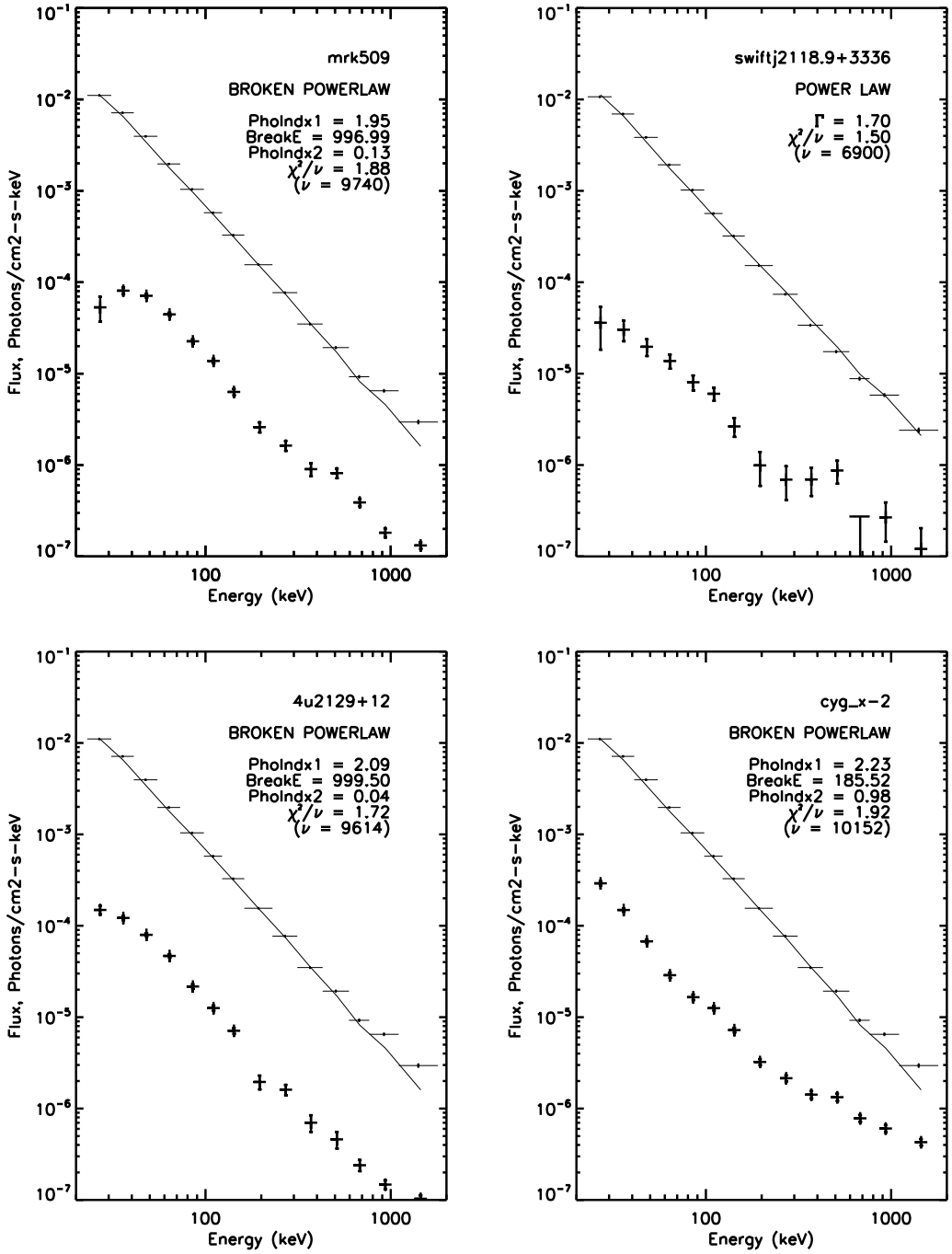

Figure B.1: continued.

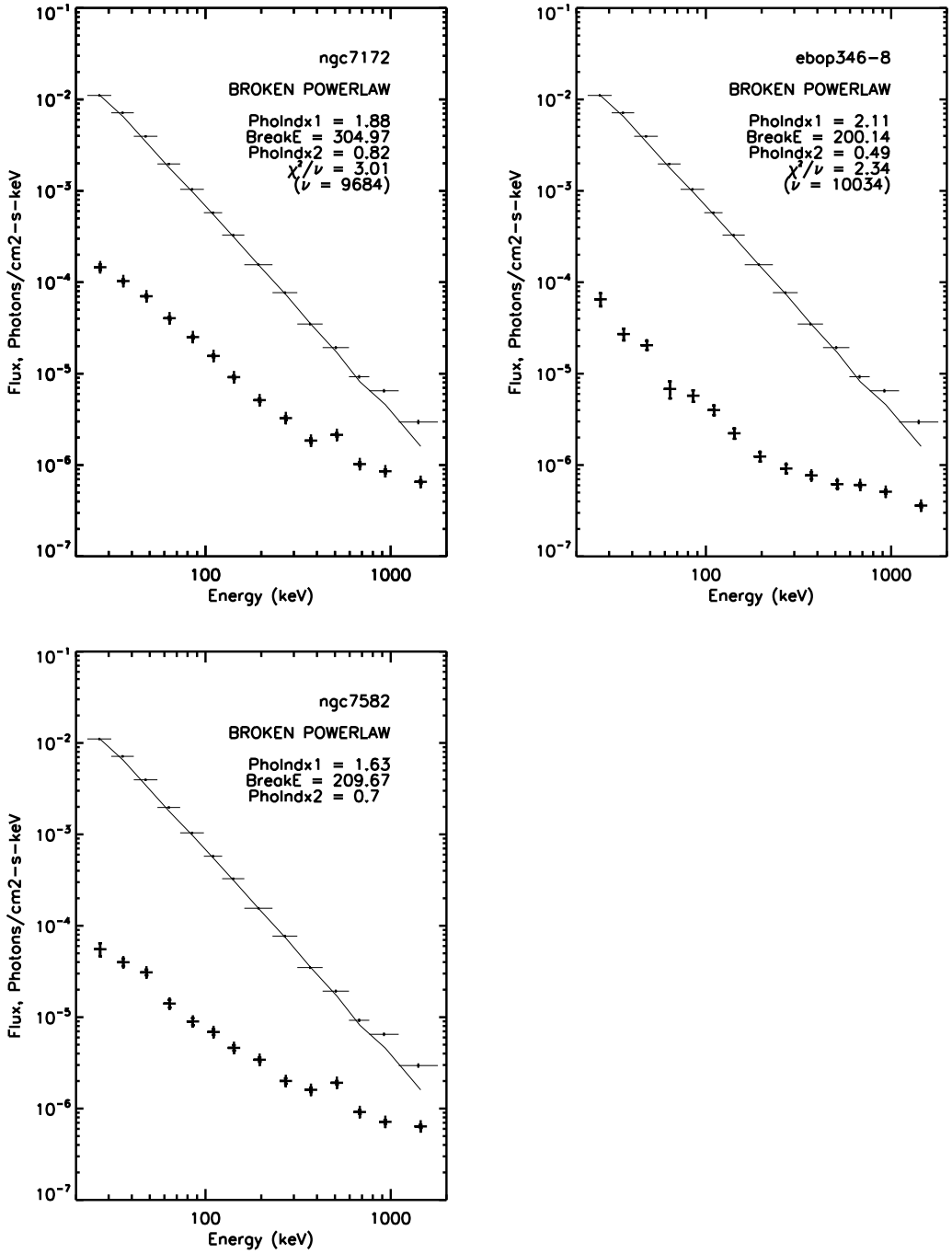

Figure B.1: continued.

Appendix C
EBOP 2013 Spectra for ON Galactic Plane Sources

Spectra for the ON Galactic Plane sources. Spectra are shown up to 300 keV integrated over the full 9 years of the CGRO mission, without blank source background subtraction. The Crab spectrum is shown for comparison. Parameters are shown for the best fit to either a power law, broken power law, or Compton spectrum.

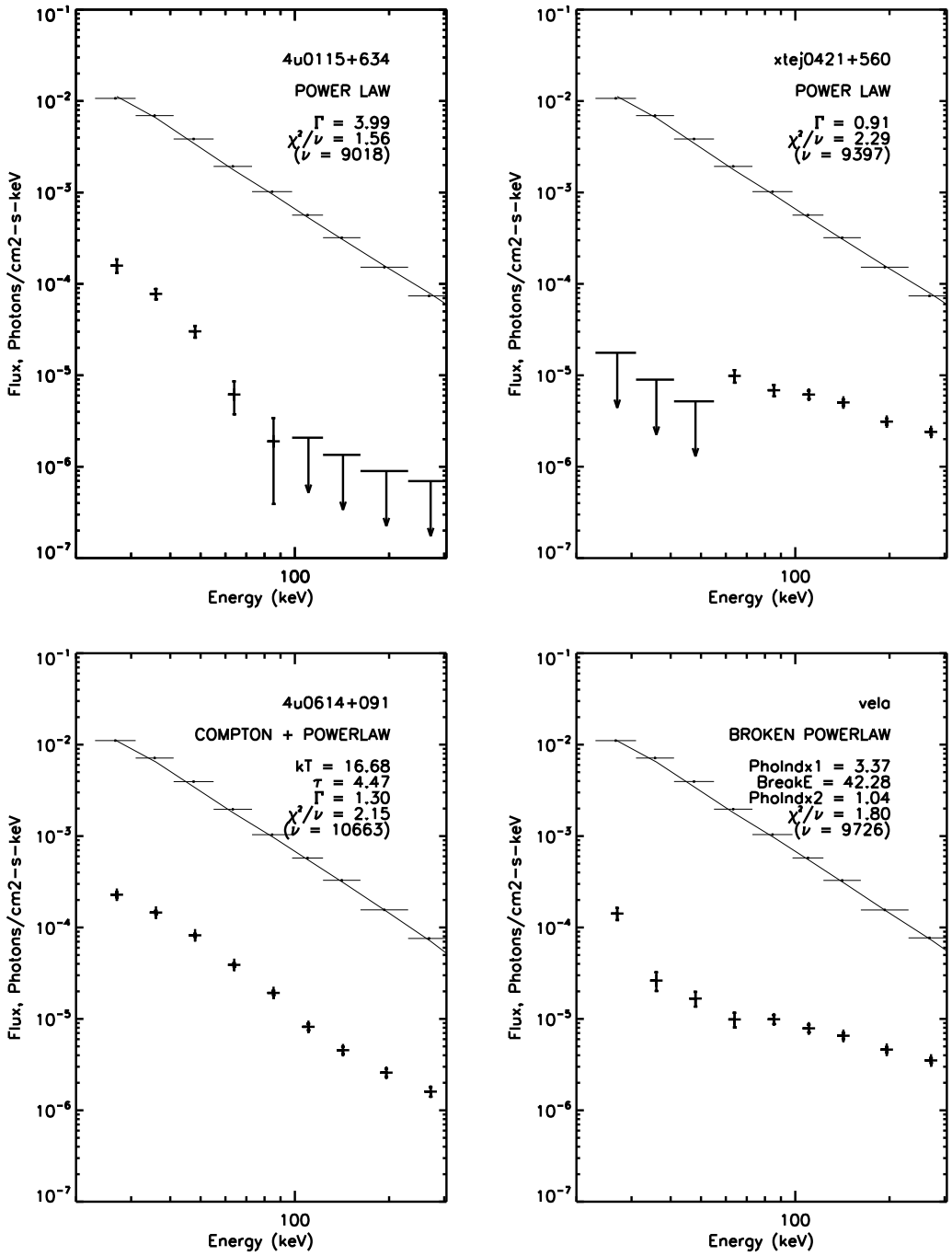

Figure C.1: EBOP 2013 spectra for ON Galactic Plane sources before blank sources subtraction.

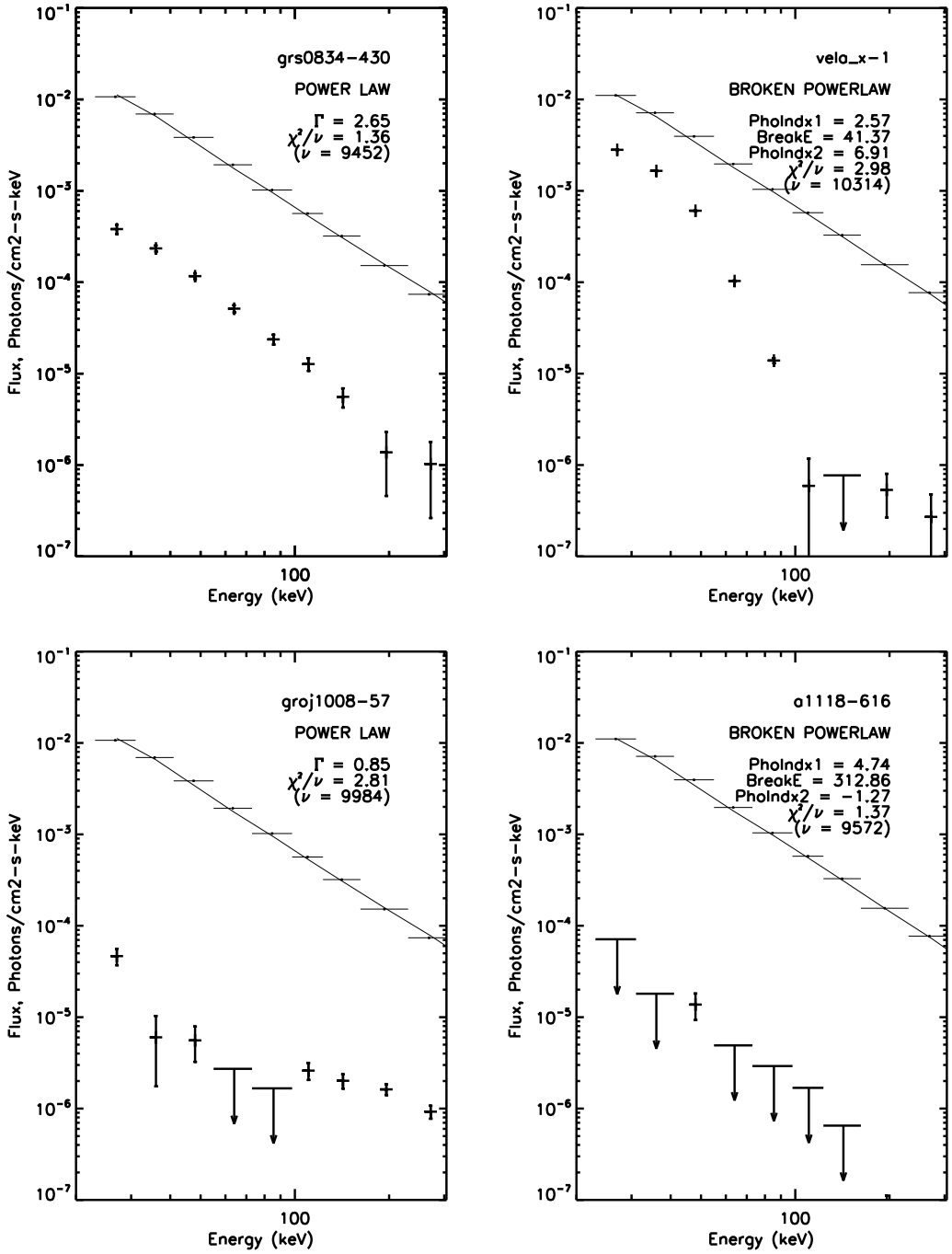

Figure C.1: continued.

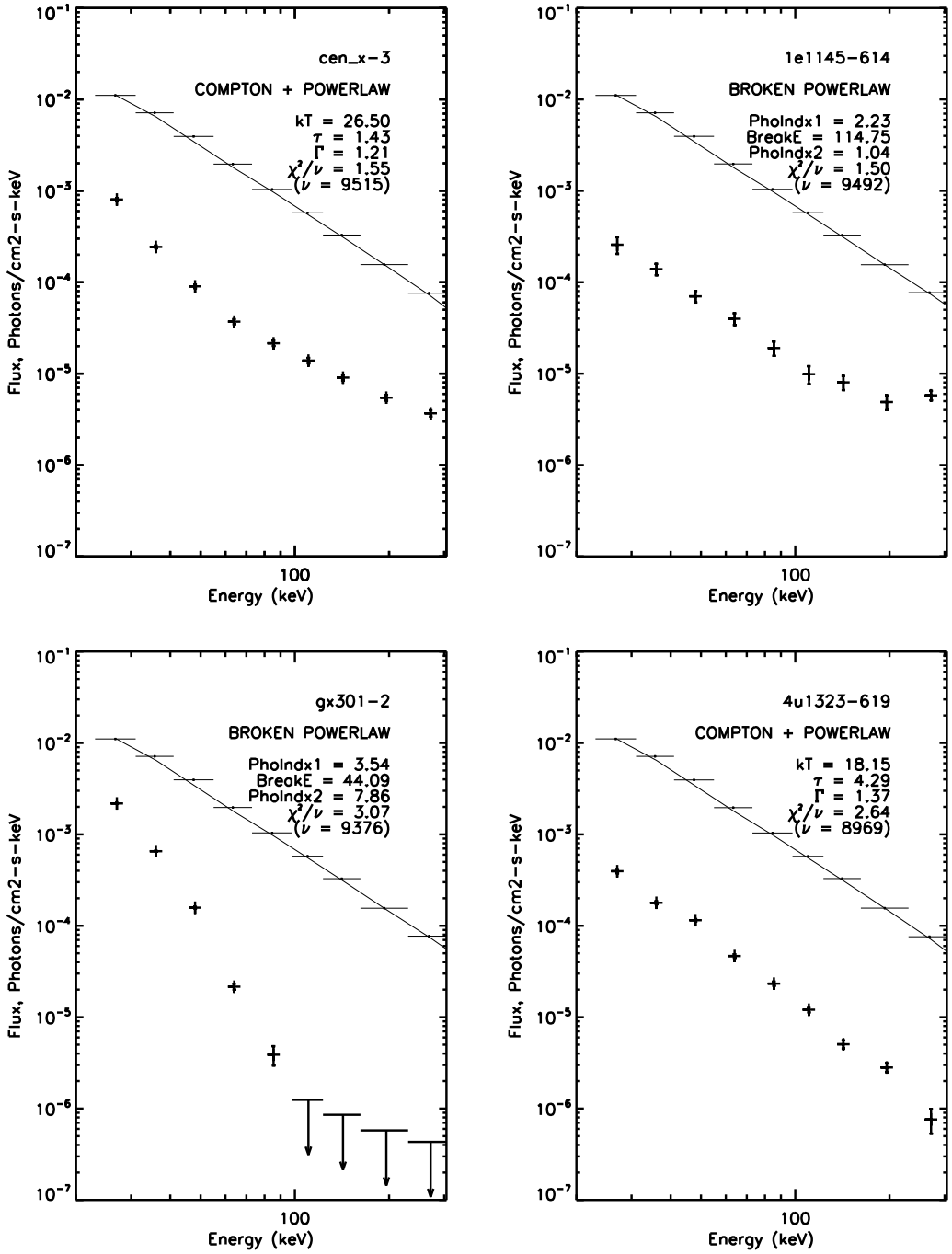

Figure C.1: continued.

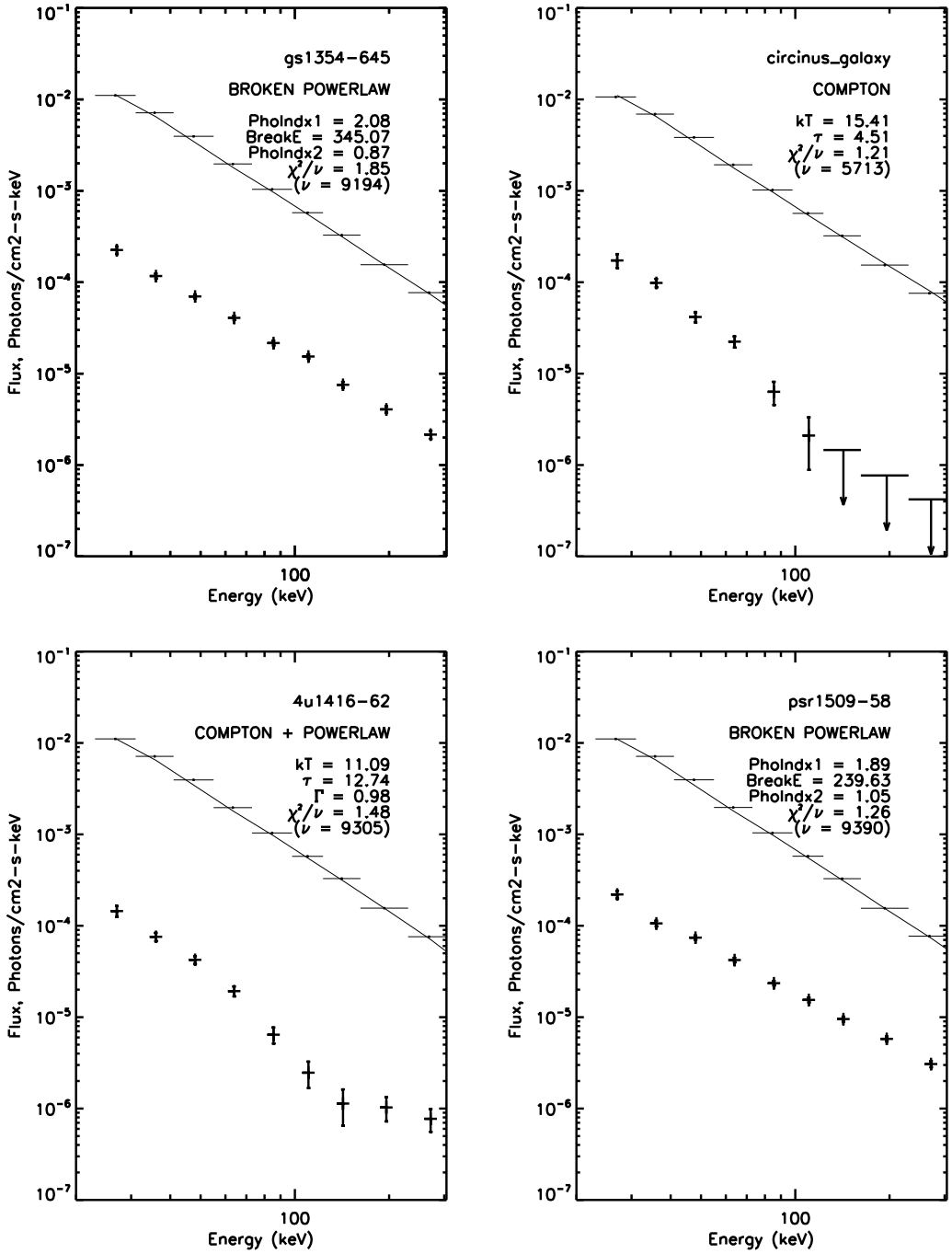

Figure C.1: continued.

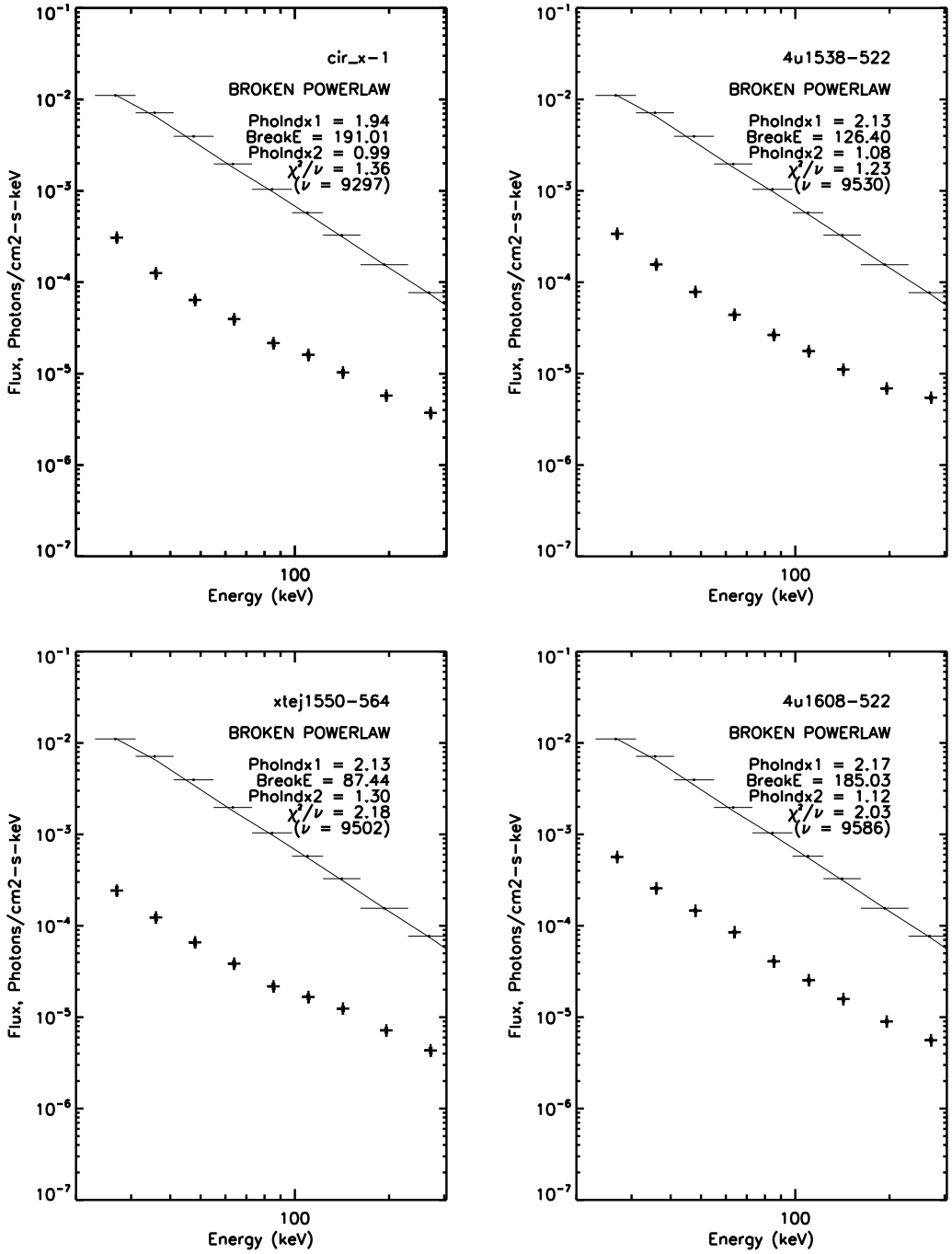

Figure C.1: continued.

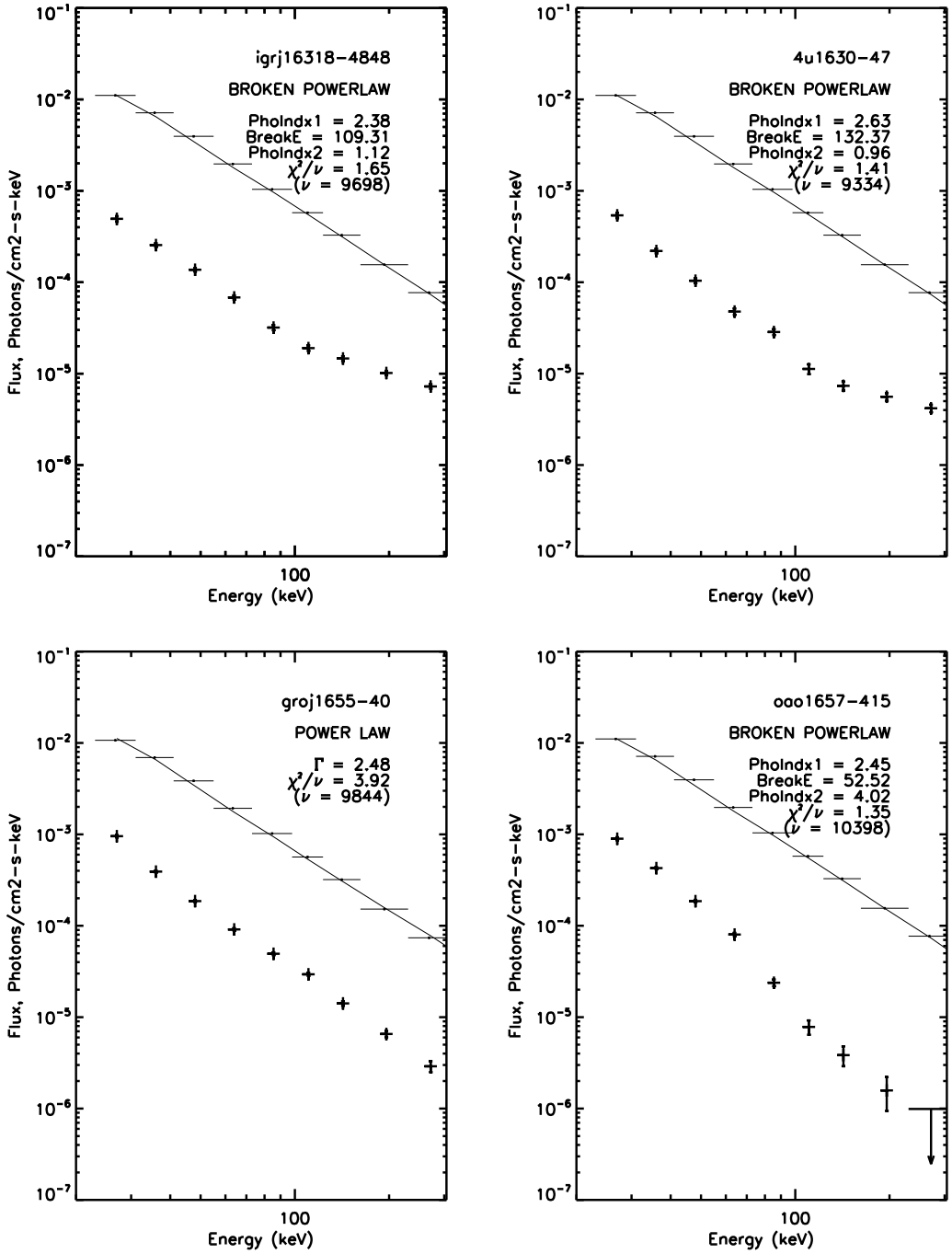

Figure C.1: continued.

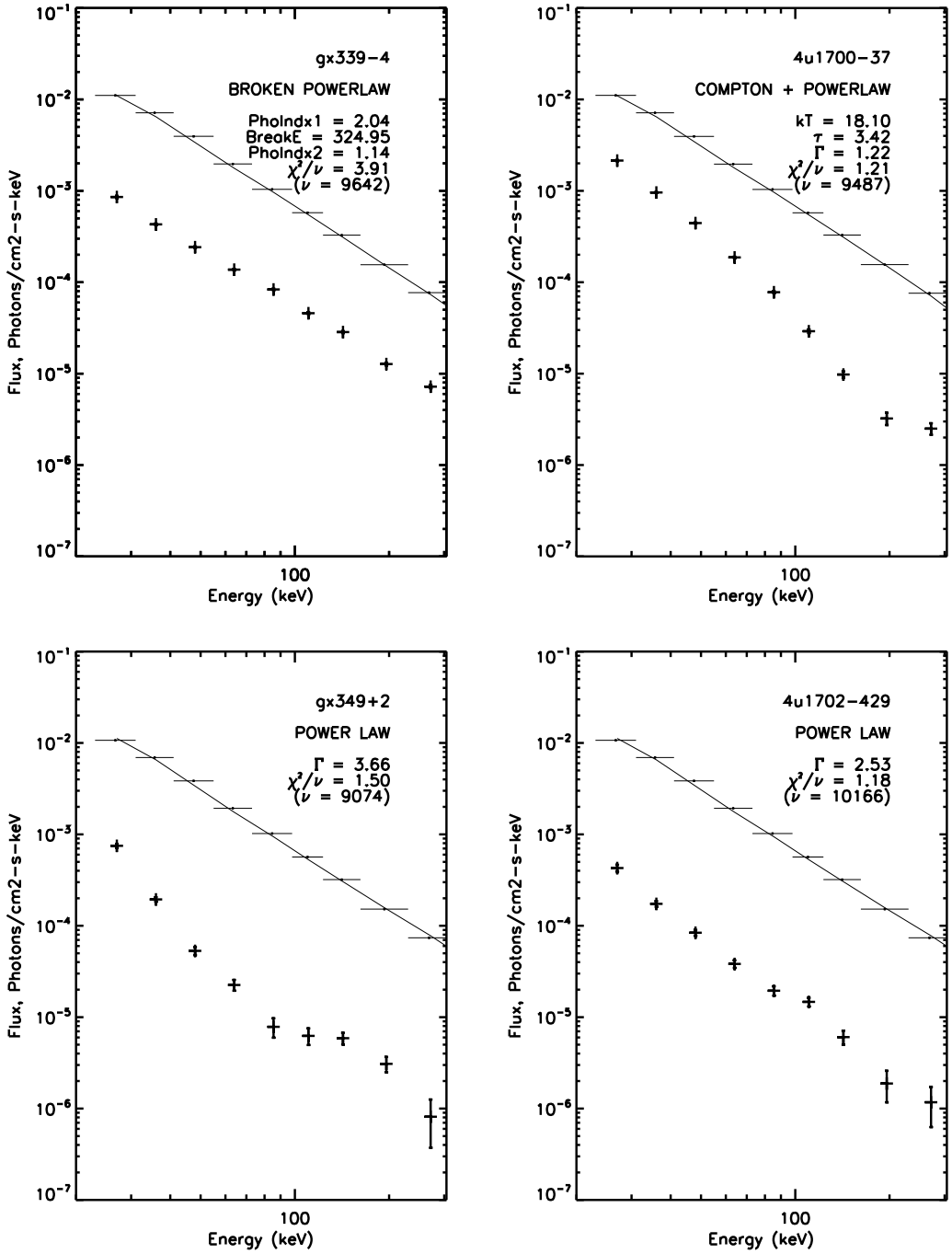

Figure C.1: continued.

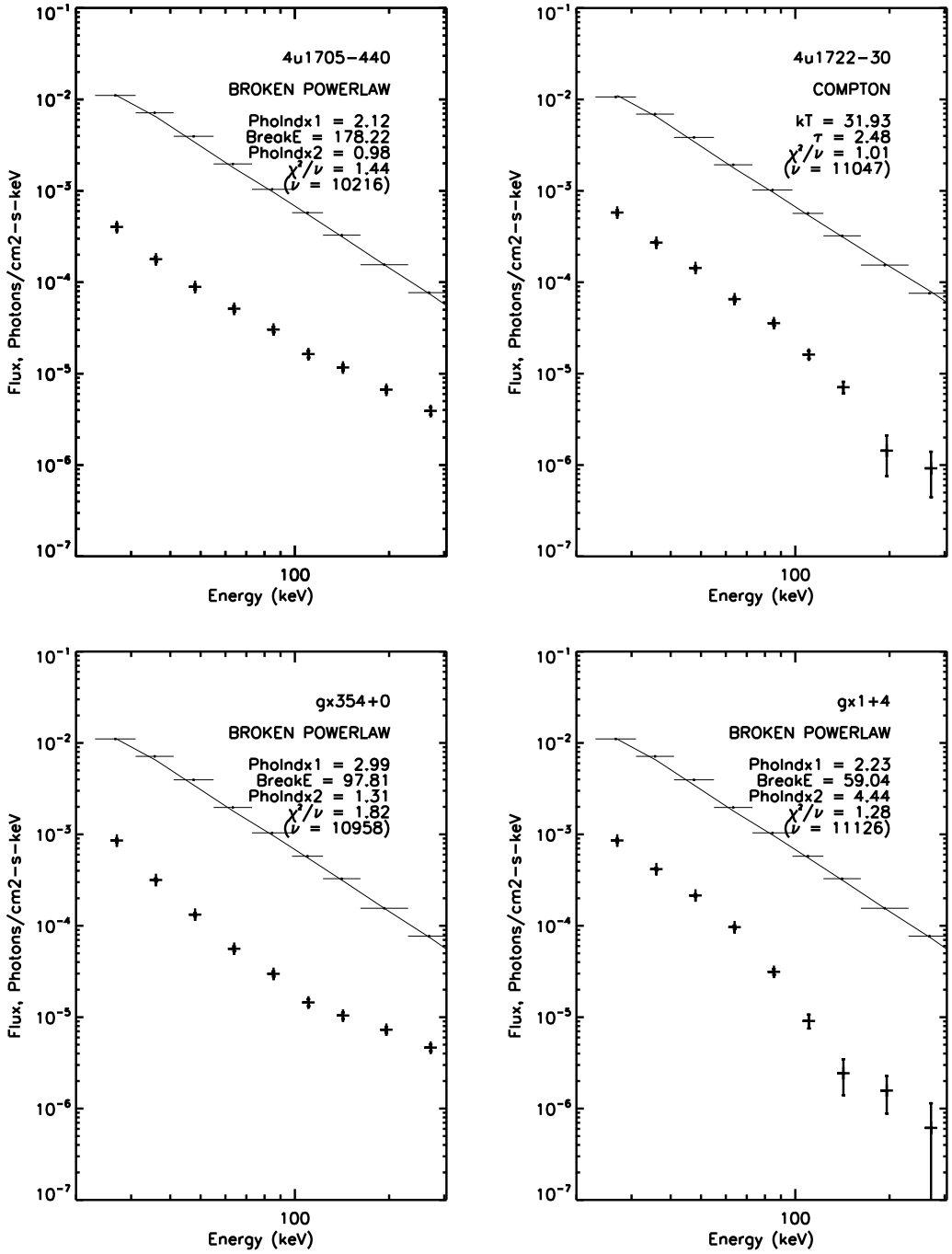

Figure C.1: continued.

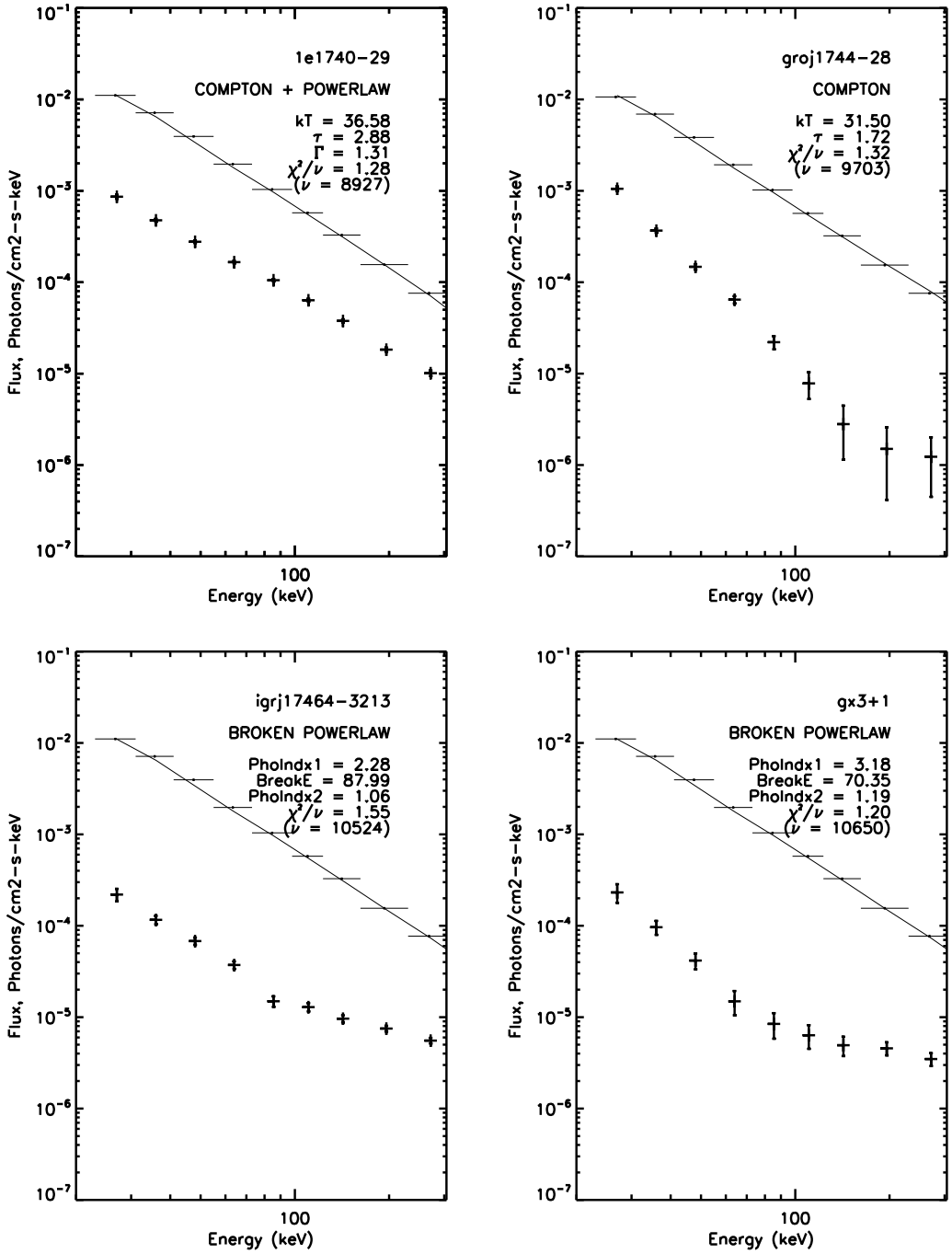

Figure C.1: continued.

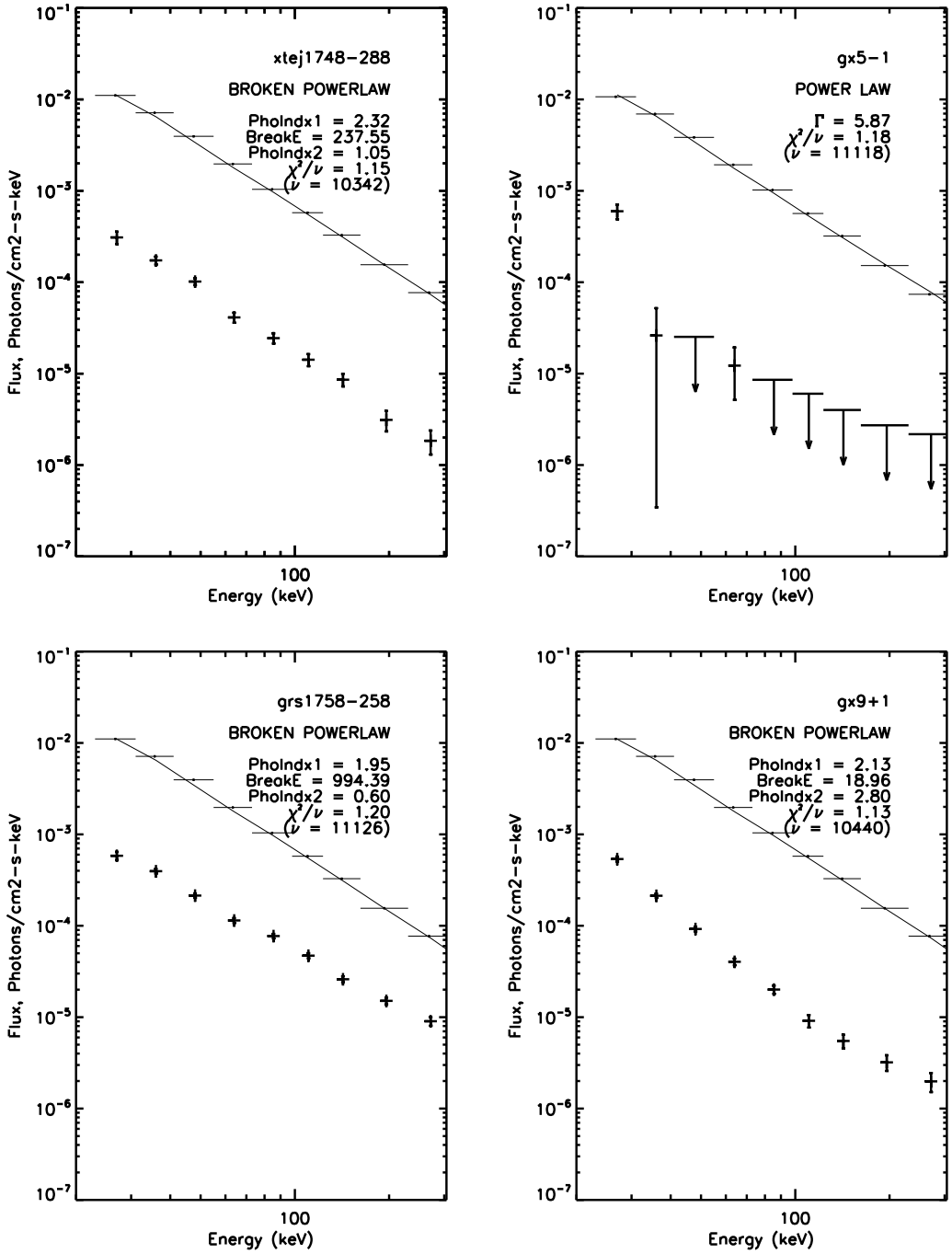

Figure C.1: continued.

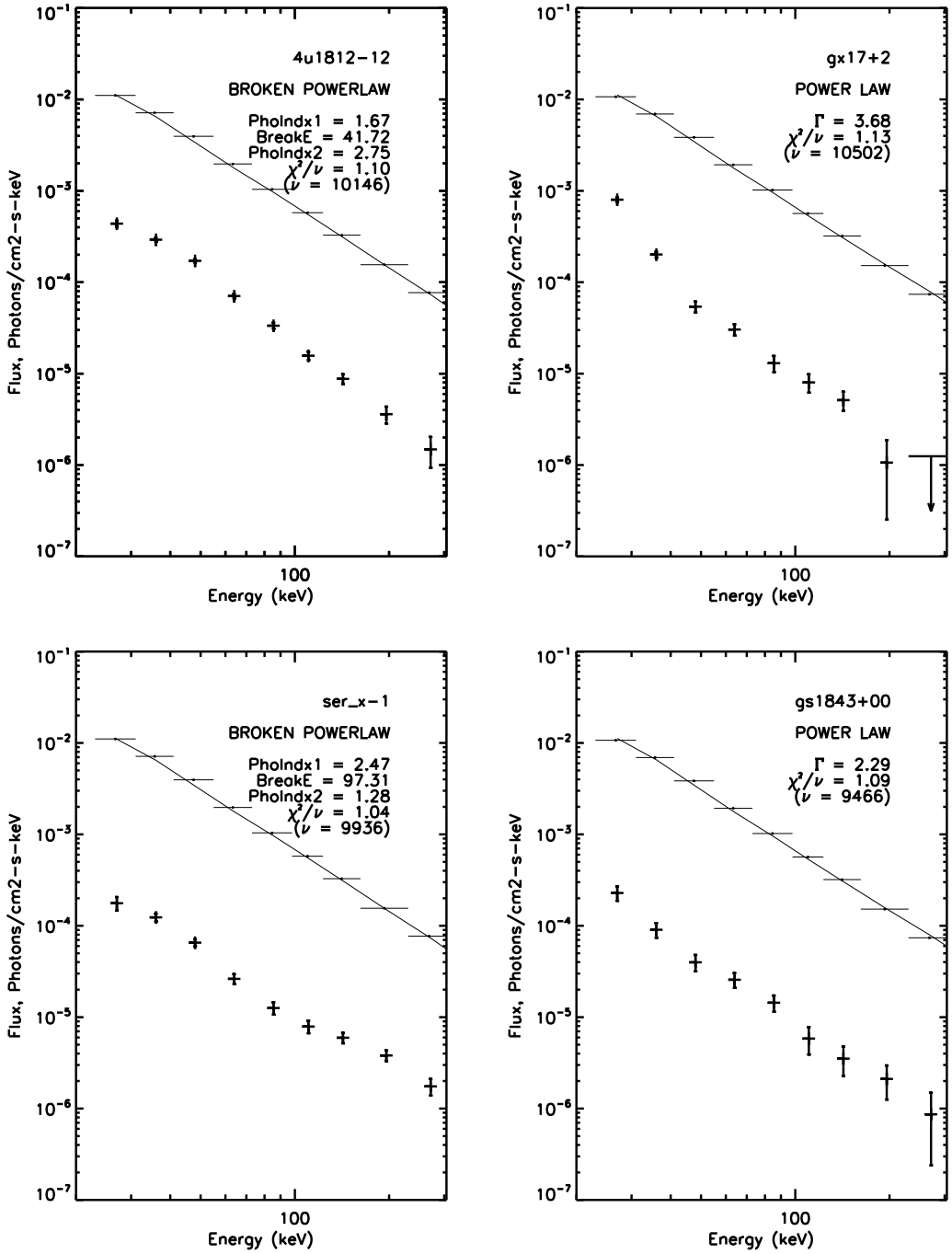

Figure C.1: continued.

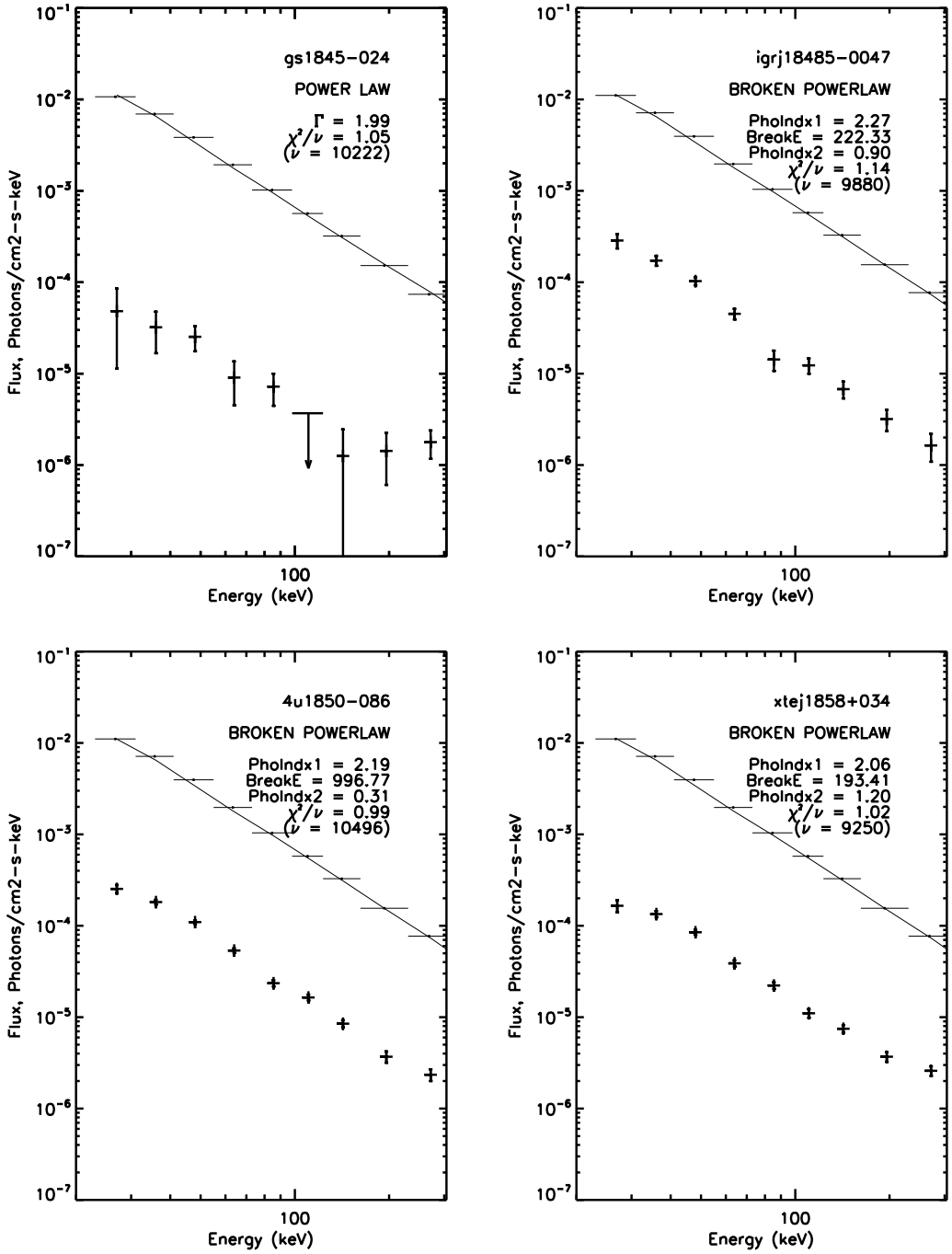

Figure C.1: continued.

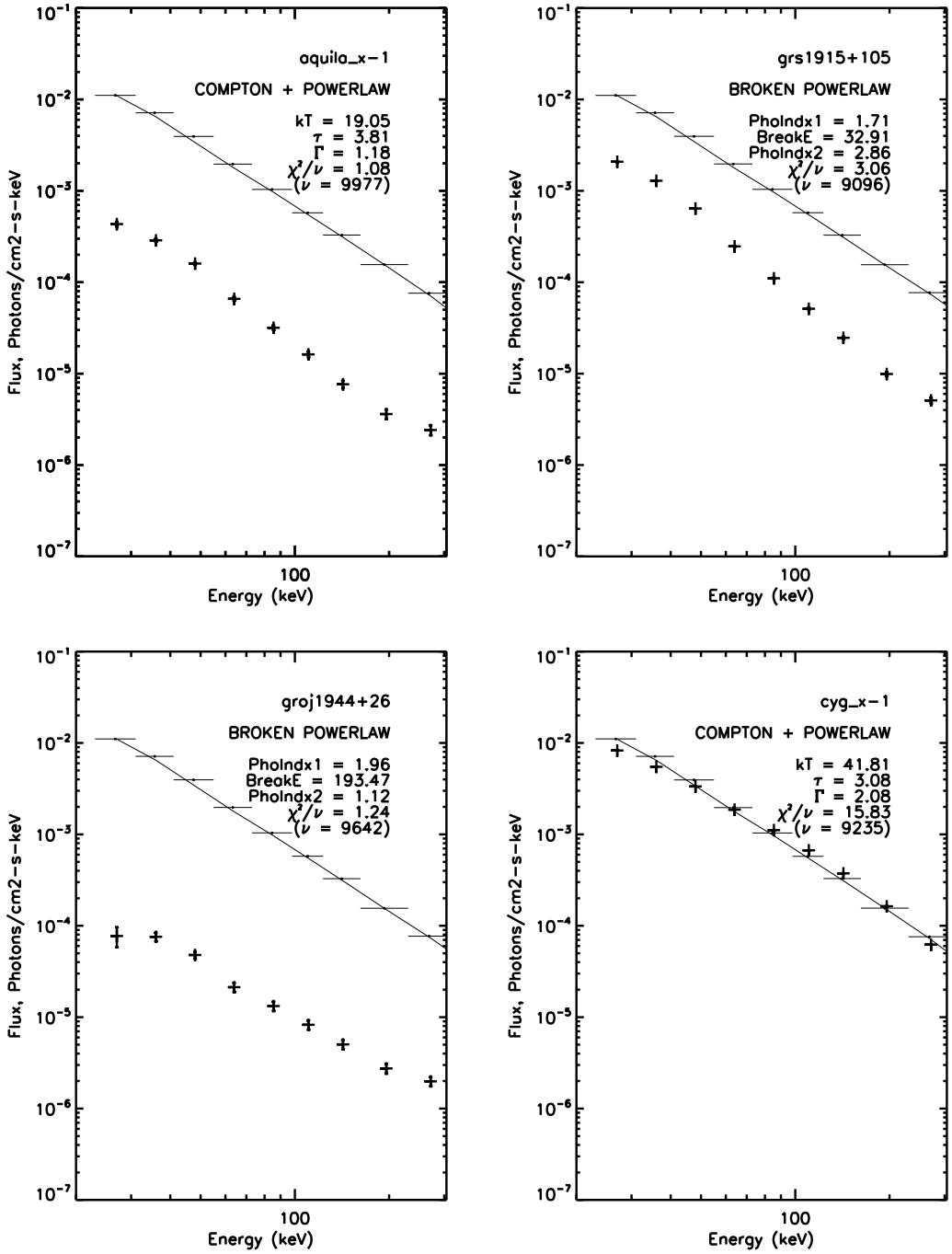

Figure C.1: continued.

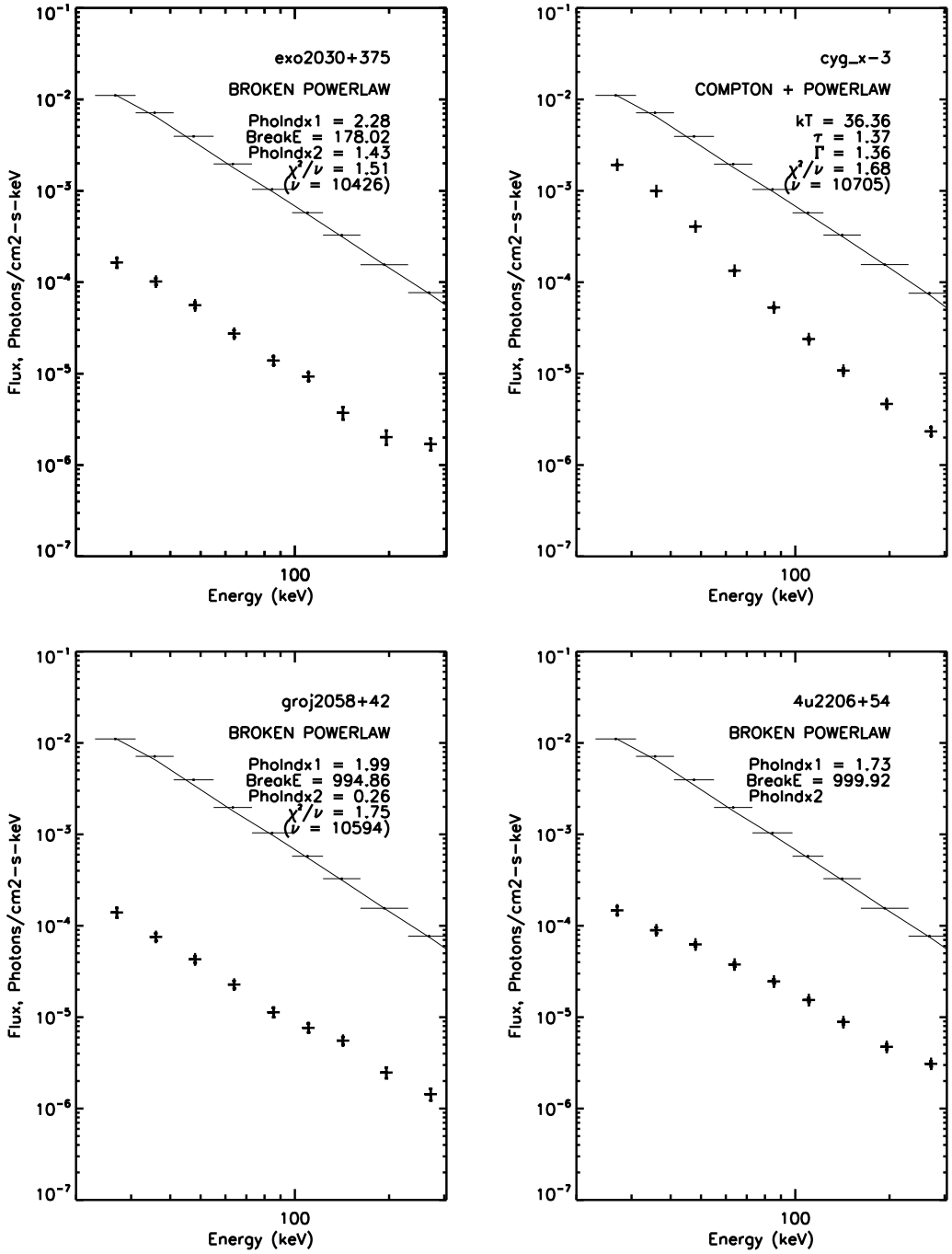

Figure C.1: continued.

Appendix D
EBOP 2013 Spectra for ON Galactic Plane Sources Subtract Averaged Blank Sources

Spectra for the ON Galactic Plane sources. Spectra are shown up to 2 MeV integrated over the full 9 years of the CGRO mission, with the phase-by-phase average of the ON-plane blank sources subtracted. The Crab spectrum is shown for comparison.

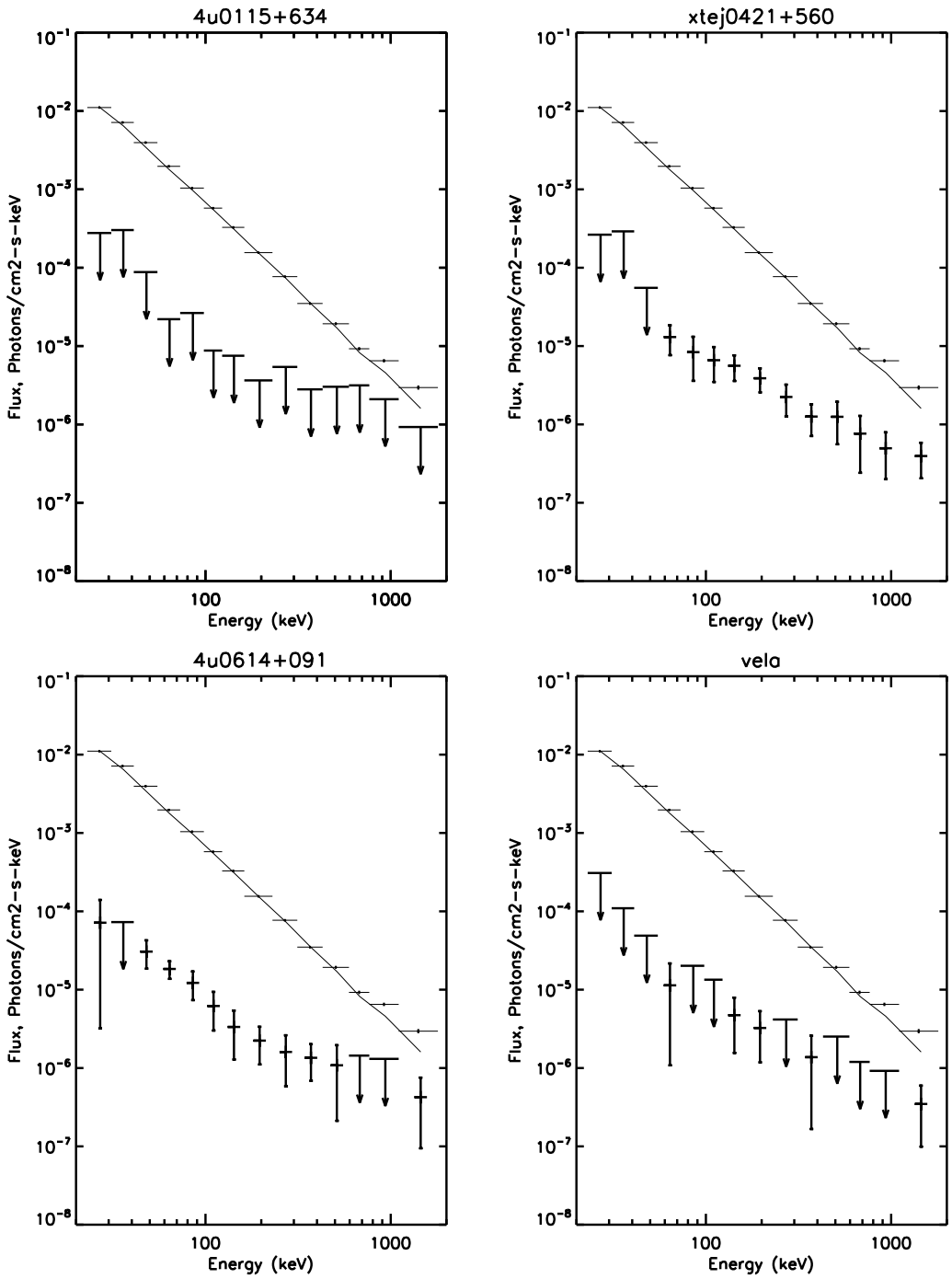

Figure D.1: EBOP 2013 spectra for ON Galactic Plane sources after blank sources subtraction.

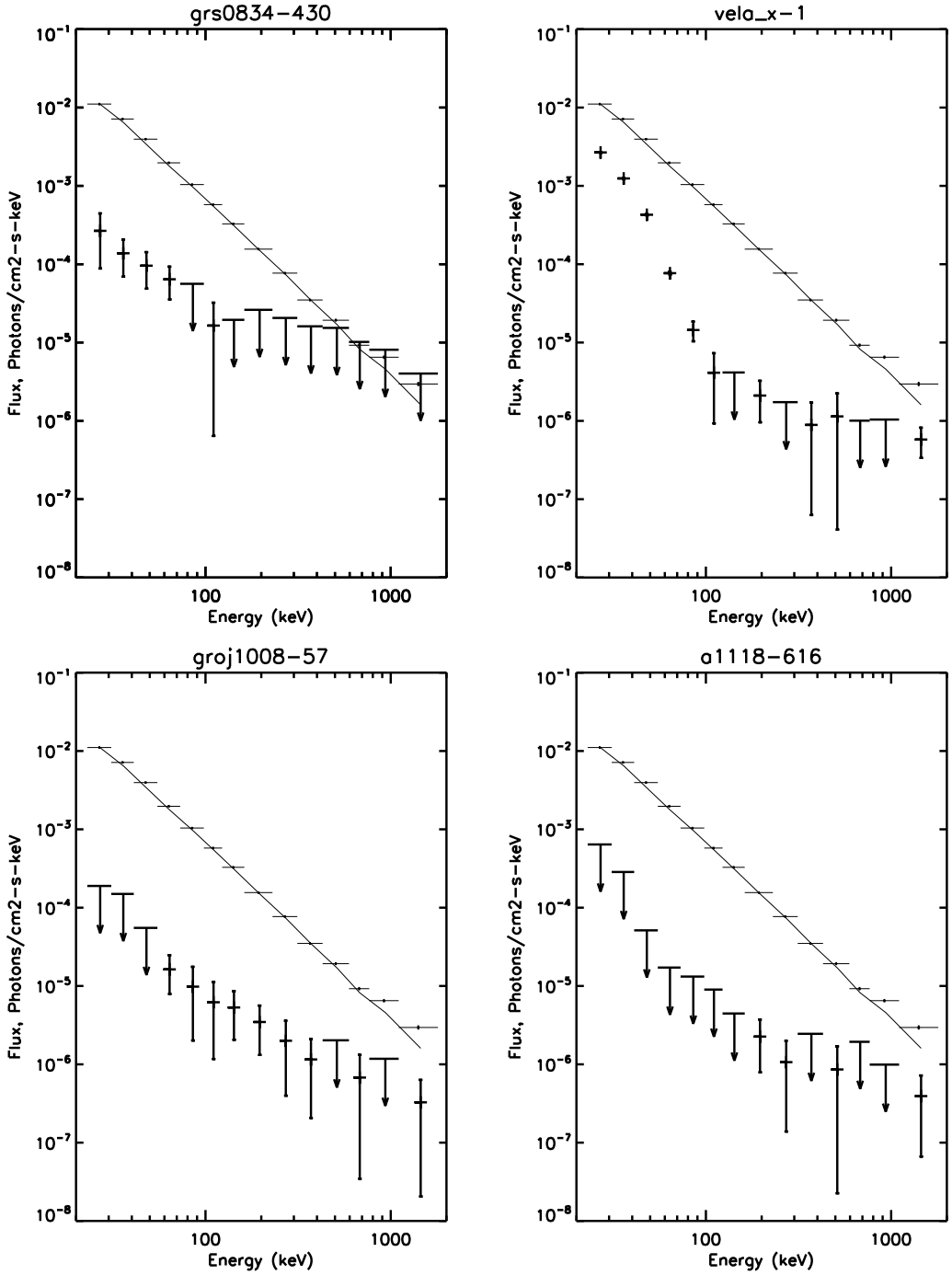

Figure D.1: continued.

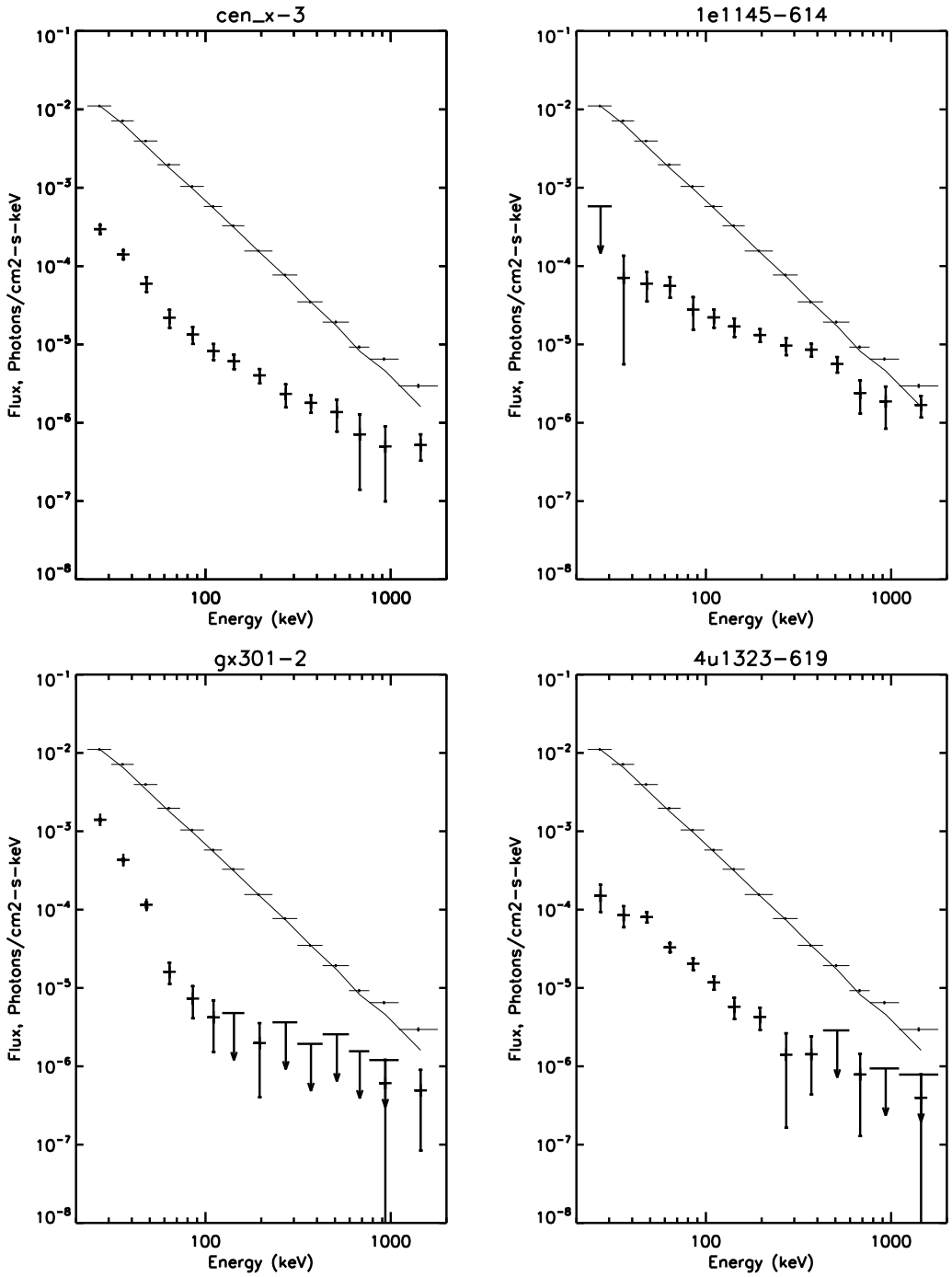

Figure D.1: continued.

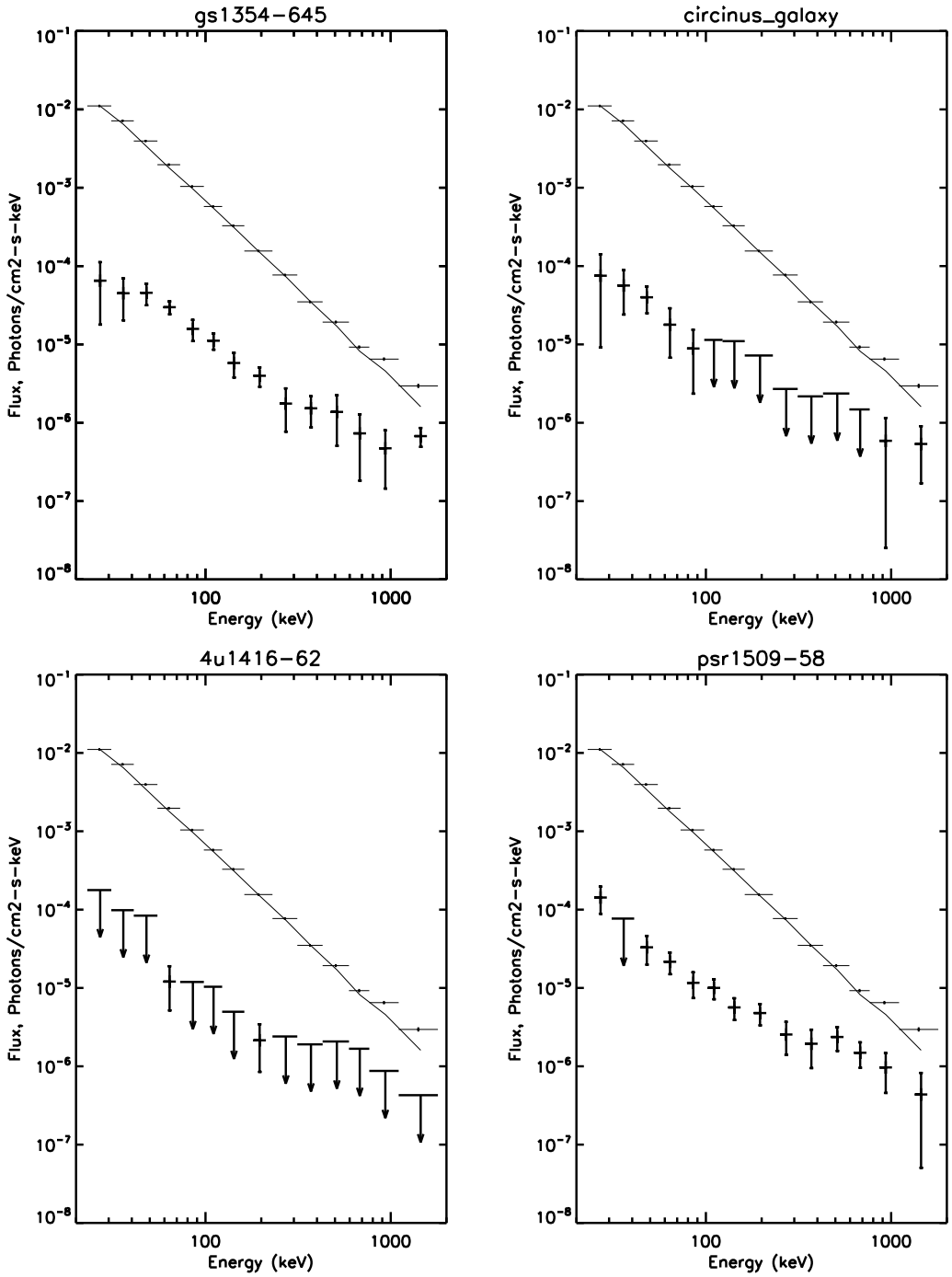

Figure D.1: continued.

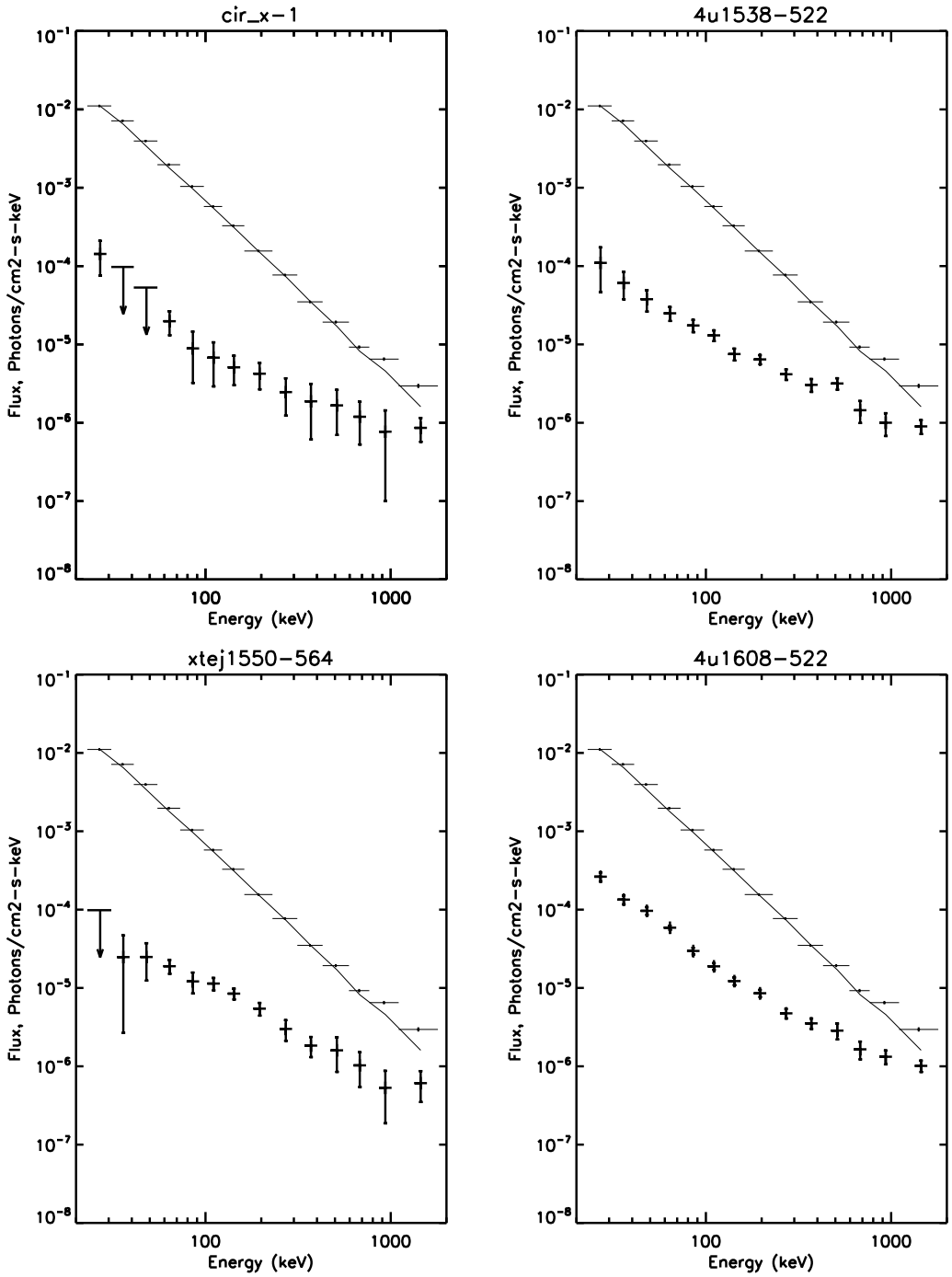

Figure D.1: continued.

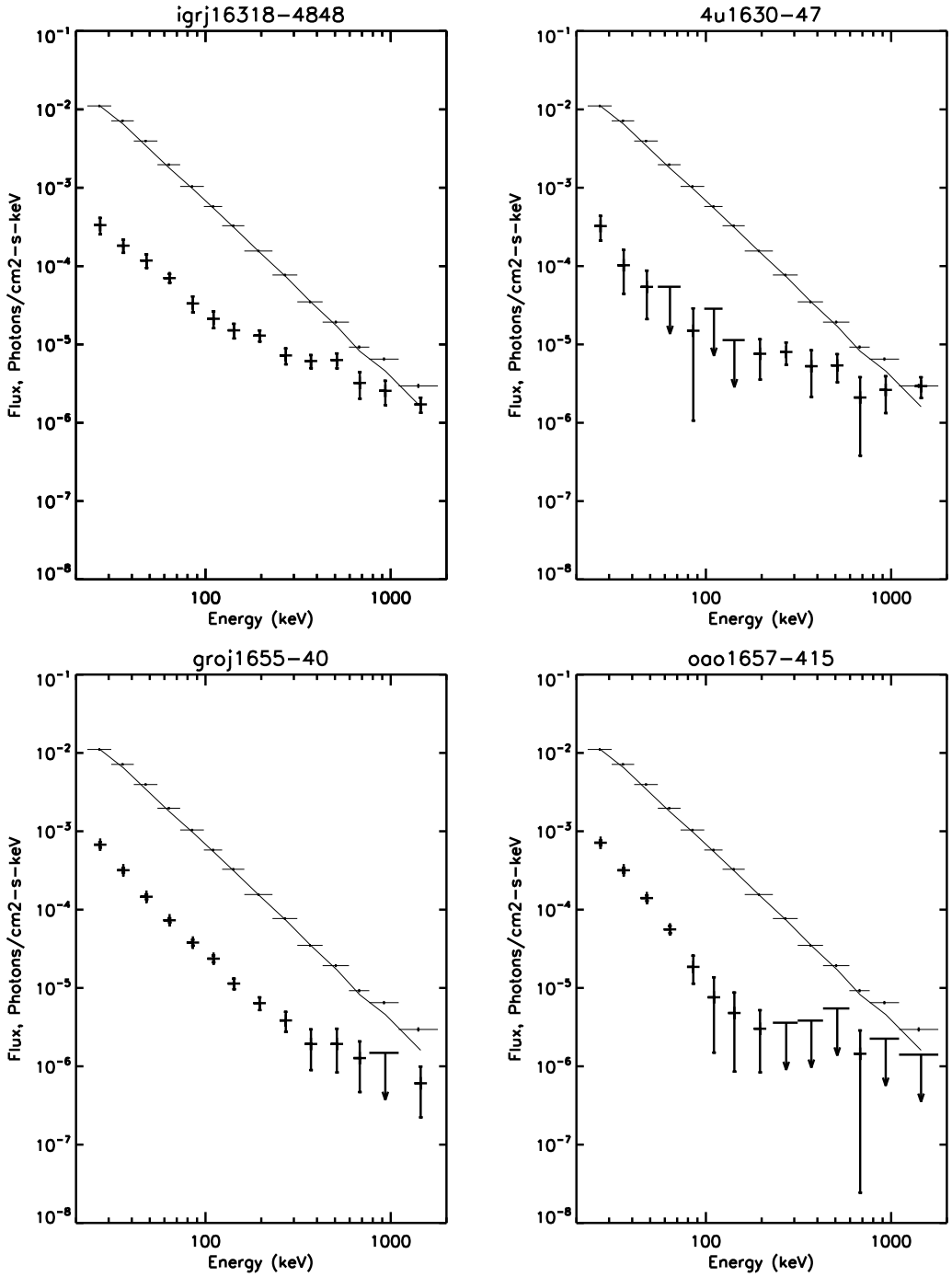

Figure D.1: continued.

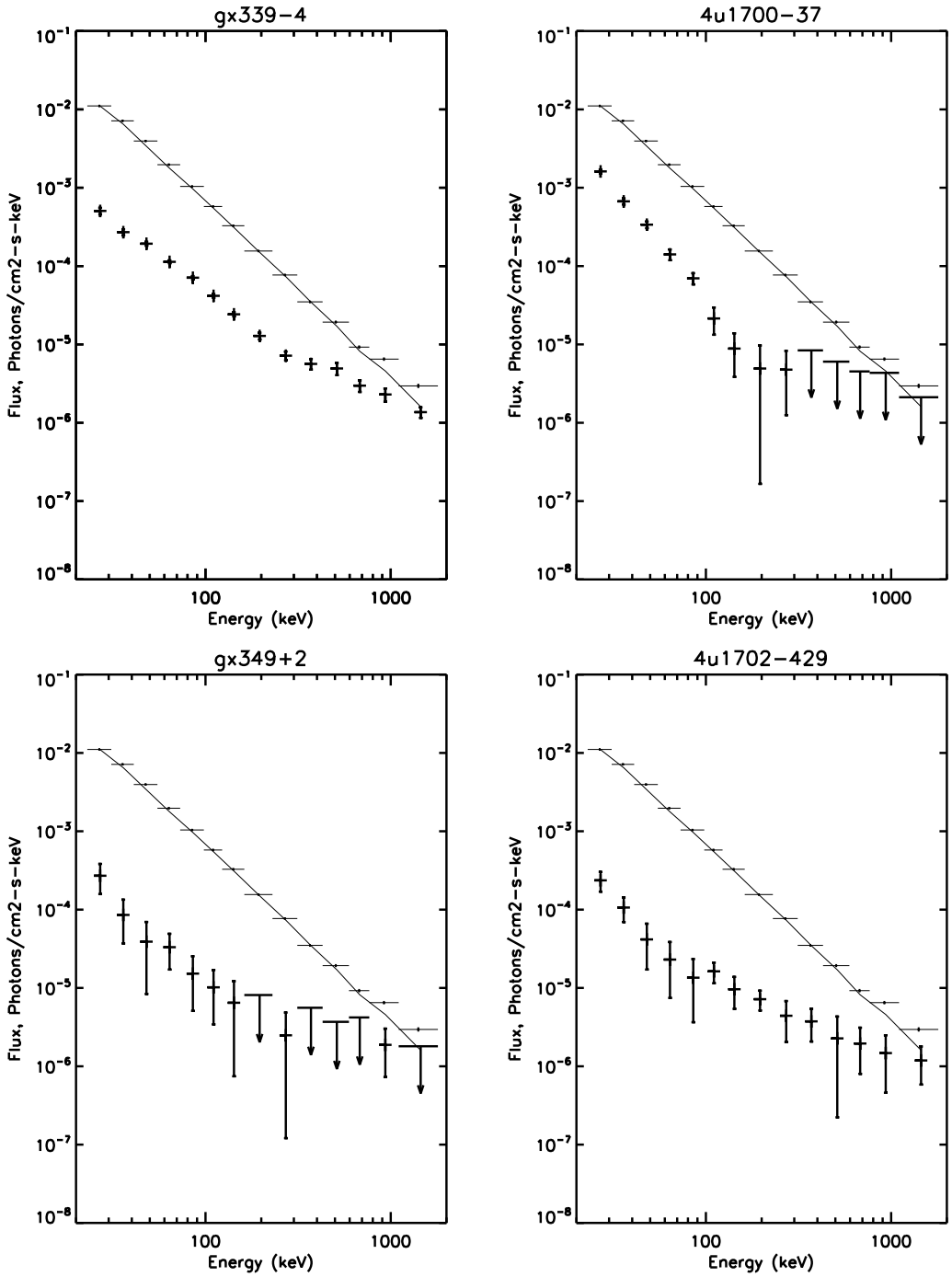

Figure D.1: continued.

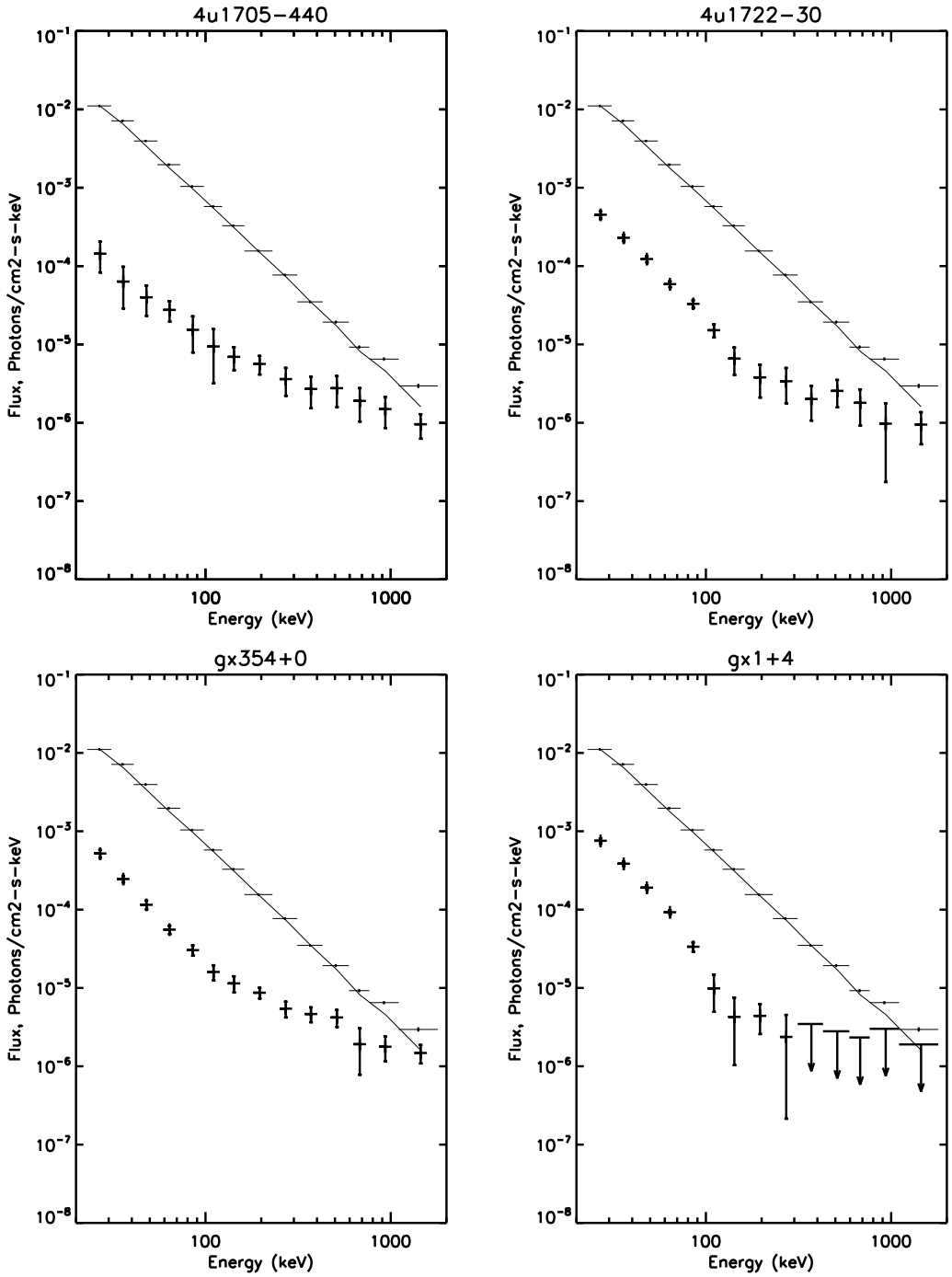

Figure D.1: continued.

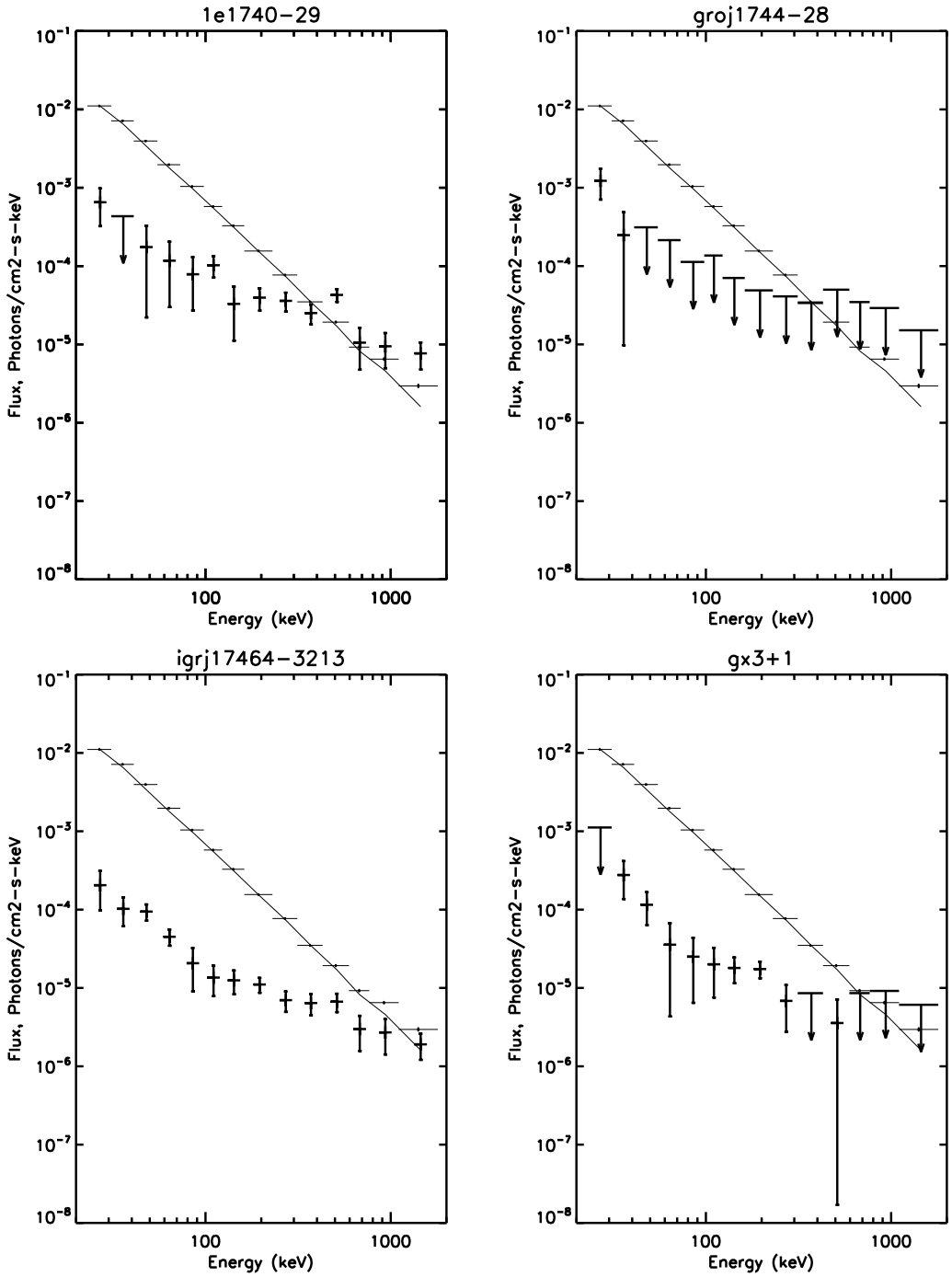

Figure D.1: continued.

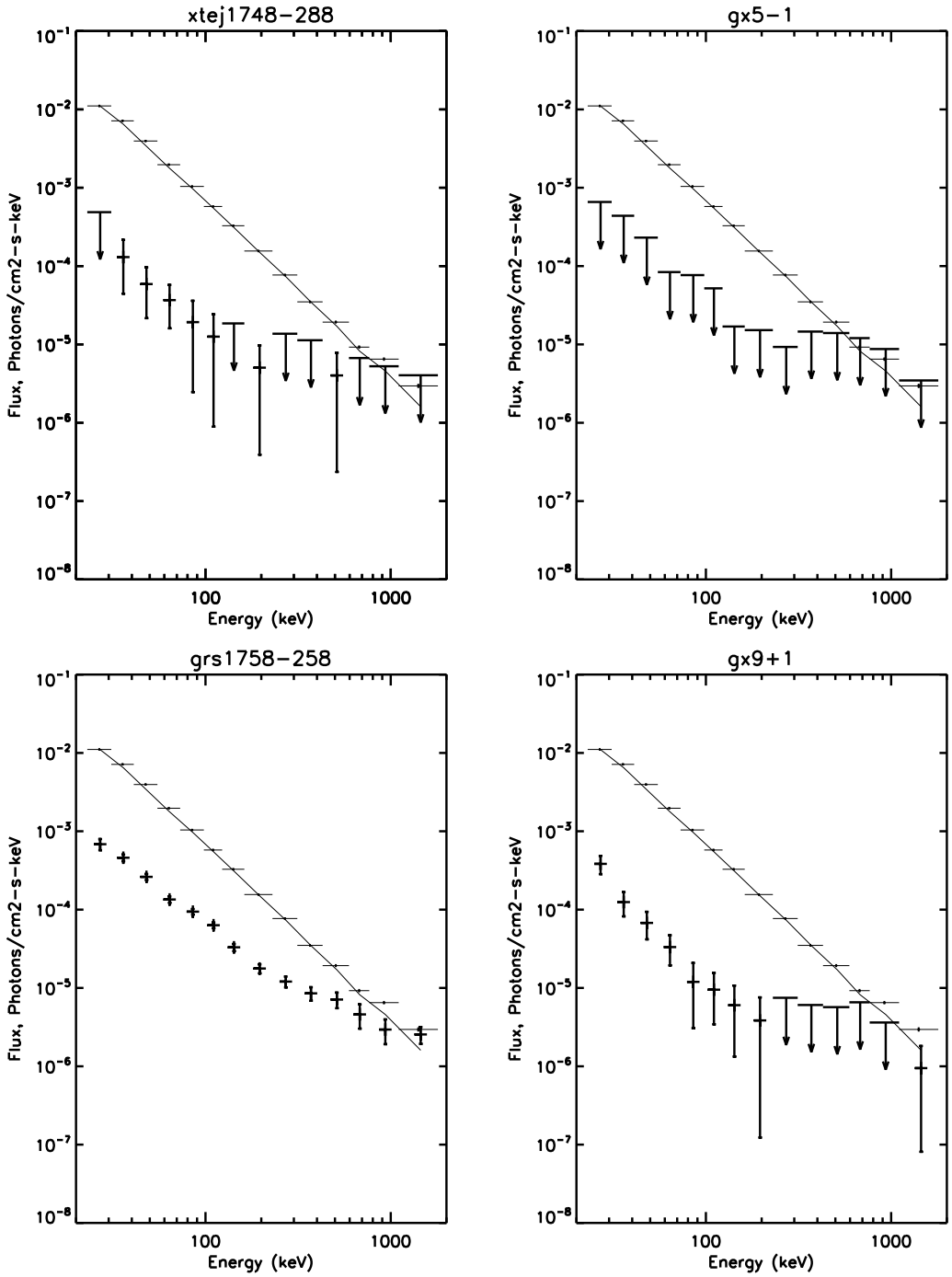

Figure D.1: continued.

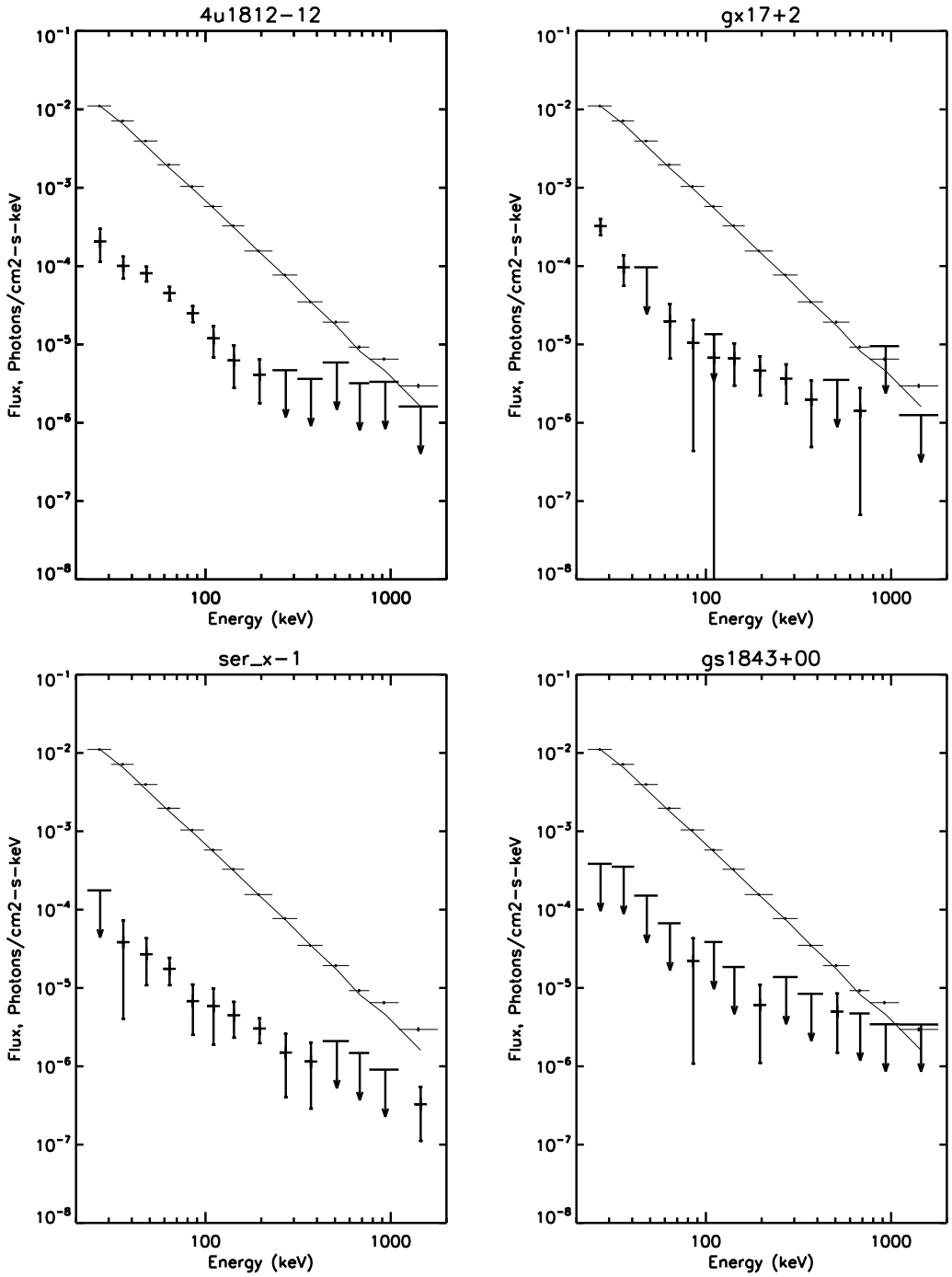

Figure D.1: continued.

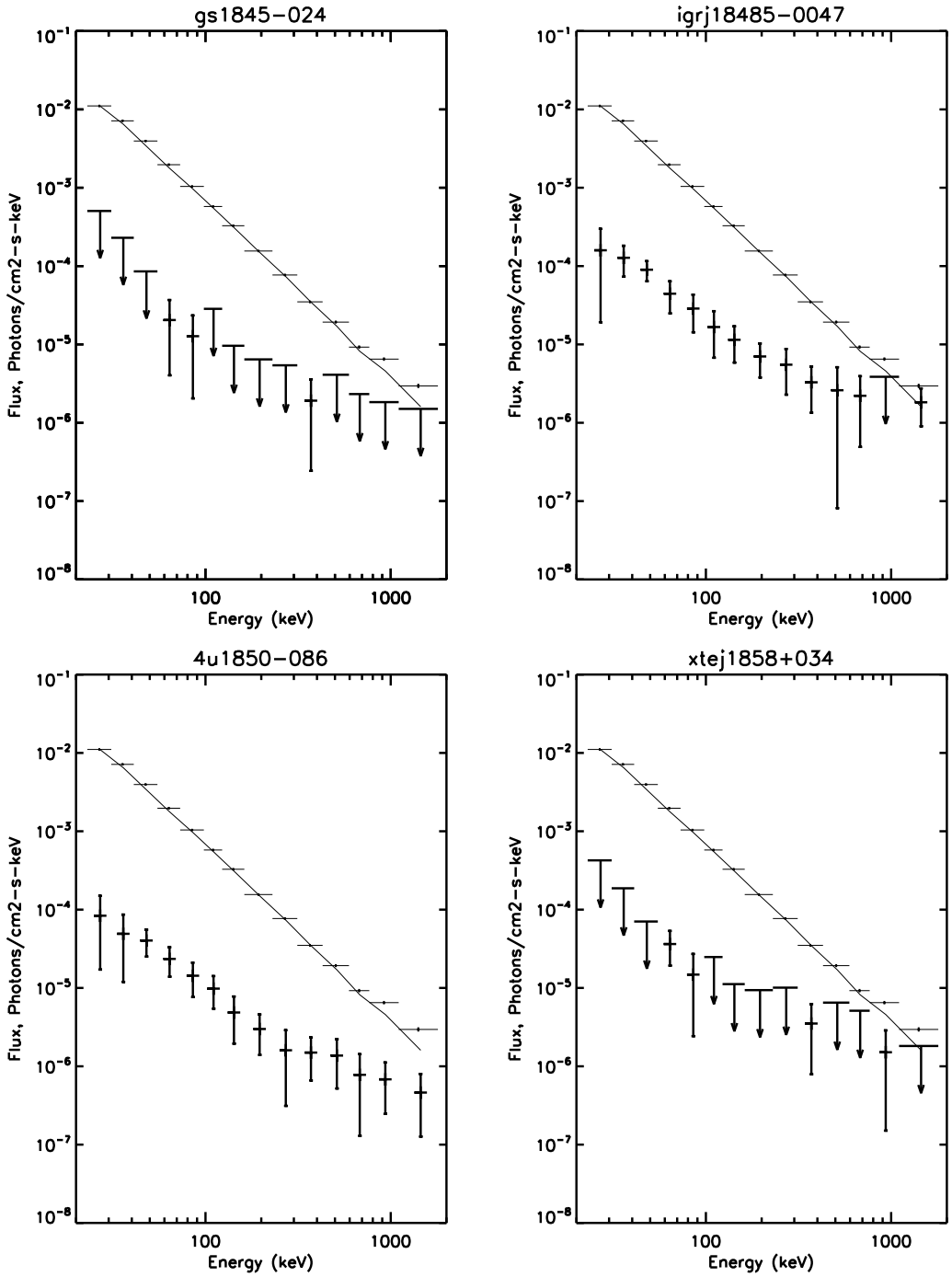

Figure D.1: continued.

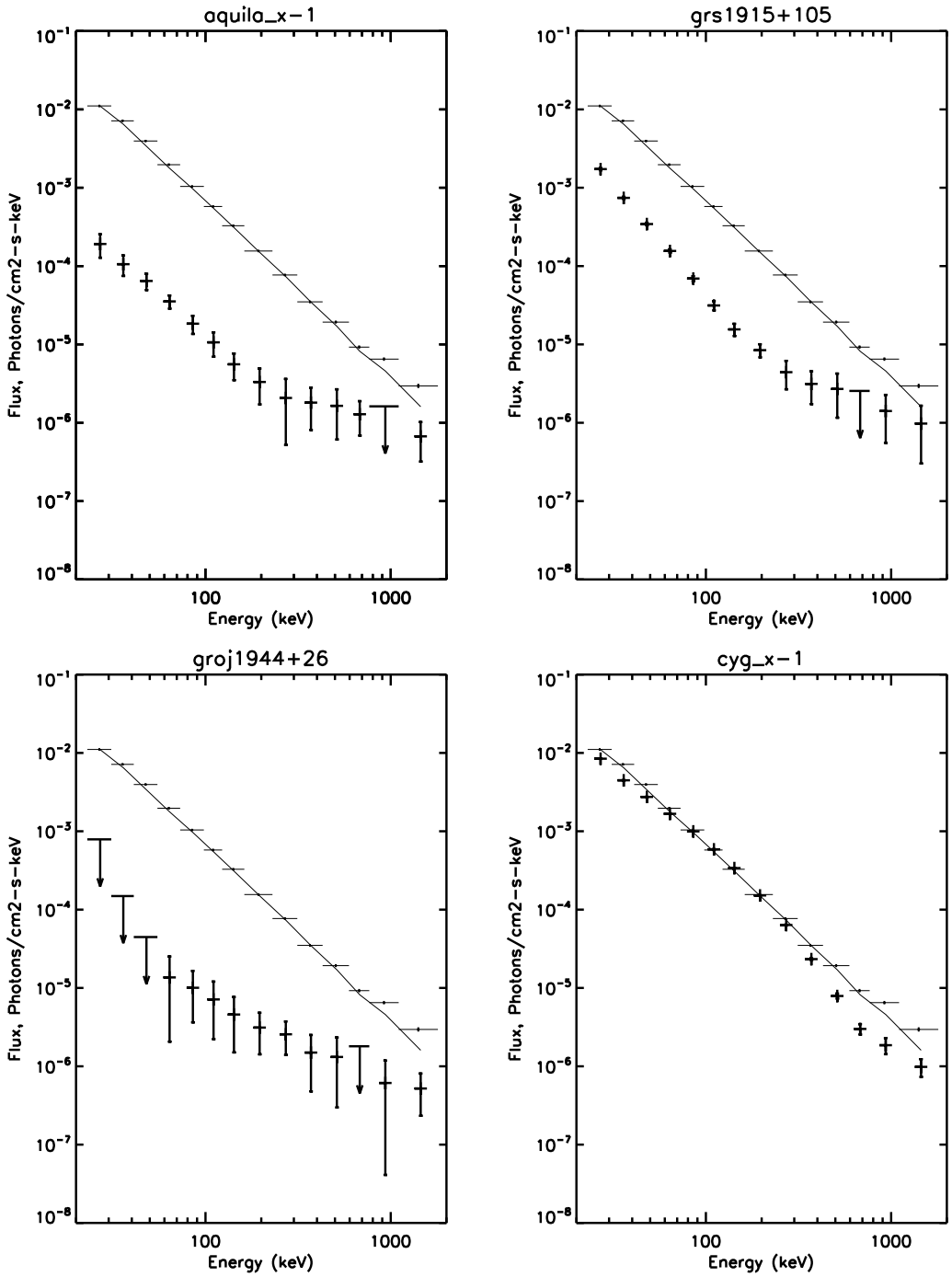

Figure D.1: continued.

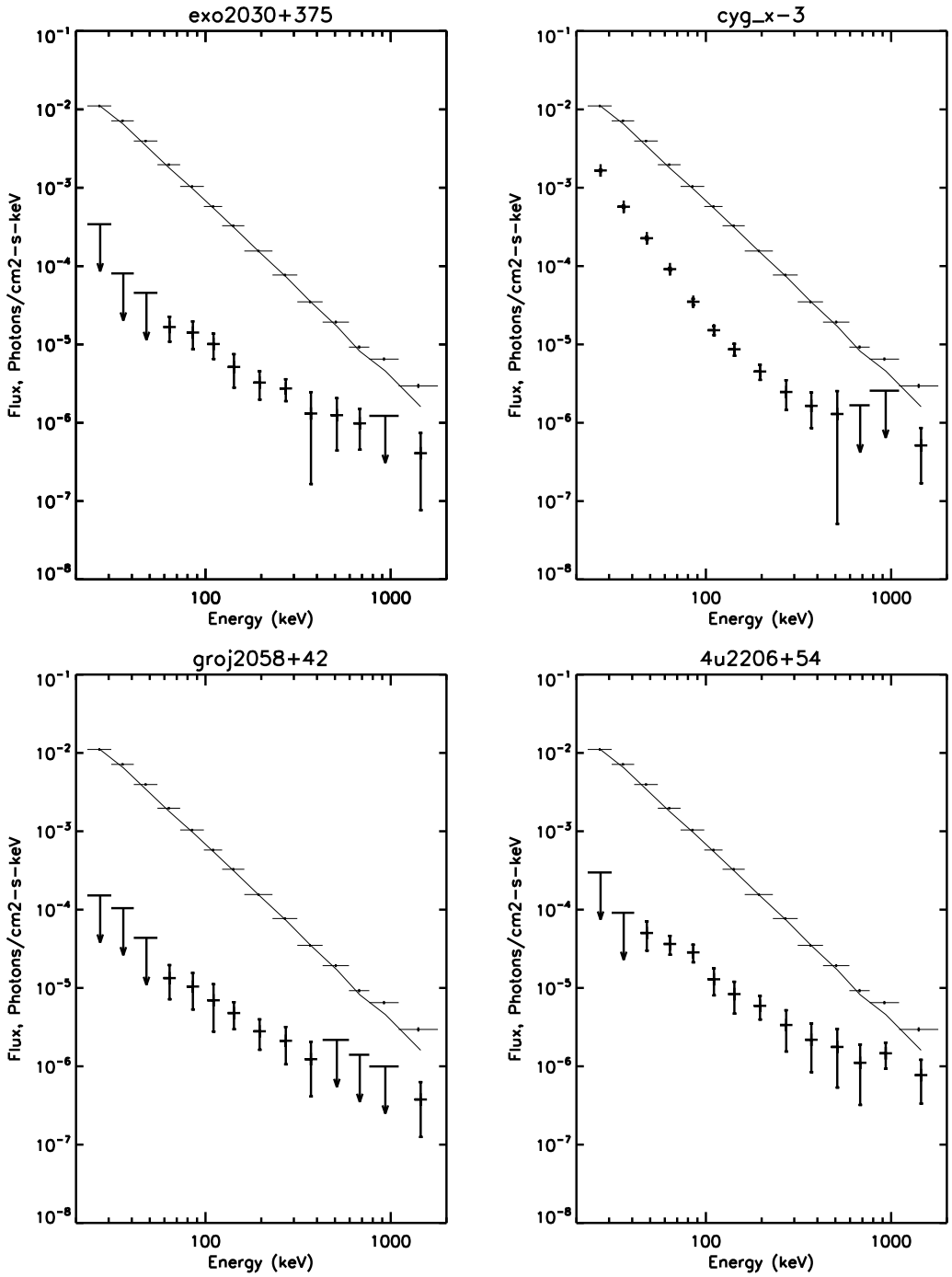

Figure D.1: continued.

Appendix E
Reprint Permission

E.1 Reprint Permission for Fig. 1.1

11/07/2013

Dear Dr. Krivonos,

I would like to use a figure from " INTEGRAL/IBIS nine-year Galactic Hard X-Ray Survey" paper from A&A 2012, 545, A27, in my PhD dissertation on Hard X-ray/soft Gmma-ray imaging with BATSE/CGRO. A&A requires that I get permission from one of the authors. I would like to use Fig. 5 showing the sky map around GC.

May I have your permission to use Fig. 5 in your paper?

Thanks

Yuan

11/07/2013

Dear Yuan,

yes, I confirm my permission to use Fig.5 from our paper in your PhD dissertation. Thank you for the interest in our work.

Best regards,

Roman Krivonos

SSL, UC Berkeley

krivonos@ssl.berkeley.edu

Astronomy and Astrophysics
Editor in Chief: T. Forveille

T. Forveille
Astronomy & Astrophysics
Observatoire de Paris
61, avenue de l'Observatoire
75014 Paris, France

Tel.: 33 0(1) 43 29 05 41
Fax: 33 0(1) 43 29 05 57
e-mail: annda.paris@obspm.fr
Web: http://www.annda.org

merging
Annales d'Astrophysique
Arkiv for Astronomi
Bulletin of the Astronomical Institutes of the Netherlands
Bulletin Astronomique
Journal des Observateurs
Zeitschrift for Astrophysik
Bulletin of the Astronomical Institutes of Czechoslovakia

Paris, November 8, 2013

Reprint Permission

Material:
Figure 5 from Krivonos et al. 2012, A&A, 545, A27

To be used in:
PhD dissertation, Louisiana State University

Permission granted to:
Yuan Zhang
Dept. of Physics and Astronomy, LSU
Email: yzhan16@tigers.lsu.edu

Thierry Forveille
A&A Editor-in-Chief

Sponsored by Argentina, Austria, Belgium, Brazil, Chile, Czech Republic, Denmark, Estonia, Finland, France, Germany, Greece, Hungary, Italy, Netherlands, Poland, Portugal, Slovak Republic, Spain, Sweden, and Switzerland.
Produced and distributed by EDP Sciences for ESO.

Figure E.1: The reprint permission from A&A for Fig. 1.1.

E.2 Reprint Permission for Fig. 1.6 and Fig. 5.1

11/07/2013

Dear Dr. Ling,

I would like to use two figures from "A BATSE Earth Occultation Catalog of 0.031.8 MeV Gamma-Ray Source Spectra and Light Curves for Phases 13 (1991-1994) " paper from The Astrophysical Journal Supplement Series, 127:79-124, 2000 March, in my PhD dissertation. ApJS requires that I get permission from one of the authors.

The figures are Fig. 3, EBOP flow chart, and Fig. 8, the spectra plots for 1E 1740-29 and 4U 1543-45.

May I have your permission to use these figures in your paper?

Thanks
Yuan

11/07/2013

Yuan,

You have my permission to use the two figures you requested in your PhD dissertation.

Jim

11/11/2013

Dear Yuan Zhang

Thank you very much for your permissions enquiry relating to material published previously in the journals of the American Astronomical Society.

On behalf of AAS, we are pleased to grant the necessary permission for your use of this material and we ask that the Society is acknowledged through the wording: "Reproduced by permission of the AAS". We note that you have already obtained the approval of the original authors for your planned reuse of their material.

Thank you again for your interest in the AAS journals.

Yours sincerely

Jill Membrey

Managing Editor, Copyright and Permissions

Vita

Yuan Zhang was born in Urumqi, Xinjiang, China, in August 1984. In 2002, she began her undergraduate studies at Tsinghua University, the Academic Talent Program for Physics and Mathematics. She pursued her concentration on Astrophysics with Dr. Shuang-Nan Zhang in her junior year. She earned a bachelor of science in Physics and Mathematics in 2006.

Yuan started her graduate study in Louisiana State University in Baton Rouge, LA, US, since 2006. She is in pursuit of the degree of Doctor of Philosophy in Physics in 2013 under the supervision of Dr. Michael L. Cherry, with a minor in Piano Pedagogy under the supervision of Dr. Pike.